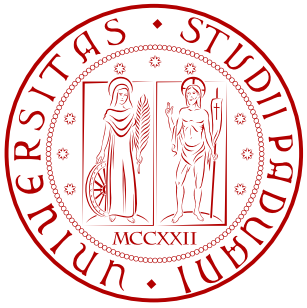

UNIVERSITÀ DEGLI STUDI DI PADOVA
Facoltà di Scienze MM.FF.NN.
Dipartimento di Fisica "G. Galilei"

Charm suppression in Pb–Pb collisions at the LHC measured using $\mathrm{D}^0 \to \mathrm{K}^-\pi^+$ reconstruction with the ALICE experiment

Direttore della Scuola: Ch.mo Prof. Andrea Vitturi

Supervisore: Ch.mo Prof. Giuseppe Viesti

Correlatore: Dott. Andrea Dainese

Dottorando: Davide Caffarri

Scuola di Dottorato di Ricerca in Fisica
Ciclo XXIV

Abstract

The thesis is focused on the measurement of the nuclear modification of charm quark production, in lead-lead collisions at the Large Hadron Collider. This observable is sensitive to the interaction of this quark with the high-density strongly interacting medium formed in ultra-relativistic heavy-ion collisions and, thus, to the properties of the state of matter. The partons traversing the medium lose energy via gluon radiation or elastic collisions with other partons already present in the medium. The charm quark allows to study the mass and colour charge dependences of the energy loss, since heavy quarks are expected to behave differently from light partons.

The measurement presented in this thesis is performed for the first time in nucleus-nucleus collisions, with the full reconstruction of D mesons via their hadronic decay. The strategy to reconstruct D^0 mesons in the two-prong decay $\mathrm{D}^0 \to \mathrm{K}^-\pi^+$, with the ALICE experiment, will be described. Results obtained in Pb–Pb collisions at $\sqrt{s_{\mathrm{NN}}} = 2.76$ TeV will be shown. In particular, the selection cut optimization was studied to compute the raw signal of D mesons with an invariant mass analysis. Selection and reconstruction efficiencies were considered with the detector acceptance, to correct for experimental effects. The corresponding data systematic uncertainties were evaluated in detail.

The comparison with the production cross section obtained in proton-proton collisions at the same energy allows then to compute the nuclear modification of D^0 meson, the first direct evidence of the charm quark energy loss. The measurement was compared with other open heavy flavour results and with light-charged hadrons suppression, measured at the LHC, to test the mass and colour charge dependences of the interaction with the medium. Results have been also compared with models that compute the charm quark energy loss using different theoretical approaches. These results were recently approved by the ALICE Collaboration and a publication has been proposed and is being review by the Collaboration.

Abstract

La tesi descrive la misura della modifica della produzione di quark charm, in collisioni tra ioni piombo al Large Hadron Collider. Questa misura permette di studiare l'interazione del quark charm con il mezzo ad alta densità e fortemente interagente, formato in collisioni di ioni pesanti ad energie ultra-relativistiche e le proprietà di questo stato della materia. I partoni che attraversano il mezzo perdono energia per emissione di gluoni (gluonnstrahlung) e collisioni elastiche con gli altri partoni del mezzo. Il quark charm permette di studiare come variano le proprietà dell'interazione in funzione della massa e della carica di colore del quark, poiché i modelli teorici prevedono un comportamento diverso dei quark pesanti nel mezzo, rispetto a quelli leggeri.

La misura presentata in questa tesi è la prima fatta in collisioni tra nuclei pesanti, attraverso la ricostruzione esclusiva dei mesoni D nel loro decadimento adronico. In particolare, verrà presentata la strategia di ricostruzione del mesone D^0 nel suo decadimento in due corpi $D^0 \to K^-\pi^+$, fatta con l'esperimento ALICE. Verranno, quindi, illustrati i risultati ottenuti con i dati di collisioni Pb–Pb a $\sqrt{s_{\rm NN}} = 2.76$ TeV. In particolare, è stata studiata l'ottimizzazione dei tagli di selezione per misurare il segnale, estratto con un'analisi di massa invariante. Le efficienze di selezione e ricostruzione delle particelle e gli effetti di accettanza del rivelatore, sono stati considerati con uno studio Monte Carlo, per considerare gli effetti sperimentali. Nella tesi viene anche descritto in dettaglio lo studio sulle incertezze sistematiche.

Il confronto delle sezioni d'urto di produzione ottenute in collisioni Pb–Pb e protone-protone, alla stessa energia, permette di misurare il fattore di modifica nucleare del mesone D^0, prima evidenza diretta di perdita energia del quark charm nel mezzo. La misura è stata confrontata con altri risultati ottenuti nel settore dei quark pesanti alla stessa energia, e con la soppressione degli adroni carichi, per valutare le dipendenze dalla massa e dalla carica di colore del quark, nella sua interazione con il mezzo. I risultati sono stati confrontati con modelli teorici che descrivono la perdita di energia del quark charm, utilizzando diversi metodi di calcolo. I risultati sono stati recentemente approvati dalla collaborazione ALICE, una pubblicazione è stata proposta ed è in fase di review nella collaborazione.

Contents

Introduction . . . 13

1 Physics of Quark Gluon Plasma and Ultra-relativistic heavy-ion collisions 15
1.1 The Quark Gluon Plasma Phase . . . 16
1.1.1 Quantum Chromo Dynamics . . . 16
1.1.2 QCD phase transition . . . 18
1.1.3 Lattice QCD calculations . . . 20
1.1.4 QGP in the laboratory: ultra-relativistic heavy ion collisions . . . 22
1.2 Characterization of the medium from RHIC to LHC . . . 24
1.2.1 Global event properties . . . 24
1.2.2 Collective Phenomena . . . 26
1.2.3 Strangeness enhancement . . . 31
1.2.4 Quarkonium suppression at SPS, RHIC and LHC . . . 33

2 Heavy flavour as a probe of the QGP at RHIC and LHC 39
2.1 Heavy flavour production in high energy hadron collisions . . . 39
2.1.1 Heavy flavour production in *pp* collisions . . . 39
2.1.2 Bjorken x estimate at the LHC . . . 40
2.1.3 pQCD prediction for heavy quark production at the LHC . . . 41
2.1.4 Heavy flavour in Pb–Pb collisions . . . 41
2.2 Energy loss effect in a strongly interacting medium . . . 43
2.2.1 Mechanisms of in-medium QCD energy loss . . . 44
2.2.2 Heavy-quark energy loss . . . 46
2.2.3 Jet quenching models . . . 47
2.3 Jet quenching results at RHIC and LHC . . . 54
2.3.1 Charged hadron suppression . . . 54
2.3.2 Di-hadron correlations . . . 57
2.3.3 Jet suppression . . . 57
2.3.4 Electromagnetic probes . . . 59
2.4 Open heavy flavour production measurements . . . 60
2.4.1 Measurements in *pp* collisions . . . 60
2.4.2 Measurements in A–A collisions . . . 62

3 A Large Ion Collider Experiment 65
3.1 The Large Hadron Collider - LHC . . . 65
3.2 Luminosity and luminous region . . . 68
3.2.1 Interaction region parameters in 2010 data taking . . . 69
3.3 The ALICE experiment: Detector Layout . . . 70

3.4 Central rapidity detectors . . . 71
3.4.1 Tracking detectors . . . 71
3.4.2 Particle Identification detectors . . . 75
3.5 Forward detectors . . . 78
3.5.1 Muon spectrometer . . . 78
3.5.2 V0 detector . . . 79
3.5.3 Zero Degree Calorimeters . . . 79
3.5.4 Time Zero Detector -T0 . . . 80
3.6 Trigger System . . . 80
3.7 ALICE offline computing . . . 82
3.7.1 The AliRoot framework . . . 82
3.7.2 AliEn: ALICE analysis framework on the GRID . . . 83
3.8 ALICE track reconstruction . . . 83
3.9 ITS alignment . . . 84
3.10 ITS tracking performance . . . 87

4 Interaction vertex reconstruction in the ALICE detector 91
4.1 Primary vertex reconstruction in ALICE . . . 91
4.1.1 SPD vertexers . . . 93
4.1.2 VertexerTracks . . . 94
4.2 Online and offline vertex measurements in ALICE . . . 95
4.3 Vertex reconstruction performance . . . 97
4.3.1 Performance in *pp* collisions . . . 99
4.3.2 Vertexer results in Pb–Pb collisions . . . 103
4.4 Mean vertex constraint . . . 106
4.5 Monitoring of the beam spot parameters . . . 108

5 $D^0 \to K^-\pi^+$ reconstrunction in Pb–Pb collisions 113
5.1 D mesons reconstruction strategy in ALICE . . . 113
5.2 D^0 in Pb–Pb collisions . . . 116
5.2.1 Raw signal extraction . . . 116
5.2.2 Efficiency determination . . . 124
5.2.3 Feed-down correction . . . 126
5.2.4 Systematic uncertainties on the invariant yield . . . 128
5.2.5 D^0 invariant yield in Pb–Pb collisions . . . 131
5.3 D^0 in *pp* collisions at $\sqrt{s} = 7$ TeV and $\sqrt{s} = 2.76$ TeV . . . 132
5.3.1 Normalization to the cross section . . . 133
5.3.2 D^0 cross section at $\sqrt{s} = 7$ TeV . . . 134
5.3.3 D^0 cross section at $\sqrt{s} = 2.76$ TeV . . . 136

6 D^0 nuclear modification factor 139
6.1 D^0 Nuclear Modification Factor in Pb–Pb collisions: ingredients . . . 139
6.1.1 *pp* scaled reference . . . 139
6.1.2 *b* quark energy loss hypothesis . . . 142
6.2 D^0 Nuclear Modification Factor in Pb–Pb collisions: results . . . 143
6.2.1 Systematic uncertainties on R_{AA} . . . 143
6.2.2 R_{AA} as a function of transverse momentum . . . 145
6.2.3 R_{AA} as a function of centrality . . . 145

6.2.4 Comparison with D^+ and D^{*+} . . . 147
6.3 D mesons nuclear modification factor: comparisons . . . 148
6.3.1 Nuclear shadowing . . . 148
6.3.2 Charged hadrons . . . 148
6.3.3 Comparison with other open heavy flavor measurements . . . 149
6.3.4 Comparison with theoretical models . . . 150
Conclusions . . . 156

Introduction

This thesis reports the results on the first measurement of D mesons high-p_{t} suppression in Pb–Pb collisions at $\sqrt{s_{\mathrm{NN}}} = 2.76$ TeV, using the $\mathrm{D}^0 \to \mathrm{K}^-\pi^+$ reconstruction with the ALICE detector.

The interaction between quarks is described with the Quantum Cromo Dynamics (QCD) theory, where the colour charge is the conserved quantity from the theory invariance. The main difference between QCD and Quantum Electro Dynamics (QED) is the self-interaction of the boson carrier of the colour charge, the gluons. The gluon self-coupling is related to two effects that are peculiar of the subnuclear interaction: asymptotic freedom and confinement. Asymptotic freedom allows to consider partons as free within hadrons, in processes with high momentum transfer, where the coupling of the interaction is very small. On the other side, the coupling of the strong interaction increases when the exchanged momentum decreases and it reaches a potential wall for distances of the order of the hadron size. Quarks and gluons are thus confined within hadrons.

On the basis of thermodynamical considerations and QCD calculations, nuclear matter is sensitive to modifications of its temperature and density, which can change its state as it happens for water. For high temperature or density of the system, a deconfined Quark Gluon Plasma (QGP) phase is expected. In these conditions, the density of gluons and quarks becomes so high that partons are interacting, but not confined within hadrons anymore. The hot Bing Bang model of cosmology assumes that, after the electro-weak phase transition, the expanding Universe was in a state of plasma of deconfined partons, that would have reached the hadronic phase during the expansion of the system, about 1 μs after the Big Bang.

The deconfined phase can be studied experimentally with ultra-relativistic heavy-ion collisions, since the energy density and temperature reached in these collisions would allow to form the QGP and to explore different regions of the QCD phase diagram. At high energy, thousands of partons are produced in the following nucleon - nucleon collisions, forming a "fireball" in local thermal equilibrium, that rapidly expands and cools down. Hadronization occurs only when the system temperature falls below the critical temperature of the phase transition. Early experiments with heavy ion collisions started in 1990s at the Alternating Gradient Synchrotron (AGS) and at the Super Proton Synchrotron (SPS) at CERN, at collision energies of $\sqrt{s_{\mathrm{NN}}} = 4.6,\ 17.2$ GeV respectively. First indications of the deconfined phase were observed at the SPS, in terms of strangeness enhancement and J/Ψ suppression. In 2000, the Relativistic Heavy-Ion Collider (RHIC) started delivering Au–Au collisions at $\sqrt{s_{\mathrm{NN}}} = 200$ GeV, allowing to measure several properties of deconfined matter. In November 2010, the first heavy-ion collisions were delivered by the Large Hadron Collider (LHC) at $\sqrt{s_{\mathrm{NN}}} = 2.76$ TeV.

The first chapter of this thesis describes the phase transition that foresees the QGP formation and the lattice QCD calculation that allows to predict some of the thermodynamical parameters of the transition. After a more detailed explanation on the dynamics

and geometry of the ion-ion (A–A) collisions, the second part of the chapter is devoted to the main measurements that allow to characterize the deconfined medium created in heavy ion collisions, from RHIC to LHC. The review of the results is aimed at comparing the properties of the medium formed at RHIC energies with the one formed at the LHC, in a new energy regime. The main results obtained with the 2010 Pb–Pb run were presented at the conference Quark Matter 2011 in Annecy.

The second chapter of the thesis is focused on heavy quark production in *pp* and Pb–Pb collisions. Heavy quarks are important probes to study the deconfined matter, since they are produced in hard scatterings, during the very first stage of the collision. They can experience the interaction with the medium via energy loss due to gluon radiation and elastic collisions with other partons. The energy loss mechanisms are described in the chapter, together with different theoretical models that study the dynamics of interactions with a coloured deconfined medium. The chapter ends with a review of recent measurements on heavy quark production, in *pp* and A–A collisions. The study of heavy quark energy loss is performed measuring the nuclear modification factor ($R_{\rm AA}$), that compares the production in A–A and in *pp* collisions (scaled by the number of binary collisions). The nuclear modification factor quantifies deviations from binary scaling that indicate medium effects such as energy loss. Heavy quarks are foreseen to loose less energy via gluon emission, since the emitted gluon spectra is suppressed by the introduction of a mass term in the heavy quark propagator. Collisional energy loss is usually a small correction to the total energy loss, but for heavy quarks with low $p_{\rm t}$ can become a relevant contribution.

A Large Ion Collider Experiment (ALICE) is the heavy-ion dedicated experiment at the LHC. Chapter 3 is focused on the performance of the detector, reached few months after the beginning of the *pp* data taking. In ALICE, the charm analysis is based on the reconstruction of secondary decay vertices, displaced of about few hundred microns from the primary vertex. The Silicon Pixel Detector (SPD) is the closest detector to the beam pipe and it is the main part of the Inner Tracking System (ITS) used to study heavy flavour decay, like $\rm D^0 \to K^-\pi^+$. The Particle IDentification (PID) is another important selection that allows to reduce the background coming from combinatorial association of pions. The kaon identification is performed with the Time-Of-Flight (TOF) detector and the Time Projection Chamber (TPC).

A good resolution on the primary vertex is necessary to separate displaced secondary vertices from charm decays. The primary vertex reconstruction is one of the main checks needed at the beginning of the data taking for a new experiment. ALICE has two main procedures to reconstruct the primary vertex. The first exploits only SPD information, using a local reconstruction of data, without the full information of the event. The second algorithm is based on the full tracks and it is more precise. Heavy flavour secondary decays are reconstructed with almost the same procedure used in the track vertex algorithm. Results on the performance of the two procedures are shown, considering their resolution and efficiency.

The fifth chapter presents the analysis of $\rm D^0$ meson production in Pb–Pb collisions. These mesons are reconstructed via their two particles hadronic decay channel $\rm D^0 \to K^-\pi^+$, exploiting the secondary vertex reconstruction and the PID selection. In the chapter, the measurement strategy is described, starting from the raw yields extraction, based on a invariant mass analysis. The raw yields are then corrected for selection and reconstruction efficiencies and for detector acceptance. A Monte Carlo based approach has been used to subtract the fraction of D mesons coming from beauty hadron decays, in order to consider only prompt charmed mesons. The results are the $\rm D^0$ transverse momentum distributions, for two different centrality classes: central and semi-peripheral.

The last chapter describes the measurement of the D^0 nuclear modification factor (R_{AA}). The measurement has been performed as a function of the transverse momentum of the meson and of the centrality of the collision. The nuclear modification factor is computed using the charm production cross section in *pp* collisions at the same energy. Since the LHC delivers *pp* collisions at $\sqrt{s} = 7$ TeV, a scaling procedure, based on pQCD theoretical predictions, has been developed to compute the charm cross section at $\sqrt{s} = 2.76$ TeV. After an introduction on the ingredients needed to compute the R_{AA}, results are compared to those for D^+, D^{*+} and to other open heavy flavour measurements. As introduced in the second chapter, heavy quark energy loss can be studied by comparing the R_{AA} of D mesons to that of light-flavour charged hadrons. This comparison is also shown in this chapter, together with a comparison to several theoretical models that implement charm energy loss in the strongly interacting, hot and dense medium.

1 Physics of Quark Gluon Plasma and Ultra-relativistic heavy-ion collisions

The Quantum Chromo Dynamics (QCD) is the theory of the strong interactions between partons. It foresees that strongly interacting (nuclear) matter can exist in different phases by varying the temperature and the density of the system. Extreme conditions of high temperature and energy density for the nuclear matter can be obtained with ultra-relativistic heavy-ion collisions. These collisions allow to recreate a state of matter, called Quark-Gluon Plasma where quarks and gluons are interacting between themselves without be confined into hadrons. According to the hot big bang model, this state of the nuclear matter should be the one created after the electro-weak phase transition, 10^{-6} s after the Big Bang. Lattice QCD calculations predict that the critical temperature, for which this state of matter can occur, is $T_{\mathrm{c}} = 170$ MeV, corresponding to a critical energy density $\epsilon_c \sim 0.7$ GeV/fm^3.

Since about 25 years, the studies on heavy-ion collisions are ongoing to discovery the deconfined phase and to understand its properties. The first attempts were done in 1986 with light nuclei of silicium at the Alternating Gradient Synchrotron (AGS) at the Brookhaven National Laboratory (BNL) and at the Super Proton Synchrotron (SPS) at CERN, with collisions of sulphur nuclei. At the beginning of 1990s, both facilities switched to heavier nuclei: gold ions at the AGS accelerated at $\sqrt{s_{\mathrm{NN}}} = 4.6$ GeV and lead nuclei at the SPS at $\sqrt{s_{\mathrm{NN}}} = 17.2$ GeV. At the SPS, the first indications of the creation of the deconfined phase were found. BNL then decided to built the Relativistic Heavy-Ion Collider (RHIC), where heavy-ions (mainly Au and Cu) collide at the energy of $\sqrt{s_{\mathrm{NN}}} = 200$ GeV. The higher collision energy meant a larger, hotter and longer living QGP phase than what observed at the SPS. Last year, another step in this direction has been achieved when the Large Hadron Collider (LHC) delivered Pb–Pb collisions at $\sqrt{s_{\mathrm{NN}}} = 2.76$ TeV, half of its design energy. At the moment, the increase in the energy of the collisions is 15 times what was achievable at RHIC.

In this first chapter a quick review of Quantum Chromo Dynamics will be introduced in order to understand the basic properties that lead to the formation of the deconfined phase. The temperature of the QGP formation and other termodynamical quantities of the deconfined phase can be studied with lattice numerical calculations. The second part of this chapter is then dedicated to a summary of the main measurement that allowed to characterize this phase at the SPS, at RHIC and at the LHC. The main results like the strangeness enhancement and the J/Ψ suppression will be described, together with other important measurements, to understand the properties of the QGP.

1.1 The Quark Gluon Plasma Phase

1.1.1 Quantum Chromo Dynamics

The interaction between protons and neutrons within the nucleus has been studied since the discovery of the atomic structure. Protons were postulated to be held together by an interaction stronger than the electromagnetic one. In 1932 Chadwich discovered the neutron and its presence within the nucleus confirmed that the nuclear force was totally charge blind [1]. The introduction of quarks as elementary constituents of protons, neutrons and all other hadrons opened new possibilities to understand the basis of nuclear force [2]. The *Quantum Electro-Dynamics* - QED has been the first local gauge theory that explained the interaction between electrons and photons through the electric charge current, introduced by an Abelian group U(1) [3]. For the strong force, quarks spin and flavours were used to classify hadrons in multiplets, but they were not able to describe the quarks interaction. The interpretation of the quark-gluon interaction as a gauge field theory has been the main theoretical development in order to describe the deep nature of this interaction. Only with the introduction of the quark colour charge and the local gauge symmetry $\mathrm{SU(3)_{colour}}$, it was possibile to define *Quantum Chromo-Dynamics* - QCD, the most important theory that allows to explain parton interactions within hadrons [4]. Let's consider a quark, represented by the triplet:

$$\psi = \begin{pmatrix} q_{\mathrm{red}} \\ q_{\mathrm{blue}} \\ q_{\mathrm{green}} \end{pmatrix} \tag{1.1}$$

Similarly to the QED case, it is possible to apply the formalism of the Yang-Mills theories at the group $\mathrm{SU(3)_{colour}}$ and obtain the QCD Lagrangian

$$\mathcal{L} = \sum_{i=1}^{N_f} \bar{\psi}_i \left(i\gamma^\mu \mathcal{D}_\mu - m_i \right) \psi_i - \frac{1}{4} \sum_{A=1}^{8} \left(F^A_{\mu\nu} F^{A\mu\nu} \right). \tag{1.2}$$

The first term of the equation sums over the number of flavours (N_f), while the second one is over the number of gauge bosons foreseen in the theory. The gauge covariant derivative relates the coupling of the interaction between the fundamental constituent g and the gauge fields $\mathbf{G}_\mu$, bearer of the colour interaction, the gluons:

$$\mathcal{D}_\mu = \partial_\mu - ig\mathbf{G}_\mu \tag{1.3}$$

$$\mathbf{G}_\mu = \sum_A t^A G^A_\mu. \tag{1.4}$$

Since gluons are colour charged, they can interact with each other, showing an opposite behaviour with respect to photons that are not charged. QCD is a non abelian theory and the evolution term of the gauge fields is defined as:

$$F_{\mu\nu} = \partial_\mu G_\nu - \partial_\nu G_\mu + g f_{abc} G^b_\mu G^c_\nu. \tag{1.5}$$

The last term of equation (1.5), shows that gluons can interact with each other with the same coupling g as quarks do. The coefficients f_{abc} are the structural constants of the $\mathrm{SU(3)_{color}}$ group, obtained from the commutation rules of its generators. The generators of this group, in its fundamental representation, are linked to the 8 Gell-Mann hermitian and squared matrices, with the same dimensions of the colour charges: $t^A = \frac{1}{2}\lambda^A$. The

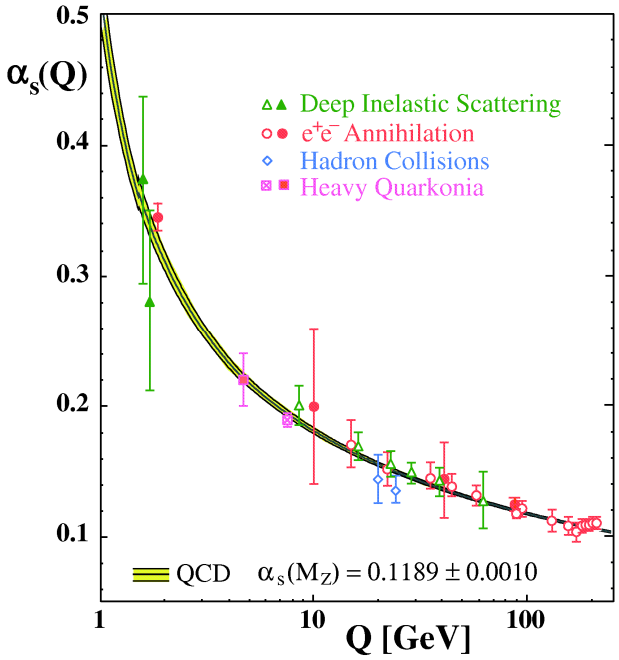

Figure 1.1: Coupling coefficient α_s as a function of transfert momentum in the collisions Q, measured with different colliding systems [5].

gluons self-coupling is a main and peculiar property that characterizes the strong force with respect to the others. The coupling of the strong interaction $\alpha_s = g^2/4\pi$ varies with the transverse momenta exchanged in the interaction (Q) among the fundamental constituents. The α_s coefficient decreases for higher and higher Q of the interactions, as shown in Fig. 1.1 for many colliding systems [5].

From the measurements performed and summarized in Fig. 1.1, two of the main physics results related to QCD can be introduced:

- asymptotic freedom,

- confinement.

The gluons self-coupling and the possibility to have bosonic loops in the Lagrangian introduce the"anti-screening" of the colour charge. For interactions at high transverse momentum, the coupling decreases and it reaches a fixed ultraviolet point:

$$\lim_{q^2 \to \infty} \alpha_s(q^2) = 0. \tag{1.6}$$

In this situation, quarks interaction can be studied through the parton model, where fundamental particles, for the strong interaction, can be considered as free within hadrons (asymptotic freedom) [6, 7]. On the other side, the coupling increases when the exchanged momentum between coloured objects decreases and it reaches a potential wall when distances between quarks are of the order of the *fermi* (hadrons size). Due to this effect, quarks and gluons are confined within hadrons and they cannot be "seen" one-by-one. For the confinement, at the moment, there are neither theoretical explanations on its origin nor on its phenomenology.

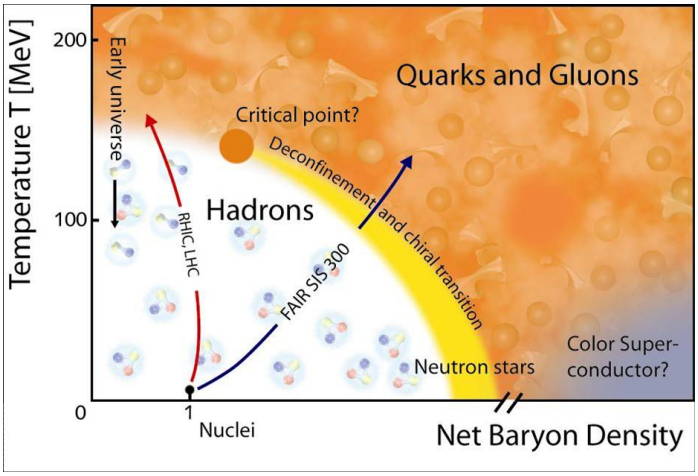

Figure 1.2: QCD phase diagram.

1.1.2 QCD phase transition

On the basis of thermodynamical considerations and QCD calculations, strongly interacting matter is expected to exist in different states. Its behaviour can change for different conditions of temperature and baryonic chemical potential μ_B. The baryo-chemical potential is defined as the energy (E) needed to increase of one unity the total number of baryons and anti-baryons (N_B): $\mu_B = \partial E/\partial N_B$. Fig. 1.2 shows an illustration of the phase diagram of nuclear matter, varying its temperature and baryo-chemical potential.

At low temperatures and for $\mu_B \simeq m_p \simeq 940$ MeV, nuclear matter is in its standard conditions (atomic nuclei). Increasing the energy density of the system, "heating" the nuclear matter (upward in the plot) or increasing the baryo-chemical potential (left in the diagram), an hadronic gas phase is reached. In this state nucleons interact and form pions, excited states of the protons and neutrons (Δ resonances) and other hadrons. If the energy density is further increased, a deconfined Quark Gluon Plasma (QGP) phase is predicted. The density of gluons and quarks, in this phase, becomes so high that partons are still interacting but not confined within hadrons anymore. For extreme values of baryo-chemical density, nuclear matter should be in conditions of quark colour superconductivity.

There are many "paths" on the phase diagram, that the phase transition can follow, varying the temperature and the baryo-chemical potential. In the early Universe, for example, the transition from a QGP phase to hadron matter took place for $\mu_B \approx 0$ as a consequence of the Universe expansion and the decrease of its temperature. In that case the transition phase evolved from a deconfined state of partons to hadronic matter. On the other hand, in the formation of neutron stars, the gravitational collapse causes an increase in the baryonic density for temperature very close to zero.

The phase transition is characterized by how fast the free energy of the system is varied, for a neighborhood of the transition temperature. The transition between different states belongs to the first order, if it happens with a discontinuos pattern in the first derivatives of the free energy. In a first order transition, entropy varies with discontinuity and latent heat is present. If the phase transition occurs with discontinuos derivatives after the first, it is a second order transition. Second order transitions are, for example, the ferromagnetic transition or the superfluid transition. Phase transitions can also occur without fast modification of the parameters of the system, so with a continuos behaviour

for the free energy and its derivatives. These transitions are called cross-over. In peculiar conditions of thermodynamic parameters, the process can pass from a first to a second order transition. These conditions are called critical points and usually two states of matters are coexisting.

Phase transitions are also characterized by changes in the symmetry of the system. In case a symmetry is broken in a phase transition, it can be necessary to introduce new variables to describe the system; these variables allow to identify the order of the transition and they are called order parameters. An important symmetry that can play a role in the QCD phase transition is related to the quark masses. Let's consider quarks as massless particles, the QCD Lagrangian becomes invariant with respect to the SU(2) group, that brings the isospin conservation. The QCD Lagrangian is also invariant with respect to another SU(2) global transformation, where Pauli's matrices (σ^i) are introduced:

$$\psi \rightarrow \exp\left(-i\alpha^i \frac{1}{2}\sigma^i\gamma^5\right)\psi \tag{1.7}$$

For both global symmetries considered, a conserved charged is foreseen according to the Noether theorem: Q^i are the charges due to SU(2) isospin and Q^i_5 those for the second transformation. By the combination of these two, it is possible to define two generators with opposite parity that define the chiral transformation:

$$Q^i_L = \frac{1}{2}\left(Q^i - Q^i_5\right), \tag{1.8}$$

$$Q^i_R = \frac{1}{2}\left(Q^i + Q^i_5\right). \tag{1.9}$$

Due to the isospin invariance within the chiral symmetry, each isospin multiplet should have a degenerate quantum state, with opposite parity. The number of left- and right-handed quarks should be separately conserved in QCD. Since this degeneration is not shown in the hadrons hierarchy and quarks are massive particles, the chiral symmetry has to be spontaneously broken. Massive quarks, indeed, can only be described as a superimposition of helicity eigenstates. Chiral symmetry breaking can occur via the dynamics of the theory itself.

In QCD, the vacuum is considered to be unstable with respect the formation of a condensate of tightly bound $q\bar{q}$ pairs. Let's consider the vacuum of the strong interaction $|0\rangle$ and the field operators which create or destroy a quark when acting on a ket as $\bar{\psi}$ or ψ:

$$\langle\bar{\psi}\psi\rangle = \langle 0|\bar{\psi}_L\psi_R + \bar{\psi}_R\psi_L|0\rangle \neq 0. \tag{1.10}$$

Since neither $|0\rangle$ is annihilated by ψ, nor $\langle 0|$ by $\bar{\psi}$, the vacuum must contain $q\bar{q}$ pairs. The chiral symmetry breaking is also related to the dynamically-generated mass, called constituent mass, as opposed to the quark's intrinsic mass. Only the sum of left- and right-handed quarks is a conserved quantum number related to the symmetry, not the left- and right-handed quarks separately. A left-handed quark, propagating through the vacuum can be annihilated by its anti-quark (ass seen in Eq. 1.10). The coupled antiright-handed quark of the vacuum can then create its anti-quark with the same momentum of the first.

The QCD vacuum can be described as a dynamic vacuum that is responsible of the constituent quarks mass formation. With the spontaneous chiral symmetry breaking, a large value for the QCD vacuum is reflected into a large constituent mass with respect to

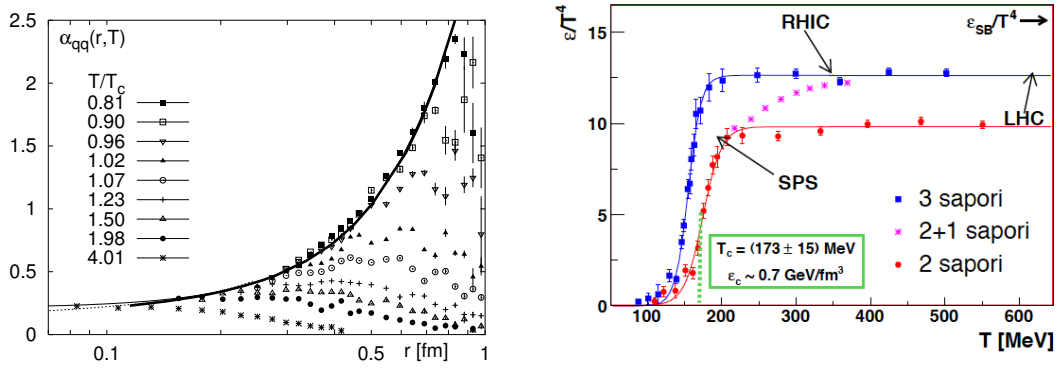

Figure 1.3: Coupling of the strong interaction as a function of the distance between two partons, varying the critical temperature of the system. Increasing the temperature, the coupling tends to vanishing and opens the possibility to a deconfined phase (left) [10]. Energy density of the system as a function of its temperature. For values larger than the critical temperature a clear increase of the degrees of freedom of the system is visible (right) [9].

the intrinsic mass of the quarks, due to this dynamical mass generation. The proton (uud) mass, for example, is $\approx$ 1 GeV/c^2, while the intrinsic mass of its constituent quarks is $\lesssim$ 20 MeV/c^2. The constituent mass of quarks u and d is of the order of 300 MeV, 450 MeV for the strange quarks. Going from an hadronic state of nuclear matter to the deconfined one, the chiral symmetry should be restored and with it the independent conservation on left and right-handed quarks.

1.1.3 Lattice QCD calculations

QCD theory allows perturbative calculations only for values of the coupling smaller than 1, in the high transferred momenta region. For lower energies, the perturbative approach cannot be applied and numerical methods have to be used. The lattice QCD method is based on simulations on a space-time lattice, where each point of the system evolves through numerical equations. In this way it is possible to study large-distance aspects of QCD and partially account for non perturbative effects. With this method, lattice QCD allows to explore, from a theoretical point of view, the qualitative aspects of the strong interacting matter, making quantitative predictions about its properties. At present the limit for these calculations is the assumption of a zero baryonic density, a finite value for the baryo-chemical potential cannot be introduced [8, 9].

Lattice QCD allows to study the interacting potential of quark-antiquark pairs as a function the radius of the hadrons, varying the temperature of the system. The potential seems to decrease till zero values with an increase of the temperature, allowing a deconfined phase where partons are interacting but not constraint within hadrons anymore (Fig. 1.3, left) [10]. The critical temperature where this should happen is about $T_C = 179$ MeV.

Before the transition, the system should be described with hadrons, while after it, partons become the main characters of the system, with their many more degrees of freedom. Let's consider a gas made of quarks and gluons, where the energy density is proportional to the temperature to the fourth power (ϵ/T^4), through a constant related to the number of degrees of freedom of the system. Results of ϵ/T^4 versus temperature

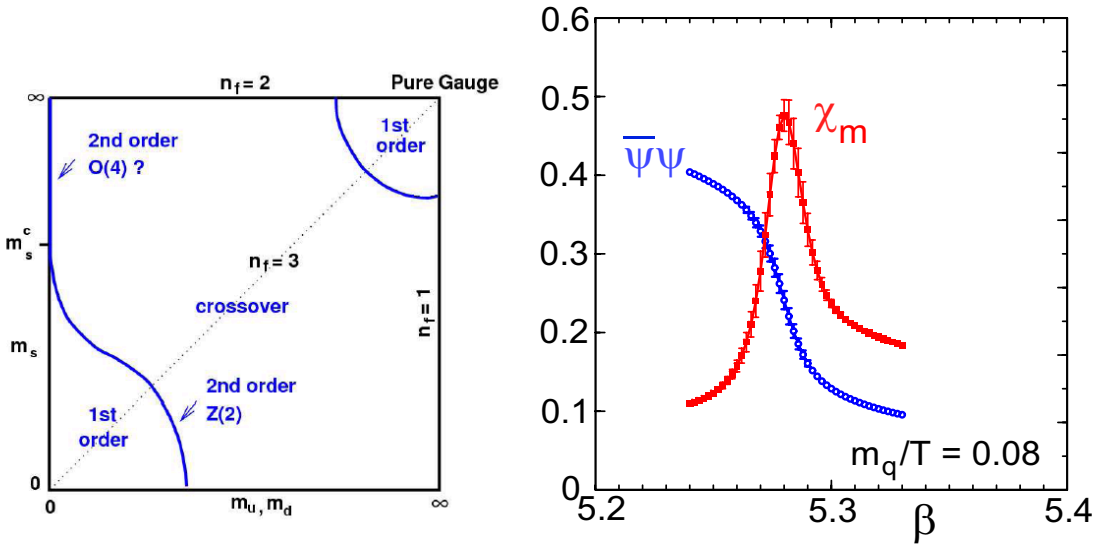

Figure 1.4: Study of the possible orders of the phase transition as a function of the quark masses involved (right) [11]. Chiral condensate and its susceptivity as a function of the temperature of the system (left) [12].

are reported in Fig. 1.3 (right), for 2 and 3 light quarks considered in the calculation, or with 2 lights and 1 heavier (strange quark). The latter case should be the closest to the physically realized quark mass spectrum. The"jump" in this ratio is an evidence of the increase of the degrees of freedom of the system, going from 3 for a pion, to 37 (with 2 flavours) in case of deconfined phase. In a pion gas the degrees of freedom are only the three isospins of pions; in case of a deconfined phase, it is necessary to consider the 8 gluons and all the combinations of flavour, colour and spin of the quarks. The number of flavours and quarks mass values, that play a role in the transition, are the main uncertainties in the determination of the critical temperature and critical energy density. In this case the temperature of the phase transition is estimated to be $T_C = (175 \pm 15)$ MeV and with a energy density $\epsilon_c \sim (0.3 - 1.3)\text{GeV/fm}^3$.

As it was described also in Sec. 1.1.2 quark masses can play an important role in the transition, both for critical temperature and for the restoring of chiral symmetry. For the latter case, masses can change the order of the phase transition and this can also be studied with lattice QCD calculations. Fig. 1.4 (left) shows how the order of the phase transition can change with different hypotheses on the quark masses and on the number of light quarks entering in the"game". If up, down and strange quarks have zero masses, the transition should be of the first order. If only up and down quarks are considered in the Lagrangian, then the transition is of the second order. The more realistic scenario is $m_s > m_{u,d}$ and it foresees that the transition happens in a fast way but without any discontinuity, following a cross-over.

Lattice QCD calculation can also study the chiral condensate as a function of the temperature (Fig. 1.4 right). For $T < T_C$ the chiral condensate is large, picking out the symmetry breaking. While for temperatures bigger than the critical one, the chiral condensate reaches lower values, showing the restoring of the chiral symmetry and the characterization of quarks by their current masses in the deconfined phase. In the same plots also the susceptivity of the chiral condensate is shown (χ_L). This quantity indicates

how strongly the thermodynamic observables fluctuate, peak or even diverge at the phase transition, since it is obtained from the negative derivatives of the condensate with respect to its temperature.

1.1.4 QGP in the laboratory: ultra-relativistic heavy ion collisions

The experimental link between the QCD phase transition and the measurement of temperature, pressure and energy density of the deconfined phase, are ultra-relativistic heavy-ion collisions. Complex system, composed of many particles and behaving like a collective entity can be associated to thermodynamic phases and equation of states. Nucleus-Nucleus collisions are characterized by an high number of following nucleons-nucleons collisions in a very small region. The high energies and the following collisions can recreate the energy density and the temperature needed to allow the deconfined phase to occur and to explore different regions of the QCD phase diagram. At high energy, thousands of partons produced in these collisions create a "fireball" in local thermal equilibrium that rapidly expands and cools down. For high energy in the centre of mass of the collisions, the fireball is initially made of interacting quarks and gluons that hadronize only when the system temperature falls below the temperature needed to the phase transition to occur (critical temperature).

The early experiments with heavy-ion collisions (Au or Pb) started in 1990s at the AGS with a centre of mass energy $\sqrt{s_{\rm NN}} = 4.6$ GeV per colliding pair and the fixed target experiments at the SPS with an energy of $\sqrt{s_{\rm NN}} = 17.2$ GeV (Pb or In). In the Brookhaven National Laboratory (BNL) a dedicated heavy-ion collider has started its operation since the 2000. The Relativistic Heavy-Ion Collider (RHIC) is still delivering Au–Au, Cu–Cu and *pp* collisions to two out of four experiments installed on the ring: PHENIX and STAR, BRAMS and PHOBOS ended their data taking. Finally the Large Hadron Collider at CERN started collecting *pp* data in November 2009 and one year later, the first Pb–Pb collisions were delivered with an energy in the center of mass per nucleon pair of $\sqrt{s_{\rm NN}} = 2.76$ TeV. The design LHC energy for Pb–Pb is $\sqrt{s_{\rm NN}} = 5.5$ TeV and it will be reached after the two years shutdown foreseen in 2013-2014. More details on the LHC will be given in Sec. 3.1. ALICE, ATLAS and CMS are the three experiments that take data during the Pb–Pb run.

Dynamics of heavy-ion collisions

The fireball, created in high energy density and temperature conditions, rapidly expands and thermalizes. The evolution of the fireball is very similar to the evolution of the early Universe after the Big Bang. The hot big bang model of cosmology assumes that, after the electro-week phase transition (electromagnetic and weak forces become differentiated $\approx 10^{-11}$ s after the Big Bang), the expanding Universe was a plasma of partons. When the critical temperature is reached, nuclear matter changes its state from a deconfined plasma phase to an hadronic one, where partons form baryons and mesons.

In ultra-relativistic heavy-ion collisions, nuclei approach each other with a disk-like form, since they are Lorentz contracted along the beam direction by a factor $\gamma = E_{beam}/M$, where E_{beam} is the energy of the accelerated nuclei and M its mass. After the impact (~ 0.1 fm/c), following collisions between nucleons start. These collisions involve hard collisions between partons with large momentum transfer. The inelastic scatterings between incoming partons produce an high parton density and the formation of the fireball.

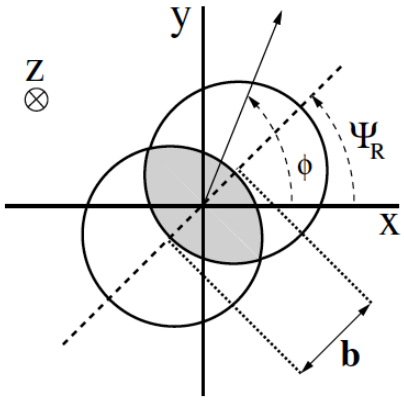

Figure 1.5: Geometry of a nucleus-nucleus collisions. $\vec{b}$ defines the impact parameter vector of the collision, Ψ_{R} defines the reaction (or event) plane.

Once the QGP is formed, it expands and cools down, for the effect of the exerted pressure on the vacuum surrounding the system. When the temperature goes down, below the critical temperature for the phase transition to occur, the QGP converts to a gas of hadrons and the available energy is not sufficient to modify the species of the particles. The "chemical" composition of the hadronic system is now frozen and the "chemical freeze-out" of the system is reached. Once the particle species are defined, hadrons keep interacting quasi-elastically, cooling the fireball until the kinematic freeze-out is reached. Momentum spectra of particles can change due to these elastic collisions or due to resonances decay, but ratios of produced particles are frozen [13].

Geometry of heavy-ion collisions

Since nuclei are not point-like objects, the geometry of the collision plays an important role in the study of the nuclear matter effects and QGP formation. In Fig. 1.5 the collision of two nuclei is schematically represented as seen in the plane transverse to the beam direction (z axis). Let's consider a nucleus of mass number A and $r_0 \sim 1.25$ fm the radius of a nucleon, the maximum distance of the two colliding nuclei is $2R_A \approx 2A^{1/3}r_0$. The most important quantity related to the overlapping region of the colliding nuclei, is the impact parameter vector $\vec{b}$, that is the vector between the centres of the two nuclei in the transverse plane. A central collision is characterized by a small impact parameter, the two nuclei collide almost head-on and almost all nucleons within the nucleus participate in the collision; in the opposite case, a peripheral collision has large impact parameter.

Collisions are usually grouped in centrality classes, in terms of percentiles of the nucleus-nucleus hadronic cross section ($\sim 4\pi R_A^2$). Centrality can be measured using two methods. The goal of both methods is to measure or estimate the number of nucleons that participate in the collisions (N_{part}) and the "spectator" nucleons ($2A - N_{\mathrm{part}}$) that do not interact. The first method exploits the correlation between the centrality and the number of particles produced in the collision. For this method it is necessary to use a geometrical model in order to describe hadronic processes. The Glauber Model [15] assumes straight line nucleon trajectories and a nucleons-nucleons cross section independent of the number of collisions that nucleons have undergone before. The nuclear density profile of

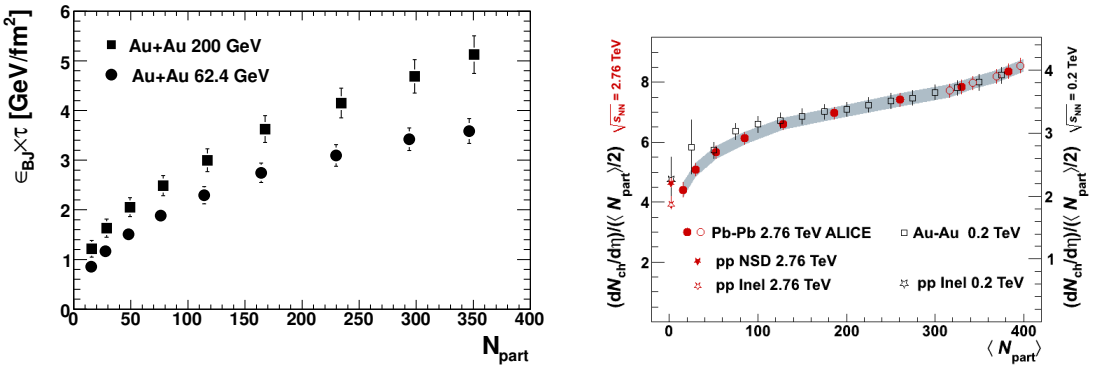

Figure 1.6: Measurement of the Bjorken energy density multiply by the formation time as a function of the number of participants at RHIC [18] (left). Charged particle pseudo-rapidity density per participant pair as a function of N_{part} in Pb–Pb collisions at $\sqrt{s_{\text{NN}}} = 2.76$ TeV and Au–Au collisions at 200 GeV (right) [20].

the nucleus is given by a Woods-Saxon distribution [16]. With this modeling of the collision geometry it is possible to estimate N_{part}, assuming that the impact parameter b is monotonically related to particle multiplicity [15]. The second method, used to measure centrality, exploits the spectator nucleons that do not take part in the collisions. The energy of these nucleons is measured in the forward zero-degree calorimeters, set close to the beam pipe, in the forward region. This method allows to measure directly the number of participants, without any geometrical models, but nuclear fragmentation breaks the simple relation in the measured variables and it has to be correlated with another measurement. A relevant quantity related to collisions geometry is the number of collisions N_{coll} defined as the number of incoherent nucleon-nucleon collisions. The impact parameter vector is also important for the determination of the event plane of the collision, defined by the beam direction (z axis) and the impact parameter vector. The angle Ψ_{R} between the x axis and the impact parameter direction identifies the reaction plane.

1.2 Characterization of the medium from RHIC to LHC

From the AGS to the LHC, during almost thirty years, several experiments have studied heavy ion collisions with many colliding systems at different energies. At the beginning of the research on this field the main goal was to understand whether the deconfined phase was formed or not. The strangeness enhancement, measured at the SPS, has been defined as the first clear effect of QGP formation, since no hadronic model could explain it. The second clear indication of the QGP was thought to be the anomalous J/Ψ suppression measured in Pb–Pb collisions at the SPS. With the subsequent experiments at RHIC and LHC, the main goal was the understanding of the properties of strongly interacting deconfined matter. A review of the most important results on the medium properties will be shown in the next sections.

1.2.1 Global event properties

The first step of the strongly interacting medium characterization is the measurement of the energy density ϵ produced in the mid-rapidity region of the collision. The rapidity of

a particle with a four-momentum $(E, \vec{p})$ is defined as in Eq. (1.11), where z is the beam direction. For ultra-relativistic particles ($E \approx p$) rapidity can be approximated by the pseudo-rapidity (Eq. 1.12), defined in terms of the polar angle with respect to the beam direction.

$$y = \frac{1}{2} \ln \frac{E + p_z}{E - p_z} \tag{1.11}$$

$$\eta = \frac{1}{2} \ln \frac{p + p_z}{p - p_z} \tag{1.12}$$

The energy density of the central rapidity region can be estimated with the Bjorken formula:

$$\epsilon_{Bj}(\tau) = \frac{1}{S_\perp \tau} \frac{dE}{dy}|_{y=0} \tag{1.13}$$

where τ is the proper time, $S_\perp$ is the transverse area of the incident nuclei and dE/dy denote the energy of the collision products per unit of rapidity [14]. Usually it is possible to approximate the total energy with the transverse energy, that is related to the hadron multiplicity:

$$\frac{dE}{dy}|_{y=0} \sim \frac{dE_\perp}{dy}|_{y=0} \sim \langle E_\perp \rangle \frac{dN}{dy}|_{y=0}, \tag{1.14}$$

where $\langle E_\perp \rangle$ is the average hadron transverse energy and dN/dy is the hadron multiplicity density, in the same rapidity interval. To estimate the transverse energy, experiments have measured the energy of charged hadrons with their tracking system, for example, corrected then by the fraction of neutral particles not accessible by tracking detectors. The Bjorken formula is based on the assumption of longitudinal boost invariance and formation of a thermalized central region at an initial time τ_{zero}. A reference QGP formation time τ_0 is considered between 0.2 and 1 fm/c At the SPS Pb–Pb collisions at $\sqrt{s_{\text{NN}}} = 17.2$ GeV, with $\tau = 1$ fm/c the estimated energy density was estimated as $\epsilon_{Bj} = 3.1 \pm 0.3$ GeV/fm^3, a value sufficient for the phase transition to occur [17]. Fig. 1.6 (left) shows the measured value of $\epsilon_{Bj} \times \tau$ from the STAR Collaboration as a function of number of participant for two collision energies. The energy density is estimated to be between 5 and 25 GeV/fm^3, depending on the chosen formation time [18]. At the LHC the multiplicity of charged particles has been measured in the central rapidity region with the very first data collected in 2010 [19]. Fig. 1.6 (right) shows the charged particle pseudo-rapidity density per participant pair in the $|\eta| < 1$ region as function of N_{part}, measured by the ALICE experiment. Compared to RHIC results, also shown in the figure, there is an increase of about a factor 2.1, but the centrality dependence is very similar, at least for $N_{\text{part}} > 100$ [20].

In Fig. 1.7 (left), the total energy per participant pair is shown as a function of N_{part}, measured at LHC [21]. As the multiplicity, it shows a steady rise with the number of participants, very similar to that shown at RHIC but increased by a factor 2.5. Considering the most central value of $dE_\perp/dy$, it gives an $\epsilon_{Bj} \times \tau = 16$ GeV/fm^2 at LHC, about a factor 3 larger then the corresponding one at RHIC. To summarize, Fig. 1.7 (right) shows the charged particle multiplicity for different energies in pp and A–A collisions. With respect to RHIC energies the charged particle multiplicity is increased by a factor 2.1 at LHC, but only by 1.9 in pp collisions at similar energies. The growth with energy is therefore different in pp and A–A collisions, confirming the interplay of N_{part} and N_{coll} dependence in the particle production mechanism for heavy-ion collisions. The energy dependence of the charged multiplicity exhibits a power-low scaling (red line Fig. 1.7 right) stronger than the logarithmic scale (dotted line) suggested by the lower energy data [19].

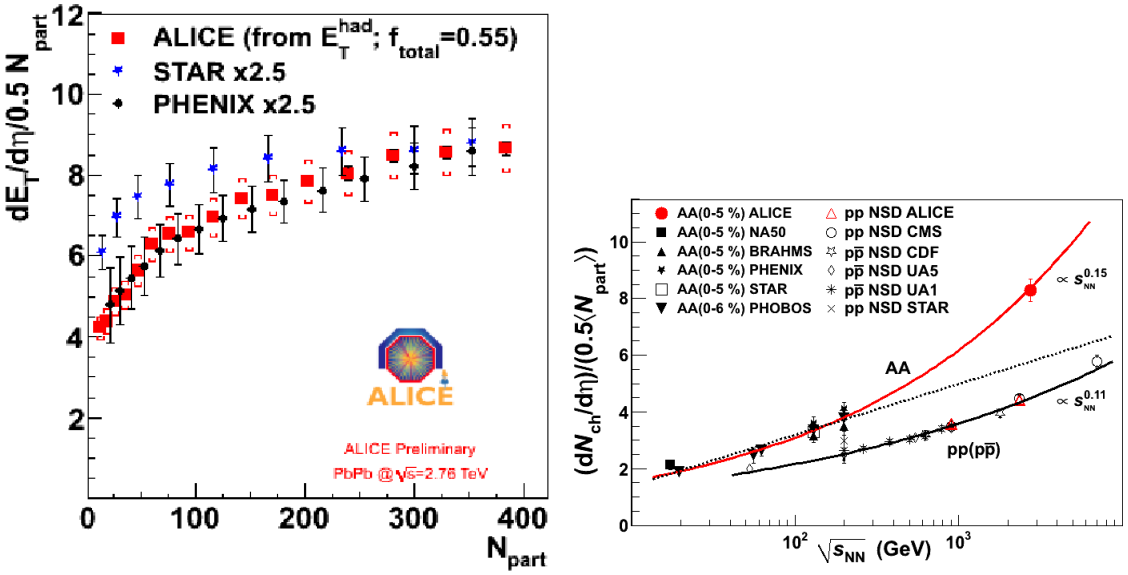

Figure 1.7: Transverse energy per participant pairs as a function of $N_{\rm part}$ in Pb–Pb collisions at $\sqrt{s_{\rm NN}} = 2.76$ TeV and Au–Au collisions at 200 GeV. RHIC data are multiplied for a factor 2.5 (left) [21]. Charged particle pseudo-rapidity density per participant pairs for the 0-5% central collisions and non single diffractive pp collisions as a function of $\sqrt{s_{\rm NN}}$ (right) [19].

1.2.2 Collective Phenomena

Collective flow indicates a correlation between the average momentum of the particles and their space-time position. Considering a generic space-time point x in the fireball, it is possible to define an infinitesimal volume element centered at this point x. The four-momentum of the volume element is obtained by summing up all the component of the partons within this volume. The average flow velocity $\vec{v}(x)$ is obtained by dividing the three-momentum over the associated total energy of the volume. The flow velocity is then separated into its component along the beam direction ("longitudinal flow" $v_{\rm L}$) and the one in the transverse plane to the beam direction ("transverse flow" $v_{\perp}$). The magnitude of the transverse flow depends on the angle around the beam direction and it is larger for semi-central collisions with not zero impact parameter. Since the QGP is an approximately-thermalized system of quarks and gluons, it has a thermal pressure, that compared to the one of the surrounding vacuum, make the QGP expands in a collective way. The absence of collective flow would indicate the absence of pressure and therefore the absence of the hot thermalized expanding system. The collective flow allows to extract important information about the properties of the fireball.

Identified particle spectra

The measured hadron yields spectra reflect the properties of the bulk of the matter at the kinetic freeze-out, after elastic collisions among hadrons have ceased. At this stage the system is already diluted and "cold", but this information can be linked to properties at an earlier and hotter stage. The integrated yields of the different hadron species reflect the particle abundances and the chemical composition of the expanding fireball, since these

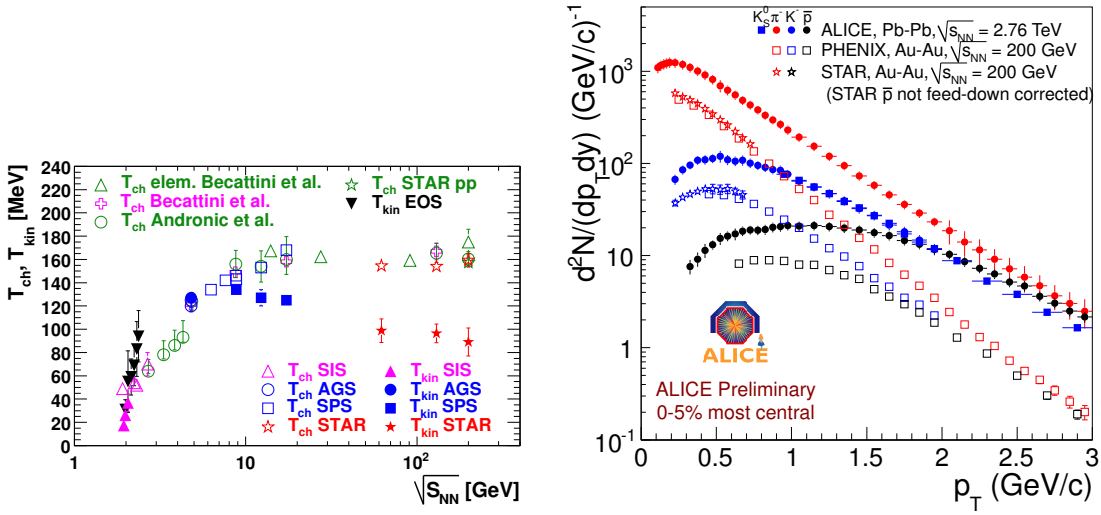

Figure 1.8: Kinetic freeze-out temperature extracted in different experiments for central collisions as a function of collision energy (right) [18]. Comparison of identified particle spectra measured by ALICE and RHIC experiment (left) [23].

yields are "frozen" at the hadronization stage and they are weakly affected by hadronic rescattering. The chemical equilibrium among hadrons constraints the microscopic chemical reaction processes and their timescales. The kinetic freeze-out temperature T_{kin} can be estimated with the analysis of the measured transverse momentum spectra for different particles. These identified spectra are usually fitted with blast-wave model [22]. This model assumes that particles are locally thermalized at a kinetic freeze-out temperature and they are moving with collective transverse radial flow velocity. The expected momentum spectra shape is used to fit particle spectra simultaneously ($\pi^{\pm}$, $K^{\pm}, p, \bar{p}, \cdots$). The temperature of the kinetic freeze-out and the average transverse flow velocity $\langle\beta\rangle$ are free parameters of the fit. In Fig. 1.8 (right) the kinetic freeze-out temperature is shown, together with the chemical freeze-out temperature, for different collision energies [18]. The values of both temperatures measured by STAR are very similar for $\sqrt{s_{\rm NN}} = 62.4,\ 130,\ 200$ GeV, while they strongly depend on the charged particle multiplicity, i.e on the initial energy density. This suggested that a higher initial energy density is reflected in larger flow velocity, due to the larger expansion rate and longer expansion time. A larger flow velocity means a lower kinetic freeze-out temperature.

In Fig. 1.8 (left), the spectra in 0-5% most central collisions, measured at the LHC by ALICE, have been compared to previous results at $\sqrt{s_{\rm NN}} = 200$ GeV [23]. For ALICE data, K^0_s data are also shown, to cover a wider $p_{\rm t}$ range, and feed-down from weak decays are subtracted for the different hadrons. Only PHENIX $\bar{p}$ spectrum is shown in the figure because it is feed-down subtracted and it can be directly compared to ALICE results. Like for RHIC results, ALICE π and p spectra cross at $p_{\rm t} \simeq 3$ GeV/c. A strong change in the shape between the two spectra is observed, with the spectra at the LHC being harder, indicating a stronger radial flow and much flatter at low-$p_{\rm t}$. In Fig. 1.9 (right) ALICE data are also compared with a hydrodynamical prediction [23]. Hydrodynamical models are a macroscopic approach to describe the dynamical evolution of the expansion stages of heavy-ion collisions. These phenomenological models describes the evolution of thermodynamic quantities like energy density, pressure, temperature, without introducing

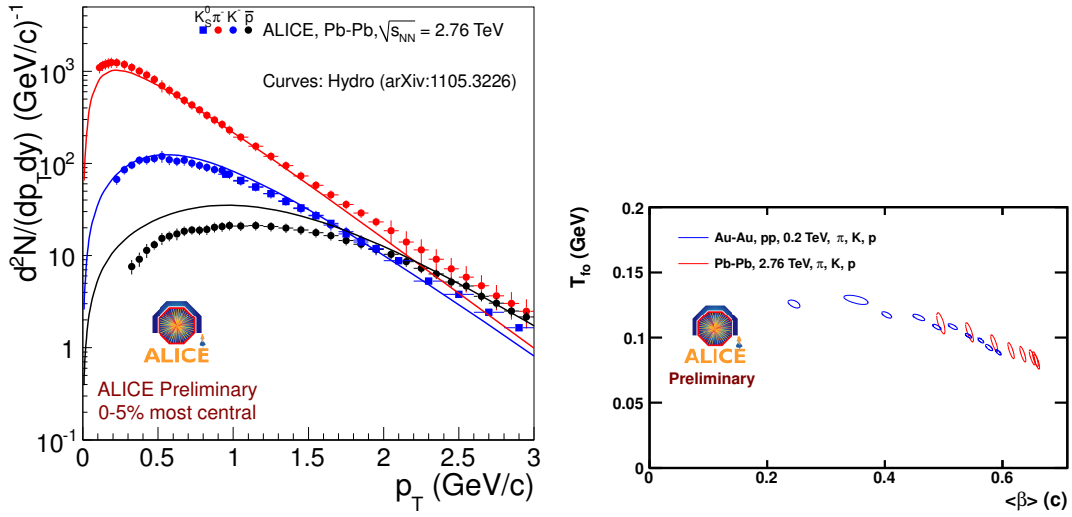

Figure 1.9: ALICE identified particle spectra compared with hydrodynamical predictions (right). RHIC and LHC data results for the fit with a blaste-wave function, in order to obtain the kinetic temperature freeze-out as a function of the transverse flow velocity (left) [23].

unknown microscopic parameters. Hydrodynamic treatment requires a large, macroscopic system in local thermal equilibrium and an adiabatic expansion stage. The specific model shown in the figure seems to be in good agreement for π and K, but it is overestimating the yield of protons and also with a different trend versus p_{t}. As for RHIC data, LHC spectra have been fitted with a blaste wave function in the ranges: 0.3 - 1 GeV/c for pions, 0.2 - 1.5 GeV/c for kaons and 0.3 - 3 GeV/c for protons. The results of the fit are shown in Fig. 1.9 (left) for different centrality bins and they are shown with similar STAR fits. In this figure the kinetic freeze-out temperature (T_{fo}) is studied as a function of the average transverse flow velocity. At LHC a $\sim$ 10% increase of radial flow is observed for central collisions.

Elliptic flow

Flow anisotropies are generated during the early stage of non central collisions. These azimuthal anisotropies originate from spatial asymmetries due to the initial shape of the nuclear overlapping region that are reflected to pressure gradients. Due to larger pressure gradient, matters expands faster in the direction where the fireball size is smaller. Elliptic flow is sensitive to the equation of state of the QGP phase, since it is generated before matter reaches the critical temperature and hadronizes. Large anisotropies indicate a strong collective behaviour and early local thermal equilibrium of the fireball.

Particles are initially produced in isotropic partonic interactions and re-scattering processes among these particles can lead to a modified momentum space distribution. The momentum anisotropy manifests itself as an azimuthal anisotropy of the measured hadron spectra. The magnitude of the anisotropic flow depends strongly on the friction of the strongly interacting matter, characterized by the viscosity over entropy density ratio (η/s).

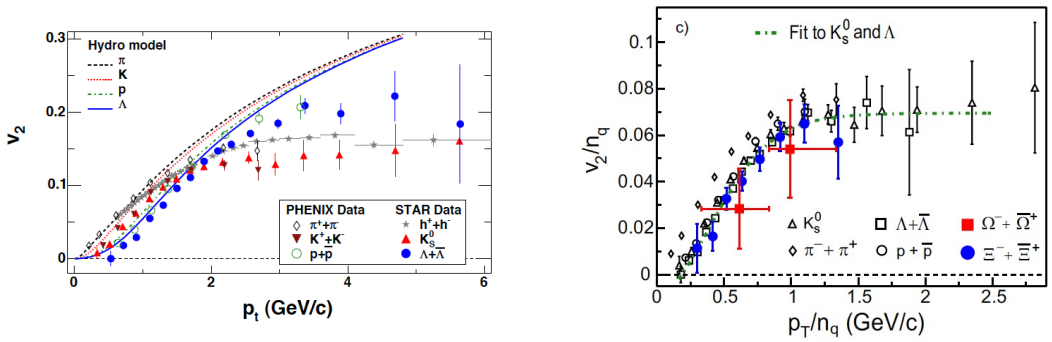

Figure 1.10: v_2 flow coefficient as a function of p_t measured at PHINIX and STAR; a comparison with hydrodynamical model is also shown (left) [24]. v_2 coefficient trend as a function of p_t, both normalized to the number of valence quarks for different particles (right) [26].

The particle azimuthal distribution can be expanded in a Fourier series:

$$E\frac{d^3N}{d^3p}d\phi = \frac{1}{2\pi}\frac{d^2N}{p_\mathrm{t}dp_\mathrm{t}dy}\left(1+\sum_{n=1}^{\infty}2v_n(y,p_\mathrm{t})\cos n\left(\phi-\Psi_\mathrm{R}\right)\right), \tag{1.15}$$

where Ψ_R is the angle that defines the reaction plane (see also Sec. 1.1.4) and $v_n(y,p_\mathrm{t}) = \langle\cos[n(\phi_i-\Psi_\mathrm{R})]\rangle$ are the coefficients used for the quantitative characterization of the event anisotropy. The sine terms in the expansion vanish due to symmetry with respect to the reaction plane. The $v_n(y,p_\mathrm{t})$ coefficients are computed by averaging the angular difference over the particles, summed over all events in the (p_t,y) bin of interests.

At RHIC energies, the evidence of elliptic flow in non-central collisions was clear. In Fig. 1.10 (left), results on flow measurement at $\sqrt{s_\mathrm{NN}} = 200$ GeV are reported for the two experiments STAR and PHENIX [24]. These results have been compared to hydrodynamical models of a ideal fluid with almost zero viscosity and temperature $T_C = 165$ MeV. Each particle species has its own v_2 coefficient since at low p_t, the elliptic flow depends on the mass of the particle, being smaller for larger masses due to the common radial flow velocity. At RHIC, the v_2 has also be studied normalized to the number of constituent quarks for the different hadrons species ($n_q = 3$ for baryons, $n_q = 2$ for mesons) as a function of the transverse momentum normalized to the same quantity. In Fig. 1.10 (right) it is shown that for all hadrons the trend of v_2 is the same if scaled by the number of valence quarks up to 2 GeV/c. This common behaviour would point to a mechanism of recombining quarks to form hadrons. This effect is called coalescence and it foresees that partons already present in the deconfined matter are combined together [25]. For $p_\mathrm{t} > 2$ GeV the fragmentation mechanism should be favoured.

In Fig. 1.11 (left) results for p_t integrated elliptic flow measured at LHC energies are reported [26]. Blue and red symbols in the figure correspond to two different methods of measuring the correlations between particles in the event. The results of these two methods are different mainly for the non-flow contributions and for event-by-event flow fluctuation. The LHC results are also compared to the RHIC ones (blue and red line in the same figure) for the same correlation methods. The integrated flow is studied as a function of centrality and the highest value of this effect is measured between 30% and 50% centrality, where the asymmetry of the collision is more enhanced. The integrated

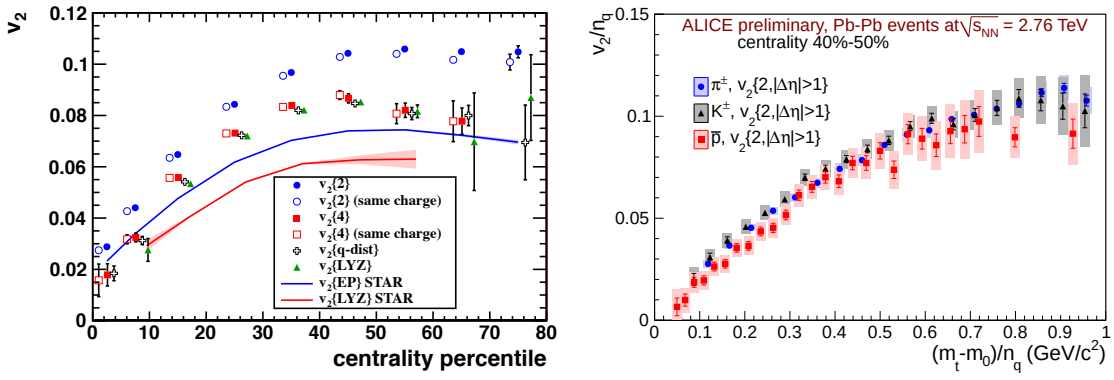

Figure 1.11: Integrated charged hadrons elliptic flow as a function of centrality measured by ALICE (left) [26]. Elliptic flow versus transverse kinematic energy both divided by the number of constituent quarks, measured with ALICE. Protons seems not to follow the previous trend, probably due to the higher flow present at the LHC (right) [27].

elliptic flow of charged particles increases by about 30% compared to RHIC. This indicates that the hot and dense matter created at LHC still behaves like a fluid with almost zero viscosity. Identified particle elliptic flow at LHC shows a stronger dependence on particle mass than at RHIC, with light (pions) and heavy (protons) particles pushed further apart from each other due to the increased radial flow. Also at the LHC v_2 was scaled by the number of constituent quarks for different hadrons species [27]. Results are reported in Fig. 1.11 (right). The same trend observed at RHIC is visible for pions and kaons, while protons seem not to follow this trend, possibly due to the higher radial flow. The quark number scaling seems to be valid up to $p_{\mathrm{t}} \sim 2$ GeV.

Particle ratios

After the fireball thermalization, the hadron species are a in a chemical equilibrium, forming a statistical ensemble. In the chemical equilibrium model, the system is described in a grand-canonical ensemble and the distribution functions for each particle species are derived via the Maximum Entropy Principle, where the global energy, baryon and strangeness conservation are imposed. Particle abundances in a thermal system of volume V are characterized by few parameters:

$$\frac{N_i}{V} = \frac{g_i}{(2\pi)^3}\gamma_s^{S_i}\int \frac{1}{\exp\left(\frac{E_i-\mu_B B_i-\mu_S S_i}{T_{ch}}\right)\pm 1} d^3p. \tag{1.16}$$

N_i is the abundance of particle species i, g_i the spin degeneracy, B_i and S_i are the baryon and strangeness numbers carried by the particle species i, E_i is the particle energy; the integration is over the whole momentum space. The two cases considered (± 1) are for bosons (-) and fermions (+), to take into account the different statistics that they follow. The parameters left in the model are the temperature of the system, the baryon and strangeness chemical potential and the *ad-hoc* strangeness suppression factor, γ_s. The measured particle abundance ratios are fitted in order to obtain the parameters of the system at the chemical freeze-out. In Fig. 1.12 (left) the results obtained by the STAR collaboration for the ratio of different particle abundances are shown [28]. The baryon chemical potential decreases smoothly with increasing collision energy (new baryons and

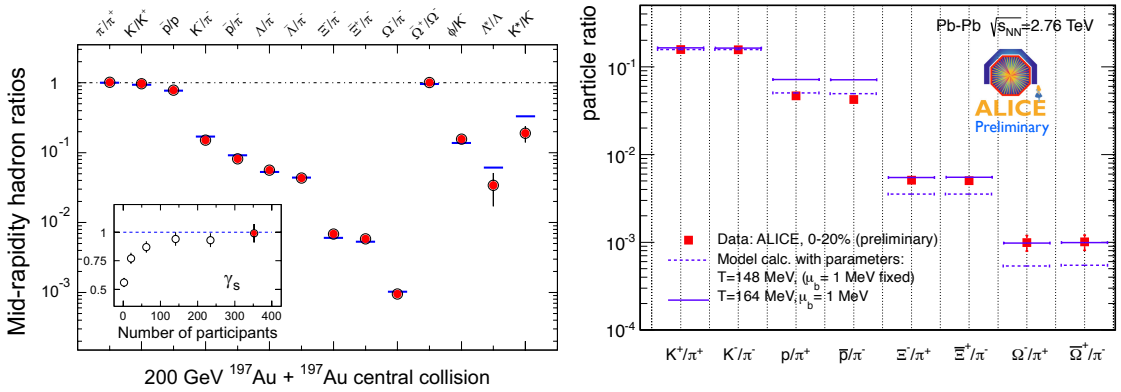

Figure 1.12: Particle ratios measured by STAR for central Au–Au collisions at $\sqrt{s_{\rm NN}} =$ 200 GeV. Horizontal bars represent statistical model fits to the measured yield ratios. The variation of the γ_S factor with the centrality is shown in the inset (left) [28]. Particle ratios measured by ALICE in Pb–Pb collisions at $\sqrt{s_{\rm NN}} = 2.76$ TeV (right). The chemical temperature extracted from the fits at both are compatible [29].

anti-baryons can be created more easily). The strangeness chemical potential is close to zero: the ratio μ_S/μ_B is approximately constant and equal to 0.110 ± 0.0019. The chemical freeze-out temperature T_{ch}, extracted from the data from many experiments (see also Fig. 1.8 left) is slightly higher than 160 MeV. First measurement of the particle ratios have been performed also at the LHC. ALICE has extracted from its particle ratios, built with π, K, p and some strange baryons, the parameters of the thermal model (Fig. 1.12 right) [29]. Results are in agreement with the same chemical temperature as for RHIC experiment, around 164 MeV. Only the ratios involving protons seem to be slightly lower than the model expectation. It is important to notice that the same temperature is recovered for systems with different initial conditions (different centralities, colliding nuclei, collision energies): the chemical freeze-out temperature seems to be unique for all high energy central heavy-ion collisions. This temperature is close to the critical temperature that should characterize the hadronization phase as estimated by lattice QCD calculations.

1.2.3 Strangeness enhancement

The strangeness enhancement has been one of the two main signatures of the formation of a deconfined phase, in high-energy Pb–Pb collisions. With the QGP formation, the QCD chiral symmetry should be restored. Thus the threshold for the production of a $s\bar{s}$ pair reduces from twice the mass of the constituent strange quark ($\sim$ 900 MeV) to twice the intrinsic mass of the quarks ($\sim$ 300 MeV) [10, 12]. Due also to the high energy density of the fireball, a copious production of $s\bar{s}$ pairs, mostly by gluon fusion, is expected. The deconfined phase can also enhance the production of multi-strange baryons (i.e with higher strangeness content) due to recombination mechanisms. An enhanced production of multi-strange baryons such as Ξ and Ω is therefore expected to be a signal of deconfined phase [30]. From the experimental point of view, the reconstruction of multi-strange baryons is performed exploiting their weak decay, this have a separate decay vertex from the interaction point. Evidence of strangeness enhancement has been observed at the

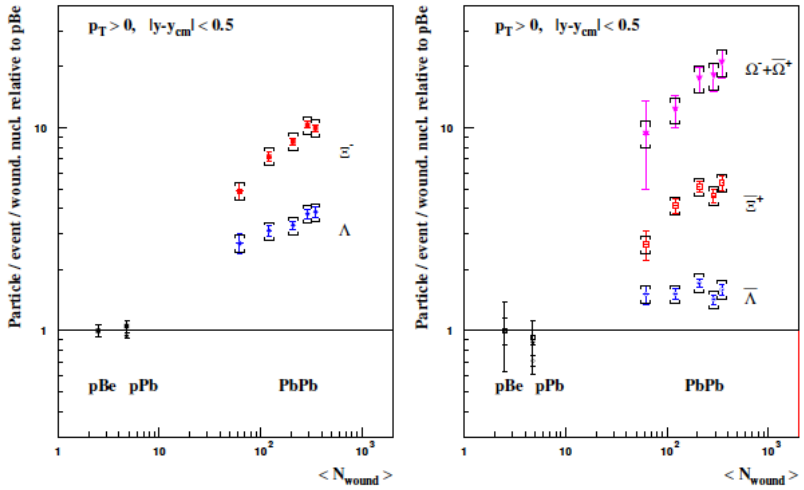

Figure 1.13: First evidence of strangeness enhancement measured at the SPS by the NA57 experiment. The enhancement is defined as the particle yield normalized by the number of participant nucleons in the collision and divided by the measured yield in p–Be collisions. On the left panel the enhancement is shown for hadrons, in the left panel for anti-baryons. Ωs are summed together for statistical reason [31].

fixed target NA57 experiment in Pb–Pb collisions at $\sqrt{s_{\rm NN}} = 17.2$ GeV [31]. Yields in Pb–Pb collisions were then normalized to the participant nucleons in the collisions. The enhancement was then computed by dividing the scaled yields by reference yields measured in p–Be collisions.

Fig. 1.13 shows the enhancement for Λ, Ξ (left) and their anti-particles (right). For statistical reasons, Ω results are considered together for particles and anti-particles. For p–Pb collisions there is no evidence of enhancement. For Pb–Pb collisions an enhancement increasing with centrality was observed. The effect is larger for particles with higher strangeness content up to a factor about 20 for Ωs. No hadronic model has reproduced these observations and they can be interpreted as clear signal of QGP state formation. Also at RHIC, the strangeness enhancement has been measured, but with a lower magnitude than the one observed at the SPS, a part for Λs [18]. In Fig. 1.14 a comparison between, SPS, RHIC and LHC data has been reported [32]. At the LHC, for the moment, the measurement for Ξs and Ωs has been performed in 4 centrality classes. As for the other cases the enhancement has been compared with *pp* data. At the LHC, these *pp* data have been obtained with an interpolation of different energies: $\sqrt{s} = 0.9$ and 7 TeV, since LHC data at the same energy of Pb–Pb collisions were not enough to perform this measurement. As already observed at the SPS and at RHIC, enhancements increase with the number of participants of the collision and with the strangeness content of the baryon. Also the collision energy dependence seems to confirm the trend already observed: at LHC the enhancement is smaller then compared to RHIC and SPS, for Ωs, for example, it reaches a factor of 8, while for at SPS was about a factor 20 bigger than p–Be results. An explanation of this behaviour is given in terms of a statistical model, with canonical strangeness conservation [33]. In a large system with large number of produced particles, the conservation low of quantum numbers (like strangeness), can be implemented on the average by using the corresponding chemical potential. In a small system, with

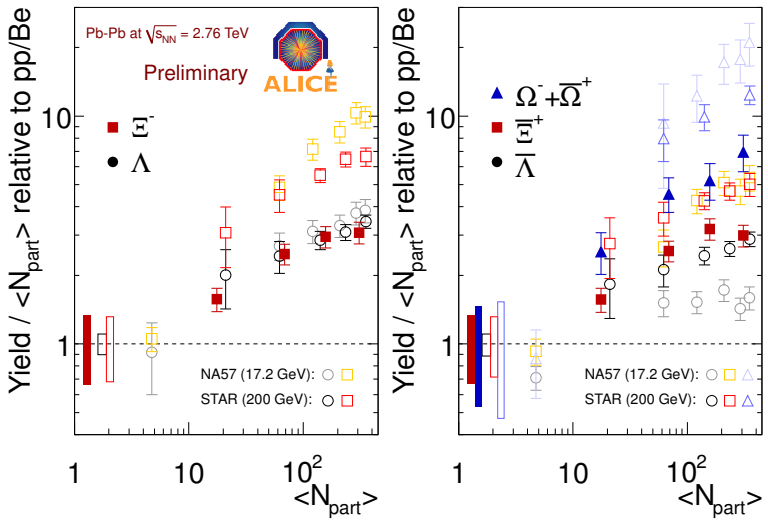

Figure 1.14: Strangeness enhancement measured by ALICE in Pb–Pb collisions at $\sqrt{s_{\rm NN}}$ = 2.76 TeV. The same trend is observed as at the SPS and RHIC (in the figure also these results are plotted). The enhancement decreases with the energy of the colliding system [32].

small particles multiplicities, conservation lows must be applied locally, event-by-event. The conservation of quantum numbers is known to reduce the phase space available for particle production. This canonical suppression factor decreases with lower energy in the centre of mass of the collisions and could explain the larger enhancement for lower energy systems [34].

1.2.4 Quarkonium suppression at SPS, RHIC and LHC

Heavy quark production and suppression provides another unique probe of the strongly interacting matter created in the relativistic heavy-ion collisions. Heavy quarks are produced during the hard scattering processes at the early stage of the collision so that they subsequently interact with the medium. Different behaviour is expected for open heavy flavour hadrons and for quarkonia states. For the former a review of their energy loss will be presented in the next chapter.

Together with the strangeness enhancement effect, the J/Ψ suppression has been considered the second experimental indication of the QGP, because only a deconfined phase could explain how $c\bar{c}$ pairs were suppressed in A–A collisions with respect to pp collisions. In an electromagnetic plasma, the binding potential between two opposite charged particles is reduced by the presence of the surrounding charges (Debye screening). Matzui and Staz, in 1986, proposed the same effect for quarkonia suppression (in particular charmonium states) in heavy-ion collisions, as a QGP signature [35]. In the plasma phase the interaction potential between quarks is expected to be screened beyond the Debye length (λ_D), as in the electromagnetic case. Charmonium and bottomonium states with $r > \lambda_D$ would not bind and their production would be suppressed. The Debye length and, therefore, which of the bound states will be suppressed depend on the temperature of the system. For low energy, like at the SPS, the probability of later combining $Q\bar{Q}$ pairs at the hadronization stage is negligible, due to low number of $c\bar{c}$ produced in the collisions. The

only chance to produce a quarkonium bound state is shortly after the pair is produced. At RHIC and, in particular, at the LHC energies uncorrelated pairs, composed of one quark and one antiquark which do not originate from the same initial interaction, can recombine together and they should contribute to the lower part of the p_t spectra of the produced J/Ψ, leaving a signature on the overall p_t slope. A softening of the p_t spectrum would indicate an increased contribution to charmonium production due to uncorrelated pairs at lower p_t [36].

J/Ψ suppression

At the SPS experiments NA38/50/60 a "normal" suppression of J/Ψ was observed in p–Pb and lighter ion collisions, that was attributed to nuclear absorption. An "anomalous" suppression was observed in Pb–Pb and In–In collisions [37]. Fig. 1.15 (left), reports the ratio of measured over expected J/Ψ (taking into account also the nuclear absorption) as a function of the estimated energy density. The anomalous suppression sets in for $\epsilon \sim 2.3$ GeV/fm^3 that corresponds to an impact parameter of about 8 fm. The suppression seems to increase for more central collisions and this may be interpreted as a successive melting of the χ_c and the J/Ψ. Since the QGP formed at RHIC has longer lifetime and higher energy density, the extrapolation of the SPS scenario predicted an almost total J/Ψ suppression. RHIC results on the J/Ψ suppression were reported in terms of nuclear modification factor ratio R_{AA}. This ratio is defined as:

$$R_{AA}(p_t) = \frac{dN_{AA}/dp_t}{\langle N_{\rm coll}\rangle \times dN_{pp}/dp_t} \tag{1.17}$$

where dN_{AA}/dp_t and dN_{pp}/dp_t are the measured differential yield in nucleus-nucleus and proton-proton collisions respectively; $\langle N_{\rm coll}\rangle$ is the estimated number of binary collisions defined from the Glauber model (see also Sec. 1.2.1). A nuclear modification factor equal to unity can be interpreted with the A–A collisions being a simple superimposition of many nucleon-nucleon collisions. A nuclear factor lower than one indicates an effect of the medium formed during the collisions. RHIC experimental data showed that J/Ψ suppression has the same magnitude as at the SPS energy. These data also showed that the suppression is larger at larger rapidities (Fig. 1.15 right) [38]. All models reproducing the magnitude of J/Ψ suppression at the SPS predicted larger suppression at RHIC. Secondary mechanisms of J/Ψ production have to be taken into account to explain this behaviour, like the recombination of initially uncorrelated $c\bar{c}$ pairs, cold nuclear matter effect, shadowing or charm quark energy loss.

At LHC the J/Ψ suppression has been measured with 2010 data. The CMS experiment reconstructs J/Ψ in the rapidity region $|y| < 2.4$ and with $p_t > 6.5$ GeV/c due to the minimum momentum needed to the muons to reach the muon chambers. CMS observed that the tendency of high p_t J/Ψ's to survive at RHIC [40] is not seen at the LHC (Fig. 1.16 right) [39] . Furthermore, CMS measured less suppression at forward rapidity for high p_t J/Ψ.

At LHC ALICE measured the $R_{\rm AA}$ of J/Ψ's reconstructed via their muon decay in the rapidity region $2.4 < y < 4$ for $p_t > 0$ [41]. Fig. 1.16 (right) shows a comparison of the suppression as a function of centrality, measured in ALICE and in PHENIX for the forward rapidity region. ALICE results are presented with $< N_{\rm part} >$ weighted by $N_{\rm coll}$ to better show the comparison of the two experiments. The suppression measured at the LHC in the forward region is strongly lower than at RHIC.

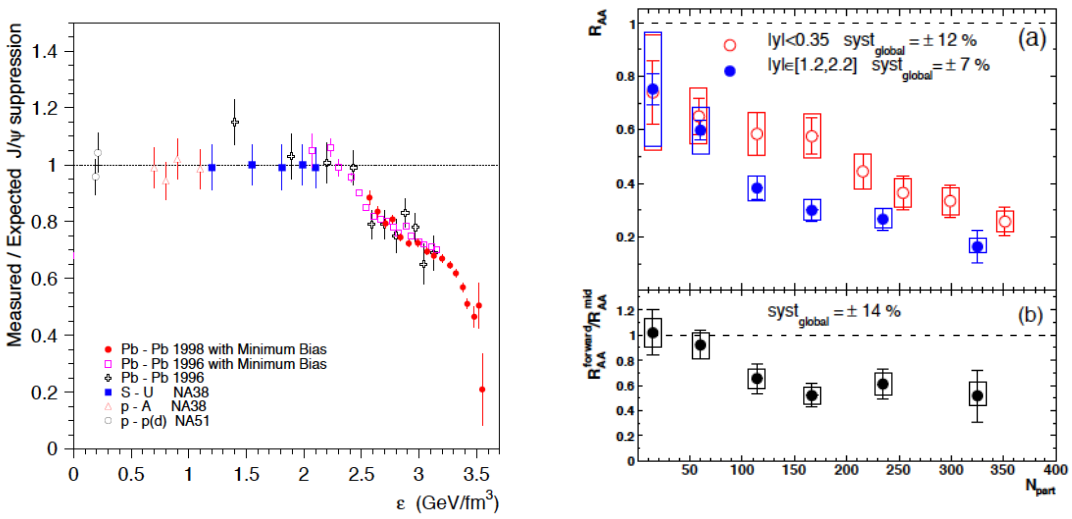

Figure 1.15: J/Ψ "anomalous" suppression measured at the SPS. The ratio is computed with respect to what expected, considering nuclear absorption and shadowing effect (left) [37]. J/Ψ suppression measured at RHIC in $Au-Au$ collisions at $\sqrt{s_{\rm NN}} = 200$ GeV. The suppression is larger in the forward rapidity region, with respect to the mid-rapidity one (right) [38].

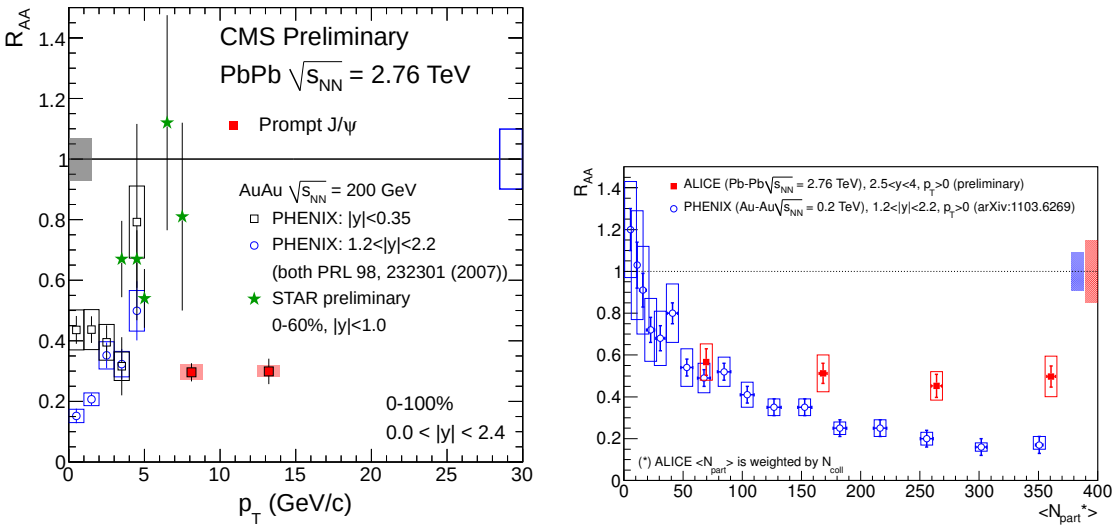

Figure 1.16: J/Ψ R_{AA} versus $p_{\rm t}$ measured by the CMS experiment and compared with RHIC experiment. The high $p_{\rm t}$ J/Ψ shows a suppression of a factor about 4, showing a different behaviour respect to what observed at RHIC (left) [39]. J/Ψ R_{AA} as a function of the mid-rapidity charged-particle density measured in Pb–Pb collisions at $\sqrt{s_{\rm NN}} = 2.76$ TeV compared to PHENIX results in $Au-Au$ collisions at $\sqrt{s_{\rm NN}} = 0.2$ TeV at forward rapidity (left) [41]. ALICE results are shown as a function of $< N_{\rm part} >$ weighted by $N_{\rm coll}$.

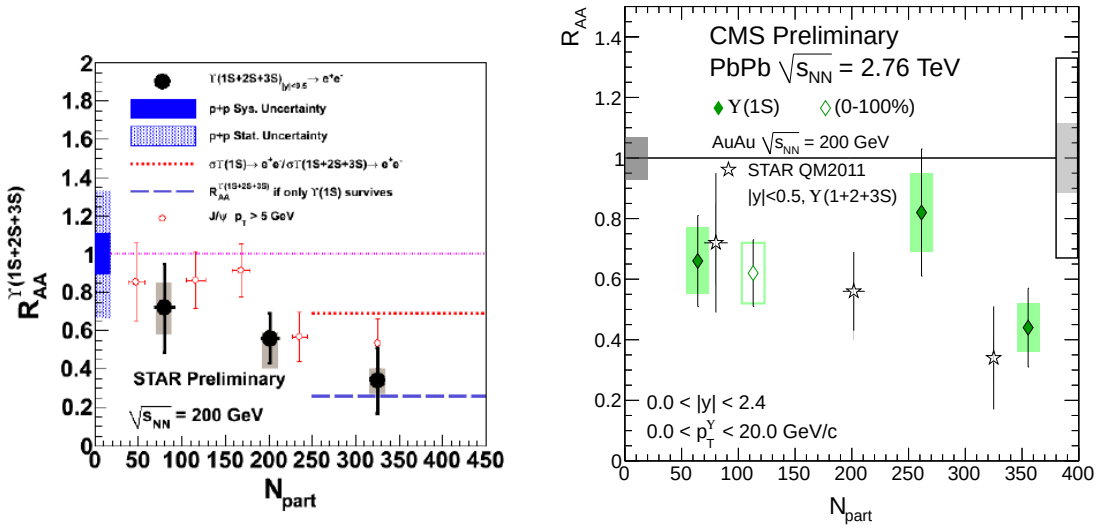

Figure 1.17: R_{AA} of the three Υ states versus centrality, measured at STAR experiment (left) [46]. Υ (1S) state R_{AA} measured as a function of centrality by the CMS experiment. In the same figure also the STAR point are reported (right) [39].

Υ suppression

First measurements of Υ suppression in heavy ion collisions were presented during the Quark Matter conference, held in Annecy at the end of May 2011. STAR presented the results on the nuclear modification factor (R_{AA}) of the three Υ's state together, reconstructed at mid-rapidity via their electronic decay channel [46]. Fig. 1.17 (right) shows R_{AA} versus centrality for the three Υ states in the rapidity region $|y| < 1$. The results show a suppression of about a factor 3 for the most central class, even if the measurement has a large statistical error, since the beauty production cross section at RHIC energy is small. A clear trend versus centrality is also observed. The Υ measurement has also been presented by CMS. In this case, bottomonium states are reconstructed via their muonic decays and the different states are resolved thanks to the excellent transverse momentum resolution. CMS measured R_{AA} for Υ(1S) state as a function of $p_{\rm t}$, y and centrality [39]. A suppression of a factor 2.3 is observed for low $p_{\rm t}$. The rapidity dependence indicates a slightly smaller suppression at forward rapidity, but in both cases the statistical uncertainties are too large to draw any strong conclusion. The Υ(1S) state is suppressed of about of a factor 2 in the 0-10% central collisions, in agreement to what showed by STAR experiment (Fig. 1.17, right).

CMS also separated the $\Upsilon(1S)$ state from higher states in Pb–Pb as in pp collisions [39]. The suppression for the higher mass Υ states has been quantify with an un-binned maximum likelihood simultaneous fit to pp and Pb–Pb mass spectra. The ratio $\Upsilon(2S+3S)/\Upsilon(1S)$ in Pb–Pb and in pp can represent this suppression and it can benefit from an almost complete cancellation of possibile acceptance and efficiencies differences between the two cases:

$$\frac{\Upsilon(2S+3S)/\Upsilon(1S)|_{\rm Pb–Pb}}{\Upsilon(2S+3S)/\Upsilon(1S)|_{pp}} = 0.31^{+0.19}_{-0.15}(\text{stat.}) \pm 0.03(\text{syst.}) \qquad (1.18)$$

The suppression of the states $\Upsilon(2S+3S)$ is evident for Pb–Pb collisions computed with

respect to the ground state ($\Upsilon(1S)$) and it could indicate that the ground state suppression in Pb–Pb collisions is due to the melting of excited states.

Conclusions on the QGP and its properties

From the results shown in 2011 Quark Matter conference ultra-relativistic heavy-ion collision entered in a new era, with the starting of the LHC. The strongly interacting medium formed at the LHC:

- has an energy density of about $\epsilon_{B_j} \times \tau = 16$ GeV/fm^2, a factor 3 larger then the corresponding one at RHIC.

- From Hanbury Brown - Twist interferometry the system created at the LHC expands significantly more than at RHIC, with an estimate increase by about a factor of 2 of the volume for central collisions.

- From particle ratios measured by the ALICE experiment it is possible to extract the chemical freeze-out temperature T_{ch} using a statistical model fits to the particele yield. The chemical freeze-out temperature is confirmed to be close to the one measured at RHIC $T_{\mathrm{ch}} = 164$ MeV.

- Elliptic flow, already measured at RHIC experiments, is also measured for the expanding fireball produced at the LHC and it shows an increase of about 20% compared to RHIC: although the events at the LHC are on the average harder than those at RHIC, the hydrodynamical properties of the two system seems to be rather similar. The hot and dense matter created at the LHC still behaves fluid with almost zero viscosity.

- Strangeness production confirms what was already shown in RHIC and SPS experiments: the enhancement of the strangeness production is visible in Pb–Pb but the enhancement is lower for higher collisions energy.

- Quarkonium suppression can give indications on the temperature of the fireball, since $c\bar{c}$ pairs could be screened from the other colour charges present in the plasma. J/Ψ suppression is at the LHC more puzzling then at lower energies since the number of charm pairs produced is larger to allow recombination effects, as it was already shown at RHIC. Υ states suppression was measured for the first time at the LHC, especially for the two higher masses state of the bottomonium.

2 Heavy flavour as a probe of the QGP at RHIC and LHC

The heavy quark production and their interaction with the strongly interacting medium, formed in high-energy heavy-ion collisions, is the main topic of this thesis. The charm production cross section in *pp* collisions is the reference for the heavy-ion measurement. Theoretical calculations and perturbative QCD (pQCD) predictions for heavy quark production in *pp* collisions are shown in the first part of this chapter. In the first section also the heavy flavour production in Pb–Pb collisions is described. The second section of the chapter is devoted to the description of partonic energy loss mechanisms in the strongly interacting medium and how this effect is treated for different jet quenching models based mainly on three calculations: pQCD, AdS/CFT and transport models. For each of these approaches, it is explained how they treat heavy quark energy loss, if this can be done within their framework. Sections 3 and 4 are focused on the experimental results. Jet quenching results from RHIC to LHC are described in section 3, for three different measurements, and compared to the theoretical models previously introduced. The last section is devoted to open heavy flavour measurements both in *pp* and A–A collisions at different energies. This represents the state of the art of the measurements before the starting of the LHC, for which the results will be described in the next chapters.

2.1 Heavy flavour production in high energy hadron collisions

2.1.1 Heavy flavour production in *pp* collisions

Given their large masses charm and beauty quarks are produced in hard-scattering processes with large momentum transfer ($Q^2 \gtrsim 4\mathrm{m}^2_{\mathrm{c,b}}$). In this Q^2 region, the QCD coupling is smaller than unit and a perturbative calculation for heavy quark production can be performed. For the threshold of charm production, α_S sets in the range $0.25 \lesssim \alpha_S(Q^2, \mu_{\mathrm{R}}) \lesssim 0.6$, depending on the renormalization scale (μ_{R}); for these values it is possible to expand the hard-scattering amplitude in terms of α_S powers. The single-inclusive differential cross section for heavy flavour hadron ($\mathrm{H_Q}$) production can be expressed, according to the factorization theorem, as:

$$\frac{d\sigma^{\mathrm{pp}\to\mathrm{H_Q X}}}{dp_{\mathrm{t}}} = \sum_{i,j=q,\bar{q},g} f_i(x_i,\mu_{\mathrm{F}}^2) \otimes f_j(x_j,\mu_{\mathrm{F}}^2) \otimes \frac{d\hat{\sigma}^{ij\to\mathbf{Q}\bar{\mathbf{Q}}}(x_i,x_j,\mu_{\mathrm{F}}^2)}{dp_{\mathrm{t}}} \otimes D(z,\mu_{\mathrm{F}}^2), \qquad (2.1)$$

where **Q** is the charm or beauty quark, p_{t} its transverse momentum and μ_F the factorization scale. In Eq. (2.1) it is possible to recognize three different terms:

- the parton distribution functions $f_i(x_i, \mu_{\rm F}^2)$,
- the partonic cross section $d\hat{\sigma}/dp_{\rm t}$,
- the fragmentation function $D(z, \mu_{\rm F}^2)$

The parton distribution functions (PDFs) represent the probability of finding a quark or a gluon i that carries a momentum fraction x_i of the nucleon (also called Bjorken x). Initial values of the PDFs, at low Q^2, are obtained by fitting ep collisions data. The parton distribution functions are evolved in Q^2 up to the factorization scale $\mu_{\rm F}$ using DGLAP equations [47].

The partonic cross section is the production cross section of heavy quark pair, starting from two colliding partons. The partonic cross section can be computed by perturbative QCD:

$$\hat{\sigma}(\hat{s}, m_{\mathbf{Q}}^2, \mu_{\rm R}, \mu_{\rm F}) = \frac{\alpha_s^2(\mu_{\rm F})}{m_{\mathbf{Q}}^2} \sum_{k=0}^{\infty} (4\pi\alpha_s(\mu_{\rm F}))^k \sum_{l=0}^{k} F_{ij}^{k,l}(\xi) \ln^l \left(\frac{\mu_{\rm R}^2}{m_{\mathbf{Q}}^2} \right), \tag{2.2}$$

where $\hat{s}$ is the centre of mass energy squared of two partons i and j carrying a momentum fraction $x_i,\ x_j$; this energy is related to the variable ξ of the scaling functions ($F_{ij}^{k,l}$): $\xi = \hat{s}/4m_{\mathbf{Q}}^2 - 1$. The cross section is calculated as an expansion in powers of α_s with $k = 0$ corresponding to Leading Order (LO) cross section. The first correction, $k = 1$, correspond to the Next-to-Leading Order (NLO) cross section. At low $p_{\rm t}$, heavy quarks are mainly produced, via pair creation by gluon fusion ($gg \to \mathbf{Q\bar{Q}}$) and $q\bar{q}$ annihilation ($q\bar{q} \to \mathbf{Q\bar{Q}}$). At next-to-leading order, more complicated topologies contribute, like flavour excitation and gluon splitting, not relevant at high-$p_{\rm t}$. The total cross-section for heavy flavour production has been calculated up to NLO order [48].

The fragmentation function represents the probability for the heavy quark $\mathbf{Q}$ to hadronize as a specific hadron $\rm H_{\mathbf{Q}}$ with a momentum fraction $z = p_{\rm H_{\mathbf{Q}}}/p_{\mathbf{Q}}$. This function is obtained by fitting a phenomenological model to fragmentation data, from e^+e^- collisions.

2.1.2 Bjorken x estimate at the LHC

At LHC energies, it is possible to probe the parton distribution functions of the nucleon down to never explored values of x. Let's consider heavy quark pair production ($\mathbf{Q\bar{Q}}$) in pp (or Pb–Pb) collisions. Invariant mass and rapidity of the pair can be written as:

$$M_{\mathbf{Q\bar{Q}}}^2 = \hat{s} = x_1 \frac{Z_1}{A_1} x_2 \frac{Z_2}{A_2} s_{pp} \tag{2.3}$$

$$y_{\mathbf{Q\bar{Q}}} = \frac{1}{2} \ln \left[\frac{E + p_z}{E - p_z} \right] = \frac{1}{2} \ln \left[\frac{x_1}{x_2} \cdot \frac{Z_1 A_2}{Z_2 A_1} \right], \tag{2.4}$$

where $Z_1 Z_2$ and $A_1 A_2$ are the atomic and mass numbers for the two colliding nuclei and s_{pp} is the energy in the centre of mass of the collisions. From the previous relations it is possible to extract x_1 and x_2:

$$x_{1,2} = \frac{A_{1,2}}{Z_{1,2}} \cdot \frac{M_{\mathbf{Q\bar{Q}}}}{\sqrt{s_{pp}}} e^{\pm(y_{\mathbf{Q\bar{Q}}})} \tag{2.5}$$

In the central rapidity region, the two values are almost equal and they depend only on the invariant mass and the collision energy.

At the threshold for $\mathbf{Q\bar{Q}}$ pair production, the x values accessible at the SPS, RHIC and LHC are reported in the table 2.1. Smaller x values are accessible through charm

Table 2.1: Bjorken x values corresponding to charm and beauty production at central rapidity

Machine	SPS	RHIC	LHC	LHC
System	Pb–Pb	Au–Au	Pb–Pb	pp
$\sqrt{s_{\rm NN}}$	17 GeV	200 GeV	2.76 TeV	7 TeV
$c\bar{c}$	$x \simeq 10^{-1}$	$x \simeq 10^{-2}$	$x \simeq 8 \cdot 10^{-4}$	$x \simeq 3 \cdot 10^{-4}$
$b\bar{b}$	-	-	$x \simeq 8 \cdot 10^{-3}$	$x \simeq 3 \cdot 10^{-3}$

production, due its lower mass (for $c\bar{c}$ production in pp collisions at 7 TeV $x \sim 3 \cdot 10^{-4}$). With the ALICE detector it is possible to cover the central rapidity region with the barrel detectors; the forward rapidity muon arm covers the rapidity range $2.5 < y < 4$, allowing to probe x values down to $\sim 10^{-5}$.

2.1.3 pQCD prediction for heavy quark production at the LHC

The cross section for heavy-flavour production at different LHC energies have been estimated with NLO pQCD calculations implemented in the program HVQMNR [49, 120].

The main sources of theoretical uncertainties are related to the value of the mass of heavy quarks and to the renormalization and factorization scales. These are usually varied in the ranges: $1.3 < m_c < 1.7$ GeV, $4,5 < m_b < 5.0$ GeV, and $0.5 < \mu_F/\mu_0 < 2$, $0.5 < \mu_R/\mu_0 < 2$, where μ_0 is approximately the transverse mass of the produced heavy quark.

The state-of-the-art of perturbative QCD calculations of heavy quarks production as now, it is Fixed-Order-Next-to-Leading-Log (FONLL) calculations, where large logarithmic terms beyond next-to-leading order are accounted in the next-to-leading-log resummation for the higher-$p_{\rm t}$ region [50]. The other major improvement of FONLL with respect to previous calculations is the fit of the moments of the fragmentation functions using Kartelishivili form for the fit functions [51]. This last improvement allowed to obtain very good agreement with beauty cross section results measured at Tevatron [52]. The fixed-order NLO order calculation in HVQMNR coincides with FONLL calculations in the low and intermediate $p_{\rm t}$ region.

A different implementation of the pQCD calculations is called general-mass variable flavour number scheme (GM-VFNS). This approach starts from the $p_{\rm t} \gg m$ region and absorbs the large logarithms $\ln(p_{\rm t}^2/m^2)$ into c-quark PDF of the incoming hadrons and the fragmentation function for the $c \rightarrow {\rm hadron_c}$. In Fig. 2.1 (left) the ${\rm D^0} \rightarrow {\rm K^-}\pi^+$ $p_{\rm t}$-differential cross section is shown for FONLL calculation (red) and GM-VFNS (blue) computed for LHC pp collisions at $\sqrt{s} = 7$ TeV. In Fig. 2.1 (right) the FONLL cross section it is shown for prompt ${\rm D^0}$ (green) and for the ones coming from the decay of beauty hadrons (yellow).

2.1.4 Heavy flavour in Pb–Pb collisions

Hard partons are well-suited probes to study the strongly interacting medium formed in heavy-ion collisions. The interaction of coloured probes within the medium is described by partons energy loss, via gluon radiation emission or via collisions with other partons formed in the deconfined phase.

Heavy quarks are produced in the early stages of the collision, during primary, hard scatterings, like gluon fusion and quark-antiquark annihilation. These scatterings have

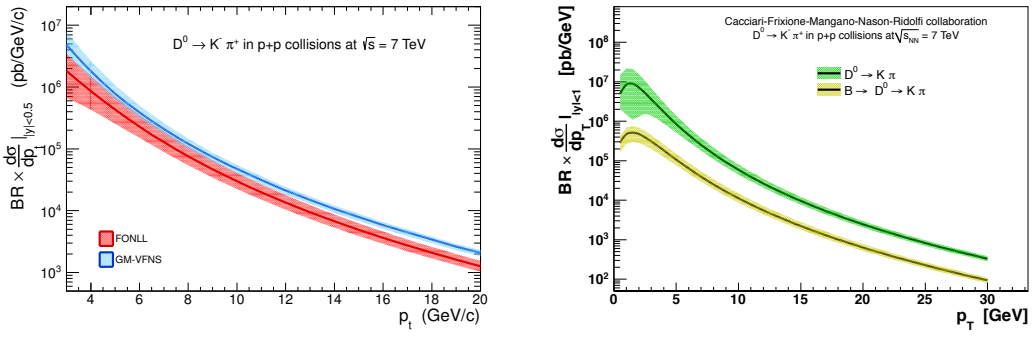

Figure 2.1: $D^0 \to K^-\pi^+$ cross section predictions as a function of p_t, for FONLL [50] (red) and GM-VFNS [53] (blue) calculations (right). Theoretical calculation for the $D^0 \to K^-\pi^+$ cross section for prompt D^0 and D^0 coming from beauty hadrons decays in pp collisions at $\sqrt{s} = 7$ TeV (left).

large virtuality Q and, consequently, they are characterized by small temporal and spatial scales. Therefore heavy quark production is not affected by the properties of the medium.

The large virtuality of the collisions assures the reliability of the perturbative QCD approach used to compute the cross section. These calculations can be also used to obtain energy interpolations needed to compare the results for the different colliding systems, in case they are not measured at the same energy, as it is the case at the LHC.

Once heavy quarks are produced, they undergo energy loss while moving through the medium. This mechanism, regulated by QCD, will be described in the next section. The energy loss mainly depends on density, opacity and size of the medium. Therefore, heavy quarks, and hard partons in general, can be used to probe these properties of the QGP.

The comparison between pp and Pb–Pb collisions has to be considered, taking into account possible initial state effect that can alterate the binary scaling and the estimate of the energy loss contribution. Final states effects, like jet quenching, charmonium suppression, parton energy loss, are expected to be present only in Pb–Pb interactions. Initial state effects can be present both in Pb–Pb and p–Pb: a p–Pb measurement would be necessary then to separate the two effects. One of the most important initial state effect that can play a role for low-p_t charm measurement is the nuclear shadowing. This effect is due to a change in the PDFs of the nuclei with respect to the parton ones. Large-x partons in one of the two colliding Pb nuclei interact with the other incoming nuclei as a superimposition of gluons. Gluons are so many within the nuclei that the low momentum-ones tend to merge together and to have larger x. As a consequence of this shift towards larger x, the nuclear parton densities function are depleted in the small-x region with respect to the proton parton densities [54]. No direct measurement of the shadowing effect are available for the LHC energies, only theoretical parametrization and extrapolation of the nuclear-modified PDFs can give some estimate of the effect.

The evaluation of the energy loss effect is done with the experimental measurement of the nuclear modification factor, as already introduced for the J/Ψ suppression (Sec. 1.2.4). The nuclear modification factor ($R_{\rm AA}$) is defined as the ratio of the particle yields measured in Pb–Pb and pp collisions, where the latter are scaled by the corresponding number of binary nucleon-nucleon collisions, obtained by the Glauber model calculations [15]. The $R_{\rm AA}$ can also be computed using the overlap nuclear function ($T_{\rm AA}$), connected to the

number of binary collisions through the nucleus-nucleus inelastic cross section. Eq. (2.6) shows both definitions.

$$R_{AA}(p_{\mathrm{t}}) = \frac{dN_{AA}/dp_{\mathrm{t}}}{\langle N_{\mathrm{coll}}\rangle \times dN_{pp}/dp_{\mathrm{t}}} = \frac{dN_{AA}/dp_{\mathrm{t}}}{\langle T_{\mathrm{AA}}\rangle \times d\sigma_{pp}/dp_{\mathrm{t}}} \tag{2.6}$$

The nuclear modification factor of J/Ψ ("hidden" charm) has been measured at RHIC and at the LHC as shown in Sec. 1.2.4. The R_{AA} of open charm particles (hadrons with one charm quark and one or two light quarks) has never been measured directly with the full decay channel reconstruction. At RHIC, as it will be shown in Sec. 2.4.2, the R_{AA} for electrons coming from the decay of heavy flavour hadrons has been measures but without separation of beauty and charm contributions. Moreover, the measurement through the semi-leptonic decay does not allow to reconstruct the p_{t} of the heavy flavour hadrons, since the full reconstruction is not available.

The goal of this thesis is the first measurement of direct charm nuclear modification factor using the D^0 meson, reconstructed in its two prongs decay channel $\mathrm{D}^0 \to \mathrm{K}^-\pi^+$ with the ALICE detector. This measurement allows to give the first direct result on the charm quark energy loss in ultra-relativistic heavy-ion collisions.

2.2 Energy loss effect in a strongly interacting medium

What has been briefly discussed in Sec. 2.1.4 will be deeper described and generalized in this section. Not only heavy flavour production, but all high virtuality processes can be good probes to study medium interactions. Jets and high-p_{t} hadrons (also called "hard-probes") are produced with hard partonic scatterings in a very short time scales. Also photons and electromagnetic probes are very important as calibration probes, since their colourless state allows to confirm the coloured partonic structure of the medium. As it was done for the J/Ψ anomalous suppressions (Sec. 1.2.4), the main observable to study the interaction of the "hard probes" with the medium is the nuclear modification factor R_{AA}, that compares the behaviour of the probe in pp and Pb–Pb collisions (Eq. 2.6). The interaction with the medium is mainly described considering that partons lose energy passing through it. Induced gluon radiation and elastic collisions with other partons are the two main mechanisms causing the hard probes energy loss, similarly to what happens in QED.

As already mentioned, the energy that a parton loses in the medium (ΔE) provides fundamental informations on its properties. The energy loss depends both on the probes characteristics (energy E, mass m and colour charge) and the plasma properties (temperature T, particle-medium interaction coupling α_s, size L). Some variables are used to characterize the medium-particle interactions:

- *mean free path* $\lambda = 1/\rho\sigma$ is related to the medium density ρ and the cross section of interaction for the particle in the medium (σ)
- *opacity* is the number of scatterings expected in a medium of thickness L: $N = L/\lambda$
- *Debye mass* m_D is the inverse of the screening length introduced in the Sec. 1.2.4, it is related with the temperature of the medium and the momenta exchanged between the probe and the medium.
- *transport coefficient* is probably the most important, since it describes the probability of a scattering to occur in the medium, linking the thermodynamical and dynamical

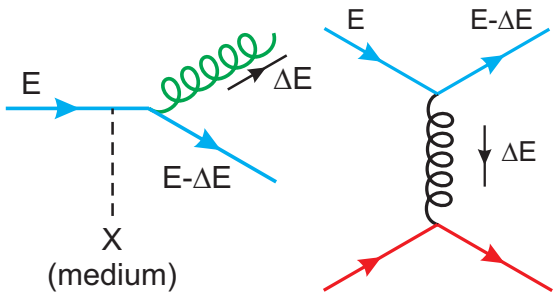

Figure 2.2: Diagrams for radiative (left) and collisional (right) energy losses of a quark of energy E traversing a quark medium and loosing a fraction of energy ΔE.

properties of the medium:

$$\hat{q} = \frac{m_D^2}{\lambda} = m_D^2 \rho\sigma = \frac{\langle k_\perp^2 \rangle}{\lambda}, \tag{2.7}$$

where $\langle k_\perp^2 \rangle$ is the exchanged between the parton and the medium during the interaction.

- *diffusion constant* D is important for heavy non-relativisitic particles traversing the plasma and it is related to the momentum diffusion coefficient and the momentum drag coefficient.

2.2.1 Mechanisms of in-medium QCD energy loss

The total energy lost by a particle traversing the medium is given by the sum of the collisional and the radiative energy loss: $\Delta E = \Delta E_{\text{coll}} + \Delta E_{\text{rad}}$. Depending on the energy of the particle, one of the two mechanisms will be more important in the total energy loss [55]. The main differences in the energy loss treatment from QED to QCD are related to the non Abelian nature of QCD (Sec. 1.1.1). The QCD coupling runs faster than the α_{em} and the scale μ_F at which the coupling is evaluated has to be considered, since it can change significantly for different ranges of the scale.

In QCD, in addition, quarks and gluons have different coupling with the medium, due to their different colour charges. The relative strengths of the three QCD vertices (gg, gq, $q\bar{q}$) are determined by the structure (Casimir Factors) of the gauge $\text{SU(3)}_{\text{colour}}$ group. The probability for a gluon to radiate a gluon is proportional to the colour factor $C_A = 3$, for a quark the same probability is proportional to $C_F = 4/3$. In the limit where gluons carry a small fraction of the original parton momentum, a gluon can radiate $C_A/C_F = 9/4$ higher number of gluons than a quark. That is also the reason why jets coming from gluon fragmentation have a larger and softer hadrons multiplicity than those coming from quark fragmentation.

Collisional energy loss

Collisional energy loss is related to elastic scatterings of the coloured charges with the medium (Fig. 2.2 right). It dominates for low momentum particles. The average energy lost in one scattering, in a medium of temperature T, is:

$$\langle \Delta E_{coll}^{1scatt} \rangle \approx \frac{1}{\sigma T} \int_{m_D^2}^{tmax} t \frac{d\sigma}{dt} dt, \tag{2.8}$$

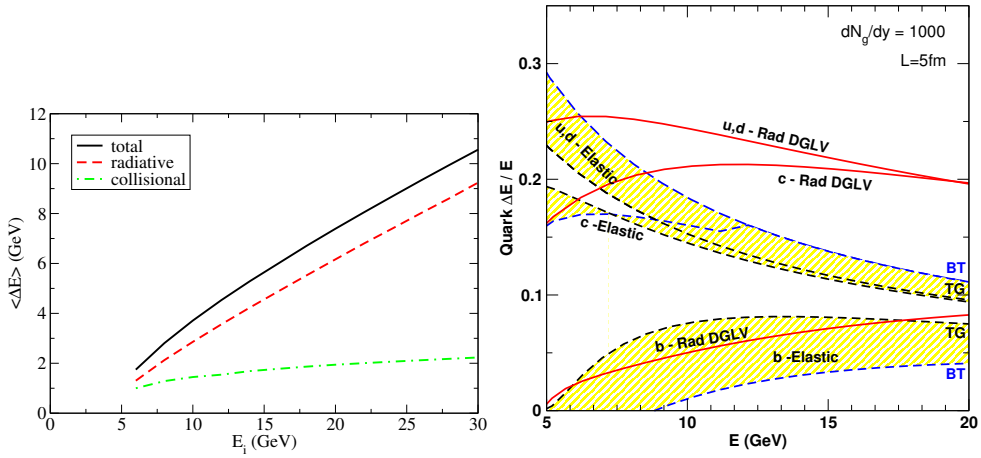

Figure 2.3: Comparison of the average radiative and elastic energy loss of light quarks (left) and light and heavy quarks (right) passing through the medium produced in central Au–Au collisions at RHIC energies obtained with two different energy loss models [55, 56, 59].

where $t = Q^2$ is the momentum transferred in the scattering and σ is the integrated cross section of the particle-medium interaction [55]. In the previous equation it is possible to consider the limits of the integral as the QGP Debye mass squared and the total energy available in the scattering $t_{max} = s \sim ET$, where E is the initial parton energy. The main cross section contribution comes from the parton-parton t-differential cross section:

$$\frac{d\sigma}{dt} \approx C_i \frac{4\pi\alpha_s(t)}{t^2}, \text{ with } \alpha_s(t) = \frac{12\pi}{(33 - 2n_f)\ln(t/\Lambda^2_{QCD})}, \tag{2.9}$$

where $C_i = 9/4, 1, 4/9$ are the colour factors for gg, gq, $q\bar{q}$ scattering respectively. For $E \gg M^2/T$ (with M the mass of the quark), the collisional energy loss can be computed as:

$$-\frac{dE_{coll}}{dl}|_{q,g} = \frac{1}{4} C_{F,R}\alpha_s(ET)m_D^2 \ln\left(\frac{ET}{m_D^2}\right) \text{ for light quarks, gluons} \tag{2.10}$$

$$-\frac{dE_{coll}}{dl}|_{\mathbf{Q}} = -\frac{dE_{coll}}{dl}|_{q,g} - \frac{2}{9} C_F \pi T^2 \left[\alpha_s(M^2)\alpha_s(ET)\ln\left(\frac{ET}{m_D^2}\right)\right] \text{ for heavy quarks} \tag{2.11}$$

The energy variation (ΔE), obtained by the integration of previous equations over the path length L, is linear with the medium thickness and it depends only logarithmically on the initial parton energy (E). Let's consider a charm quark $M = 1.3$ GeV/c^2, with initial energy $E = 20$ GeV, and a medium with $T = 0.4$ GeV and $m_D = 1$ GeV/c^2, the elastic energy loss per unit-length is $dE_{coll}/dl = 2.3$ GeV/fm for the collision with a light quark.

Radiative energy loss

Radiative energy loss is related to inelastic scatterings within the medium and it is the most important mechanism at higher partons momenta. The QCD radiative energy loss behaves exactly as the radiative photon emission of an accelerated charged particles in a electromagnetic field, that is also why it is called *gluon bremsstrahlung* (Fig. 2.2 left). The energy variation (ΔE_{rad}) can ben determined from the double differential gluon bremsstrahlung

spectra:

$$\Delta E_{rad}^{1scat} = \int^{E} \int^{k_{T,max}} \omega \frac{d^2 I_{\rm rad}}{d\omega dk_\perp^2} d\omega dk_\perp^2, \tag{2.12}$$

where ω is the energy and $k_\perp$ the transverse momentum of the radiated gluon. In case of incoherent scatterings the total energy loss for radiation is obtained by considering the opacity of the medium: $\Delta E_{rad}^{tot} = N \cdot \Delta E_{rad}^{1scat} = L \Delta E_{rad}^{1scat}/\lambda$.

To compute the radiation probabilities in QCD it is necessary to start with the DGLAP splitting functions in the vacuum, modified to take into account the enhanced medium-induced radiation. The effects of the medium modification are taken into account with the transport coefficient $\hat{q}$.

In case of thick media, i.e for $L \gg \lambda$, the gluon bremsstrahlung can be approximated using Landau-Pomeranchuk-Migdal (LPM) approximation [57]. This approximation introduces a suppression in the radiative spectra due to formation time effects for small energies: $t_{form} \simeq 2\omega/k_\perp^2$ and from that $\langle k_\perp^2 \rangle \lesssim \sqrt{2\omega\hat{q}}$. For the LPM case, it is also necessary to differentiate two cases on the basis of the hardness of the gluon emission with respect to the characteristic gluonsstrahlung energy $\omega_c = \frac{1}{2}\hat{q}L^2$:

$$(\omega < \omega_c) \quad \omega \frac{dI_{\rm rad}}{d\omega} \approx \alpha_s \sqrt{\hat{q}L^2/\omega} \Rightarrow \Delta E_{rad}^{LPM} \approx \alpha_s \hat{q} L^2 \tag{2.13}$$

$$(\omega > \omega_c) \quad \omega \frac{dI_{\rm rad}}{d\omega} \approx \alpha_s \hat{q} L^2/\omega \Rightarrow \Delta E_{rad}^{LPM} \approx \alpha_s \hat{q} L^2 \ln\left(E/(\hat{q}L^2)\right) . \tag{2.14}$$

The QCD radiative energy loss shows a L^2 dependence on the path length, that is characteristic of the medium-induced energy loss as observed also in case of QED plasmas. Again the main difference of the QCD energy loss, with respect to the QED one, is related to the different colour factors for q and g, since $\hat{q}$ is proportional to the interaction cross section of the parton in the medium (Eq. 2.7). In case of hard gluon emission, the energy loss has an additional logarithmic dependence on the energy of the traversing particle. For a gluon with an energy of $E = 20$ GeV in a medium with $\hat{q} = 2$ GeV^2/fm and $L = 6$ fm, the dE_{rad}/dl is of the order of 10 GeV/fm, while in almost the same condition it has been computed as to be 2 GeV/fm for the collisional energy loss. Fig. 2.3 shows a comparison of the average radiative and collisional energy loss of light quarks (left) and light and heavy quarks (right) passing through the medium produced in central Au–Au collision at RHIC energies for AMY energy loss model [56]. The total ΔE is dominated by the contribution of radiative energy loss, corrected by a small fraction due to the elastic contribution. Collisional part can be an important contribution for heavy quarks, due to the correction factor related to the larger mass of the quark introduced in Eq. (2.11).

2.2.2 Heavy-quark energy loss

Due to kinematic constraints, the gluon radiation of heavy quarks differs from that of a massless parton already in the vacuum, since the gluon radiation is suppressed by the introduction of a mass term in the heavy quark propagator. Heavy quarks with energy $M/E > 0$, propagate with a velocity $\beta = \sqrt{1-(M/E)^2}$, smaller than the speed of light [55]. A corrective term enters then in the gluonsstrahlung spectra:

$$\omega \frac{dI_{rad,Q}}{d\omega dk_\perp^2} = \frac{\alpha_s C_{\rm F}}{\pi} \frac{k_\perp^2}{(k_\perp^2 + \omega\theta_0^2)^2} \approx \omega \frac{dI_{rad}}{d\omega dk_\perp^2} \cdot \left(1 + \frac{\theta_0^2}{\theta^2}\right)^{-2}, \quad \theta_0 = \frac{M}{E} = \frac{1}{\gamma}. \tag{2.15}$$

As a consequence, in the vacuum, gluon radiation at angles θ smaller than the ratio of their mass/energy is suppressed; this behaviour is known as "dead cone" effect [60].

In the medium, the total amount of reduction depends on some variables of the system (E, M, L). For a gluon emission angle, considered as $\theta \simeq (\hat{q}/\omega^3)^{1/4}$, the dead cone suppression decreases for higher energy of the heavy quark and it increases for harder gluon emissions. This last dependency shows that the high-energy part of the gluon radiation spectra can be suppressed by the dead cone effect. The multiplicative factor that in Eq. (2.15) differentiates the heavy quark gluonsstrahlung spectra, with respect to the light hadrons one, is called heavy-to-light suppression factor ($F_{\mathrm{H/L}}$). This factor increases as the heavy quark energy increases, the suppression is then lower when the mass of quark play a less significant role in the energy balance. The effect of the dead cone correction is visible also in Fig. 2.3 (right panel) for pQCD radiative and elastic energy loss model [59]. The quark relative energy loss is shown as a function of its initial energy, for both energy loss processes. For quark with $p_{\mathrm{t}} < 8$ GeV/c the DGLV model shows a clear hierarchy in the relative energy loss of the different quarks [59]. Light quarks lose around 25% of their energy, charm quark about 20% and beauty quarks less than 10%. At higher p_{t} all the curves for collisional energy loss seems to converge around a 10% relative energy loss, while the difference is still clear for radiative energy loss of beauty with respect to the other quarks.

To compare this difference in the energy loss, an important observable can be the heavy to light ratios. The heavy to light ratios for D and B mesons, $R_{D/h}$ and $R_{B/h}$ are defined as the ratio of the nuclear modification factor of the heavy flavour meson to the light flavour hadrons (h):

$$R_{D(B)/h}(p_{\mathrm{t}}) = R_{AA}^{D(B)}(p_{\mathrm{t}})/R_{AA}^{h}(p_{\mathrm{t}}) = \frac{[d^2N_{AA}^{D(B)}/dp_{\mathrm{t}}dy]/[d^2N_{pp}^{D(B)}/dp_{\mathrm{t}}dy]}{[d^2N_{AA}^{h}/dp_{\mathrm{t}}dy]/[d^2N_{pp}^{h}/dp_{\mathrm{t}}dy]} \tag{2.16}$$

Following the different models results, a $R_{D/h}(p_{\mathrm{t}}) > 1$ is expected for $p_{\mathrm{t}} < 10$ GeV/c, where charm energy loss should be smaller than the light mesons one; for higher p_{t} the ratio should converge at one. The $R_{B/h}(p_{\mathrm{t}})$ should be strongly enhanced due to the large b mass even for $p_{\mathrm{t}} > 10$ GeV/c.

Fig. 2.4 shows a Monte Carlo study with an estimate of the heavy-to-light ratio for different configurations of the medium created in central ultra-relativistic heavy-ion collisions, for nominal LHC energies. Two hypotheses on the charm quark mass ($m_{\mathrm{c}} = 0$, $m_{\mathrm{c}} = 1.2$ GeV) are considered, together with different transport coefficients of the strongly interacting medium. The heavy to light ratio ranges from 2.5 up to 1 for particles between 5 and 25 GeV/c. A difference between light particles and charmed mesons energy loss is visible computing this the ratio.

In conclusions, these ratios are suggested to be sensitive to colour charge and to the mass dependence of the medium-induced parton energy loss.

2.2.3 Jet quenching models

The in-medium energy loss presented in the previous section (Sec. 2.2.1) refers to an idealistic situation with a static and uniform QGP characterized by an ideal gas equation of state. The plasma formed in heavy-ion collision is more complex and its properties are more difficult to measure. It is not possible, indeed, to measure directly the parton that experienced the energy loss. What is measured is its hadronic final state, after fragmentation. The properties of the plasma are position and time dependent, since the medium is expanding with large longitudinal velocities. The finite size of the medium and associated energy loss fluctuations have also to be considered.

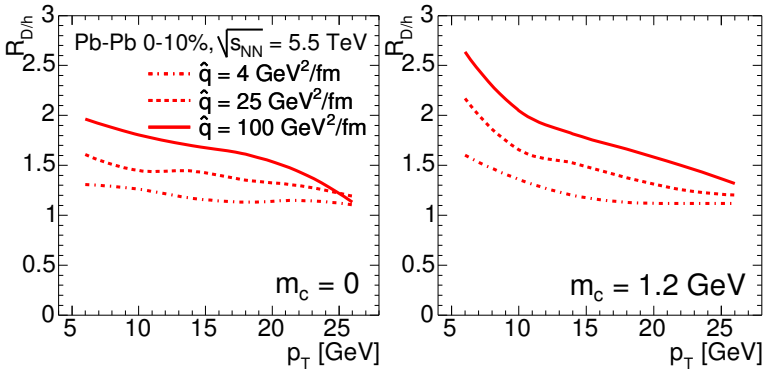

Figure 2.4: Study of the heavy-to-light ratio as a function of p_t for D mesons. The simulation is performed with two different hypotheses on the charm quark mass and three estimates for the transport coefficient of the medium. The difference between the energy loss of charm and light hadrons can reach also a factor 2.5 in case of medium with $\hat{q} = 100$ GeV^2/fm [67].

To take into account these effects, that can change the dependencies of the analytical energy loss equations, phenomenological approaches have been developed to connect the QCD energy loss calculations with experimental observables. Some models are based on pQCD factorized approach, where energy loss is concentrated on the calculation of the medium-modified parton fragmentation function into final hadrons. The differences between the approaches are on the different relationship between scales, size of the medium and approximation on its space-time profile.

A different starting point to understand the problem uses the AdS/CFT calculation, where dual quantum field theory can be used to compute the transport properties of strongly coupled plasma. This theory is involving black holes in anti-de Sitter (AdS) space, based on the insight derived from string theory. This duality allows to connect weakly coupled gravity theories in higher dimensions with four-dimensional gauge theories in strong coupling limit.

The last model considered is the heavy quark transport model, where the transport coefficients are derived from the interaction of only heavy quarks with the strongly interacting medium. This model starts from the description of the dynamics of the charm quark in the medium, with Brownian approximation and using the Boltzmann equation. From the dynamical evolution it is possibile to compute the drag and diffusion forces that act on the heavy quark.

Path Integral approach to the opacity expansion - BDMPS-LCPI / ASW

The approaches of Baier, Dokoshitzer, Mueller, Peignè and Schiff (BDMPS) [61, 62, 63] and the Light Cone Path Integral (LCPI) [64, 65] compute radiative energy loss in a coloured medium with a muliple-soft scatterings approximation. A hard parton traversing the medium interacts with various scattering centres and splits into an outgoing lower energy parton and a radiated gluon. The propagation of the traversing parton and radiated gluons is expressed using Green's functions, obtained by a path integral over the fields. The final outcome of the calculation is an analytical expression of radiated gluon energy distribution $\omega dI/d\omega$ as a function of $\hat{q}$.

The medium-modified parton to hadron fragmentation functions ($D_{i\to h}^{med}(z', Q^2)$) differ from the vacuum ones for the quenching weights $P(\Delta E, \hat{q}, L, C_{\mathrm{R}}, m)$ (Eq. 2.17). These coefficients, computed by Armesto, Salgado and Wiedemann (ASW) [63], give the probability (assumed to be Poissonian) that the traversing parton loses a fraction of energy ΔE due to n gluon emissions.

$$D_{i\to h}^{med}(z', Q^2) = P(\Delta E, \hat{q}, L, C_{\mathrm{R}}, m) \otimes D_{i\to h}^{vac}(z, Q^2). \tag{2.17}$$

The quenching weights have been implemented in a Monte Carlo model, called Parton Quenching Model (PQM) [90], that considers a realistic parton production point in a static medium. The longitudinal expansion of the medium is taken into account by rescaling the transport coefficient, using a time dependence plasma density [66]:

$$\langle\hat{q}\rangle = \frac{2}{L^2}\int_{\tau_0}^{\tau_0+L} d\tau(\tau-\tau_0)\hat{q}(\tau) \quad \text{where} \quad \hat{\mathrm{q}}(\tau) = \hat{\mathrm{q}}(\tau_0)\left(\frac{\tau_0}{\tau}\right)^{\alpha} \quad \text{and} \quad \rho(\tau) \propto \tau^{-\alpha}. \tag{2.18}$$

A purely longitudinal expansion corresponds to $\alpha = 1$ and it is often assumed in phenomenological applications. The transport coefficient $\hat{q}$ is used as a fit parameter and comparison for the data.

Focusing then to the heavy quark sector, the BDMPS method implemented specific quenching weights to consider the medium-induced effects of the emitted parton spectrum, in case of heavy quark energy loss [67]. The quenching weights calculation starts from the medium-induced distribution of gluons energy and transverse momentum, radiated off by the hard massive quarks, due to multiple scattering in the spatially extended medium. The parton mass dependence enters in the gluon energy distribution, through a phase factor related to the three momentum conservation of initial quark, final quark and emitted gluon. With these quenching weights, partons are fragmented as if they are in the vacuum, according to FONLL fragmentation functions.

DGLV approach

The Gyulassy-Lèvai-Vitev (GLV) [59, 68] approach calculates radiative parton energy loss in a dense deconfined medium made of static scattering centres, producing a screened Coulomb potential, as for the BDMPS approach. The difference between the two approaches is related to the "hardness" of the gluon bremsstrahlung radiation. DGLV starts from a single-hard radiation spectrum which is then expanded to account for gluons emission from multiple scatterings. In the BDMPS phenomenology, a multiple-soft bremsstrahlung radiation is considered.

Let's consider a parton with transverse momentum $q_\perp$ that radiates, before or after the scattering, a gluon with a certain momentum k. Applying a recursive procedure, it is possible to obtain the gluon spectra differential distribution expanded to given order in opacity. Each emission at given opacity is assumed independent and the parton loses an energy fraction ϵ in n tries following a Poissonian distribution as for the BDMPS approach:

$$P_n(\epsilon, E) = \frac{e^{-\langle N^g\rangle}}{n!}\prod_{i=1}^{n}\left[\int d\omega_i \frac{dI}{d\omega_i}\right]\delta(\epsilon E - \sum_{i=1}^{n}\omega_i), \tag{2.19}$$

where $\langle N^g\rangle$ is the mean number of gluons radiated per coherent interaction set. The sum over the tries (n) gives the probability $P(\epsilon)$ for an incident parton to loose a momentum fraction ϵ due to its passage through the medium. The medium-modified fragmentation functions are then derived considering this energy loss. The medium property, usually

obtained from fits to the experimental data is the initial gluon density per unit of rapidity dN^g/dy.

For the DGLV approach, heavy quark energy loss in a hot QCD plasma is computed taking into account the competing effects due to suppression of zero-order gluon radiation below the plasma frequency and the enhancement of gluon radiation due to first order medium induced bremsstrahlung [69]. Heavy quark medium induced radiative energy loss is then derived to all orders in opacity. To compute the heavy quark energy loss a shift of all frequencies in the GLV opacity series is applied, considering a factor for the mass dependence of the quark [70].

The DGLV approach considers the interplay between radiative and collisional energy loss, where also geometric path length fluctuations are taken into account (WHDG approach [71]) . This description is used for both light and heavy quarks so that a direct comparison with data can be performed for the two different cases. Results of this approach compared with RHIC results are shown in [71].

Higher Twist (HT)

Processes in which more than one parton from the same hadron or nucleus interact coherently are called "higher-twist" processes. The higher-twist approximation, then, describes radiative energy loss via multiple scatterings using power corrections to the leading-twist cross section [72, 73]. These corrections are enhanced by the medium sizes, since the multiple scattering can occur more frequently, but suppressed by the power of the hard scale Q^2, since they are higher order processes. The main difference with respect to the other approaches is the possibility to compute multiple Feynman diagrams. They are then combined coherently to compute directly the modification of the fragmentation function as an additive contribution. The medium effects are incorporated in the nuclear quark-gluon correlation term. The normalization of this correlation is defined by fitting data point from which it is possible to calculate the medium-modified fragmentation functions an then the final hadron spectra. For the higher twist approach there are no studies on the heavy quark energy loss.

AMY

In the Arnold-Moore-Yaffe (AMY) approach, radiative parton energy loss is described in a hot QGP in thermal equilibrium [56, 58]. The hard parton scatters other partons in the medium, transferring momentum and inducing collinear radiation. Multiple scatterings of the incoming parton and the radiated gluon are combined to get leading order gluon radiation rate. The transition rates of a parton a into a radiated gluon g and another parton b are computed using temperature dependent Bose-Einstein (for gluons) and Fermi-Dirac (for quarks) exponential factors for the medium partons. These rates are then used to evolve the original distribution of partons over the medium length. The medium-modified fragmentation functions are obtained from a convolution of the vacuum fragmentation functions with the hard partons distributions when exiting the plasma, obtained considering the transition rates. The medium is evolved in a space-time profile starting from for the initial temperature T. AMY approach was not applied to heavy quarks energy loss calculation.

To summarize the differences between pQCD models:

- BDMPS/ASW and DGLV can be applied to thin and thick media, but they do not consider the energy flow into the medium. Both models have prodictions for heavy

quark energy loss.

- HT can compute directly the medium-modified fragmentation function and it can be used to study multi-hadron correlations but the approach is more appropriate for thin than thick media. No predictions for heavy quark energy loss.

- AMY considers processes where thermal gluons are absorbed by the hard partons and the collisional losses can be included in a simple way. This approach can not be applied to non-thermalized media. No predictions for heavy quark energy loss.

AdS/CFT energy loss

The AdS/CFT approach has a totally different starting point to explain the partonic energy loss within the medium. This calculation is based on the duality between weakly coupled gravity and gauge theories in a strong coupling limit. With pQCD based approaches, parton energy loss is considered within ideal an QGP. The medium produced at RHIC, for example, has a temperature in a range where lattice QCD still predicts deviations with respect to the asymptotic ideal gas behaviour. The lattice QCD predictions are more oriented to a weakly coupled plasma description. Many experimental evidences at RHIC are consistent with the formation of a strongly coupled plasma (sQGP) [74].

The coupling Γ is defined as the average potential energy over the average kinetic energy. The parameter Γ is used to measure the interaction strength in electromagnetic plasmas. For $\Gamma \ll 1$ plasmas behave like gases (weakly coupled behaviour), while for $\Gamma \gg 1$ plasmas are strongly coupled and behave like low viscosity liquids and as solides for larger and larger Γ. The analogy with the QCD plasma cannot be applied rigorously but it can be used to qualify its properties. At RHIC, for example, some experimental evidences were found, indicating that the QGP behaves like a "nearly perfect liquid" as electromagnetic plasma, but for the QCD case the long and short range colour interaction properties do not change.

Another important parameter to study the strength of the interaction is the shared viscosity, computed with the η/s ratio, where η represents the viscosity while s is the entropy density of the system. This ratio is supposed to be very small in the QGP from the hydrodynamical calculations and their comparison with experimental data.

The AdS/CFT energy loss approach is developed within dual quantum field theory involving black holes in anti-de Sitter (AdS) space, based on the analogy with string theory. Weakly coupled gravity theories in higher dimensions can be dual to four-dimensional gauge theories in the strong coupling limit. AdS/CFT techniques presently have the limitation that no higher-dimensional gravity or string theory is known to be dual to QCD [75, 76]. Recent applications of this formalism have lead to the determination of transport properties of strongly coupled plasma as its viscosity, the transport coefficient $\hat{q}$ and the heavy quark diffusion coefficient.

The propagation of a parton trough a medium can be computed in terms of Wilson lines. The $\hat{q}$ parameter is identified with the coefficient in the exponential of an adjoint Wilson loop averaged over the medium length $\langle W^A(C)\rangle \propto \exp(\hat{q}L)$. The gravity dual of this Wilson loop is given by the classical action of a string stretching in a AdS space. After solving the equation of motion of the string, the $\hat{q}$ parameter is found to be:

$$\hat{q}_{sym} = \frac{\pi^{3/2}\Gamma(3/4)}{\Gamma(5/4)}\sqrt{g^2 N_c}T^3 \tag{2.20}$$

For standard values of $\alpha_s = 0.5$ and $N_c = 3$, the $\hat{q}$ is computed to range between $4.5 - 20.7$ GeV^2/fm for $T = 0.3 - 0.5$ GeV [55]. This results is in agreement with what has been found at RHIC. It is important to stress that the approach starts from the hypothesis of infinite coupling and number of colours.

Within the AdS/CFT framework, it is also possible to compute the diffusion coefficient of heavy quarks (Eq. 2.21), in a four dimensions Super-Symmetric Yang Mills plasma, that can be used to compare heavy flavour energy loss to the pQCD ones [76]. As for the DGLV and BDMPS cases, the AdS/CFT calculations allows to compare the energy loss for light and heavy quarks, simply considering the initial energy of the quarks, its relativisitic or not relativistic motion and the properties of the medium ($\hat{q}$) [77].

$$D \approx \frac{0.9}{2\pi T}\left(\frac{1.5}{\alpha_s N_c}\right)^{(1/2)} \tag{2.21}$$

Heavy quark transport

Differently from the other models presented, this approach focuses on the heavy quark interaction mechanisms within the QGP. The study of the dynamics of charm propagation in the QGP can lead to the determination of the drag and diffusion forces which act on the charm quark. The motion of a charm quark in the QGP can be described using the Brownian approximation, starting with the Boltzmann equation for the density ($f(x,p,t)$) of charmed quarks in the phase space:

$$\left[\frac{\partial}{\partial t} + \frac{p}{E}\frac{\partial}{\partial x} + F\frac{\partial}{\partial p}\right] f(x,p,t) = \left[\frac{\partial f}{\partial t}\right]_{\text{collisions}}, \tag{2.22}$$

where E is the charm quarks energy and F reppresents external forces acting on it. The right-hand term of the equation contains the interactions with nearby plasma light quarks and gluons. If it is possible to neglect the interaction of the charm quark with other heavy quarks and with background colour fields, the external forces acting on the charm quark are null ($F = 0$). In case of a uniform plasma and with the absence of the external forces, the variation of the density f with time is due only to the collisions:

$$\frac{\partial}{\partial t} f(p,t) = \left[\frac{\partial f}{\partial t}\right]_{\text{collisions}}. \tag{2.23}$$

In the Landau approximation, only soft scatterings are allowed in the collision integral. In this case, Eq. (2.23) is a Fokker-Plank equation [78]. In this scenario it is possible to interpret the collision terms as due to drag forces and diffusion induced by random collisions. Fig. 2.5 shows the drag coefficient as a function of momentum at the temperature $T = 200$ MeV, assuming QCD coupling $\alpha_s = 0.6$ and Debye screening mass $\mu = 200$ MeV. The contribution to the drag coefficient of quarks (dashed-dotted line) is smaller than that of gluon (dashed line) [78].

The calculation of the transverse and longitudinal momentum diffusion coefficients can be performed with a generalization to the QCD case for the heavy quark pairs propagator. This approach describes heavy (static) particles in a hot plasma of electrons, positrons and photons also computing the transport coefficient of the heavy quark pair. Once these transport coefficients were obtained, they were inserted in a relativistic Langevin equation, allowing to follow the stochastic momentum evolution of the heavy quark in the QGP [79].

The numerical results show that for large temperatures ($T = 600$ and T = 800 MeV), the thermalization of c-quarks should be quite fast so that the elliptic flow of the charmed

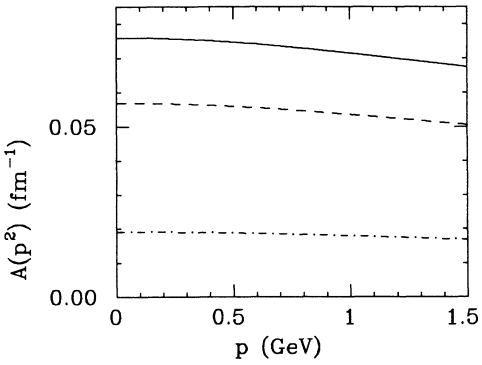

Figure 2.5: Drag coefficient expectation at the temperature $T = 200$ MeV. Quarks and gluons contributions are plotted separately, summed together in the solid line [78].

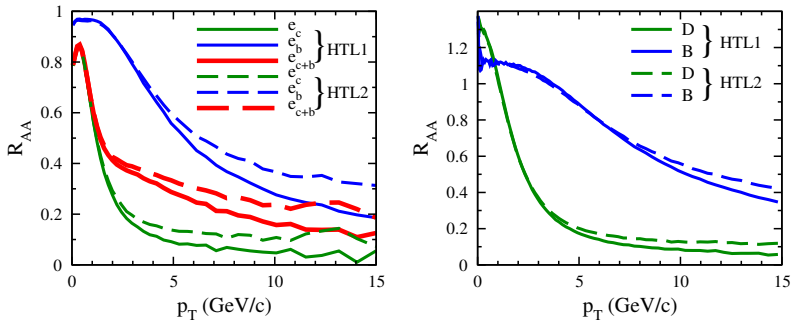

Figure 2.6: R_{AA} for heavy flavour electrons (right) and D, B mesons (left) computed with Langevin equations, expected in Pb–Pb collisions at the LHC in the 0-10% most central events [81].

mesons should be different from zero. Instead the relaxation of b-quark spectra toward equilibrium would be too slow to allow them to follow the flow of the expanding medium [80]. Also the nuclear modification factor of charm and beauty can be extracted with this calculation. Fig. 2.6 shows the results for heavy flavour electrons (right) and D, B mesons for Pb–Pb collisions at the LHC for $\sqrt{s_{\rm NN}} = 2.76$ TeV, in the 0-10% most central events obtained with two slightly different calculations [81]. If the transport coefficients methods allows to have estimates about the nuclear modification factor and the flow of heavy quarks, they cannot access any predictions on light quark energy loss.

Another approach based on the transport model is based on the heavy quark resonant scattering [82]. As already mentioned in previous sections, the heavy quark production time is smaller than the QGP lifetime and heavy quarks can pass through the entire evolution of the fireball. The heavy quark equilibration time is of the order of the QGP lifetime, but smaller than the light-quark one. Since the mass of the heavy quark is bigger than the temperature of the medium, the momentum exchanged by collisions with other partons and the dynamics of these collisions can be treated as a Brownian motion by means of the Fokker-Planck equation. The different aspect of this model with respect to the one introduced before, is the usage of a finite-temperature T-matrix approach to study the problem of the heavy quark interactions in the medium, considering possible

bound states and scattering of heavy quarks. This method can be used since the three-momentum transfer in the scattering dominates over the energy; in this case it is possible to introduce a potential and directly link the heavy quark physics with heavy quark free energy in lattice QCD [83].

The formation of D- and B-meson resonances excitations in the deconfined phase can be introduced, as non perturbative mechanism, to explain the strong charm energy loss observed at RHIC (that will be discussed in Sec. 2.4.1) [115]. The heavy quark interactions terms were introduced at leading order, using an effective theory, where the main parameter are the coupling $G_{S,V}$, related to scalar and vector heavy quark mesons. The presence of these heavy quark resonances at moderate QGP temperatures can accelerate the kinetic equilibrium of c-quarks compared to using perturbative interactions. In this case, indeed, the transport cross section is larger than pQCD calculation and together with an hadronization mechanism, including coalescence, can better explain the results obtained at RHIC [84, 85]. Also in this case the charm flow is an important measurement to validate the theory, but no predictions on light quark $R_{\rm AA}$ are accessible.

2.3 Jet quenching results at RHIC and LHC

One of the "hard probes" used to study the quark gluon plasma and its properties is the so called "jet quenching". The jet quenching was first referred to the attenuation or the disappearance of bunches of hadrons, close in the phase space. These hadrons are the result of partons fragmentation after they have experienced the energy loss interacting with the medium. The jet quenching does not refer only to jet measurement but it became a common name used in the field to study parton energy loss that is reflected in the "hadronic" final state. There are three important measurements used to study the jet quenching effect:

- the single inclusive charged high-$p_{\rm t}$ hadron suppression,
- the high-$p_{\rm t}$ di-hadrons (ϕ, η) correlations,
- the full jet reconstruction studies.

As a proof of the coloured partonic structure of the QGP, the behaviour of the electromagnetic probes has also been measured.

2.3.1 Charged hadron suppression

The high-$p_{\rm t}$ hadron suppression is the first evidence of jet quenching effect measured in heavy-ion collisions. Since most of the energy of the fragmentation parton goes into a single leading hadron, QCD energy loss was predicted to results in a suppression production of high-$p_{\rm t}$ hadrons [86]. As already shown for J/Ψ (Sec. 1.2.4), the"estimator" to evaluate the suppression is the nuclear modification factor. The R_{AA} gives a direct comparison of the yield measured in pp and A–A collisions: in-medium energy loss effects are reflected in a $R_{\rm AA} < 1$, considering initial state effects. The $R_{\rm AA}$ has been used also as a comparison quantity used by theorists to compare their models with data.

Fig. 2.7 (left) shows the π^0 spectrum measured in pp collisions compared with the one measured in central Au–Au collisions at $\sqrt{s_{\rm NN}} = 200$ GeV by the PHENIX experiment [87]. The pp spectra have been scaled by the correspondent T_{AA}, that is nuclear overlap function, which is proportional to the number of binary collisions at the mean

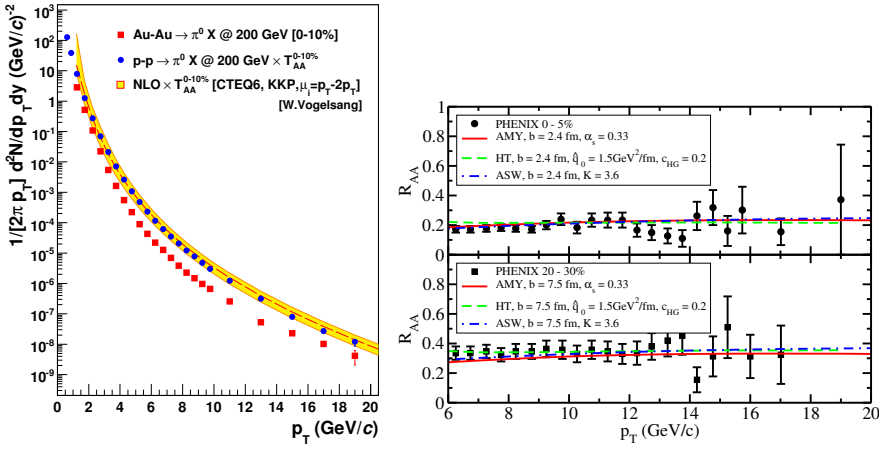

Figure 2.7: π^0 invariant spectra measured at RHIC in pp and Au–Au central collisions. The suppression with respect to scaled pp collisions is clearly visible. No suppression, instead, is visible for peripheral collisions (right) [87]. Nuclear modification factor comparison, computed with ASW [66], HT [72] and AMY [56] approaches, with same hydrodynamic evolution of the medium. Calculations are compared with RHIC $R_{\rm AA}$ charged hadron data measured in Au–Au collisions (0-5% top) and (20-30% bottom) (left) [92].

impact parameter (b). In the figure it is also shown the comparison with NLO pQCD calculations. Central collisions (0-10% centrality class) shows a clear difference between the two spectra, the suppressions of π^0 as well as charged hadrons (dominated by $\pi^{\pm}$) is of a factor 5 with respect to an $R_{\rm AA} = 1$. An $R_{\rm AA} = 0.2$, for different finally produced hadrons is consistent with a scenario where the energy loss is a partonic mechanism that takes place before the fragmentation into hadrons. The suppression factor at RHIC energies is very close to the one expected in a strong quenching limit, where only hadrons coming from partons produced at the surface of the medium shows no final-state modifications in their spectra [88].

The high-$p_{\rm t}$ Au–Au suppression can be well reproduced by parton energy loss models that assume the formation of a very dense system with initial gluon rapidity density $dN^g/dy \approx 1400$ [89], transport coefficient $\hat{q} \sim 13$ GeV^2/fm [90], or plasma temperatures $T \approx 0.4$ GeV [91]. A comparison of three energy loss schemes, presented in the previous Sec. 2.2.3 has been performed within a common "framework" [92]. Not only the usage of the same realistic three dimensional relativistic fluid dynamics was used to compare ASW, HT and AMY approaches, but also identical parton distribution functions and final fragmentation functions. So for the three models only medium tunable parameters are left, that can be related to the transport coefficient.

In Fig. 2.7 (right) it is shown the charged hadrons $R_{\rm AA}$ as a function of $p_{\rm t}$ in Au–Au collisions at 0-5% (top) and 20-30% (bottom) centrality calculated with ASW, HT and AMY approaches, compared to data from PHENIX [92]. The parameters of the different calculations are fixed to one data point in the 0-5% centrality calculation, so that the $p_{\rm t}$ and centrality dependence become predictions of the three approaches. The parameters of the calculations can be tuned in order to describe the data reasonably well for the two cases. The ASW calculations predict a higher transport coefficient respect to AMY an HT. For ASW it was obtained a value between 10 -18.5 GeV^2/fm, for HT 2.3 - 4.3 GeV^2/fm and for AMY 4.1 GeV^2/fm. The variation in the first two models is related to different

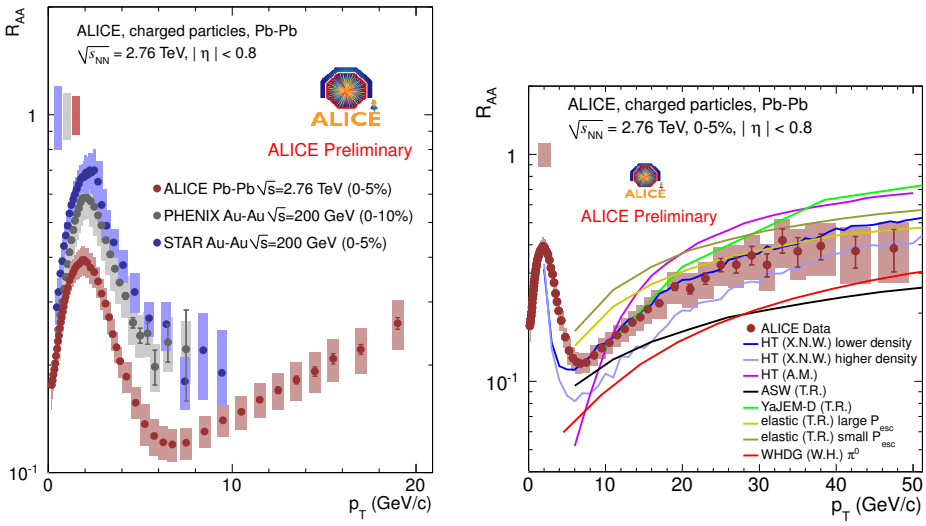

Figure 2.8: Inclusive charged hadrons $R_{\rm AA}$ measured by the ALICE experiment up to $p_{\rm t} = 20$ GeV/c compared with the $R_{\rm AA}$ obtained by PHENIX and STAR (right). Inclusive charged hadron $R_{\rm AA}$ measured by the ALICE experiment up to $p_{\rm t} = 50$ GeV/c compared with different energy loss models [96] (left).

assumption on the scaling of the $\hat{q}$ parameter. The $\hat{q}$ at RHIC can be constraint only within a factor of 2-3 using these models. The main variability of the values of $\hat{q}$ is probably due to the usage of one single observable in the comparison and to the assumptions on the equation of state and time evolution of the medium.

At RHIC the $R_{\rm AA}$ remains almost flat as a function of $p_{\rm t}$ up to the highest values measured $p_{\rm t} = 20$ GeV/c. The rise of the $R_{\rm AA}$ with $p_{\rm t}$ is expected for any model in which the energy loss does not strongly depends on the initial parton energy. This rise is sensitive to the energy loss probability distribution, reflected in the quenching weights coefficients $P_E(\epsilon, \hat{q})$ (Eq. 2.17).

At LHC, ALICE measured inclusive charged hadron suppression from 0.2 GeV/c up to 50 GeV/c using the Pb–Pb data collected in 2010, in the centrality class 0-5%. The $p_{\rm t}$ resolution is $\approx 10\%$ for $p_{\rm t} = 50$ GeV/c. In Fig. 2.8 (left) $R_{\rm AA}$ measured by ALICE is compared to measurements done at STAR and PHENIX experiments [96]. At $p_{\rm t} = 1$ GeV/c the measured $R_{\rm AA}$ is similar to those measured at RHIC. The position of the maximum at $p_{\rm t} = 2$ GeV/c and the decreasing trend for higher $p_{\rm t}$ seem to be similar at the two energies. For hadrons with $p_{\rm t} \simeq 6 - 7$ GeV/c, $R_{\rm AA}$ reaches a minimum of a factor ~ 8 with respect of the superimposition of nucleus nucleus collisions. In this minimum, the suppression seems to be bigger then what measured at RHIC and it is present for different centralities with different magnitudes. The suppression is smaller going from central to peripheral collisions, but with almost the same structure as a function of $p_{\rm t}$. For $p_{\rm t} > 7$ GeV/c a significant rise in the nuclear modification factor up to $p_{\rm t} = 30$ GeV/c is visible. Fig. 2.8 (right) shows the comparison of $R_{\rm AA}$ measured in central Pb–Pb collisions with calculations from energy loss models, in particular, HT seems to agree reasonably with the data, while ASW seems to reproduce the rising trend but not the magnitude of the suppression.

2.3.2 Di-hadron correlations

The modification of the structure of the out-coming hadrons from the medium can be studied with multi-particle correlations. An high-$p_{\rm t}$ trigger particle is selected in the event and the azimuthal ($\Delta\phi = \phi - \phi_{trig}$) and pseudo-rapidity ($\Delta\eta = \eta - \eta_{trig}$) distributions are measured with respect to associated hadrons. The di-hadrons correlation is defined as:

$$C(\Delta\phi, \Delta\eta) = \frac{1}{N_{trig}} \frac{d^2 N_{pair}}{d\Delta\phi d\Delta\eta}, \tag{2.24}$$

where combinatorial background correlations and collective azimuthal effect (elliptic flow) are also part of the correlation distribution results. Different techniques can be used to remove these effects and consider only the di-hadron correlations [97, 98, 99]. As for the inclusive hadrons spectra, a comparison between pp and Pb–Pb comparison is performed in order to understand properties of the medium formed in heavy-ion collisions. In pp, without initial or final state interactions, a di-jet signal appears as two back-to-back Gaussian peaks for $\Delta\phi \sim 0$ (near-side) and $\Delta\phi \sim \pi$ (away-side). The away-side peak is naturally broader in η than the near side peak due to the longitudinal momentum imbalance between the two colliding partons with different momentum fractions (x_1, x_2).

To compute the magnitude of the modification due to energy loss effects, the yield of associated particles to the trigger particle was used, in particular, the ratio of this yield in A–A and pp collisions defines the $I_{\rm AA}$ and the ratio between central and peripheral A–A is defined as $I_{\rm CP}$. The yield of associated particles can be studied as a function of the momentum fraction $z_T = p_{\rm t}^{assoc}/p_{\rm t}^{trig}$.

At the LHC, ALICE measured the I_{AA} in central (0-5%) and peripheral (60-90%) collisions as a function of the associated particle momentum [103]. The trigger particle has been selected in the range $8 < p_{\rm t} < 15$ GeV/c. The chosen momentum range for both associated and trigger particles assures that the jet-like correlations are dominating with respect to collective correlations. The remaining background has studied and subtracted considering it as flat, or with a small v_2 contribution. The $\Delta\eta$ independent correlation can also be removed on the near-side using the η-gap method in order to provide a measurement independent of the flow strength for all harmonics.

In central collisions (Fig. 2.9 left - black points), an away side suppression ($I_{AA} \approx 0.6$) is observed, which is an evidence for in-medium energy loss. An enhancement above unity of 20-30% on the near-side has also been observed. This effect has not been observed at lower collisions energy and it could reflect an interaction with the medium also for the near-side parton. In peripheral collisions (Fig. 2.9 right - red points), both the near and the away side I_{AA} measurement don't show modifications as expected in absence of significant medium effects. With respect to the RHIC results, at LHC energies the away side suppression is smaller, although the single charged hadrons suppression is larger.

Another difference observed at RHIC [100] is the broadening of the near side pseudo-rapidity correlations , out to $\Delta\eta \sim 4$. This effect is still quite puzzling since its properties seem to be more related to a soft underlying event in the collision. More than jet fragmentation effect, the "ridge" seems a bulk matter properties [104].

2.3.3 Jet suppression

The full jet reconstruction in A–A collisions allows to study the energy and the particle multiplicity distribution within the jet, coming from the fragmentation of a quenched parton. Due to the kinematical distributions of the final hadronic states in A–A collisions, the study of jets in heavy ion collisions is particularly challenging, since the jet and

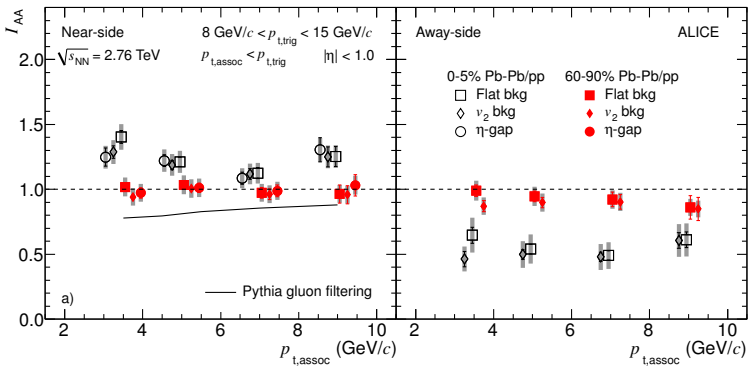

Figure 2.9: I_{AA} measured in central (left) and peripheral (right) collisions for near-side and away-side peak with the ALICE experiment. A suppression is measured for the away-side peak in central collisions, together with an enhancement of about 30% for the near side peak [103].

the background are not well separate. The definition and the measurement of a jet in hadron collisions goes into three main step: the definition of the clustering algorithm, the background subtraction and the jet corrections.

The jet reconstruction algorithm is based on the signals of the cells of hadronic and electromagnetic calorimeters, clustered together to define the hadrons belonging to the same jet. The clustering uses the relative distances in the phase space and it has to take into account soft gluons and the splitting of partons in order not to change the number of final number of reconstructed jets (i.e infrared and collinear safe jet algorithms). The jet algorithm has not to be too sensitive to soft QCD effect like hadronization, underlying event and pile up, moreover in A–A collisions the algorithm has to be fast since it has to run over very high multiplicity environment.

In hadronic collisions, jets rise up on top of large "underlying events" of hadrons coming from other softer parton-parton collisions in the same bunch interaction. Jet reconstruction is based on the definition of a geometrical radius of the jet defined as $R = \sqrt{\Delta\eta^2 + \Delta\phi^2}$. Usually R is defined between 0.3 and 0.5 to minimize the underlying event contribution. Jet can only be identified if the background energy within the cone is smaller then the signal energy. For a radius of the jet of 0.4, for example, the energy within the jet is about 80 GeV at the LHC energies, with large fluctuations, making challenging to reconstruct jets below $E_T \sim 50$ GeV. The "underlying events" background measured event-by-event has to be subtracted from the reconstructed jets. Also studies of embedded high-$p_{\rm t}$ track in the event have been carried on to evaluate how much the background and the jet shape can be modified from these effects.

As for the other jet quenching measurements also for the full reconstructed jets it is possibile to define a nuclear modification factor $R_{\rm AA}^{jet}$ to compare the medium effect in A–A collisions, using as a reference the un-modified pp spectra. In particular, if the medium induced energy loss of the parton is radiated inside the jet the $R_{\rm AA}^{jet}$ should be close to unity, differently to the charged hadrons $R_{\rm AA}$. If the radiation is emitted with large-angle, then jet spectrum is expected to be quenched and the $R_{\rm AA}^{jet} < 1$. An other important study of the structure of the jet is the modification of its shape. The differential $p_{\rm t}$ shape is defined as the average fraction of the jet momenta that lies inside a smaller cone radius, around the jet axis.

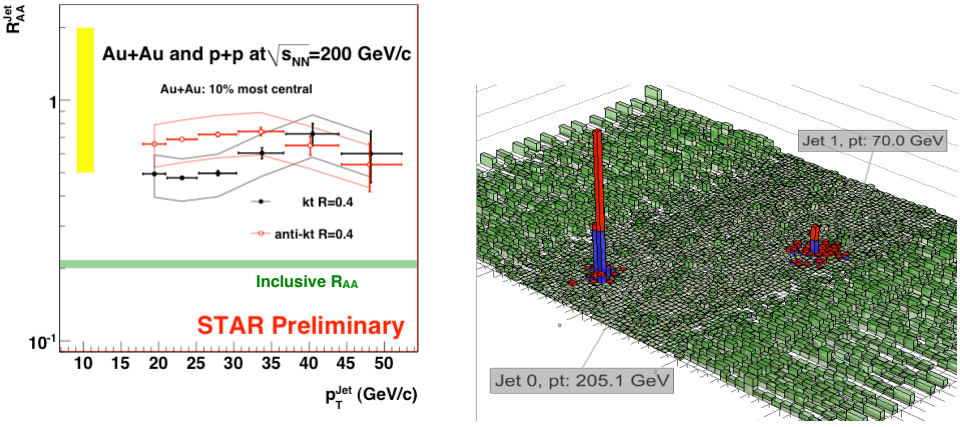

Figure 2.10: Jet R_{AA} measured at STAR in Au–Au collisions with two different reconstruction jet algorithms (right). Event display of an unbalanced di-jet events in central Pb–Pb collisions, measured by the CMS experiment [106] (left).

Fig. 2.10 (left) shows the R_{AA}^{jet} measured by the STAR experiment measured with two different jet reconstruction algorithms, that show two different sensitivities to the background [105]. The suppression is visible even if it is smaller with respect to the charged hadrons one. These results point to the direction of a large-angle radiation emission.

At the LHC, the CMS and ATLAS experiments measured a very interesting effect related to full reconstructed jets. Exploiting their 4π hadronic and electromagnetic calorimeters built for *pp* studies, they can study high energy jets, never observed before in A–A collisions. They studied the jet angular correlations in *pp* and Pb–Pb collisions, showing that no visible difference with *pp* collisions was observed and so no angular de-correlation for high-p_{t} partons traversing the dense nuclear medium [106]. Considering mainly di-jet events a strong imbalance was observed , not present in *pp* collisions, more pronounced going from peripheral to central Pb–Pb collisions. In Fig. 2.10 (right) it is shown an event display with a $p_{\mathrm{t}} = 205$ GeV jet, "un-balanced" by a second jet with only $p_{\mathrm{t}} = 70$ GeV. Moreover the difference in the di-jets is balanced by low p_{t}-particles [106].

2.3.4 Electromagnetic probes

Electromagnetic probes are important way to test the properties of the medium. Since the medium formed in A–A collisions is supposed to be dominated by strong coloured based interactions, direct leptons, photons and weak bosons (and their decay products) should not be affect by any in-medium energy loss and they should emerge with their initial energy. In this contest, an important measurement is the direct photon - jet correlations, since it allows to study the energy difference between the medium-modified jet fragmentation. At RHIC, the direct photons R_{AA} was measured by the PHENIX experiment, from 2 to 15 GeV/c [107] . No suppression is visibile as reported in Fig. 2.11 (left), where the direct photons R_{AA} is compared with the π^0 and η R_{AA} measured by PHENIX and the charged hadrons R_{AA} measured by STAR.

At LHC, the CMS experiment measured the R_{AA} of direct photons with transverse momentum between 20 and 80 GeV/c and for the first time in heavy-ion collisions, the R_{AA} of the Z^0 bosons in the 10% most central collisions [108, 109]. Both measurements

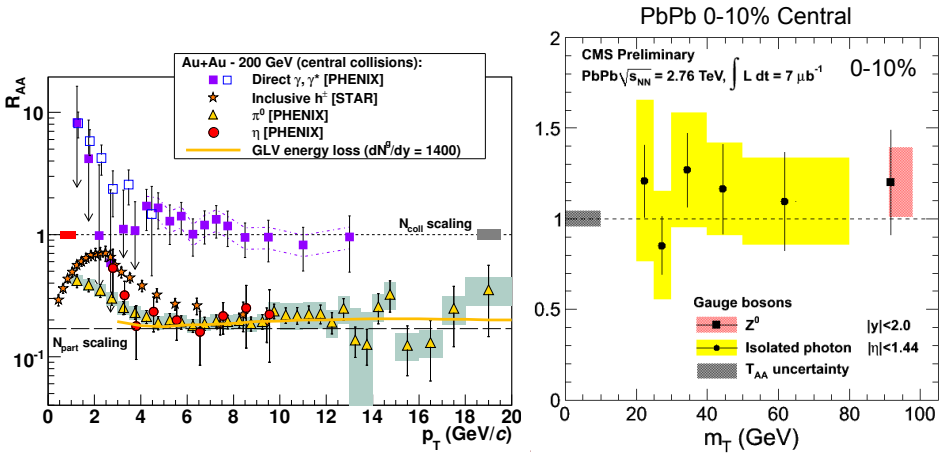

Figure 2.11: RHIC measurement for the R_{AA} of charged hadrons and π^0 shows a suppression of a factor 4, while direct photons scales with the number of binary collisions defined by the Glauber models (left) [107]. Direct photons and $Z^0 R_{\mathrm{AA}}$ measured by CMS. No suppression is evident for colourless probes in the 0-10% central collisions (right) [108, 109]

.

show $R_{\mathrm{AA}} \sim 1$ for these colourless probes, as expected from the scaling with the number of binary collisions.

2.4 Open heavy flavour production measurements

2.4.1 Measurements in pp collisions

Charm and beauty production has been measured in many colliding systems (e^+e^-, $p\bar{p}$, pp). This section will be focused on the recent measurements of the charm cross section performed at Tevatron in $p\bar{p}$ collisions at $\sqrt{s} = 1.96$ TeV and at RHIC in pp collisions at $\sqrt{s} = 200$ GeV.

The cross section for charm production has been measured at the CDF experiment via the exclusive reconstruction of D meson decays in their hadronic channels [110]. In particular CDF measured the cross section for prompt D^0, D^+ D^{*+} and D_s^+ (Fig. 2.12). The feed-down of D mesons coming from beauty hadron decay is corrected for using the different shape of the impact parameter distributions for prompt and feed-down D mesons. Results are compared with FONLL calculations [50] and though they are compatible within uncertainties, the measured differential cross sections are higher than the theoretical predictions by about 100% at low p_{t} and 50% at high p_{t}.

CDF presented also the measurement of the B^+ differential cross section in $p\bar{p}$ collisions, using an integrated luminosity of 739 pb^{-1} [111]. The reconstruction of the B mesons is performed in the decay channel $J/\Psi K^+$ where the J/Ψ decays to a muon pair. Fig. 2.13 (left) shows the cross section measured for two different energies and for the inclusive $J/\Psi X$ channel. Data ara also compared with FONLL pQCD calculations: the agreement seems to be better than for the charm case, especially at high-p_{t}.

The p_{t} differential cross section for charm production has also been measured at RHIC in pp, Au–Au and d–Au collisions at $\sqrt{s} = 200$ GeV, mainly via the analysis of non-photonic electrons. At STAR, the D^0 meson has been measured also via its hadronic

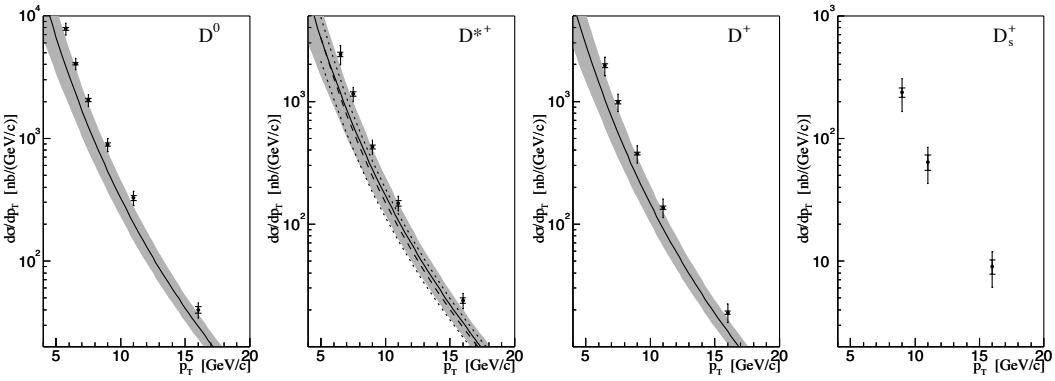

Figure 2.12: Differential cross section measurement for $|y| < 1$ for D^0, D^+, D^{*+} and D_s^+, compared with FONLL predictions [110].

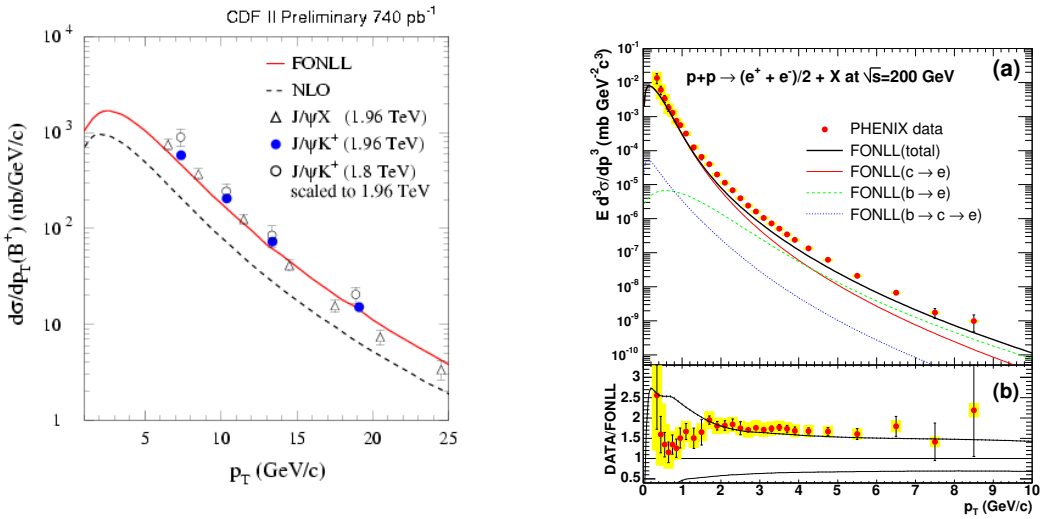

Figure 2.13: B^+ p_t differential cross section measured at Tevatron energies by the CDF experiment. Data are compared with FONLL pQCD calculations (left) [111]. Invariant differential cross section for the production of electrons from heavy-flavour decays, measured in pp collisions by PHENIX [112].

decay (next section).

The analysis of semi-leptonic decays (identified electrons or muons) provides an inclusive measurement of heavy-flavour production, without separation of charm and beauty contributions. The main source of background are electrons coming from photon conversions in the detector material, π^0 and η Dalitz decays. In the PHENIX experiment, the background subtraction is performed by the converter and the cocktail methods. The cocktail method is based on Monte Carlo simulations tuned to reproduce the measured π^0, π^+ spectra. Other contributions to the electron spectra can be considered with the m_T-scaling method or using as input the measured value, as for the π^0. At STAR experiment the background contribution from photonic sources is subtracted statistically from an invariant mass analysis of e^+e^- pairs. In the converter method, mainly used a cross-check of the first method, a thin brass layer is placed around the beam pipe, in order to enhance the conversion background. This background is then subtracted.

Fig. 2.13 (right) shows the invariant differential cross section for the production of electrons from heavy-flavour decays in pp collisions, measured by PHENIX [112]. Data are compared to the FONLL pQCD calculation. The black curve in Fig. 2.13 (right) shows the central value of the FONLL calculation for inclusive electrons. Red and green curves shows the charm and beauty contributions to the cross section. For $p_{\rm t} > 4$ GeV/c, the beauty contribution becomes dominant. In the bottom panel of the figure the ratio of the data to the FONLL calculation is shown. FONLL tends to underestimate the cross section as observed also at the Tevatron energy.

2.4.2 Measurements in A–A collisions

Heavy flavour production and energy loss have been studied in A–A collisions at RHIC. Charm production has been studied mainly via:

- exclusive reconstruction of D mesons decays in hadronic channels
- inclusive measurement of D and B meson production via muons or non-photonic electrons.

The last method includes also the leptons coming from beauty decays. The two contributions are then measured together and only with theory guidance, it is possible to define which of the two is dominant for a certain $p_{\rm t}$ interval. The reconstruction of D meson decays to charged hadrons gives a cleaner signal and the full reconstruction allows to access the $p_{\rm t}$ of the charm meson.

STAR reconstructed exclusively $\rm D^0 \rightarrow K^-\pi^+$ decays in pp, d-Au and Au–Au collisions by the invariant mass analysis of identified opposite charged kaon and pion pairs [113]. The large combinatorial background present in A–A collisions is the main difficulty for this measurement. In order to reduce this large combinatorial background it is possible to select tracks displaced from the primary vertex of about $\sim$ 100 μm , reconstructing the secondary vertex of the D mesons decay. This measurement is possible with a silicon vertex detector placed close to the beam pipe. STAR for the moment is not capable to reconstruct charm secondary vertices (a Heavy Flavour Tracker detector is foreseen to be installed in the next years). Fig. 2.14 (left) shows the $\rm D^0$ invariant mass peak in pp and Au–Au 0-80% minimum bias collisions, after same sign and mixed events background subtraction respectively. STAR measured also the nuclear modification factor of the $\rm D^0$ in the 0-80% centrality class (Fig. 2.14 right) [113]. No suppression is observed for $\rm D^0$ of $p_{\rm t} < 3$ GeV/c as could be expected.

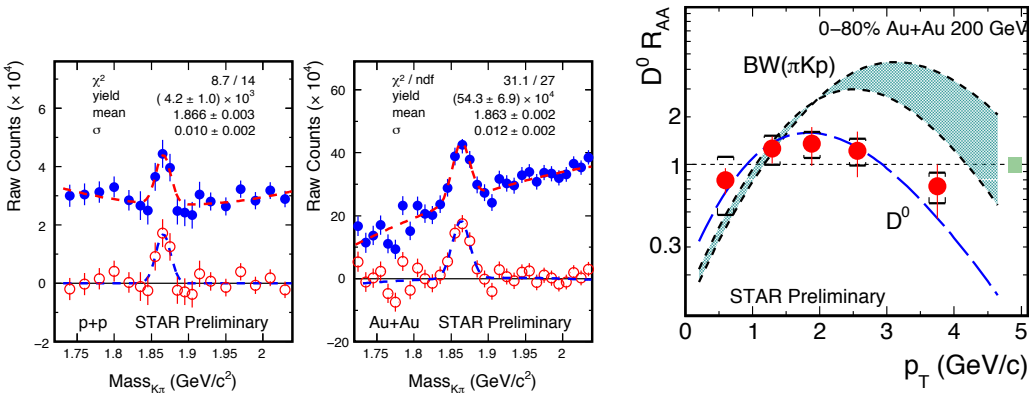

Figure 2.14: Invariant mass analysis of opposite sign Kπ pairs performed in pp collisions and Au–Au collisions in the 0-80% centrality class (left). D^0 nuclear modification factor measured in Au–Au collisions at $\sqrt{s_{\rm NN}} = 200$ GeV for $p_{\rm t} < 4$ GeV/c. No clear suppression is observed below $p_{\rm t} < 3$ GeV/c (left) [113].

The analysis of semi-leptonic decays is performed also in Au–Au collisions. The procedure is the same as in pp collisions, as described in Sec. 2.4.1. PHENIX measured the non-photonic electrons spectra between 0 and 10 GeV/c for six different centrality classes [115]. The lines in Fig. 2.16 (left) correspond to the fit of the data from pp collisions scaled by the nuclear overlap function $\langle T_{\rm AA} \rangle$ for each centrality class. For all centralities, the Au–Au spectra well agree with the pp reference at low $p_{\rm t}$, while a suppression is visible for higher $p_{\rm t}$. In central collisions (0-10%) the nuclear modification factor for non-photonic electrons measured by PHENIX, is consistent with one for low-$p_{\rm t}$ while the suppression increases at higher $p_{\rm t}$, reaching a value of ~ 0.3 for $p_{\rm t} > 4$ GeV/c (Fig. 2.16 right, top panel).

STAR also measured the nuclear modification factor of non-photonic electrons, as described in the previous section (Fig. 2.15) [114]. The measurement is performed for electrons from 1 to 5 GeV/c and the main photonic electrons sources are considered using the Monte Carlo studies. The $R_{\rm AA}$ is computed with a comparison of the nuclear modification factor in Au–Au and d-Au collisions properly scaled with the number of binary collisions.

For the first time, PHENIX also measured the flow of non-photonic electrons (Fig. 2.16 right, bottom panel), showing a large flow for low-$p_{\rm t}$ electrons [115]. A large heavy quark flow can suggest that the elliptic flow is built up at the partonic stage, while radial flow comes from hadronic scattering at a later stage, when charm is already decoupled. The large flow of heavy quarks can also indicate that the charm relaxation time is comparable to the short time scale of flow development in the produced medium.

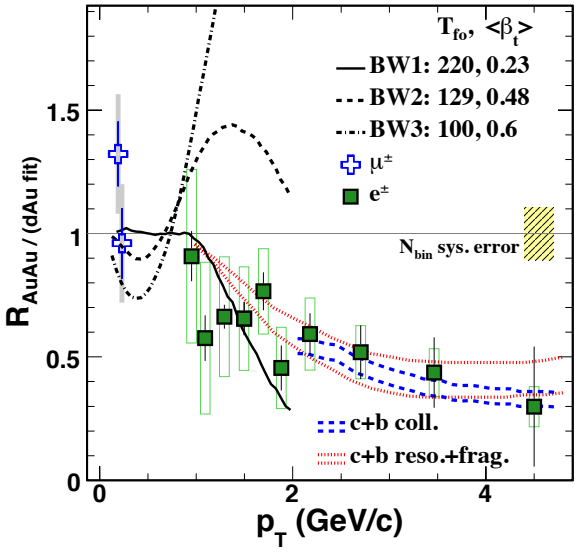

Figure 2.15: Nuclear modification factor ($R_{\mathrm{AA}}/R_{\mathrm{d-Au}}$) of 0-12% Au–Au collision for non photonic electrons and muons measured by the STAR experiment [114].

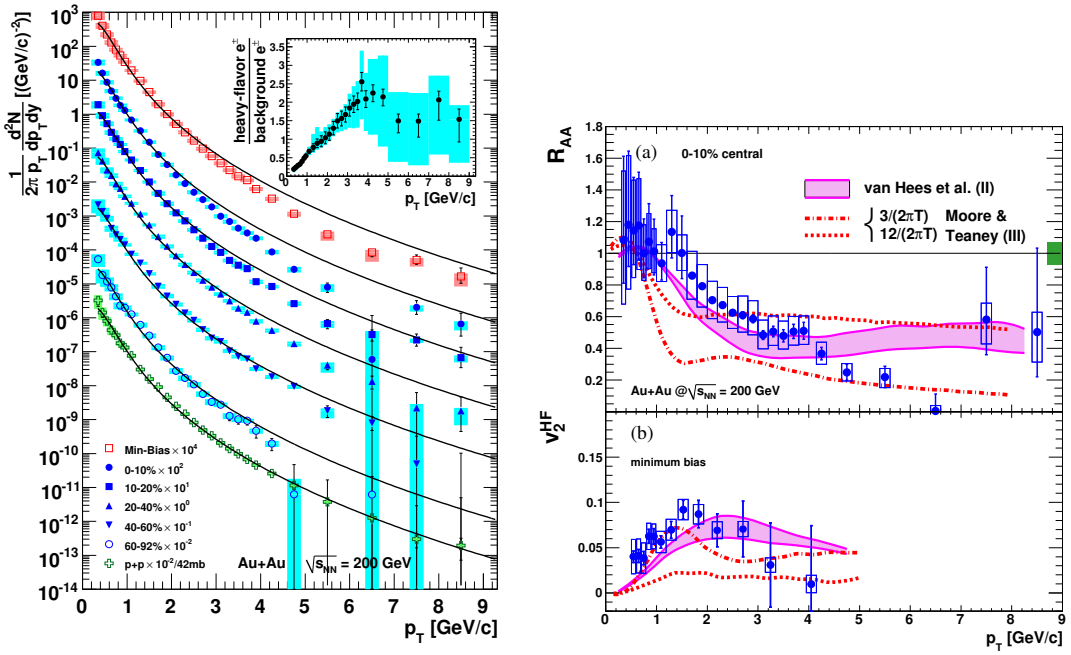

Figure 2.16: Non-phonic electrons spectra measured in Au–Au collisions for six different centrality classes. Points are compared with expected *pp* spectra scaled by the correspondent nuclear overlap function (left). Non-photonic electron nuclear modification factor (top) and elliptic flow v_2 coefficient (bottom). A suppression in visible only for electrons of $p_{\mathrm{t}} > 2$ GeV/c and a non zero flow contribution can indicate that the thermalization of charm can occur with the same relaxation time of light hadrons [115].

3 A Large Ion Collider Experiment

In this chapter the Large Hadron Collider (LHC) accelerator complex will be presented. It was built at CERN in the last ten years and switched on the 23rd November 2009, day of the first collision at $\sqrt{s} = 0.9$ TeV. A first summary on the luminosity delivered both in *pp* and Pb–Pb collisions will be given for this first year of running at half of the project energy. The dimensions of the interaction region is one of the first quantity to be monitored in a just started accelerating machine. A summary of how it can be computed and linked with the beam parameters is given in the second part of this chapter.

After the introduction on the LHC, a detailed description of the ALICE detector will be given. ALICE has been built to study ultra-relativistic heavy-ion collisions and its properties and features are very different from those of the others two general purpose experiments. ALICE has the capability to track and identify particles from very low momentum (~ 100 MeV/c) up to very high (~ 100 GeV/c) in a high multiplicity environment. Many of the sub-detectors that constitue the ALICE experiment will be described, with particular focus on those used in the analysis that will be presented in chapters 5 and 6. Many of the results shown in this chapter have been obtained with analyses on 2010 data, in order to highlight the detector performance reached just after few months from the start of the data taking.

After the detector description and performance, a section is dedicated to the trigger system and strategy adopted to collect the 2010 data, with also the summary on the total number of event and luminosity recorded. Then the chapter continues with a description of the ALICE offline computing and reconstruction system based on the GRID framework in order to exploit the maximum potentiality of the world wide system built for the LHC experiments.

The last part of this chapter is devoted to the performance of the track reconstruction in terms of efficiency both in *pp* and Pb–Pb collisions and on the impact parameter resolution that is one of the main point for the charm analysis. Related to this also the status of the alignment of the inner tracker detector will be shown.

3.1 The Large Hadron Collider - LHC

The Large Hadron Collider (LHC) is a two-ring-superconducting hadron accelerator and collider, installed in a 26.7 Km tunnel [116]. This machine has been built to produce the highest energy proton-proton collisions ever performed, in order to discover the Higgs boson or other particles beyond the Standard Model. The LHC provides ultra-relativistic heavy-ion collisions to study QGP formation and its properties. The LHC was designed to produce *pp* collisions at $\sqrt{s} = 14$ TeV and Pb–Pb collisions $\sqrt{s_{\rm NN}} = 5.5$ TeV. After the 2008 technical accident, it was decided to run the LHC at half of the design energy,

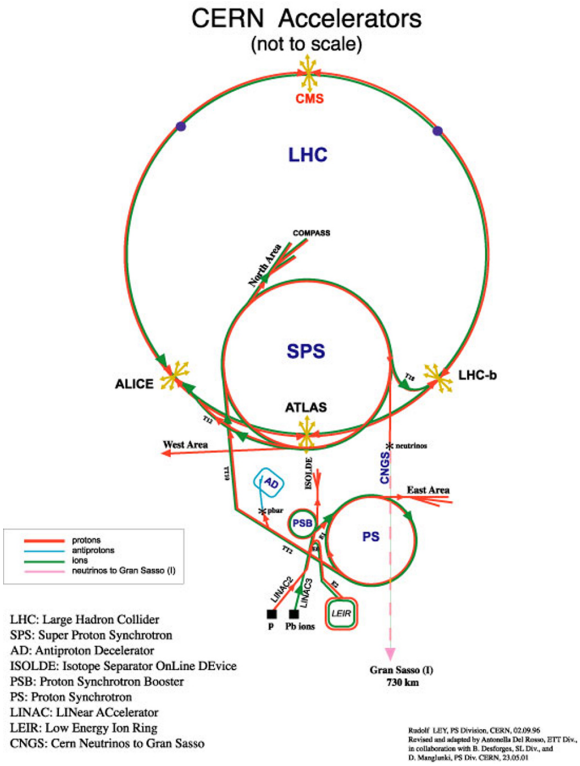

Figure 3.1: CERN accelerator complex: from sources to the LHC

i.e. $\sqrt{s} = 7$ TeV for protons, $\sqrt{s_{\rm NN}} = 2.76$ TeV for Pb–Pb. In 2013-2014, a 15 months shutdown has been foreseen in order to complete some operations on the machine, so that the LHC would be able to run at the nominal energy. From 2010 to the end of 2012 the main goal of the LHC is to reach the nominal peak luminosity and to deliver as much integrated luminosity as possibile to the experiments.

The LHC is the last stage of a complex system of accelerators that exploits the different lines built at CERN in the past 40 years (Fig. 3.1) [116]. Protons are extracted from a hydrogen tank and they are injected in the Linear Accelerator 2 (Linac2), where they are accelerated up to 50 MeV, then they pass at the Proton Synchrotron Booster (PSB), where they reach the momentum of 1.4 GeV. From the PSB, protons are injected in the Proton Synchrotron (PS) accelerator and then in the Super Proton Synchrotron accelerator (SPS), where they finally reach 450 GeV. Once the bunches are accumulated in the SPS they are injected in the LHC at the threshold energy. When the injection is completed, the procedure of ramping starts and beams are accelerated up to 3.5 TeV. For ion beams the injection chain is almost the same as for protons, the only difference is at the starting point, where ions are extracted from a piece of lead, heated to about 500° C, in order to vaporize a small number of lead atoms. A strong electric field then partially ionises the lead atoms. They are accelerated in a linear device where they become more and more ionized as more electrons are stripped off. Lead ions are injected and accumulated in a Low Energy Ion Ring (LEIR) and then in the PS [116].

Since one of the main goal of the LHC *pp* physics program is the discovery of the Higgs boson or Beyond Standard Model particles, the main requirement of the machine is to deliver a large number of collisions, to study phenomena with a production cross

section of the order of 100 pb or lower. On the LHC accelerator ring, four experiments are installed. ATLAS and CMS are the main general purpose experiments, built to study Standard Model Physics and beyond. LHCb is a B physics experiment, built to study CP-violation using these channels. ALICE is the dedicated heavy-ion experiment, built to study the QGP properties. The luminosity is the main parameter of the accelerator since it's the proportionality factor between the rate of a given process (R) and its production cross section $R = L\sigma$; it is operationally defined by colliding beams parameters at the interaction points.

The luminosity goal of the LHC is to run at $L = 10^{34}\text{cm}^2\text{s}^{-1}$ for the two general purpose pp experiments, $L = 10^{27}\text{cm}^2\text{s}^{-1}$ for Pb–Pb collisions. The LHC design foresees 2802 bunches per beam in the ring with 25 ns spacing between bunches. In order to increase the luminosity it is necessary to have high transverse beam intensity and low emittance (Sec. 3.2).

The 2010 LHC campaign was very successful. The LHC managed to start with two pp colliding bunches in the full accelerator at the beginning of 2010, reaching 368 bunches spaced by 150 ns. For the Pb–Pb beams the maximum reached in 2010 was 137 bunches with 500 ns spacing. The 2011 was a great year for the LHC that run almost the full year with 1380 bunches, spaced 50 ns, the maximum number achievable with this time delay between the bunches. An other important parameter to increase the luminosity is the intensity of the bunches (i.e. the number of protons within a bunch). In 2010 LHC started with 1×10^{11} protons per bunch, in 2011 2×10^{14} is the maximum number reached. This means also an increase on the pile-up probability. In 2011 ATLAS and CMS experiments are dealing with a mean value of 7 interaction vertices for each two colliding bunches. ALICE has required to have lower luminosity and lower pile-up due to the different detector design, mainly studied for heavy-ion collisions.

The results presented in this thesis have been obtained with 2010 data samples, both for pp and Pb–Pb collisions. For 2010 pp run, LHC reached a peak luminosity of $2 \times 10^{32} cm^2 s^{-1}$, that corresponds to an integrated luminosity of 45 pb^{-1} for the two general purpose experiments. ALICE required a lower luminosity running in order to deal with pile up in the Time Projection Chamber detector and it was delivered about 1 pb^{-1} of data (Fig. 3.2 left) [117]. This lower luminosity in ALICE was obtained by modifying the nominal LHC orbit, reducing the squeezing of the beam in the ALICE interaction point and displacing the beams in the transverse plane to the beam line. For Pb–Pb, the LHC reached a peak luminosity of $30 \times 10^{24}\text{cm}^2\text{s}^{-1}$ with an integrated value of 9 μb^{-1} for all experiments (Fig. 3.2 right.) [117].

In 2011, the LHC increased the luminosity in pp runs, reaching a peak luminosity of $3.5 \times 10^{33} cm^2 s^{-1}$, only a factor three below then the design value. The delivered integrated luminosity for ATLAS and CMS has been of more than 5 fb^{-1} [117]. In 2011 ALICE collected about 5 pb^{-1} of pp collisions. In 2011 also a special pp run was performed at the same energy as the Pb–Pb collisions ($\sqrt{s} = 2.76$ TeV). This run is very important as a reference to study comparisons between nuclear and proton interaction at the same energy.

One of the important checks at the starting of a new accelerator machine is the measurement and the monitor of the primary vertex reconstruction. This is needed both for the experiments and the machine, in order to understand the beam behavior and to perform quality checks on the data.

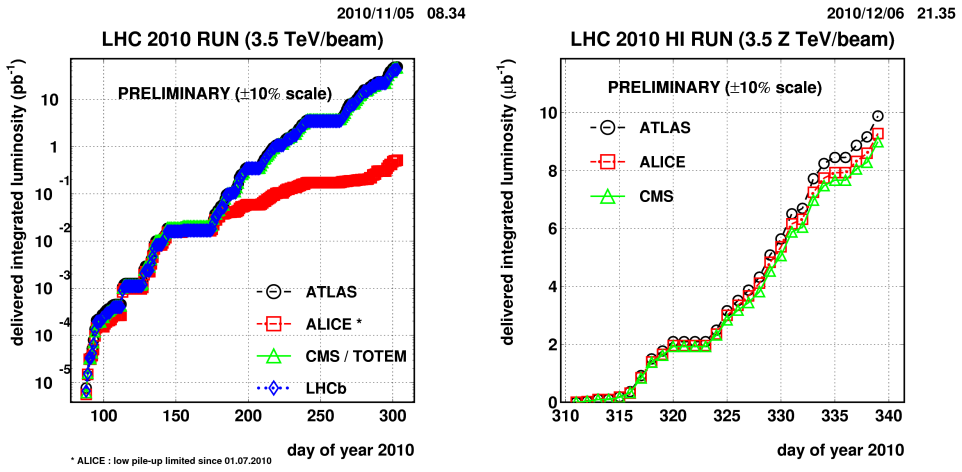

Figure 3.2: LHC delivered luminosity in 2010 pp run (left). LHC delivered luminosity in 2010 Pb–Pb run (right). Black points ATLAS, red points ALICE, green CMS.

3.2 Luminosity and luminous region

The event rate R in a collider is given by the interaction cross section σ_{int} of a certain process multiplied by a proportionality factor called luminosity (L):

$$R = L\ \sigma_{\text{int}} \tag{3.1}$$

The luminosity is defined by the colliding beam parameters at the interaction point. These beam parameters have to be optimized in order to allow all experiments to exploit their different capability.

Let's consider two colliding bunches, labelled 1 and 2. To a good approximation, the particles in the bunches will be distributed according to Gaussians in three perpendicular directions:

$$N_i(x,y,z) = N_i G(x,\bar{x},\sigma_{x,i}) G(y,\bar{y},\sigma_{y,i}) G(z,\bar{z},\sigma_{z,i}) \quad i = 1,2 \tag{3.2}$$

where N_i is the total number of particles in the bunch i and

$$G(q,\bar{q},\sigma_q) = \frac{1}{\sqrt{2\pi}\sigma_q} \exp\left[-\frac{(q-\bar{q}^2)}{2\sigma_q^2}\right] \quad q = x,y,z \tag{3.3}$$

If f is the revolution frequency and N_b is the number of bunches, the luminosity is obtained as:

$$L = f\ N_b \times \int dxdydz N_1(x,y,z) N_2(x,y,z). \tag{3.4}$$

The integration along the beam direction, z, gives 1, since the two bunches cross each other and their distributions along z are equivalent to delta function from the point of view of the interaction probability. The LHC design foresees the same number of particles (N) and the same dispersions for the bunches, the dispersion in the transverse plane is also foreseen to be the same ($\sigma_x = \sigma_y = \sigma_{x,y}$). Considering this:

$$L = f\ N_b \frac{N^2}{4\pi\sigma_{x,y}^2} \exp\left[-\frac{d^2}{4\sigma_{x,y}^2}\right], \tag{3.5}$$

where $d^2 = (\Delta\bar{x})^2 + (\Delta\bar{y})^2$ is the square of the distance between the centres of the two beams.

The interaction region, or beam size, is defined as the convolution of the two particles distributions in the two colliding bunches: the interaction vertex lies in a "luminous region" with dimensions

$$\sigma_q^{\text{lumi reg}} = \sigma_q^{\text{beam}}/\sqrt{2} \tag{3.6}$$

that do not depend on the distance d if the two distributions are gaussian. The luminous region dimensions at the interaction points depends on the transverse emittance ϵ, a beam quality parameter, and on the value of the amplitude function β^*, that depends on the LHC magnets configuration. The relation between these different parameters is:

$$\sigma_q^{\text{lumi reg}} = \sqrt{\frac{\epsilon\beta^*}{\pi}} \tag{3.7}$$

The luminosity can be tuned in the different interaction points by changing β^*: an increase of the amplitude function means a increase of the transverse size of the luminous region.

3.2.1 Interaction region parameters in 2010 data taking

pp collisions

The LHC running operation started in November 2009, with the first collisions on the 23th, at $\sqrt{s} = 0.9$ TeV. Before the end of the 2009, LHC provided also collisions at $\sqrt{s} = 2.36$ TeV, reaching the highest collision energy in the world at that time. The main operation of 2010 started the 30th of March, when the first $\sqrt{s} = 7$ TeV pp collisions have been delivered. In the table 3.1 a summary of the emittance and amplitude function parameters for different LHC 2010 energies is shown. The foreseen luminous region is computed with Eq. 3.7 for these parameters. Results of the measured luminous region from the data will be shown in section 4.3.

Table 3.1: LHC 2010 beams parameters for luminous region estimate.

	0.9 TeV	2.36 TeV	7 TeV
$\epsilon_{\text{x,y}}$	3.75 μm	3.75 μm	3.75 μm
β^*	10 m	10 m	10m, 2m
$\sigma_{\text{x,y}}^{\text{lumi reg}}$	198 μm	120 μm	70 μm, 30 μm

Pb–Pb collisions

The LHC 2010 ion runs started on November 2010, with the first collisions without stable beams on the 7th, with stable beams the day after. The energy of the collision was $\sqrt{s_{\text{NN}}} = 2.76$ TeV for each nucleon pair. For Pb–Pb collisions the amplitude function was set at 3.5 m, the emittance at about 0.5 μm for x and y directions, so that the nominal luminous region is foreseen to be about 50 μm. The emittance for the z direction was set to 1.1 μm. In the 2010 Pb–Pb run LHC delivered bunches with 1.15×10^8 ions.

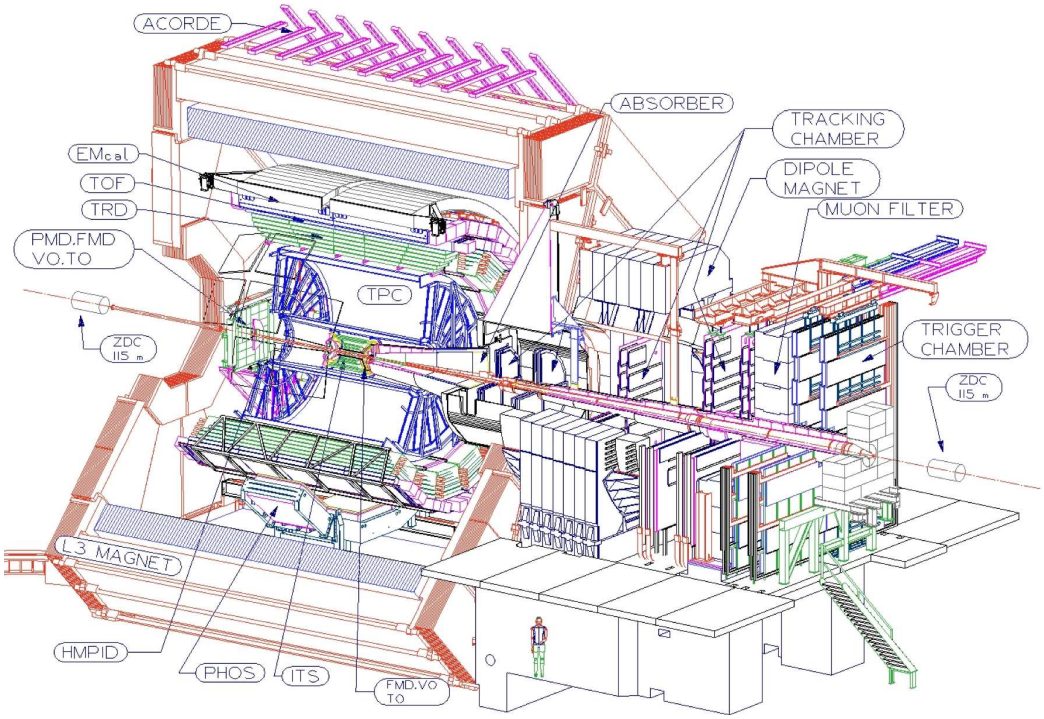

Figure 3.3: ALICE detector layout

3.3 The ALICE experiment: Detector Layout

A Large Ion Collider Experiment - ALICE is a general-purpose heavy-ion detector, built on the LHC ring, which is focused on Quark Gluon Plasma properties measurements [118]. The detector design has been chosen to perform precise measurements of the proprieties of strongly interacting matter that is formed in nucleus-nucleus collisions at extreme values of temperature and energy density (Fig. 3.3).

The design adopted for the ALICE experiment fulfills the requirements to track and identify particles from very low (100 MeV/c) up to quite high (100 GeV/c) transverse momenta in a high charged-particle multiplicity environment. Since the nominal interaction rate with ion beams at LHC is about 8kHz and radiation dose is moderate, ALICE uses slow but high-granularity detectors which make the detector substantially different form the other pp dedicated experiments.

ALICE tracking uses three-dimensional hit information with many points in a moderate magnetic field of 0.5 T. To measure particle momenta over such a broad momentum range a combination of very thin materials reduces the multiple scattering at low p_{t}, while a large tracking lever arm up to 3.5 m guarantees a good resolution at high p_{t}. Particle IDentification (PID) is important to the particle composition of the final state of Pb–Pb collisions. ALICE makes use of lot of PID techniques: ionization energy loss in gas and silicon, time-of-flight, transition and Cherenkov radiation, electromagnetic calorimetry and muon filters.

The apparatus, shown in Fig. 3.3, consists of two main parts: a central rapidity barrel and a muon spectrometer. The central system covers the mid-rapidity region $|\eta| < 0.9$ over the full azimuthal angle, it is installed inside a solenoidal magnet which generates a magnetic field of 0.5 T. The central barrel includes, from the beam pipe to the outside,

six layers of high-resolution silicon detectors (Inner Tracking System - ITS), the main tracking detector (Time Projection Chamber -TPC), a transition radiation detector for electron identification (Transition Radiation Detector - TRD) and a time of flight detector for charged-hadron identification (Time-Of-Flight - TOF). In the central system there are also three small-area detectors: an array of ring-imaging Cherenkov detectors for identification of high-momentum hadrons (High-Momentum Particle Identification Detector - HMPID) an electromagnetic calorimeter for photon and neutral-meson measurements (Photon Spectrometer -PHOS) and a second electromagnetic calorimeter to enhance the capabilities for measuring jet properties (ElectroMagnetic Calorimeter - EMCal). In the forward region there is a single-arm muon spectrometer covering the pseudo-rapidity range $-4.0 < \eta < -2.5$, a photon-counting detector (Photon Multiplicity Detector - PMD), a silicon detector to measure particle multiplicity in the forward region (Forward Multiplicity Detector - FMD) and two sets of neutron and proton calorimeters, located at 0° about 116 m from the interaction point, to measure the centrality in ion collisions (Zero-Degree Calorimeter - ZDC). Two arrays of segmented scintillator counters are used to define the minimum bias trigger, beam-gas background rejection and the centrality (V0), two scintillator counters have also been installed to measure the time of the collision (T0) and provide this information with to the TOF detector. An array of 60 scintillators is installed on top of the magnet to provide cosmic rays trigger for calibration and alignment purpose and for cosmic ray physics (ACORDE).

3.4 Central rapidity detectors

Central rapidity detectors are placed in a room-temperature solenoid built for the L3 experiment at LEP. The nominal field of the solenoid is 0.5 T and the field variations in the volume of the detectors are below 2% [118]. In the next sections single sub detectors will be described and their performance will be presented. These results have been obtained using 2010 data, apart for the EMCal, for which the installation has been completed during the Christmas 2010 LHC shutdown.

3.4.1 Tracking detectors

Inner Tracking System - ITS

The Inner Tracking System (ITS) [118] is the closest tracking detector to the LHC beam pipe. The beam pipe is a layer of beryllium, 800 μm−thick and with a radius of 2.9 cm. The ITS consists of six concentric cylindrical layers of silicon detectors that exploit three different technologies: pixels, drifts and strips, located between 4 and 43 cm (Fig. 3.4). The position and segmentation of the different ITS layers, as well as the detector technologies are summarized in Table 3.2. All these characteristics have been optimized in order to have:

- efficient track finding in the high multiplicity environment foreseen for central Pb–Pb collisions at the LHC, that for some models could reach also 8000 particles per unit of rapidity, at the time of the ALICE design. The very high granularity was indeed required to keep the system occupancy at the level of few per cent on all ITS layers.

- high resolution on the track impact parameter and momentum. The impact parameter is defined as the distance between the back-propagated track and the interaction point. For low-momentum particles, the multiple scattering in the detector affects

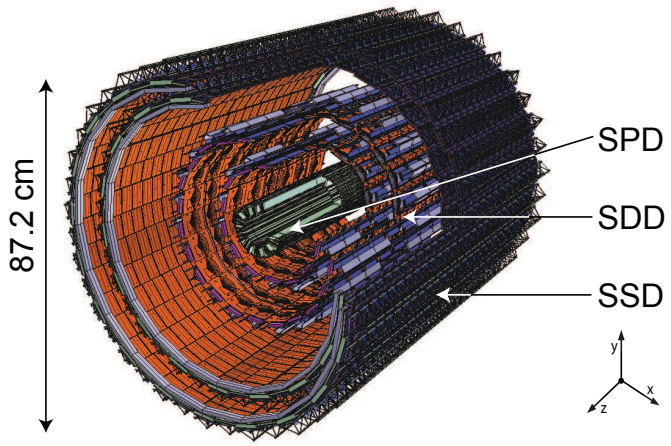

Figure 3.4: ITS layout: six different layers. Two layers of pixels detector, two layers of drift, two layers of strips detector.

the impact parameter resolution. To avoid an increase of this effect, the amount of material in the active volume has been kept to a minimum. A very good track impact parameter resolution is important to reconstruct secondary vertices from hyperons, but especially from heavy flavour hadrons decay.

- a good resolution and efficiency in the localization of interaction point of the collision.

- possibility to track and identify particles with momenta below 200 MeV/c. Four layers, out of six, provide also dE/dx measurements in order to identify very low momentum particles.

Table 3.2: Characteristics of the six ITS layers.

Layer	Type	r (cm)	$\pm z$ (cm)	Modules	Active Area per module	Material Budget (X/X_0)
1	pixel	3.9	14.1	80	12.8×70.7 mm^2	1.14
2	pixel	7.6	14.1	160	12.8×70.7 mm^2	1.14
3	drift	15.0	22.2	84	70.17×75.26 mm^2	1.13
4	drift	23.9	29.7	176	70.17×75.26 mm^2	1.26
5	strip	38.0	43.1	748	73×40 mm^2	0.83
6	strip	43.0	48.9	950	73×40 mm^2	0.86

Silicon Pixel Detector - SPD

The building block of the SPD [118] is a module consisting of a two-dimensional sensor matrix of reverse-biased silicon detectors diods, bump-bonded to 5 front-end chips. The sensor matrix consists of 256 x 160 cells of 50 μm in rϕ coordinate and 425 μm in z. The active area of each module is 12.8 mm (rϕ) x 70.7 mm (z), the thickness of the sensor is 200 μm , while the readout chip is 150 μm thick. Two modules are mounted together along the z direction to form a 141.6 mm long half-stave. Two half-staves are attached head-to-head along the z direction to a carbon-fibre support sector which houses also the

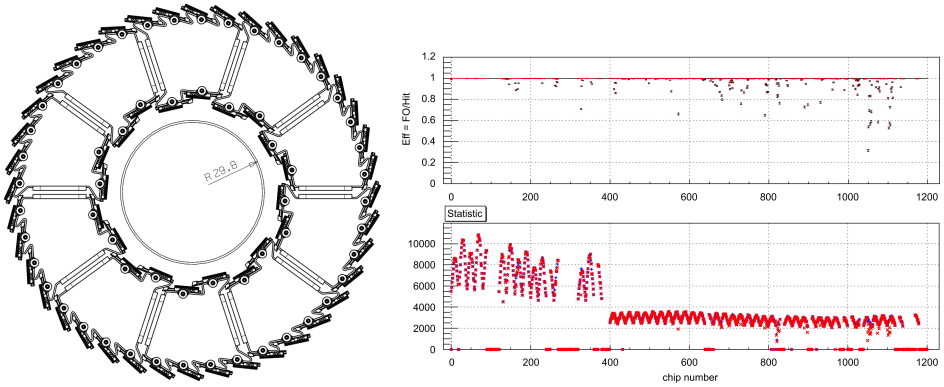

Figure 3.5: SPD geometry (left). SPD FastOr efficiencies defined as the ratio of the Fast OR signal received over the number of pixel hits fired (right). On the bottom plot there are the numerator (red) and the denominator of the efficiencies (blue), plotted in the top histogram.

cooling system of each stave. Each sector is made up of six staves: two on the inner layer and four on the outer layer. Five sectors are then mounted together to form a half-barrel and finally the two (top and bottom) half barrels are mounter around the beam pipe to close the full barrel, which is actually composed of 10 sectors (Fig. 3.5 left). In total, the SPD includes 120 half-staves, consisting of 240 modules with 1200 readout chips for a total of 9.8×10^6 cells. Since the SPD is the closest detector to the beam pipe, it plays an important role for the trigger system, especially for the minimum bias one. The SPD provides the trigger through the chips that give a signal when an hit is fired. In Fig. 3.5 (right), the efficiencies of the Fast-OR (FO) chips are plotted, when a corresponding pixel is fired. The overall FO efficiency is 98.7%.

Silicon Drift Detector - SDD

The sensitive part of the ALICE SDD detector [118] is a module with an area of 70.17 (rϕ) $\times$ 75.26 (z) mm^2 divided into two drift regions where electrons move in opposite directions under a drift field of $\approx$ 500 V/cm (Fig. 3.6 left). The SDD modules are mounted on a linear structure called ladders. The SDD inner layer is made of 14 ladders with six modules each, the outer layer has 22 ladders, each of them with eight modules. Modules are attached to the ladder space frame, which is a lightweight truss made of Carbon-Fibre Reinforced Plastic (CFRP) with a protective coating against humidity absorption. The z coordinate is reconstructed from the centroid of the collected charge along the anodes. The position along the drift (rϕ) coordinate is reconstructed starting from the measured drift time with respect to the trigger time. This reconstruction requires to know with good precision the drift speed and the time-zero, which is the measured drift time for particles with zero drift distance. The drift speed depends on the temperature ($T^{-2.4}$) and it is therefore sensitive to the temperature gradients in the SDD volumes and temperature variations with time. In order to calibrate frequently this parameters, in each of the two drift regions of the SDD module, 3 rows of 33 MOS charge injectors are set at known distance from the collection anodes. When a dedicated calibration trigger is given, the injector matrix provides a measurement of the drift speed in 33 positions along the anode coordinate for each drift region. The drift field can also be affected by non-uniformities due to non-linearities in the

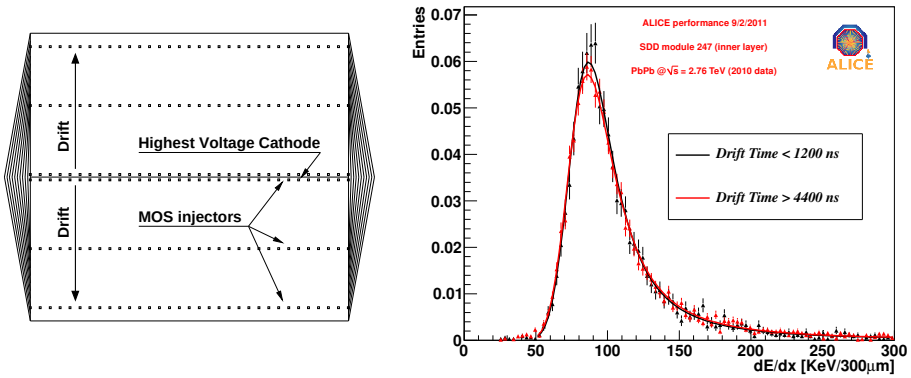

Figure 3.6: SDD module scheme (left). SDD energy loss for one module in two different drift time intervals during the 2010 Pb–Pb run (right).

voltage divider or to inhomogeneities in the dopant concentrations. To take into account this effect, a correction is applied, based on the measurement of the systematic deviations between charge injection position and reconstructed coordinates that was performed on all 260 SDD modules with an infrared laser. The SDD allows to measure the energy loss of particles passing through the detector by measuring the deposit charge. Fig. 3.6 shows the $\mathrm{d}E/\mathrm{d}x$ distribution after applying calibrations and corrections for one module with two different drift time intervals. The fit is performed with a convolution of a Landau and a Gaussian function.

Silicon Strip Detector - SSD

The building block of the ALICE SSD [118] is a module composed of one double-sided strip detector connected to two hybrids hosting the front-end electronics. The sensors are 300 μm thick and with an active area of 73×40 mm^2, respectively along rϕ and z directions. Each sensor has 768 strips on each side with a pitch of 95 μm. The stereo angle is 35 mrad which is a compromise between stereo view and reduction of ambiguities, in high particle density environment. Strips are almost parallel to the z beam axis direction, in order to provide the best resolution in the rϕ direction. Modules are assembled on ladders of the same design as those supporting the SDD. The innermost SSD layer is composed of 34 ladders, each of them with 22 modules along the beam direction, the other SSD layer is made of 38 ladders, each of them with 25 modules. The 72 ladders, carrying a total of 1698 modules are mounted in a Carbon Fibre Composite support cones in two cylindres. Also for the SSD it is possible to measure the charge collected in the different modules of the detector and correlate the charge with particles energy loss (Fig. 3.7). The energy loss of SDD ans SSD is used together with the ITS standalone tracking to define the Particle IDentification capability of the ITS, described in the last section of this chapter (Sec. 3.10).

Time Projection Chamber - TPC

The Time Projection Chamber (TPC) is the main tracking detector in the ALICE central barrel [118]. Together with other central barrel detectors, the TPC has to provide track finding, charged-particle momentum measurements and particle identification through

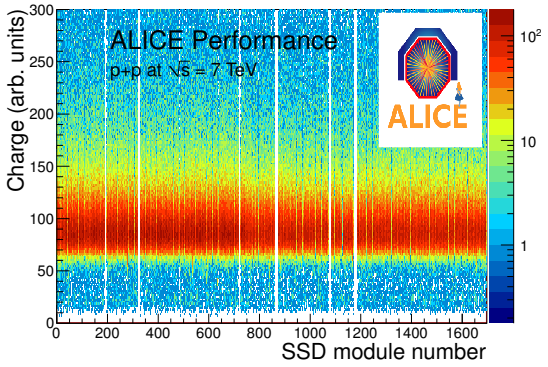

Figure 3.7: SSD energy loss distribution (obtained from the charged released in the detector) as a function of the module number.

$\mathrm{d}E/\mathrm{d}x$ measurements. The TPC covers the pseudorapidity range $|\eta| < 0.9$ over the full azimuthal angle with a good momentum resolution, shown in Fig. 3.16 that will be discussed later with the other tracking results. The TPC is cylindrical in shape with an inner radius of 80 cm, an outer radius of 250 cm and an overall length along the beam direction of 500 cm. The extremely high number of tracks, which have to be reconstructed in Pb–Pb collisions, has required a design that limits the detector occupancy at the inner radius and at the same time guarantees a good momentum resolution for high-p_{t} particles. The material budget of the TPC is kept as low as possible in order to have minimal multiple scattering and secondary particle production. The drift gas mixture $\mathrm{Ne/CO_2/N_2}$ is optimized for drift velocity, low electron diffusion and low radiation length. The electron drift velocity of 2.7 cm/μs over 250 cm set the maximum drift time of 92 μs which defines the event rate capability of the TPC. The TPC readout chambers are multi-wire proportional chambers with cathod-pad read-out. The readout planes at the ends of the volume drift are segmented in 18 sectors, each covering an angle of 20°. The radial thickness of the TPC is of 3.5% of X_0 at central rapidity and grows to 40% towards the acceptance edges. The charge collected in the TPC readout pads is used to measure particle specific energy deposit. This information, together with the momentum measurement allows to separate the various charged particle species in the low momentum region (Fig. 3.8 left).

3.4.2 Particle Identification detectors

Transition Radiation Detector - TRD

The main task of the Transition Radiation detector is to provide electron identification in the central barrel for particles of $p_{\mathrm{t}} > 1$ GeV/c. The transition radiation is produced by relativistic charged particles when they cross the interface of two media of different dielectric constant, photons of the radiation are emitted in the keV range. Electrons with momentum above the threshold radiate differently with respect to pions, so it is possibile to extend the pions rejection capability of the TPC up to very high momenta. Furthermore, the TRD provides tracking information with larger tracking lever arm, thus improving momentum resolution at high p_{t}. The main goal of the TRD is to identify electrons in order to study the electron p_{t} spectra and reconstruct light and heavy vector mesons resonances in the e^+e^- channel in pp as well as in Pb–Pb collisions. The detector

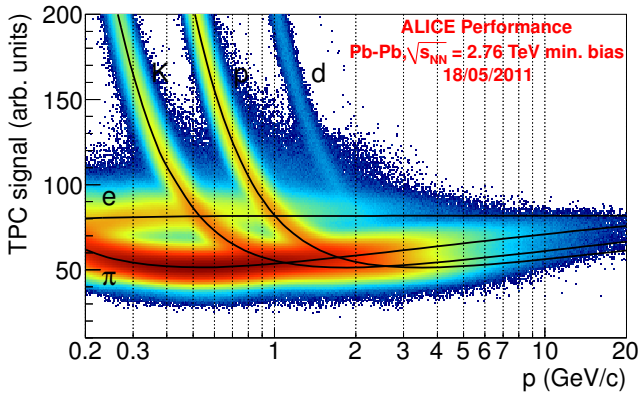

Figure 3.8: dE/dx distributions versus momentum in the ALICE TPC for Pb–Pb collisions (left).

covers the full azimuth of the mid-rapidity region ($|\eta| < 0.84$) from 2.90 m to 3.68 m from the interaction vertex. At the beginning of the data taking, in 2009, 4 out of 18 super modules were installed. During 2010 shutdown other 3 super modules were installed and others will set in place during 2011 shutdown.

Time Of Flight - TOF

The main task of the Time Of Flight detector is the charged-particle identification in the intermediate momentum range. In order to have a good separation between hadrons at intermediate p_t the global time measurement resolution is the main requirement. The active element of the TOF is a double-stack Multigap Resistive Plate Chamber (MRPC) strip with a gas mixture of $C_2H_2F_4$ (90%), i$-C_4H_{10}$ (5%) and SF_6 (5%) [118]. The MRCP is segmented into two rows of 48 pickup pads of 3.5×2.5 cm^2, for a total of about 16000 readout channels. Groups of several MRPCs are closed in a gas-tight box, the front-end electronics is mounted on the external side of this box: these two parts form the TOF module. The complete TOF system consists of 90 modules. Five modules in a row are bound together with longitudinal and transverse aluminium beams to form a SuperModule structure. Four crates are fixed in pairs at both sides of the SuperModule to contain the power supply system required for the front end readout electronics and for the readout electronics itself. The intrinsic resolution of the MRPC is below 60 ps, but other contributions on the time resolution come from the electronic front-end, the tracking and the start time resolution. As shown in Fig. 3.9 (left) the overall TOF detector resolution is around 85 ps, for Pb–Pb collisions. For pp data the resolution is about 160 ps due to the bigger uncertainties on the event time determination.

Particle identification with TOF detector

The identification of a particle can be only determined from its charge and mass. The charge of the particle can be directly measured, while the particle mass cannot. Usually to determine the mass of a particle, two kinematic variables are used, one of them has to depend on the particle mass. In high-energy experiments, particles are bent in a magnetic field to measure their momenta. With the momenta, particle velocity measurement is

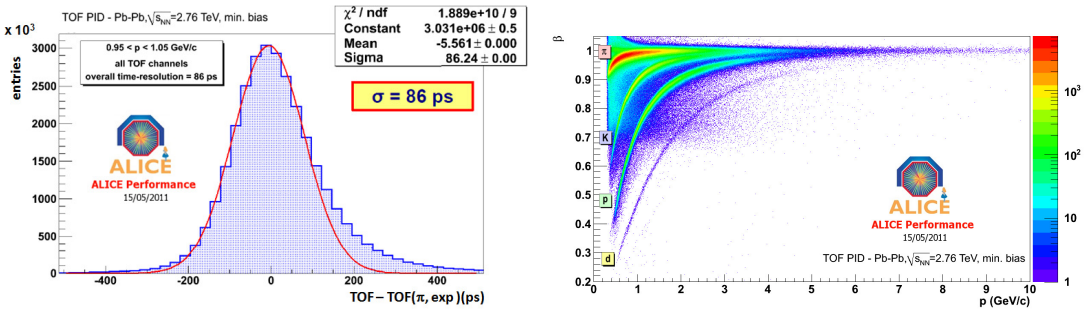

Figure 3.9: TOF resolution for selected pions (left). β factor measured by TOF as a function of momentum (right).

often used for particle identification. The Time-Of-Flight (TOF) technique is well suited for particle identification in the mid-momentum region. This technique is based on the measurement of the particle time of flight t over a known trajectory length L, in order to measure the particle velocity $v = L/t$. Once the momentum of the particle is measured the particle mass m is computed using

$$m^2 = \frac{p^2}{c^2}\left(\frac{c^2t^2}{L^2} - 1\right). \tag{3.8}$$

Fig. 3.9 (right) shows $\beta(v/c)$ versus momentum for particles produced in Pb–Pb collisions. It is possible to clearly distinguish the different hadrons species (π, K, p) and also deuterons. The mass resolution depends on the momentum and time resolution, and on the track length measurement. Since the TOF particle identification becomes worst as the square of the particle momentum, to obtain the same mass resolution, at twice the momentum of the particle, an improvement of four-times in the time resolution would be needed. The time-of-flight difference for two particles of unequal mass m_1 and m_2 having the same momentum p and the same track length is

$$t_1 - t_2 = \frac{L}{2c}\left(\frac{m_1^2c^2 - m_2^2c^2}{p^2}\right) \tag{3.9}$$

in the limit $m^2c^2/p^2 < 1$.

The particle identification capability of a TOF detector is related to the number of standard deviations in the time of flight difference of two particles, depending also on their momentum:

$$n_\sigma = \frac{t_1 - t_2}{\delta t}, \tag{3.10}$$

where δt is the time resolution. In Fig. 3.10 the number of standard deviation to separate pions, kaons and protons are shown. These results are obtained with 2010 Pb–Pb collisions with the TOF resolution shown in Fig. 3.9 (left). The ALICE TOF is able to separate pions and kaons up to 3 GeV/c and kaons and protons up to 5 GeV/c both with a 2σ separation.

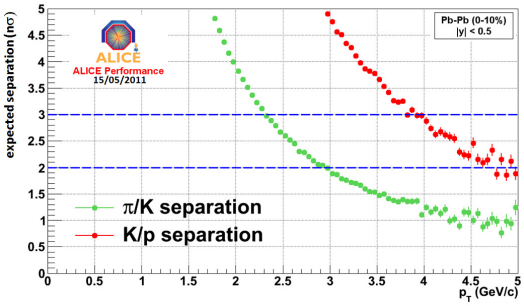

Figure 3.10: TOF Particle mass separation for π/K and K/p as a function of the transverse momentum measured in Pb–Pb collisions. A 2σ separation is achieved up to 3 GeV/c for π/K and up to 5 GeV/c for K/p.

3.5 Forward detectors

ALICE main detector in the forward rapidity region is the muon spectrometer that covers the pseudorapidity range $-4.0 \leqslant \eta \leqslant -2.5$. In the forward region there are also charged particles and photons multiplicity detectors as well as a trigger detector (VZERO) and two calorimeters at zero degree in order to measure the centrality in Pb–Pb collisions and a detector to measure the start time of the collision [118].

3.5.1 Muon spectrometer

The ALICE muon spectrometer is designed to detect muons in the pseudorapidity range $-4.0 \leqslant \eta \leqslant -2.5$. It allows to measure the complete spectrum of heavy-quark and low masses vector mesons ($J/\Psi, \Upsilon, \phi, \dots$) in the $\mu^+\mu^-$ decay channel. The muon spectrometer consists of:

- a passive front absorber for hadrons and photons coming from the interaction vertex and the secondary products;
- an high-granularity tracking system of 10 detection planes;
- a large dipole magnet that produces an horizontal field perpendicular to the beam axis;
- four planes of trigger chambers, placed after a passive muon-filter wall;
- an inner beam shield to protect the spectrometer from secondaries produced at large rapidity.

The front absorber is located inside the central barrel magnet, it is 4.3 m long and it is made predominantly of carbon and concrete [118]. The tracking chambers are designed to achieve 100 μm spatial resolution for an invariant-mass resolution of about 100 MeV/c^2 at the Υ mass. The muon-filter wall is an iron wall 1.2 m thick ($\sim 7.2\ \lambda_{int}$). It provides additional protection for the trigger chambers allowing only muons with $p > 4$ GeV/c to reach them. The building blocks of the muon trigger system are Resistive Plate Chambers (RPC) operated in streamer mode.

For the trigger system, the efficiency is computed as the probability that a given muon trigger chamber gave a signal if there are hits in the other three chambers, both in the bending and not banding planes. This efficiency measured with 2010 data has an overall value of 98%.

3.5.2 V0 detector

The V0 detector is a small angle detector consisting of two arrays of scintillator counters installed on both sides of the ALICE detector [118]. It provides, together with the SPD, the minimum-bias trigger in *pp* and Pb–Pb collisions. The V0 detector is used also to remove the collisions background produced when particles of the beam interact with residual particles in the beam pipe. The V0 is also one of the detectors that provide centrality estimation in Pb–Pb collisions, since the number of particles reaching the scintillators is correlated with the number of primary particles. In Fig. 3.11 (left) the correlation between the signal in the SPD outer layer (i.e number of clusters) and in the V0 is shown. In 2011 Pb–Pb data taking the V0 detector will provide also centrality triggers. The V0 detector is also very important for the measurement of the luminosity in *pp* collisions with a good precision ($\sim$ 4%). The V0A is located 340 cm from the vertex on the side opposite to the muon spectrometer, the V0C is placed to the front face of the hadronic absorber, 90 cm from the vertex. They cover the pseudo-rapidity ranges $2.8 < \eta < 5.1$ (V0A) and $-3.7 < \eta < -1.7$ (V0C). These detectors are segmented in 32 individual scintillators each distributed in four rings. The scintillators are connected with 1mm diameter Wave-Length Shifting (WLS) fibres, that guide the light to an Hamamatsu photo-multiplier.

3.5.3 Zero Degree Calorimeters

The centrality determination can be performed measuring the energy carried in the forward direction (0° with respect to the beam direction) by the non-interacting nucleons. In ALICE, spectator nucleons are detected using two Zero-Degree Calorimeters (ZDC). The ZDC can also give an estimate of the reaction plane in nucleus collisions and to reject parasitic collisions both in *pp* and Pb–Pb. At the injection between SPS and LHC, some small fragments of the bunch of the beams can fall in the wrong radio frequency bucket. When these fragments collide with the main bunch of the second beam, they can produce parasitic collisions, displaced about 30 cm, from the centre of the experiment.

The ALICE ZDC are located at 116 m on either side of the interaction point. Two small electromagnetic calorimeters (ZEM) are placed at about 7m from the interaction point, on both sides of the LHC beam pipe, on the opposite side with respect to the muon spectrometer [118]. After the collisions, spectator protons are spatially separated from the neutrons by the magnets in the LHC beam pipe. Each ZDC is made of two calorimeters: one for the spectator neutrons (ZN) placed between the beam pipes, and one for spectator protons (ZP), placed externally to the outgoing beam pipe where positive particles are deflected.

The hadronic ZDCs are quartz-fibre sampling calorimeters. The shower generated by incoming particles in the absorber produces Cherenkov radiation in the fibres. The read-out is divided in four independent towers. One out of every two fibres is sent to a single photomultiplier, while the remaining fibres are sent to four PMT, each one collecting light from a single tower. The ZEM technique is similar to the hadronic calorimeters, in this case 40 lead planes are placed as absorber and they are used with quartz fibres. Central collisions give a low amount of energy in the ZDC, but also very peripheral collisions, where

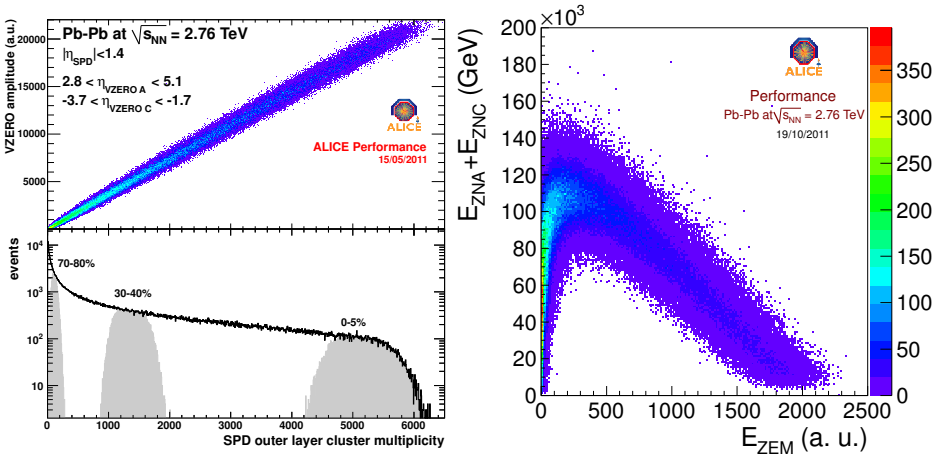

Figure 3.11: Correlation between the amplitude of the signal in the V0 detector and the SPD outer layer multiplicity. The correlation is very important to measure the centrality (left). Correlation between the energy released in the zero degrees hadron calorimeters and in the zero degree electromagnetic one (right).

spectator nucleons can bound into fragments which don't get out from the beam pipe and that cannot be detected from the ZDCs. The ZEMs are necessary to measure the event-by-event energy of particles emitted in forward rapidity. Since this energy increases with the collision centrality, it is very useful to discriminate between central and peripheral collisions. An exemple of the correlation between the energy realsed in the ZDCs and measured in the ZEM is shown in Fig. 3.11 (right).

3.5.4 Time Zero Detector -T0

The Time Zero detector was designed to generate a start time (T0) for the TOF detector. This time corresponds to the real time of the collisions and it is independent of the interaction point position. The T0 is used also for the online monitoring of the luminosity and it can also generate an early 'wake-up' signal for the TRD, prior to the L0 trigger. The detector consists of two arrays of Cherenkov counters, 12 counters per array. Each counter is based on a fine-mesh photomultiplier tube, optically coupled to a quartz radiator with 20 mm diameter and 20 mm thickness. Like the V0, two arrays are placed at the two different sides with respect to the interaction point: one at 72.7 cm (T0-C) and 375 cm (T0-A) [118].

3.6 Trigger System

The ALICE Central Trigger Processor (CTP) is designed to select events with many different properties [118]. The fast response from the trigger system has to suit the detector requirements, especially taking into account Pb–Pb collisions. The principal design requirements for tracking detector is to be able to cope with the large multiplicity foreseen in Pb–Pb collisions. The fast part of the trigger is split into two levels: a Level 0 (L0) signal, which reaches detectors at 1.2 μs, but it is too fast to collect all trigger inputs, and a Level 1 (L1) signal that arrives at 6.5 μs to collect the remaining inputs. Due to the high-multiplicity environment in Pb–Pb collisions, it is very difficult to reconstruct more than

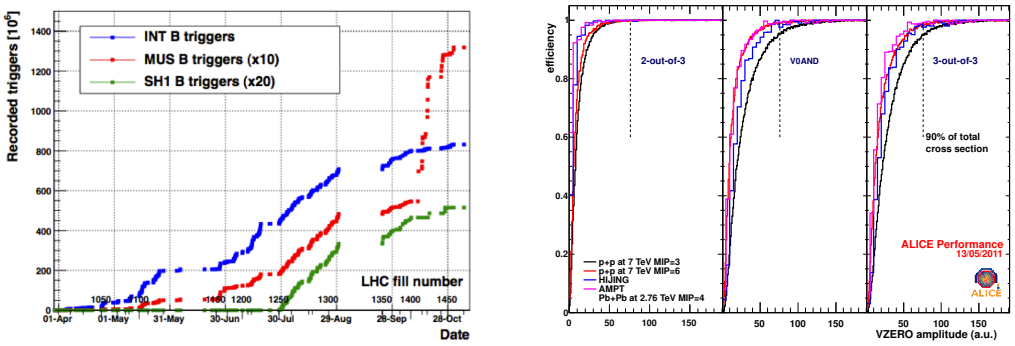

Figure 3.12: Total number of triggered events for minimum bias trigger (blue points), muon trigger (red points, multiplied by a factor 10) and high multiplicity trigger (green points, multiply for a factor 20) (right). Trigger efficiencies in the three configurations that ALICE used for the Pb–Pb 2010 data taking (right).

one central collision in one event. A 'past-future protection' interval can be added at the trigger Level 2 (L2) to avoid these situations (88 μs). L2 waits the 'past-future protection' to finish and it can also be used for running other trigger algorithms. The definition of an interaction, for a minimum bias trigger, requires a logic OR of different detectors input. The trigger class is defined in terms of the logical condition demanded for the inputs, the set of detectors required for readout (detector clusters) and the 'past-future' protection.

In *pp* 2010 data taking ALICE trigger set up was focused on the collection of minimum bias events at both energies: 0.9 and 7 TeV. The main detector involved in this trigger are the SPD and the V0. The trigger signal is given if there is at least one signal in one of the two V0 sides, or if one fast-or chip of the SPD is fired. Starting from August 2010 also an high multiplicity trigger was introduced. In this case the signal trigger was given in case 65 fast-or chips in the SPD outer layer were fired. The total number of events collected in the *pp* data taking in 2010 is around 800×10^6 for the minimum bias sample, 25×10^6 for the high multiplicity and 130×10^6 for the muon trigger (Fig. 3.12 left).

Also in Pb–Pb 2010 data taking, the minimum bias trigger was the most used for the central barrel trigger set up. To avoid the rejection of very peripheral events and ultra peripheral collisions, the beginning of the data taking was characterized by the same trigger as in *pp* minimum bias collisions. After the first data taking, the trigger has been tightened in order to reduce electromagnetic background that is two orders of magnitude bigger then the hadronic interaction rate. So the trigger logic was moved to the requirement of two out of three signals between: one of the two signals of the V0 detector and one fast-or of the SPD. In the third part of the data taking a logic AND of the two V0 scintillator sides was used. During the last part of the data taking, all the three signals were required (three out of three). A specific muon trigger was not present in 2010 Pb–Pb data taking. With this configuration we have collected about 30×10^6 minimum bias events.

Fig. 3.12 (right) shows the efficiency for the main 3 different triggers that has been run during the 2010 Pb–Pb data taking. The trigger efficiency was studied applying the Pb–Pb trigger selection to the *pp* data, assuming that the *pp* minimum interaction trigger is totally efficient after beam background rejection. The selection is then compared with the Monte Carlo simulations. The overall selection efficiencies goes from 97% to 99% with a purity of 100% in the centrality class 0-90%.

High Level Trigger

The data size of one event in Pb–Pb centrals events is about 70 MB. The data rate for all detectors, after the trigger selection, can reach 25 GB/s, while the physics content of a large number of events might be small and the DAQ bandwidth is about 1 GB/s. The HLT has to accept or reject events based on the detailed online analysis and compress the event size without loss of physics information by applying compression algorithms on the selected data. The raw data of all ALICE detectors are received via Detector Data Links (DDL) and they are processed performing basic calibration and extracting hits and clusters. The event reconstruction is done first for all detectors separately, then all informations are combined to reconstruct the whole event. At this level the HLT uses the reconstructed physics observable to select events, based on run specific physics selection criteria. The selected data is further subjected to complex data compression algorithms. In order to meet the high computing demands, the HLT consists of a PC farm up to 1000 multi-processor computers [118].

3.7 ALICE offline computing

The ALICE offline framework, AliRoot [121], is an object-oriented software framework, based on the ROOT system [122] and complemented by the AliEn system which gives access to the computing Grid [128]. These fundamental technical choices result in one single framework, entirely written in C++, with some external programs (hidden to the users) still in FORTRAN. In this way it is possible to allow simulation, reconstruction and data analysis both from collisions and cosmic events within the same framework.

3.7.1 The AliRoot framework

Event simulation

Collisions are simulated through events generators, like Pythia [123] and HIJING [127]. All informations about the generated particles (i.e. type, momentum, production process, decay products) are organized in a kinematic tree, stored in a file.

Particle transport in the detector: *hits*

The generated particles are propagated to the sensitive region of the detector, where they can interact with detector material. During this interaction particles can loose energy, decay, produce other particles or to be absorbed. Using the ROOT geometrical modeler, the detector shape, structures, positions and materials are described in the AliRoot framework as realistically as possible. To reproduce realistic interaction with materials, Geant3 [124], Geant4 [125] and Fluka [126] programs have been used within he AliRoot framework. All interactions of particles with sensitive parts are recorded as *hits*, containing position, time and energy deposit.

Digitization and raw data

The hits information is complemented with the *track references* corresponding to the location where the particles are crossing user defined reference planes. The digital output of the detector related to an hit is stored as a *summable digit*, taking into account the detector and electronics response function. Finally, the digits are stored in the specific

hardware format of each detector as raw data. This format is the minimum of the physical information available and it is the starting point of the reconstruction process both for 'real' data and Monte Carlo ones.

Cluster Finding

Signals of particles crossing the sensitive area usually are detected in some detecting elements closed one to the other. These signals are combined into a single cluster, which better estimates the position of traversing particle and it reduces the effect of the random noise.

The Event Information

The output of the whole reconstruction operation is the Even Summary Data (ESD) which contains all the information about the event both at track or event level. Technically, the ESD is a tree with objects of type AliESDEvent stored in the AliESD.root file. Since the ESD contains more information then what is needed for the analysis, Analysis Object Data (AOD) are developed. They contains both tracks and higher level reconstruction objects (jets, charmed mesons candidates, ...). The files containing ESD and AOD are distributed worldwide on the GRID.

3.7.2 AliEn: ALICE analysis framework on the GRID

In 2010 ALICE has produced around 5 PB of data on tape; the current estimate for 2011 is almost the same and even larger [128]. This amount of data requires an automate software procedure for the reconstruction of the events and for the user analyses, exploiting a large mass of computing resources. The worldwide distributed GRID facilities were designed to provide both computing power and disk space needed for the LHC experiments, to deal with this big software challenge. The big advantage of a distributed computing system is the possibility to analyze large amount of data by splitting the jobs analysis into many identical subjobs that can be run in parallel on different computer nodes. The ALICE Virtual Organization (VO) is composed of more than 80 sites distributed all over the world [129]. Each site has many Worker Nodes (WN), which are the machines were the software programs can run. The Storage Element (SE) is responsible for managing physical files in the site and providing an interface to the mass storage. The Computing Element (CE) service is an interface to the local WN batch system and it manages the computing resources of the site. The ALICE Collaboration has developed the AliEn software, that is a distributed interface needed to simulate, reconstruct and analyze the data. AliEn provides a global file system (catalogue) for data storage and the possibility to execute the jobs in a distribute environment. Once the user code is working and tested on a small size of data (typical few ESDs or AODs file) and the data sample is specified, the analysis can be run on the AliRoot or ROOT packages deployed on the GRID, using the AliEn interface to distribute the jobs.

3.8 ALICE track reconstruction

Due to the unknown multiplicity in Pb–Pb collisions at the LHC energies at its design time, ALICE tracking was foreseen to be able to deal with a multiplicity up to 8000 particles per unit of rapidity and an occupancy in the TPC inner part that can reach 40% [120].

The track finding procedure developed for the central barrel (ITS, TPC, TRD, TOF) is based on the Kalman filter algorithm, widely used in high-energy physics experiments [130]. The Kalman filter method allows to have track finding at fitting simultaneously, its main property is the possibility to extract the optimal estimate of the track geometrical parameters point by point, since it is a local based method. For this reason it is very useful also to extrapolate the track from a detector to another. In the Kalman Filter algorithm energy loss and multiple scattering are accounted for in a direct and simple way. The ALICE track reconstruction [131] is based on the following steps:

- Primary vertex determination using only SPD informations, for a fast interaction point position estimate 4.1.1.

- Track reconstruction in the TPC. Track finding in the TPC from the outer to the inner part. The outermost pad rows and the primary vertex position from previous step are used as seed.

- Track reconstruction in the ITS. TPC tracks are matched to the SSD layers and matched with ITS points down to the innermost SPD layer. First the vertex position is used to guide the track finding and maximize efficiencies for primary tracks. Without the vertex position information is possible, then, to reconstruct displaced tracks from the interaction point.

- Back-propagation and refit of the track outward in ITS and TPC, up to the outer radius of the TPC. Extrapolation and track matching in the TRD.

- Propagation to the outer layer (TOF, HMPID, PHOS, EMCal) for Particle Identification.

- Reconstructed tracks are re-fitted inward TRD, TPC, ITS and re-propagated to the primary vertex reconstructed in the first step.

- Primary vertex recalculation using tracks to obtain the optimal resolution 4.1.2. A description of the vertex reconstruction algorithm and its performances in terms of resolutions and efficiencies will be described in chapter 4.

3.9 ITS alignment

The main task of the ITS is to provide precise track and vertex reconstruction close to the interaction point. Between other task, the ITS it is important to improve the angle and the momentum resolution for tracks reconstructed in the TPC, to recover tracks that don't reach the TPC and to reconstruct secondary vertices from decay of hyperons and heavy flavour hadrons. The separation between the interaction point and the secondary vertex from heavy flavour particles is of the order of hundreds of micrometers. The proper decay length $c\tau$ of the heavy flavour hadrons is $\sim 100 - 500$ μm depending on the particle. In order to reconstruct these secondary vertices, it is important to obtain a resolution on the track distance of closest approach to the primary vertex (track impact parameter) below 100 μm. The micro-metric intrinsic resolution of the ITS sensors and the low material budget allow the ITS detector to reach a resolution on the track impact parameter of $\sim$ 10 μm at high momentum $p_{\mathrm{t}} > 10$ GeV/c. These results on the impact parameter resolution can be obtained only after the correction for the misalignment effect.

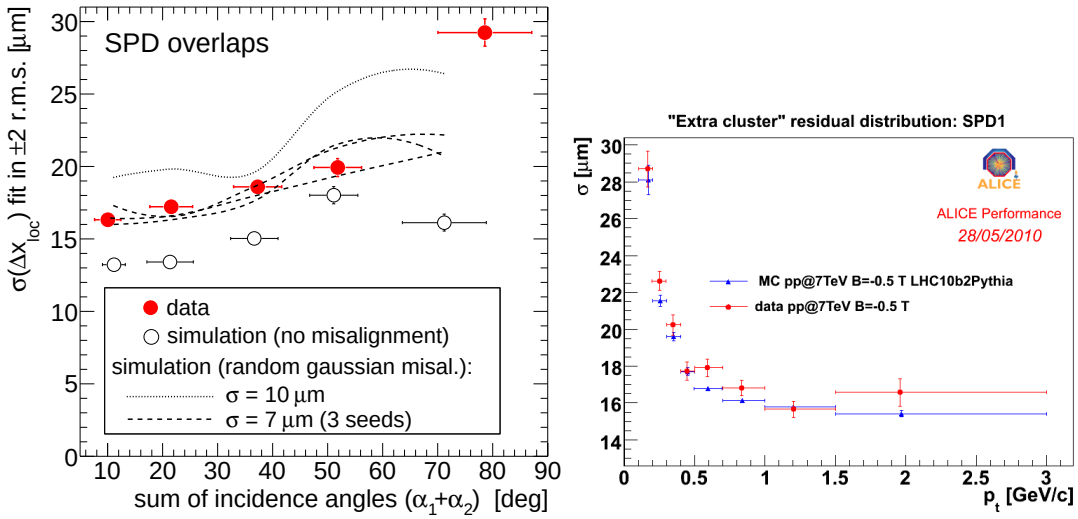

Figure 3.13: Δx_{loc} spread distribution as a function of incident angles of tracks on two overlapping modules for the SPD obtained with cosmic-rays tracks. The comparison between data and MC shows that the residual misalignment is about 7 μm (left). Δx_{loc} spread measured as a function of p_{t}. Data are compared with MC and they show good agreement. The low p_{t} rise is due to the multiple scattering effects (right).

The ITS (and most of all detectors in general) is an assembly of thousand of different modules, whose positions are different from the ideal one, because of the installation and integration of these different components. If these displacements are not taken into account, they can worsen the tracking performance of the detector and then the physics results. The alignment of the detector has to be studied by measuring the translation and the rotations of the sensitive modules. Once this is done, this displacement can be applied in the track reconstruction and properly taken into account in the performance.

The ITS alignment procedure starts with the position survey measurements, performed during the assembly and it is then refined using tracks from cosmic-ray muons (these data were taken in 2008 and 2009) and using particles produced in *pp* collisions. When the alignment is studied using track data, two approaches are followed, both based on the tracks-to-measured points residual minimization [132]. The ITS alignment procedure starts from the validation of the SSD survey measurement with cosmic-ray tracks. The SPD and the SSD are then aligned using cosmic tracks without magnetic field, in order to avoid possible bias dealing with curved tracks (i.e. radial layer deformations). Once SPD and SSD are aligned, the SDD initial time-zero calibration can be refined.

The ITS is then aligned all together using cosmic-ray tracks with and without magnetic field. Two track-based method are then used for the full ITS alignment. The main one is based on the Millepede algorithm [134], while the second is based on the module-by-module iterative approach [132, 135]. Millepede is an algorithm with a global least squares minimization approach. It tries to determine the set of alignment parameters by minimizing the residuals of a large-amount of pre-reconstructed tracks. The second approach is focus on the module that has to be aligned. Once a module is selected, all tracks, that pass through it, are fitted without using the cluster laying on it. Tracks are then propagated to the module plane and the residual between the extrapolated point and the measured clusters are then computed for all tracks. Comparable results have been

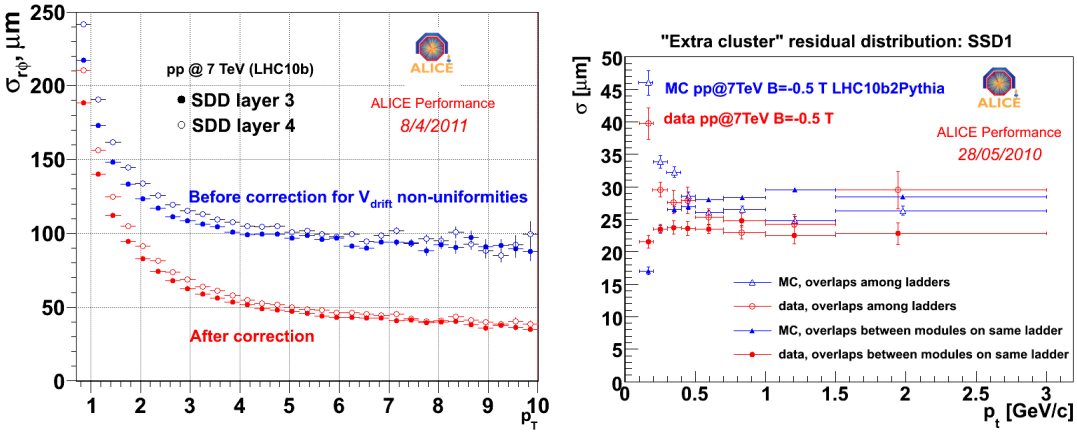

Figure 3.14: SDD points resolution in the rϕ plane after correction for non-uniformities in the drift velocity. The resolution reaches 50 μm for $p_{\rm t} > 4$ GeV/c (left). Spread of Δx_{loc} distribution as a function of $p_{\rm t}$ measured for SDD modules along the same ladder (filled, red points) and for modules of different ladders (empty red points). Data are compared with a MC with residual misalignment (corresponding blue points). (right)

obtained with the two alignment methods, in terms of alignment qualities and alignment parameters recovered [135].

The measurement of the momentum of the track can be also very useful to study detector resolution and residual misalignment due to multiple scattering as a function of $p_{\rm t}$. When ITS and TPC are aligned and calibrated internally, the relative alignment is performed. The last step of the procedure is the alignment with tracks coming from pp collisions. These tracks are important to study tracks coming in all different directions, with different incident angles and to improve the alignment in the horizontal plane, where cosmic statistic is lower. For the alignment pairs of points produced by particles crossing the acceptance overlap between two neighbour modules are also used, allowing to measure the relative position of the modules. The overlaps allow to study the effective spatial resolution of the sensor modules, that is made of the intrinsic spatial resolution and the residual misalignment.

Fig. 3.13 (left) shows the spread of the Δx_{loc} distribution as a function of the sum $(\alpha_1+\alpha_2)$ of incident angles of tracks on the two overlapping modules for the SPD, obtained with cosmic-rays tracks collected in 2008. These data are well described by the simulation with a random residual misalignment with a spread of about 7 μm. In Fig. 3.13 (right) the spread of the Δx_{loc} variable is measured as a function of $p_{\rm t}$, using pp 7 TeV collisions data. The rise at low transverse momenta is due to the multiple scattering effect, that becomes negligible for $p_{\rm t} > 1$ GeV/c. Data are compatible within errors with a Monte Carlo simulation with a random gaussian misalignment with $\sigma = 7$ μm. This values can be considered an estimate of the average misalignment for all SPD modules. For SSD the residuals between the extra points in the overlaps were studied both with cosmic-rays and collisions track. In Fig. 3.14 (right) the spread of the Δx_{loc} distribution is measured with pp data at 7 TeV as a function of $p_{\rm t}$, separately for overlaps between modules along the same ladder (filled markers) and for those between different ladders (empty marker). The results are compared with a MC simulation where the misalignment values were taken from the measurement with the survey, i.e. 5 μm in x, 10 μm in y and 5 μm

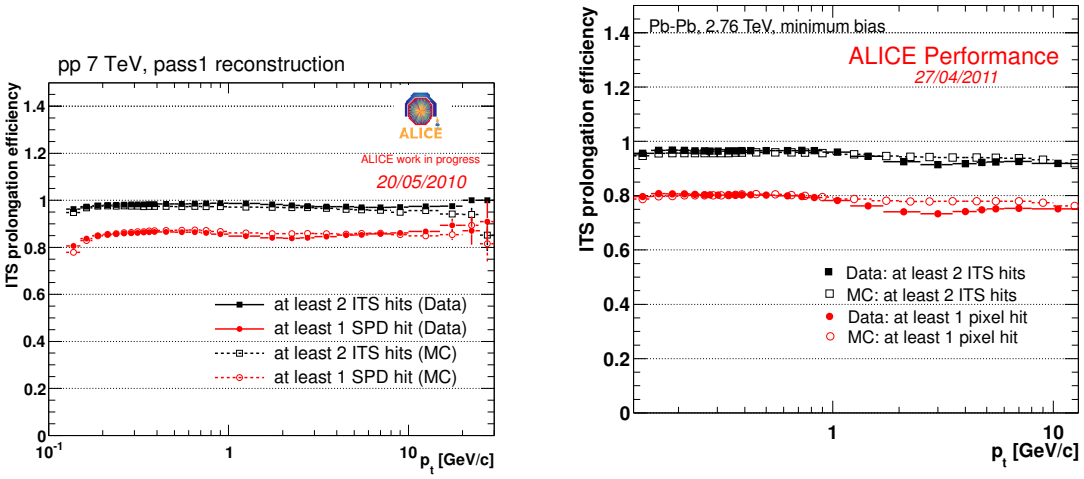

Figure 3.15: TPC-to-ITS prolongation efficiency in *pp* (left) and Pb–Pb (right) collisions compared with Monte Carlo simulation. The agreement is within 2%. The efficiencies are computed requiring two points in the full ITS (black) and one in the pixels detector (red). The lower efficiency in the last case is due to the number of active module in the SPD.

in z for the module misalignment and 10 μm in x, 10 μm in y and 50 μm in z for the ladder misalignment. The MC results seems to slightly overestimate the overall residual misalignment. For the SDD the alignment procedure is complicated by the geometrical displacement and the calibration of drift velocity and minimum drift time t_0. The t_0 and the drift velocity are considered free parameters for all 260 SDD modules within the Millepede procedure. Fig. 3.14 (right) shows the residual in the rϕ plane before (blue) and after (red) the corrections due to non-uniformities in the drift velocity calibration as a function of $p_{\rm t}$. The resolution is around 50 μm for tracks with $p_{\rm t} > 4$ GeV/c. Results are obtained with $\sqrt{s} = 7$ TeV *pp* collisions tracks.

3.10 ITS tracking performance

The ALICE global tracking was described in section 3.8. In Fig. 3.15 (left) the prolongation tracking efficiency between TPC and ITS is shown, as a function of the transverse momentum. This efficiency is computed with *pp* data using the TPC tracks as a reference and looking for the prolongation in the ITS [133]. If at least two points in the ITS are required the prolongation efficiency is above 97% and almost flat in the whole momentum range (black points). If tracks are required to have at least one of the two points in the pixels detector, there is a drop to 85%, due to the inactive modules in the pixel detector (red points). The Monte Carlo HIJING simulation (empty markers) [136] reproduces the efficiencies measured in the data with a difference below 2% in the range $0.2 < p_{\rm t} < 10$ GeV/c. The prolongation tracking efficiency was also studied in minimum bias Pb–Pb collisions and the results are well compatible with the *pp* ones (Fig. 3.15 right). The high ITS segmentation and low material budget are the key points to have practically the same tracking performance in *pp* and Pb–Pb collisions, despite the different multiplicity environment of the collisions. This efficiency is also studied in Pb–Pb collisions, as a function of centrality. In Fig. 3.16 (left) the ratio of the efficiencies measured in

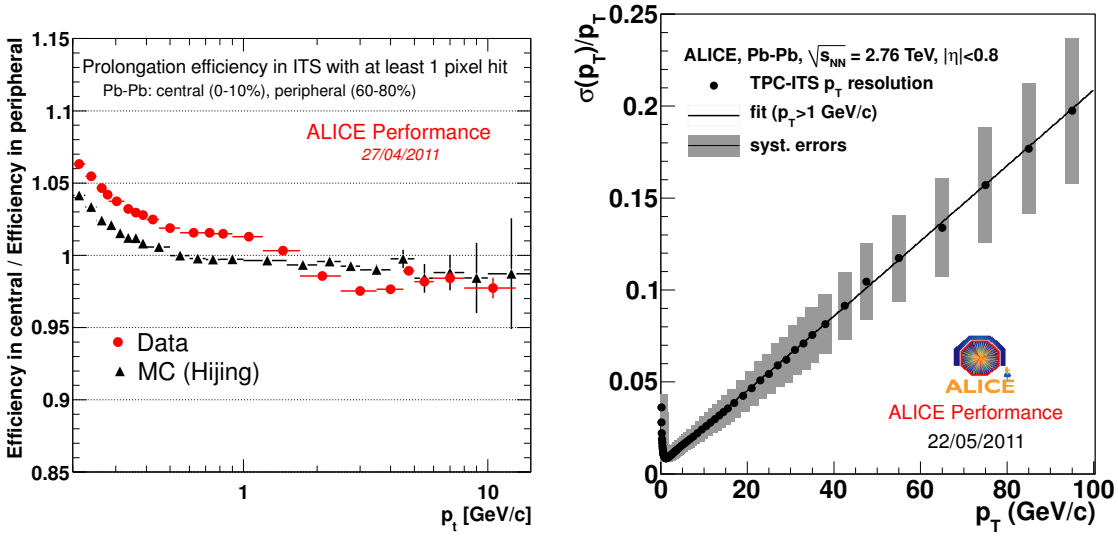

Figure 3.16: Ratio of the ITS-to-TPC prolongation efficiency, measured in central and peripheral Pb–Pb events. The results are compared with a Monte Carlo simulation, the discrepancy between the two is of the order of 2% (left). ALICE global tracking momentum resolution measured in Pb–Pb collisions (right).

central (0-10%) and peripheral (60-80%) collisions is plotted (red points), together with a comparison with the same ratio extracted with Monte Carlo HIJING [136] simulation. Both data and Monte Carlo efficiencies are larger at high-p_{t} in the central events, due to the fake tracks reconstructed with combinatorial points. The difference between data and Monte Carlo is of the order of 2% at low p_{t} ($p_{\mathrm{t}} < 1$ GeV/c). At high p_{t} the difference is compatible within errors. This results shows no dependence on the multiplicity for the tracking prolongation efficiency.

The transverse momentum resolution of the global TPC+ITS ALICE tracking is shown in Fig. 3.16. The momentum resolution reaches 20% for tracks of about 100 GeV/c, down to 5% and lower for tracks below 20 GeV/c.

The impact parameter resolution was also measured using primary tracks, but requiring two points in the pixels detector. For each track, its impact parameter was estimated with respect to the primary vertex reconstructed without using the selected track; this was done in order to avoid any bias on the primary vertex resolution. The primary vertex was reconstructed using the knowledge of the luminous region, to constraint the interaction point. This procedure helps in improving the primary vertex resolution especially for events with low multiplicity (see sec 4.4). The impact parameter resolution includes the convolution of the track position and primary vertex resolution. In Fig. 3.17 (left), the impact parameter resolution is shown as a function of p_{t} for pp collisions. Data (red) are compared with MC simulation (black), in which a residual misalignment is taken into account; the results are in good agreement. For a track of $p_{\mathrm{t}} \sim 1$ GeV/c the impact parameter resolution is around 75 μm. For tracks with a p_{t} of 10 GeV/c, the resolution goes down to 25 μm. The same results are obtained for minimum bias (0-80%) Pb–Pb collisions. In this case for a track of $p_{\mathrm{t}} \sim 1$ GeV/c the impact parameter resolution is around 50 μm, while for high p_{t} tracks it reaches 15 μm as shown in Fig. 3.17 (right). The difference between pp and Pb–Pb is mainly due to the to the high multiplicity of central Pb–Pb collisions that implies a better primary vertex resolution, as it will be shown in

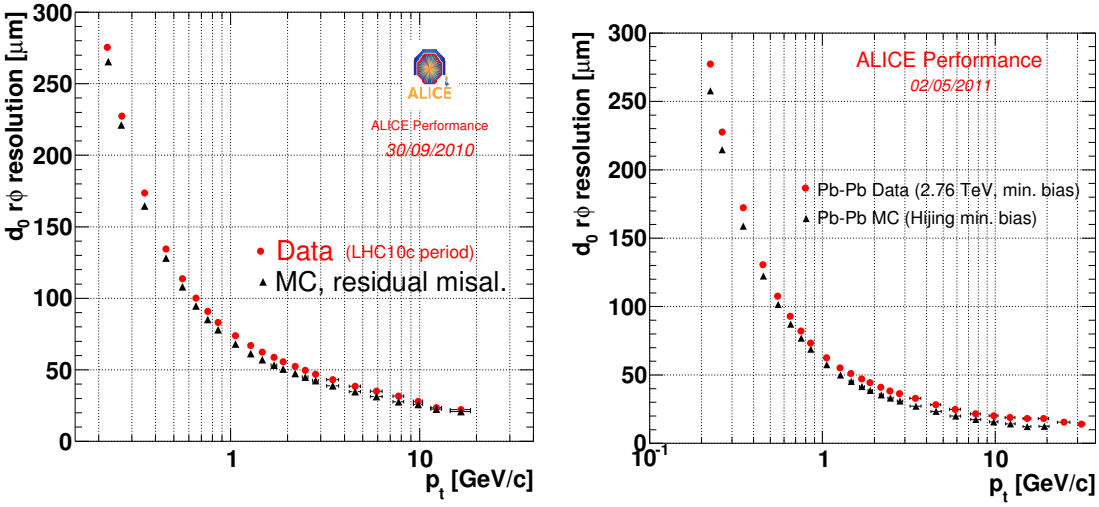

Figure 3.17: Impact parameter resolution in the rϕ plane, measured in pp (left) and Pb–Pb (right) collisions for primary tracks. Data (red) were compared with MC simulation measurement (black).

Sec. 4.3.2 . Also in this case the luminous region constraint is applied but it affects only peripheral events.

To recover very low momentum particles, ALICE has also a second tracking algorithm, that exploits only the ITS capability. The main difference with respect to the global tracking, is the starting point. The ITS StandAlone (ITS SA) tracking starts from the primary vertex and it reconstructs tracks, matching the clusters coming from the different ITS layers through selected angolar windows. This tracker has been optimized to reconstruct very low momentum particles that don't reach the TPC. Exploiting the charge measurement of drift and strip detectors, it is also possible to identify particles at very low momenta. In Fig. 3.18 (top) electrons can be identified from 80 MeV/c up to 160 MeV/c with a 2σ separation from π. Pions are separated from kaons up to 0.6 GeV/c and kaons from protons up to 0.8 GeV/c. Similar results have been obtained in Pb–Pb collisions as it is shown in Fig. 3.18 (bottom) for (0-5%) central events.

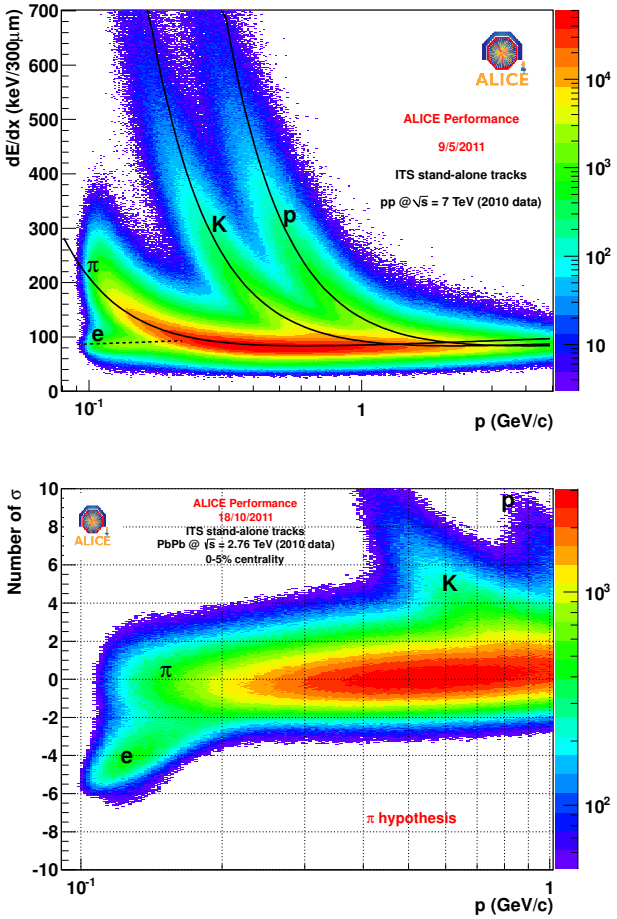

Figure 3.18: Energy loss signal for particles tracked with the ITS standalone algorithm, measured in *pp* collisions (top). Separation in terms of number of standard deviation for electrons, pions, kaons and protons using ITS SA tracking and ITS energy loss, measured in Pb–Pb collisions (bottom).

4 Interaction vertex reconstruction in the ALICE detector

The interaction (primary) vertex reconstruction is among the first checks needed at the beginning of the data taking for a new experiment at a new collider. The position of the interaction point allows to define, then, primary tracks, secondaries and to understand the topology of the event. Also from the machine point of view, experiments can provide important information on the colliding region of the two beams. The size of this region, called luminous region, is defined by the orbit parameters of the bunches as described in Sec. 3.2. The luminous region needs to be unfolded from the vertexer algorithm resolution in order to measure the region where the two particle distributions in the two bunches collide.

The primary vertex resolution is also related to the decay of heavy flavour hadrons, since it is possible to separate these secondary vertices only achieving good resolution in the measurement of the interaction point.

It is also important to compare the resolution and efficiency of the primary vertex reconstruction obtained with the data, with the ones expected in Monte Carlo simulations. The vertex reconstruction capability has to be considered when computing the Monte Carlo correction factors for the analysis.

In the first part of the chapter the general ALICE strategy for the primary vertex reconstruction will be introduced. The algorithms, used to measure the position of the interaction points in ALICE, will be also described. They use full or partial reconstruction, in order to balance between resolution and computation speed.

The second part of the chapter will be devoted to the different measurements of the primary vertex done with online or offline procedures.

Then, a summary on the main vertexer algorithms performance will be given. This performance is evaluated in terms of resolution and efficiency of the primary vertex reconstructions. The last part selected examples of monitoring of the beam spot parameters are presented; they were provided as a feedback to the LHC machine experts.

4.1 Primary vertex reconstruction in ALICE

Primary vertex reconstruction is an important task in the ALICE experiment for several reasons:

- During data acquisition it is important to measure and monitor online the beam position and the beam spread along the three coordinates x, y and z (introduced in Sec 3.2).

- During offline reconstruction, the position of the primary vertex is used to build the so-called track seeds that are used as starting points for the kalman filter algorithm. Hence an efficient determination of the vertex interaction is required before starting the tracking phase. This is achieved using points reconstructed in Silicon Pixel Detector (SPD - Sec. 3.4.1)

- During the analysis it is important to have a good measurement of the primary vertex position in order to study short-lived particles, such as those with open charm and open beauty. This can be obtained reconstructing the primary vertex from tracks (after the tracking phase).

Three algorithms for primary vertex reconstruction will be discussed:

- *VertexerSPDz*: it provides the measurement of the z coordinate of the interaction point from the SPD-reconstructed points. It requires the knowledge of the average x and y coordinates (Sec. 4.1.1).

- *VertexerSPD3D*: it provides a three-dimensional measurement of the primary vertex using SPD informations (Sec. 4.1.1).

- *VertexerTracks*: it provides a three-dimensional measurement of the primary vertex from the reconstructed tracks (Sec. 4.1.2).

For a more detailed discussion of primary vertex reconstruction algorithms, see [137] and references therein.

The general ALICE strategy for the vertex reconstruction is based on different steps and different vertex algorithms, in order to obtain the best compromise between precision and speed of the measurements. The interaction point is estimated online using the VertexerSPD3D. This is a fast algorithm that can reconstruct the vertices online while the data taking is ongoing: a event is collected, the SPD data are reconstructed and the values obtained are used to fill histograms of the three coordinates distributions. The mean and r.m.s values of these histograms (for x and y coordinates) are then written to the ALICE Offline Conditions DataBase (OCDB) [118]. The information written in the OCDB (called Mean Vertex SPD) is then used as a seed of the full track reconstruction in the central barrel.

Between the online data taking and the full reconstruction, a specific calibration data process is foreseen within the ALICE computing model (cPass0 - Sec. 4.4). During this calibration process the measurement of the luminous region is performed, using the full track reconstruction, available for a subsample of the events. The vertex reconstruction with tracks is more precise and it allows to measure a luminous region of the order of 20 μm. The calibration procedure writes the Mean Vertex object to the OCDB: mean values of the position are obtained with a Gaussian fit of the distributions; the r.m.s of the distributions are de-convoluted from the vertexer algoritm resolutions in order to obtain the size of the luminous region.

During reconstruction, the possibility of using the precise information on the luminous region allows to constrain the event-by-event primary vertex to belong to the luminous region and improve the resolution especially for low-multiplicity pp events, where the vertexer algorithm is less precise.

4.1.1 SPD vertexers

The SPD vertexers use information coming only from the two layers of the SPD detector. The algorithms for the estimation of the primary vertex consist in the correlation of reconstructed points belonging to the first layer of the SPD with reconstructed points belonging to the second one within a small azimuthal window (by default set to $\Delta\varphi_{12}$=0.01 rad). Matching pairs of points on the two layers define candidate *tracklets*. In this way, only high momentum tracks are selected (i.e. straight lines in the bending plane), the combinatorial background is reduced and only the tracks less affected by multiple scattering are considered. Tracklets are reconstructed in the pseudorapidity range $|\eta| < 1.6$.

VertexerSPDz

This vertexer provides a measurement of the z-coordinate of the primary vertex assuming that the beam position in the transverse plane is known with an accuracy of the order of 200 μm or better, e.g. from the interaction point measured online or from a previous reconstruction procedure. For each candidate tracklet i the intersection point z_i with the beam axis is calculated and the vertex position is calculated as the weighted mean (z_{mean}) of the z_i values, falling in a Region Of Interest (ROI) around the peak of the z_i distribution.

The calculation of z_{mean} is iterated, re-centering at each step the ROI on the value of z_{mean} from the previous iteration until a symmetric region around z_{mean} is reached. This allows to minimize possible biases due to asymmetries in the tails of the z_i distributions.

VertexerSPD3D

This vertexer provides a three-dimensional measurement of the primary vertex based on SPD tracklets. The first step of the VertexerSPD3D algorithm provides the finding and the selection of tracklets in the SPD: several requirements are needed in order to obtain a good sample of tracklets.

After a cut on the distance of closest approach between the two tracklets (DCA$<$ 1 mm), the crossing point $\mathbf{c}_{ij}$ of the pair ij is calculated; only the pairs with the crossing point in the fiducial region are kept. A three-dimensional histogram is filled with all the points $\mathbf{c}_{ij}$ and the peak (i.e. the bin with maximum density of tracklet intersections) is found. Tracklets far from the peak (distance larger than 1 mm along x and y and 8 mm along z) are removed.

The second step is the vertex determination, in which a first estimate of the primary vertex is calculated as the point of minimum distance of the selected tracklets. The coordinates of the primary vertex are re-calculated after a further selection on the tracklets based on their displacement from the first estimation of primary vertex (tracklets with distance $>$ 1 mm from the found vertex are removed).

The calculation of the vertex coordinate from a sample of selected tracklets is done by minimizing the quantity:

$$D^2 = \sum_i^N d_i^2 \tag{4.1}$$

where N is the number of tracklets used to calculate the vertex, d_i is the distance between the tracklet i and the vertex (x_0, y_0, z_0), weighted by the errors on the tracklets:

$$d_i^2 = \left(\frac{x_i - x_0}{\sigma_{xi}}\right)^2 + \left(\frac{y_i - y_0}{\sigma_{yi}}\right)^2 + \left(\frac{z_i - z_0}{\sigma_{zi}}\right)^2 \tag{4.2}$$

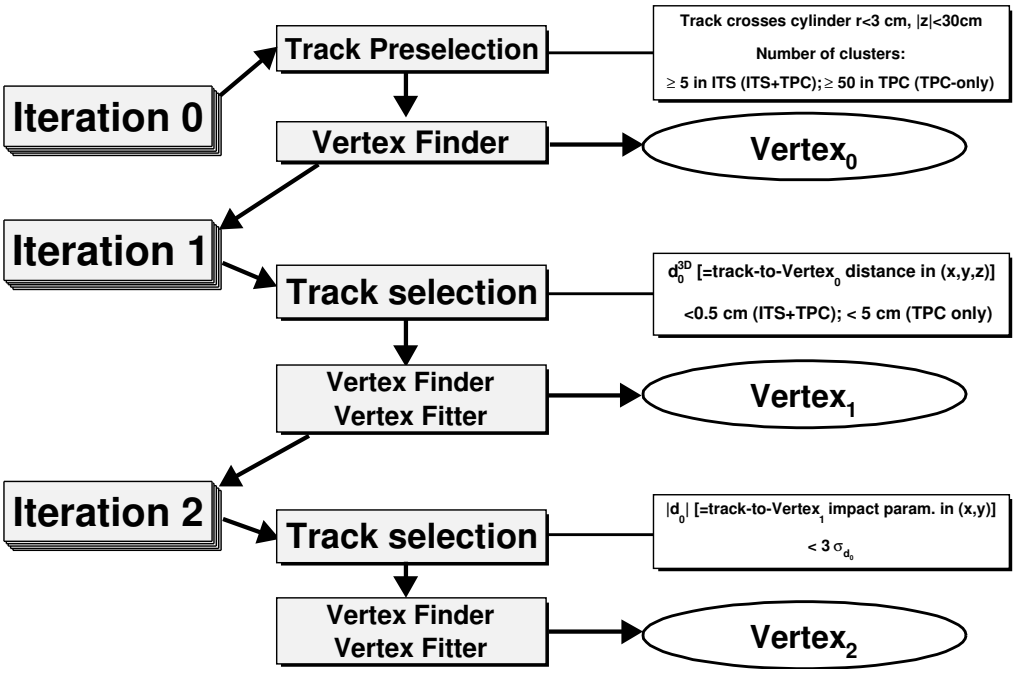

Figure 4.1: Scheme adopted for vertex reconstruction with tracks reconstructed with ITS and TPC detectors.

The entire procedure is repeated twice. In the first iteration a wide fiducial region is used for tracklet selection, while in the second iteration a smaller fiducial region centered on the position of the primary vertex found in the previous iteration is defined. Finally, an additional check on the position (the vertex must be located inside the beam pipe) and on the number of contributing tracklets (> 0) is performed.

The coordinates of the vertex are given with their errors, calculated from the weight matrix associated to each tracklet. The covariance matrix associated to the vertex is then given by inverting the sum over the N tracklets of the weight matrices.

If the vertex reconstruction with the VertexerSPD3D fails, the VertexerSPDz is called in order to avoid the rejection of the event. This happens mostly for the low multiplicity interactions, where the VertexerSPDz efficiency is larger than the VertexerSPD3D one.

4.1.2 VertexerTracks

A more precise determination of the primary interaction vertex can be obtained using tracks instead of tracklets, because the curvature is not known for tracklets.

In the VertexerTracks algorithm the primary vertex reconstruction is performed using tracks reconstructed in the whole ALICE central barrel (ITS+TPC).

The scheme used for vertex reconstruction is reported in Fig. 4.1: the procedure is performed in three iterations.

The first consists in a preselection of the tracks and in a rough preliminary vertex estimate ($vertex_0$) used as a starting point for the reconstruction. Tracks with insufficient number of associated clusters or not pointing to a fiducial cylinder with $r < 3$ cm (beam pipe radius) and $|z| < 30$ cm, are rejected at preselection stage.

Both subsequent iteration passes consist of three steps:

1. Track selection: the goal of this step is to reject displaced tracks.

2. VERTEX FINDING: a first estimate of the vertex position is obtained. This method does not require an accurate *a priori* vertex information. A specific vertex finding algorithm is also used at the track preselection stage.

3. VERTEX FITTING: tracks are propagated to the position estimated in the previous step and the optimal estimate of the vertex position, as well as the vertex covariance matrix and χ^2 are obtained via a fast fitting algorithm [138].

The information about the luminous region can be used as a constraint in this fit. Between the two last iteration passes, tighter requirements on the tracks are applied in order to select a cleaner sample of primary particles.

4.2 Online and offline vertex measurements in ALICE

The vertex position is one of the first measurements needed to understand the detector performance and to carry on physics analysis. Two tools are used for the online monitoring and determination of the beam spot position.

The Data Quality Monitor (DQM) is a tool built to check online the quality of the data during the data taking. An event is selected and from the raw data recorded, the very first available quantities are monitored using histograms that are updated online. The DQM system exploits some machines of the Data AQuisition (DAQ) to process online some of the information coming from the raw data. This includes reconstructing a first estimate of the beam positions and sizes. The algorithms used by the DQM system are the VertexerSPD3D and SPDz.

The vertex can be reconstructed online also within the High Level Trigger (HLT - Sec. 3.6). The HLT runs the same SPD algorithm used for the DQM.

On the 23rd November 2009, the LHC delivered the first pp collisions at $\sqrt{s} = 0.9$ TeV, the injection energy from the SPS. Two bunches with few 10^9 protons per bunch were injected in the LHC. The two bunches were brought into nominal position for collisions without a specific attempt to maximize the interaction rate. The first collisions candidate event that was shown in the counting room by the offline reconstruction software AliRoot [121], running in online mode is shown in Fig. 4.2.

Fig. 4.3 shows the online display of the vertex positions recorded with the HLT system, during the first run of the pp data taking at $\sqrt{s} = 0.9$ TeV on the 23rd November 2009.

During this very first data taking, the two beams were dumped after 43 minutes in order to complete the LHC commissioning program. In total 284 events were triggered and recorded during this short first run of the ALICE experiment with colliding beams.

Just after the end of the first data taking, the offline reconstruction of the events started. When the reconstruction finished, the analysis of the charged-particle pseudorapidity density at $\sqrt{s} = 0.9$ TeV started immediately.

The analysis is based on the information collected with the SPD detector in order to built the tracklets. The number of primary charged particles is then estimated by counting the number of tracklets, after applying corrections for trigger inefficiencies, detector and reconstruction inefficiencies and contamination by long-lived particles, gamma conversion and secondary interactions.

The analysis was possible also thanks to a fast quality assurance on the data, especially on the SPD pixel efficiencies and noise effects. Another important point was the rejection of the beam background coming from proton interactions with residual particles of the gas within the beam pipe.

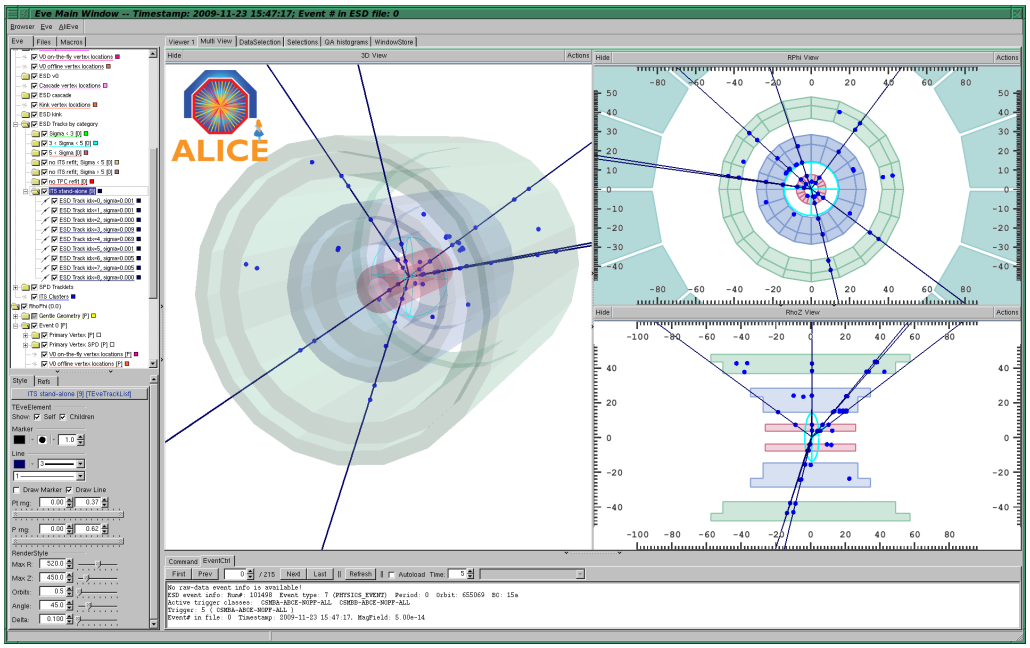

Figure 4.2: The first pp collision candidate at $\sqrt{s} = 0.9$ TeV shown by the event display in the ALICE counting room. The dots correspond to hits in the silicon vertex detectors (SPD, SDD, SSD), the lines correspond to tracks reconstructed using loose quality cuts. The reconstructed primary vertex is also visible in the figure (light blue ellipse) [141].

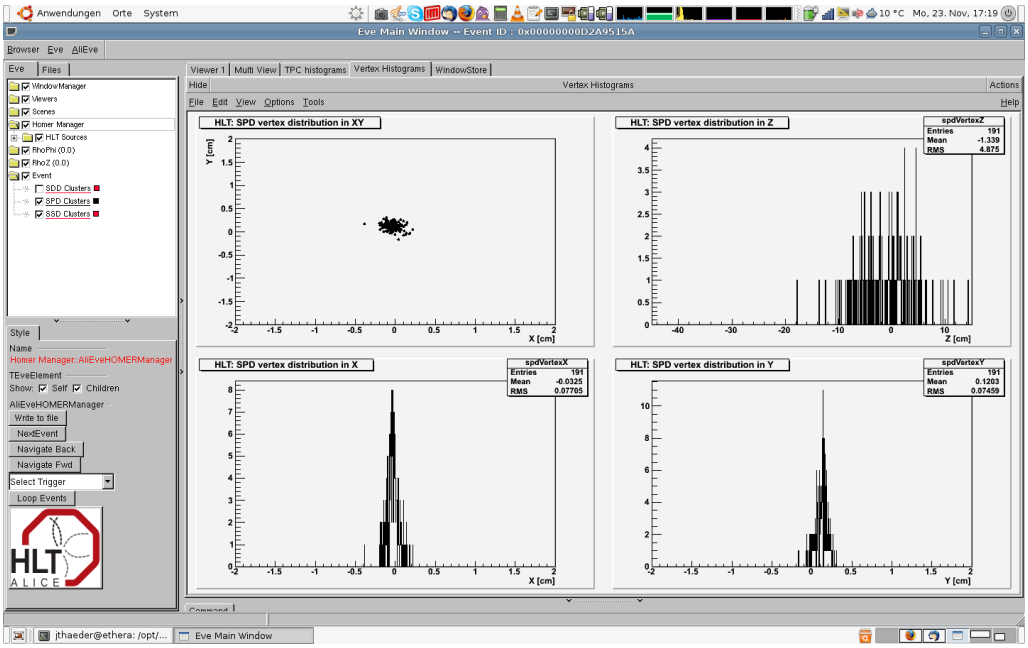

Figure 4.3: Beam spot position distributions for the three coordinates measured online, during the data taking of the first pp collisions at $\sqrt{s} = 0.9$ TeV.

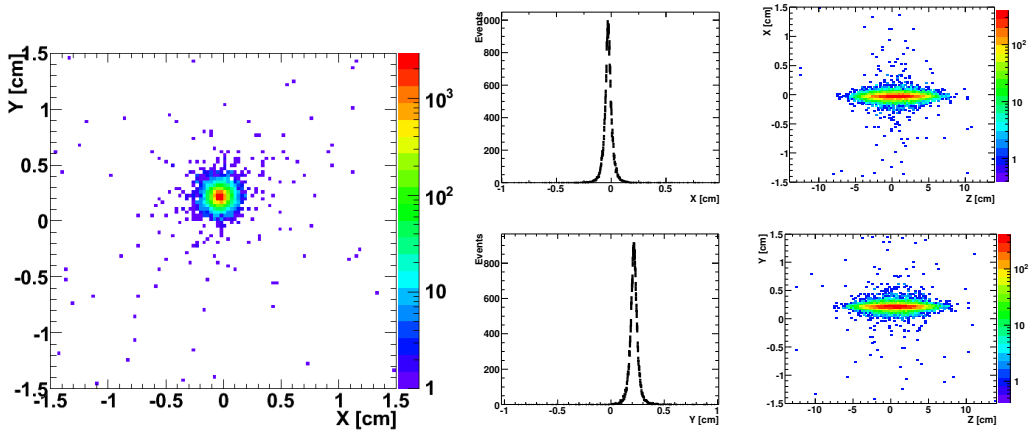

Figure 4.4: Beam spot measured offline with the VertexerTracks algorithm, in the first run of pp collisions at $\sqrt{s} = 7$ TeV collisions. Two dimensional beam spot in the xy plane (left), beam profile in xz and yz planes (right). Also the distributions in the transverse plane are shown [141],

The position and size of the beam spot were analysed offline for the full data sample, building the three Gaussian distributions used to describe the beam profile. Together with a complete description of the detector status, the primary interaction positions and sizes were set as input for the Monte Carlo simulation to reproduce the same conditions as during the data taking. This simulation was used to estimate the efficiency corrections that were applied to the raw tracklets counting, to recover the full number of charged particles produced in the collisions. This analysis allowed to publish the first paper with LHC data one week after the machine delivered the collisions [141].

Another important day for the LHC 2010 year was the 30th March, when LHC delivered the first pp collisions at 7 TeV. Also in that case the analysis of the multiplicity was fast and required a prompt quality assurance of the data as was done for $\sqrt{s} = 0.9$ TeV collisions [142]. Fig. 4.4 shows the beam spot in the xy plane and the two xz and yz profiles for the first 7 TeV data taking. For the xy case, the distribution represents the beam size without the deconvolution of the vertexer algorithms resolution.

The most important "starting" of the LHC for the ALICE experiment was the 7th November 2010, when the first Pb–Pb collisions were delivered at $\sqrt{s_{\rm NN}} = 2.76$ TeV. Fig. 4.5 shows the three gaussian distributions of the beam spot coordinates measured with the track vertex during the very first Pb–Pb data taking.

4.3 Vertex reconstruction performance

The performance of the vertexing algorithms was studied by measuring efficiencies and resolutions for different colliding systems and energies. Efficiency and resolution were studied as a function of the tracklets multiplicity of the events. Tracklets are defined as correlation of reconstructed points belonging to the first layer of the SPD with reconstructed points belonging to the second one within a small azimuthal window. The tracklets can be reconstructed in the pseudorapidity region $|\eta| < 1.6$. The number of tracklets in the events is proportional to the number of charged particles produced per rapidity unit ($dN_{\rm ch}/d\eta \sim 2 \times N_{\rm tracklets}$).

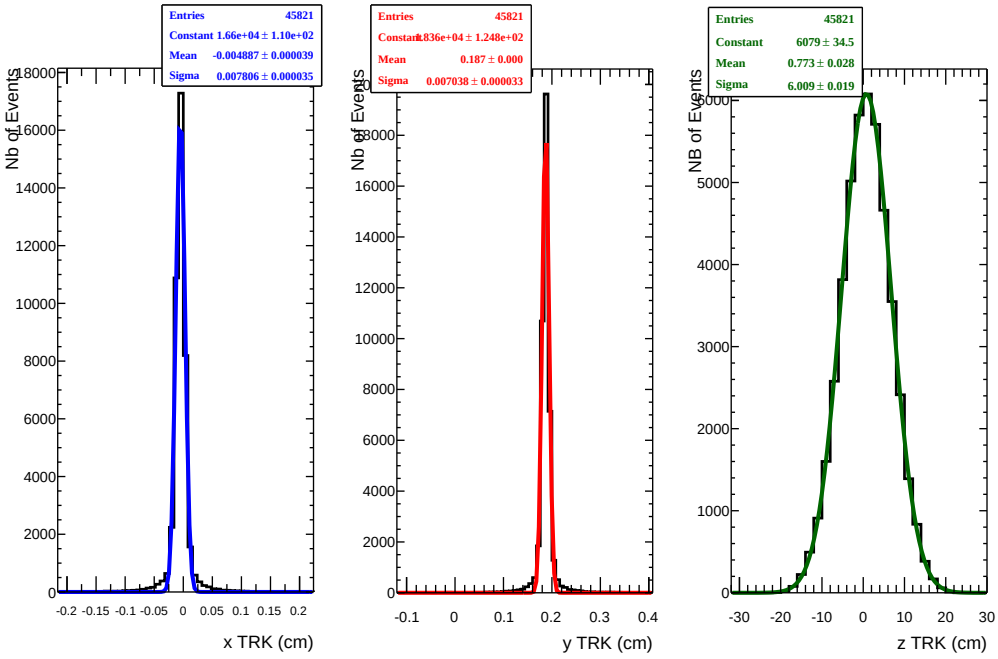

Figure 4.5: Primary vertices distributions in the three coordinates, measured in Pb–Pb collisions at $\sqrt{s} = 2.76$ TeV. The fit parameters are reported in the top panels; these values are taken as mean and r.m.s for the input of the Monte Carlo simulation, to recreate the same beam conditions.

Efficiency is defined as the fraction

$$\epsilon = \frac{reconstructed\ \&\ triggered}{triggered} \tag{4.3}$$

where the numerator is the number of triggered events in which the primary vertex has been found by the algorithm and *triggered* is the total number of triggered events after applying the beam background rejection cuts.

The resolution of the algorithms can be studied with two different methods: the vertex spread method and the half events method.

The *vertex spread method* is based on a study of the distribution of multiplicity of the event. The distribution of the beam size (Fig. 4.5) is the convolution of two different contributions: the vertexer algorithm resolution and the size of the luminous region ("diamond"), thus, the spread of the vertices is:

$$\sigma(N_{\text{tracklets}}) = \sigma_{D,\text{i}} \oplus \frac{\alpha_\text{i}}{\sqrt{N^{\beta}_{\text{tracklets}}}} \quad i = x, y, z. \tag{4.4}$$

In the Eq. (4.4) the parameter $\sigma_{D,\text{i}}$ refers to the dimensions of the luminous region, the second term of the equation refers to the resolution of the vertexer algorithm. This term has a square root dependency on the multiplicity, defined as the number of tracklets in the event. It was observed that it is useful to introduce a second parameter β in the term of the vertexer algorithm resolution so that the fit can better describe the data. The β parameter was found to be close to 1.

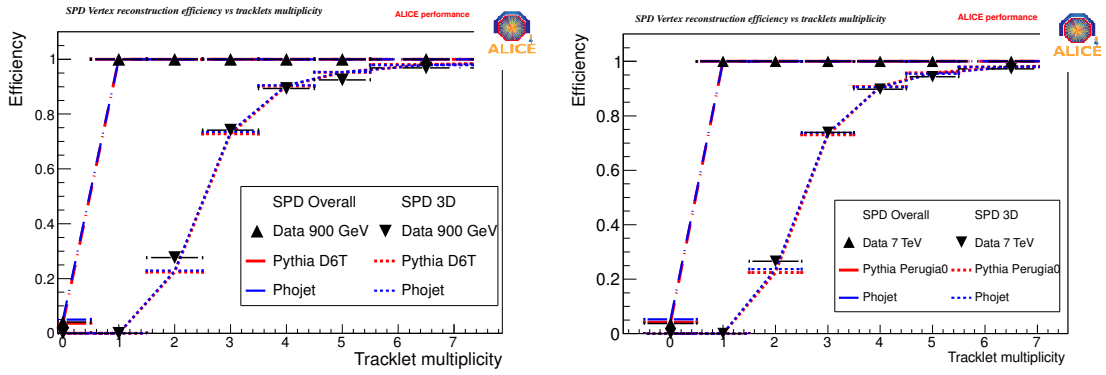

Figure 4.6: SPD vertex reconstruction efficiency as a function of tracklets multiplicity. VertexerSPD3D and overall SPD efficiencies are shown. Data are compared with two Monte Carlo simulations: PYTHIA D6T and Phojet. The right figure is for results in *pp* collisions at $\sqrt{s} = 0.9$ TeV, while the left figure is for $\sqrt{s} = 7$ TeV collisions.

Several multiplicity bins have been defined and for each of them the spread of the distribution of the vertex position was estimated by a Gaussian fit. These spreads then have been fitted with the function of Eq. (4.4).

The *half event method* is based on the separation of the tracks of the event in two sub-events. Two vertices for each event are then reconstructed, using only the tracks assigned to each sub-event. The spread of the differences in the positions of the two vertices is divided by $\sqrt{2}$ and studied as a function of the tracklets multiplicity of the sub-events.

The resolution can be estimated with a fit to the data: the information on the luminous region cannot be obtained with this method.

$$\sigma(N_{\text{tracklets}}) = \frac{\alpha_{\text{i}}}{\sqrt{N^{\beta}_{\text{tracklets}}}} \oplus K_{\text{i}} \quad i = x, y, z. \tag{4.5}$$

The half event method allows to estimate also the resolution in the z direction that cannot be measured with the vertex spread method, since the resolution on this coordinate is negligible as a function of multiplicity.

In the next sections results for the different vertexing algorithms will be shown, both in terms of efficiency and resolutions. Results are obtained using data collected in 2009-2010, in *pp* collisions at $\sqrt{s} = 0.9$ and 7 TeV, and Pb–Pb collisions at $\sqrt{s_{\text{NN}}} = 2.76$ TeV.

4.3.1 Performance in *pp* collisions

SPD vertex

The efficiency of the VertexerSPD3D is defined as in Eq. (4.3), by counting the fraction of trigger events with a reconstructed 3D vertex. When 3D fails, the more efficient VertexerSPDz algorithm is used. The overall SPD vertex efficiency is defined as the fraction of triggered events with 3D and Z vertex from SPD.

Figure 4.6 shows the two efficiencies of the SPD vertexers measured in *pp* collisions at $\sqrt{s} = 0.9$ TeV (left) and $\sqrt{s} = 7$ TeV (right). Data points (black symbols) are compared with two Monte Carlo simulation that use different generators. PYTHIA D6T tune [139]

and Phojet [140], shown with red and blu lines respectively. The comparison indicates a good agreement between data and simulation.

The overall efficiency is 100% for tracklet multiplicity larger than zero. In the low multiplicity region the largest contribution to the overall SPD efficiency comes from the VertexerSPDz.

The results on the multiplicity-integrated efficiencies for the two SPD algoritms are shown in Tab. 4.1. The 7 TeV efficiencies are larger than the 0.9 TeV one, because the mean multiplicity of the collision becomes larger with increasing energy.

Table 4.1: Vertex efficiencies integrated over multiplicity for in pp collisions at $\sqrt{s}$ = 0.9 TeV and $\sqrt{s} = 7$ TeV.

	900 GeV	7 TeV
3D reconstruction	0.65	0.76
3D + Z reconstruction	0.85	0.9

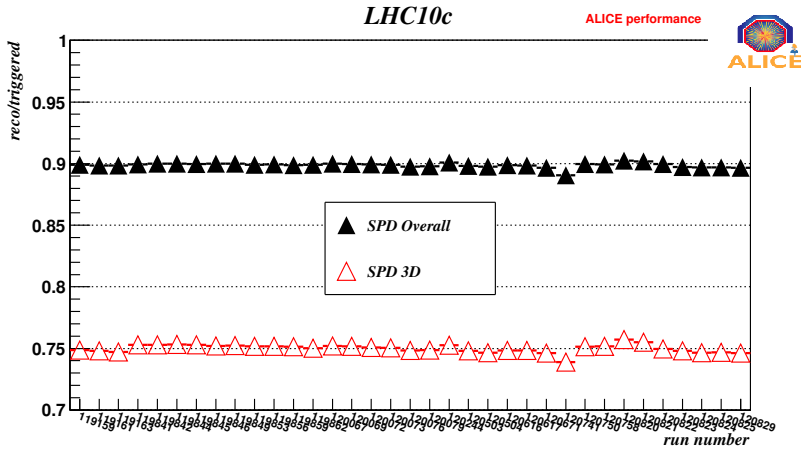

Figure 4.7: VertexerSPD3D and overall SPD efficiencies as a function of run for LHC10c periods.

The overall SPD efficiency and the VertexerSPD3D efficiency are shown in Figure 4.7 (right), integrated over multiplicity and as a function of the run number. The time dependence is quite flat, pointing to a good stability of the reconstruction of the primary vertex using SPD tracklets, over a wide time period (data collected between May 2nd, 2010 and 27th May, 2010 are shown).

The vertex spread method allows, in principle, to measure the resolution of the vertexer algorithm and the contribution of the luminous region with Eq. (4.4). As described in the general part of this section, the parameters obtained with the fit on the data should be related to the two different contributions. For the VertexerSPD3D this is not the case, since the resolution is much larger than the luminous region size, also for high multiplicity events ($\alpha/\sqrt{N_{\text{tracklets}}} >> \sigma_{\text{D}}$). Therefore it is not possible neither to extract the vertexer resolution parameters (α and β). The size of the luminous region was fixed to the value expected one measured with the VertexerTracks algorithm (see next section).

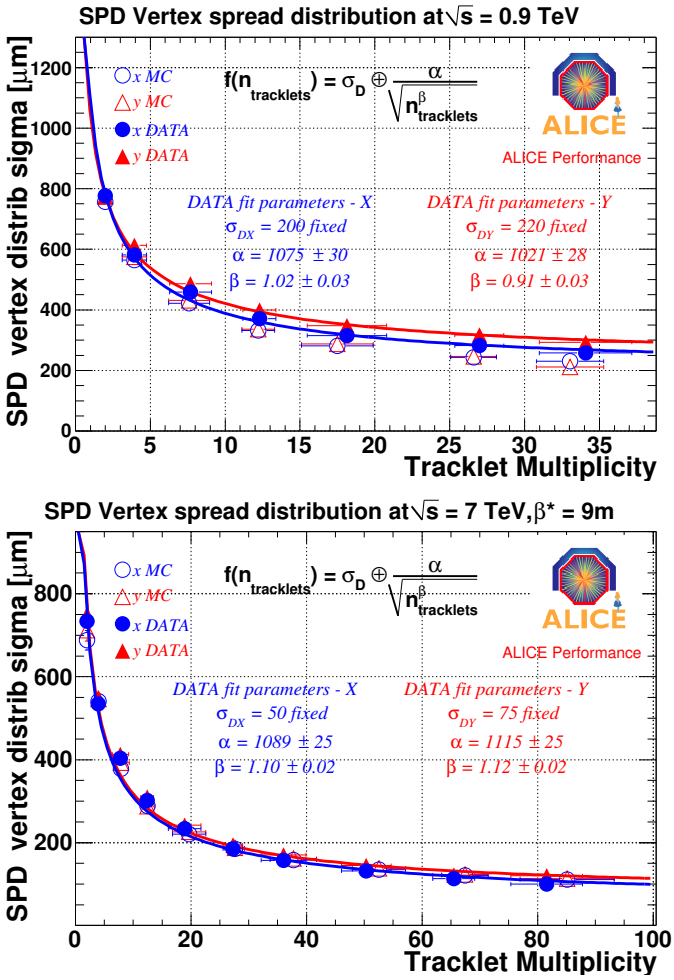

Figure 4.8: SPD3D vertexer resolutions measured at $\sqrt{s} = 0.9$ TeV (top) and $\sqrt{s} = 7$ TeV (bottom). For both cases the results are compared with those obtained with PYTHIA D6T [139] Monte Carlo simulation.

Results for 0.9 TeV are shown in Fig. 4.8 (top). The α parameter indicates a resolution of about 200 μm for events with 20 tracklets and the β parameter is around one. The agreement between data and Monte Carlo simulations is very good.

For 7 TeV data, the vertexer resolution parameters are compatible with the measurement at 0.9 TeV and the agreement with Monte Carlo is good (Fig. 4.8). The β parameter is slightly larger than one indicating a small deviation from the dependency $\propto 1/\sqrt{ntracklets}$.

VertexerTracks

The VertexerTracks efficiency is shown as a function of the number of SPD tracklets in Fig. 4.9 for 0.9 TeV data and Monte Carlo (left) and for 7 TeV data and Monte Carlo (right). The efficiency is evaluated in two different cases:

- using the beam position as a constraint in the algorithm of vertex fitting ("with constraint" curve), as will be described in Sec.4.4;

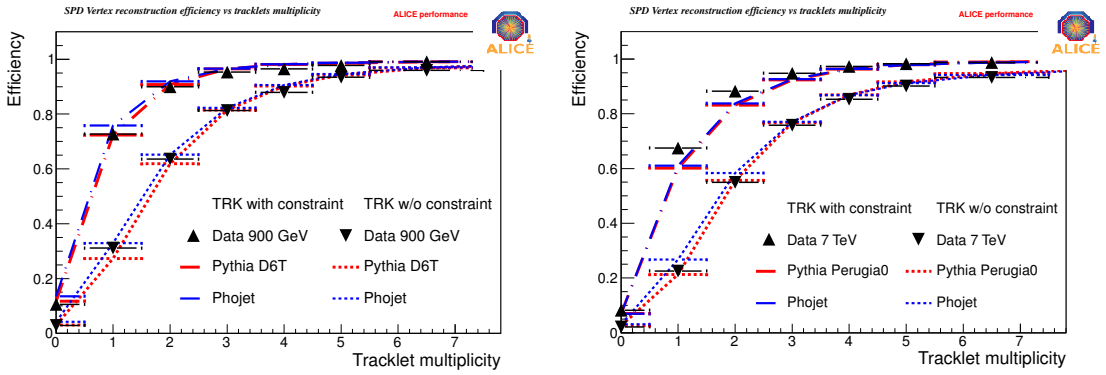

Figure 4.9: VertexerTracks efficiency as a function of tracklets multiplicity - 0.9 TeV (left), 7 TeV (right). Full symbols represent data and lines represent Monte Carlo simulations. The results are presented with and without applying the constraint to the luminous region.

- without using this information as a constraint in the fit ("w/o constraint" curve).

Simulation results with PYTHIA and Phojet prediction are reported as dotted lines. Results show that the efficiency becomes close to 100%, for events with 5 tracklets in case of reconstruction without constraint, for both energies. The constraint with the beam position enhances significantly the efficiency, especially in the low multiplicity region, bringing the efficiencies to 100%, for events with 2-3 tracklets. The VertexerTracks efficiencies integrated over multiplicity are reported in Table 4.2. As expected, 7 TeV efficiencies are larger than 0.9 TeV ones.

Table 4.2: 0.9 TeV and 7 TeV VertexerTracks efficiencies integrated over multiplicity.

	0.9 TeV	7 TeV
Vertex-track efficiency - with constraint	0.81	0.87
Vertex-track efficiency - without constraint	0.71	0.78

The VertexerTracks efficiency as a function of the run number is shown in Fig. 4.10 for the same period considered for the SPD vertex. Also in this case, the run-dependence is quite flat, hence the vertex reconstruction using tracks is a tool with good stability.

Considering the optics parameters of the beams, at $\sqrt{s} = 0.9$ TeV, the size of the transverse luminous region was expected to be of about 200 μm. Fig. 4.11 shows the comparison between data an Monte Carlo for the resolution of the VertexerTracks, measured with the vertex spread method. The agreement between data and simulations is very good. There is a difference in the measured luminous region size for the two transverse coordinates ($\sim$ 51 μm for x, $\sim$ 74 μm for y). This difference was also confirmed by the other LHC experiments, and it is due to slightly different optical parameters for the beam 2. The β parameter, introduced to better describe the data, is very close to one at this energy. The luminous region size is smaller for higher $\sqrt{s}$.

A comparison of the resolution between the VertexerTracks and VertexerSPD3D is shown in Fig. 4.12. For a sample of pp collisions at $\sqrt{s} = 7$ TeV with a $\beta^* = 2$ m. The VertexerTracks (full symbols) has a resolution about a factor of 2 better than the SPD3D

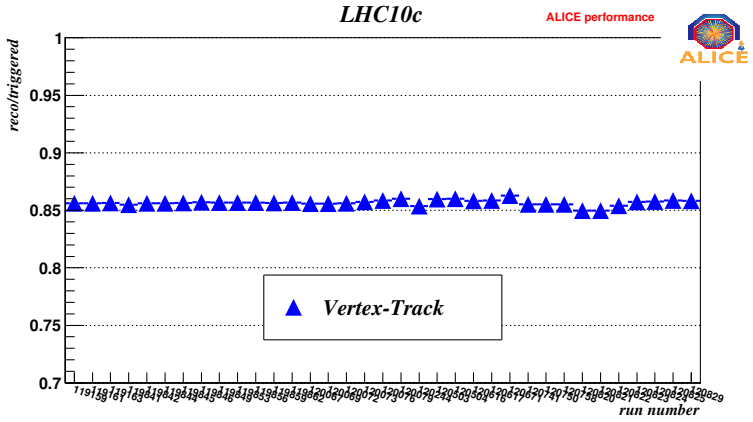

Figure 4.10: VertexerTracks efficiency (with constraint on the beam position) as a function of run for the LHC10c period.

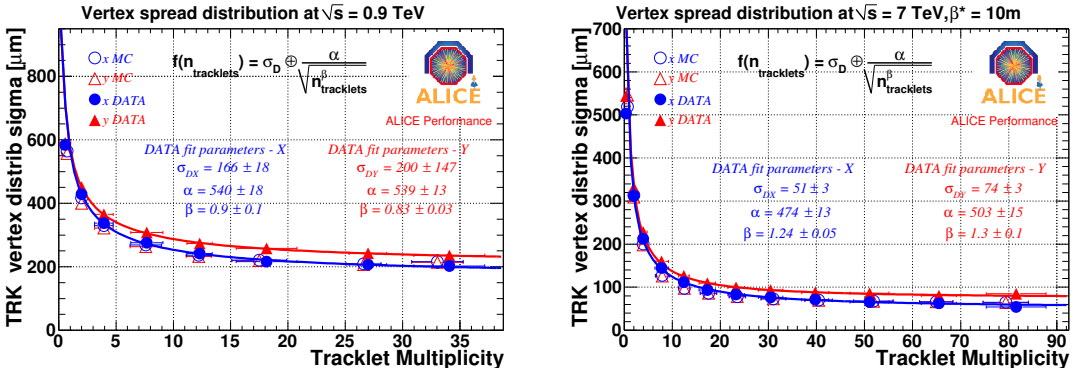

Figure 4.11: VertexerTracks resolution measured at 0.9 (left) and 7 TeV (right) with the vertex spread method. Results from the fit, on the luminous region measurement are reported in the graph for both coordinates.

one. The VertexerTracks allows to measure the luminous region, that for this optical parameters is about 30 μm.

For the VertexerTracks, it is possible to estimate the resolution also using the half event method as explained in the introduction of this section. Fig. 4.13 (left) shows the results for pp collisions at $\sqrt{s} = 0.9$ TeV. The resolutions are in agreement with PYTHIA D6T tune [139] simulations and are lower than 200 μm for events with about 10 tracklets. At higher energy, the resolution is better, gaining a factor of 2 due to the higher multiplicity of the event (Fig. 4.13 right). The resolution in the z coordinate is comparable with the x one. This shows that the resolution of the vertexer is negligible in the measurement of the luminous region in this coordinate, which is of a few centimeters.

4.3.2 Vertexer results in Pb–Pb collisions

The same vertexing algorithms were also applied to Pb–Pb collisions at $\sqrt{s_{\rm NN}} = 2.76$ TeV. Due to the high multiplicity environment, however, the strategy was optimized to speed-up the reconstruction procedure.

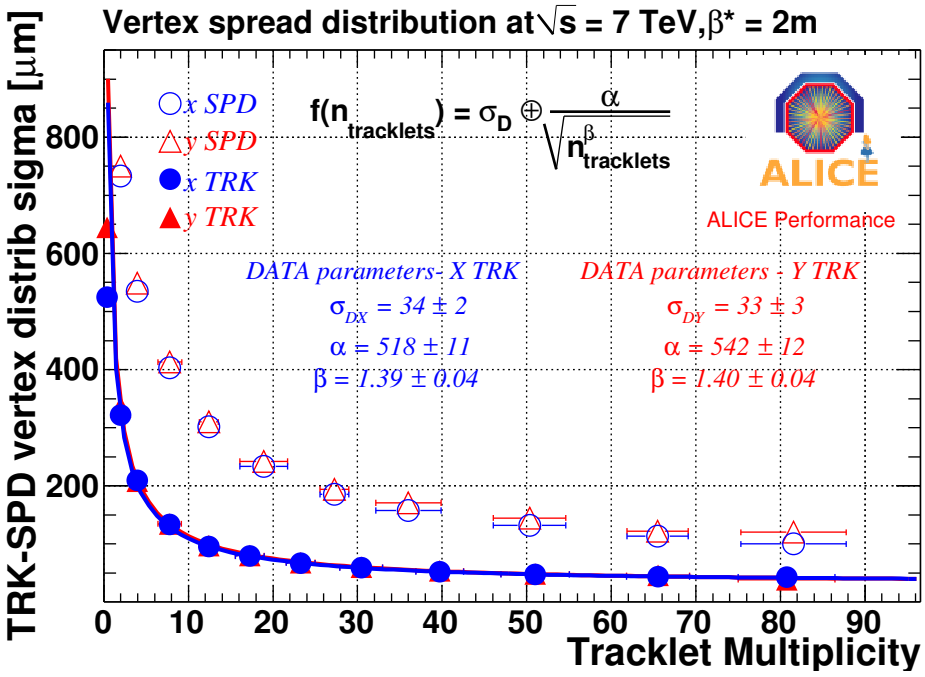

Figure 4.12: Comparison between the VertexerTracks and SPD3D vertexers resolutions. The VertexerTracks resolution is better by about a factor 2 with respect to the SPD3D one and it allows to measure the luminous region down to 30 μm.

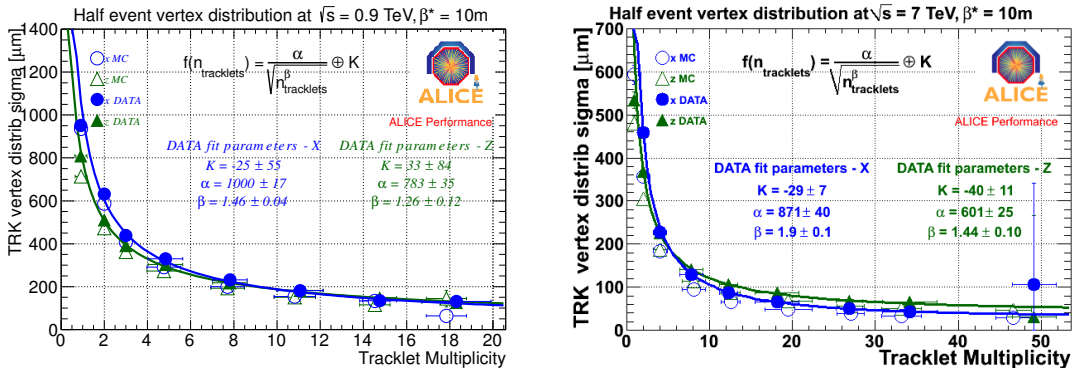

Figure 4.13: Resolution measured with the half events method for 0.9 (left) and 7 TeV (right) collisions. No measurement of the luminous region is possible with this method but the resolution in the z coordinate can be studied as a function of tracklets multiplicity.

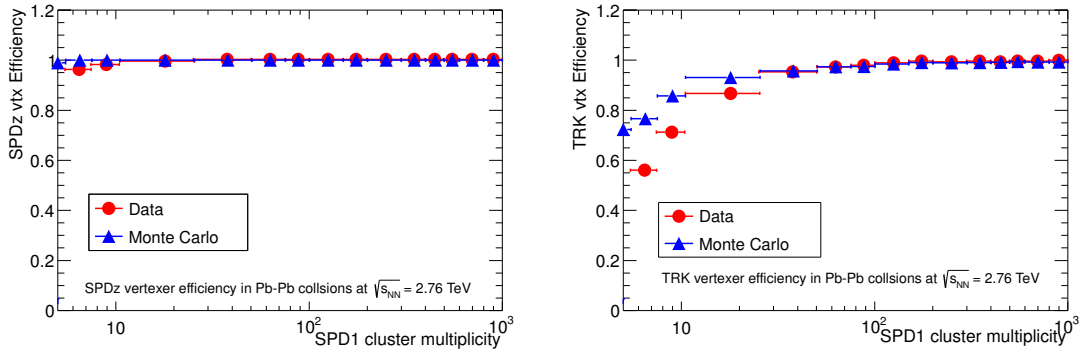

Figure 4.14: Efficiency for VertexerSPDz reconstruction (left) and VertexerTracks reconstruction (right) as a function of the number of hits in the second layer of the SPD (SPD1). This quantity is directly related to the centrality class to which the event belongs. Efficiency is 100% for both cases for events with centrality in 0-80%.

During the Pb–Pb collisions data taking, the online SPD3D vertexer was activated after applying a random selection on the sectors of the SPD used to compute the tracklets. This method allowed to reduce the combinations of tracklets and, therefore, the time required to measure online the 3D interaction point.

In the offline reconstruction, it was decided to switch off the reconstruction of the VertexerSPD3D and rely on the online measurement for the x and y coordinates. The VertexerSPDz was activated in the offline reconstruction, together with the VertexerTracks algoritm. Since only very peripheral events have low multiplicity, a vertex reconstructed with tracks should be computed for almost all events.

The results of the vertexers performance will be presented, as for the *pp* case, in terms of efficiencies and resolutions, computed with the methods introduced in Sec. 4.3.

Besides what was done in the *pp* analysis, the Pb–Pb efficiency study was performed as a function of number of hits in the second layer of the SPD (SPD1). This quantity is proportional to the centrality of the collision.

Fig. 4.14 (left) shows the efficiency for the VertexerSPDz measured as a function of the multiplicity of hits in the second layer of the SPD detector. A multiplicity between 70 and 110 hits in this layer of the SPD defines an event in the centrality class 70-80%. The vertex algorithm efficiency is 100% for all centrality classes.

Fig. 4.14 (right) shows the efficiency for the vertexer that uses tracks. Taking the same multiplicity bin as for the SPDz case, the efficiency is 98% for the lower side of the multiplicity bin (70 hits in SPD1).

For both vertexer algorithms the efficiency flatten at one for more central events. In both cases, data are compared with Monte Carlo simulation using the HIJING [136] generator. The comparison shows good agreement between data and simulation for $N_{\text{hits}} > 25$.

Resolutions are estimated for the VertexerTracks algorithm using the two data driven methods described in the introductory section: the vertex spread method and the half event method.

Fig. 4.15 (top) shows the spread of the distribution of the vertex as a function of the tracklet multiplicity of the event. Above 100 tracklets, the distributions get flat around the luminous region sizes, since the vertexer algorithm resolutions become negligible at

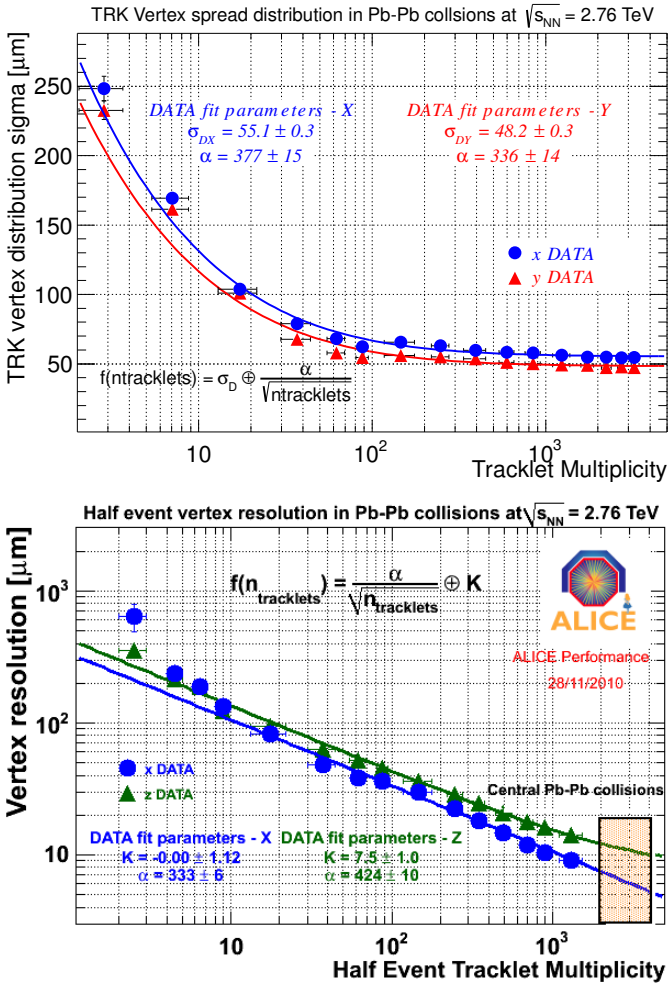

Figure 4.15: Resolution of the VertexerTracks algorithm measured with the vertex spread method (top) and the half events method (bottom) at $\sqrt{s_{\rm NN}} = 2.76$ TeV in Pb–Pb collisions. From the first method it is possible to measure the luminous region, from the second the extrapolation of the vertexer resolution for central events for the three coordinates.

such high multiplicity. A difference in the two coordinates for the luminous region size is visible: about 55 μm for x and 48 μm for y.

Fig. 4.15 (bottom) shows the results obtained with the half events method. Circles refer to the x coordinate and triangles to the z coordinate. The resolution is shown as a function of the half-event multiplicity and fitted with the same function used also for the pp case. From the fit, it is possible to extrapolate the value of the vertexer resolution for the most central events. Extrapolating the resolutions to twice the multiplicity of the half events constructed from central collisions, the resolution on the vertex position is found to be smaller than 10 μm (orange box) for central Pb–Pb collisions.

4.4 Mean vertex constraint

The mean vertex determination is important to apply the luminous region constraint and improve the resolution on the event-by-event interaction point position. The mean vertex

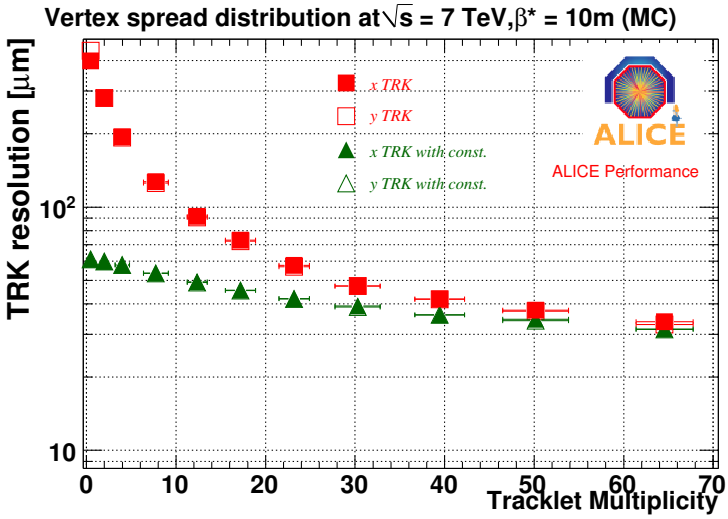

Figure 4.16: VertexerTracks resolution measured with and without applying the beam constraint on the tracks. The application of the knowledge of the luminous region size allows to improve the resolution for low multiplicity events, from 200 to less than 60 μm.

determination is part of the calibration procedure of the ALICE computing model.

The calibration scheme, also called "calibration pass0 - cPass0", is based on the reconstruction of 10% of the statistics of a run[1]. This sub-sample is used to extract the calibration parameters for that run, which will be used during the full reconstruction pass.

The Mean Vertex determination is a part of the schema. In case the VertexerTracks fails, the VertexerSPD3D is used. The reconstructed vertices of these events are used to fill histograms that are then fitted using Gaussian functions, one for each coordinate. From the Gaussian fits, the mean positions of each coordinate are measured, together with the r.m.s for the z coordinate. In case of pp collisions, the transverse size of the luminous region is determined using the method described in the previous section using Eq. (4.4). To measure the luminous region it is necessary to separate the vertex algorithm resolution from the luminous region contribution. This procedure has to be applied to pp collisions because the vertexer algorithm resolution can be relevant also for high multiplicity events (tracklet multiplicity ~ 60). For Pb–Pb collisions, no deconvolution is needed, since in the high multiplicity events the contribution of the vertexer resolution is negligible (tracklet multiplicity ~ 200).

The measured values are used to define a Mean Vertex object that the calibration procedure writes to the OCDB.

The Mean Vertex object is then applied as a constraint in order to exploit the knowledge of the beam position to improve the vertexer algorithm resolution. Fig. 4.16 shows, with a Monte Carlo study, the improvement in the vertexer resolution that is achieved using the beam constraint. In this case a luminous region size of 60 μm is considered. The resolution is measured as the spread of the difference between generated and reconstructed vertex position. The resolution improves from more than 200 μm, down to about 60 μm

[1] A run is defined as a period of online data taking, the run number is an ALICE convention to define a data sample. Runs are grouped in periods going from one LHC technical stop to another.

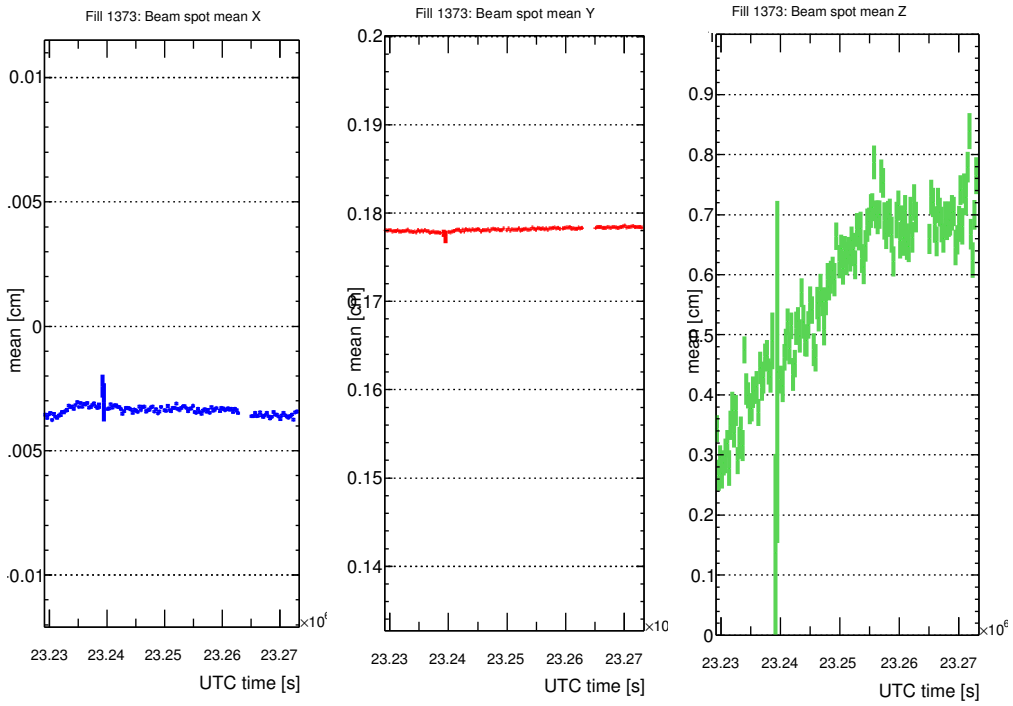

Figure 4.17: Beam spot position measured in one LHC fill lasted 12 hours of pp collisions at $\sqrt{s} = 7$ TeV. Each measurement is done summing the events collected in 6 minutes.

(the luminous region size) for events with low multiplicity.

Also the efficiency for the VertexerTracks are improved at low multiplicity as it was shown in Fig. 4.9.

4.5 Monitoring of the beam spot parameters

The beam spot parameters have to be monitored to guarantee a good data taking and to give feedback to the machine experts, so that they can study effects on the orbit of the beams or on the beam positioning counters that are placed in the accelerator. Also the effect of the growing of the emittance with time can be studied with a monitoring of the beam parameters during the full LHC fill.

LHC experts asked the four experiments to provide feedback on:

- beam positions: x, y, z coordinates obtained from the Gaussian fit of the distributions;
- beam size: the r.m.s of the interaction points distributions;
- luminous region: the beam size de-convoluted from vertexer algorithm resolution effects.

One file with these quantities and their associated error is delivered to the LHC experts for each fill of hadrons within the machine. The beam spot parameters are studied as a function of time, performing a measurement every 6 minutes. For pp collisions, the

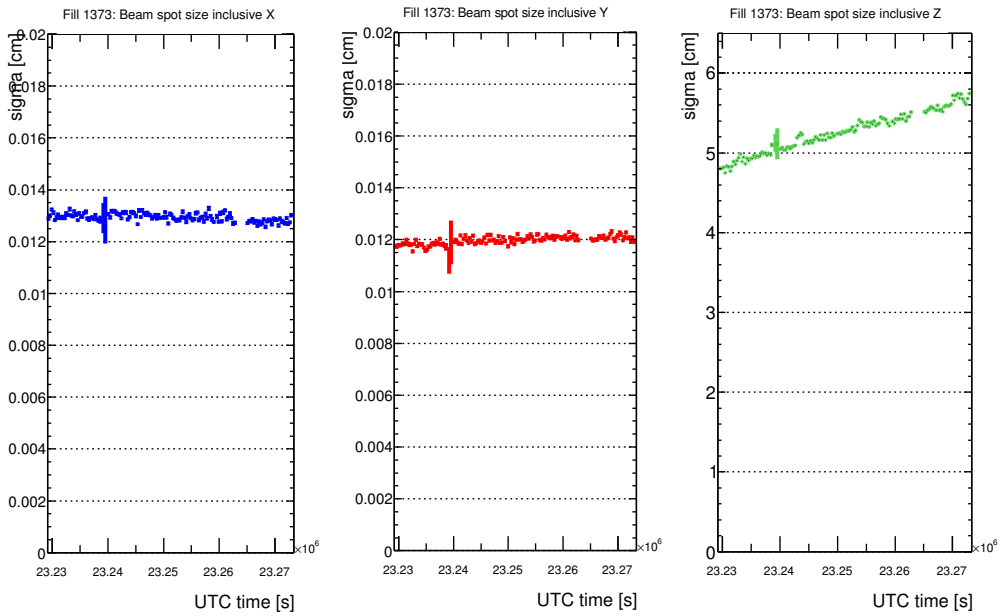

Figure 4.18: Beam size measured in one LHC fill lasted 12 hours of pp collisions at $\sqrt{s} =$ 7 TeV. Each measurement is done summing the events collected in 6 minutes.

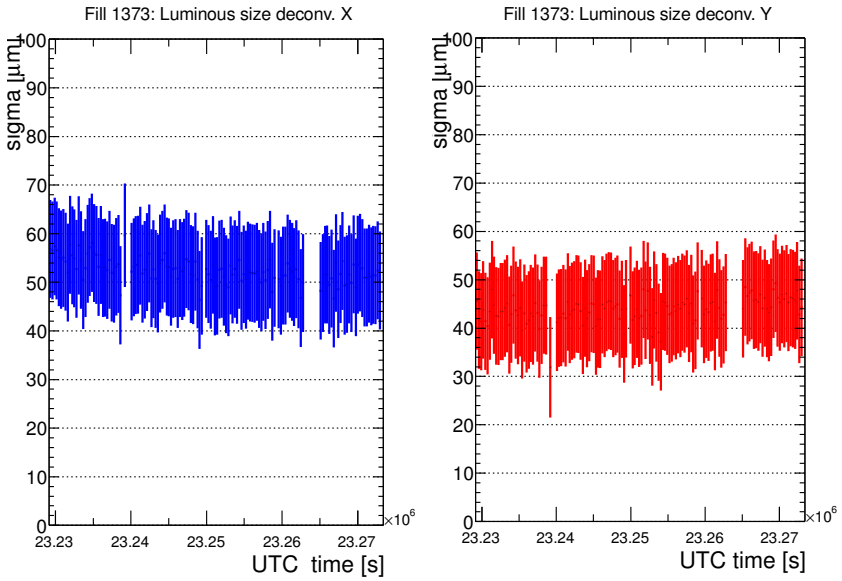

Figure 4.19: Luminous region measured in one LHC fill lasted 12 hours of pp collisions at $\sqrt{s} = 7$ TeV. Each measurement is done summing the events collected in 6 minutes.

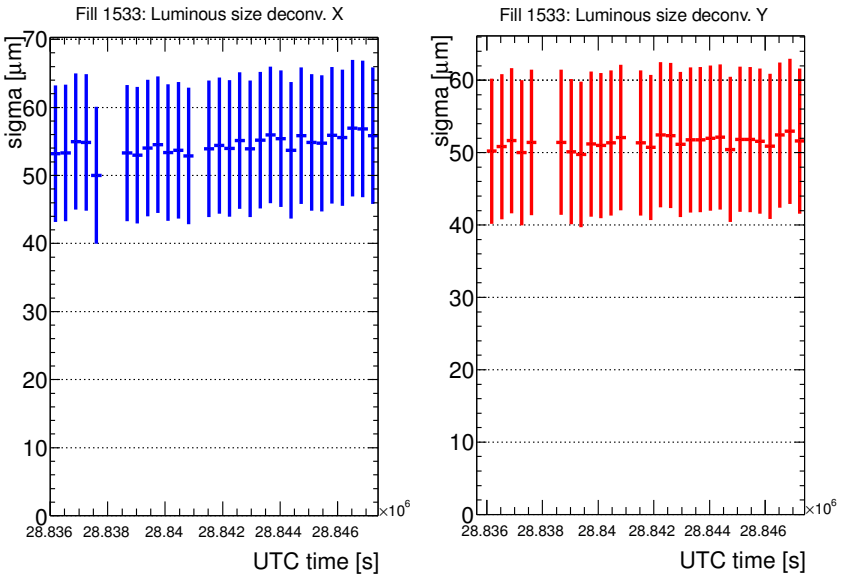

Figure 4.20: Luminous region measured in one LHC fill lasted 8 hours of Pb–Pb collisions at $\sqrt{s} = 2.76$ TeV.

luminous region has been estimated using the spread vertex method (as described in Sec. 4.3). For Pb–Pb collisions, no deconvolution is needed, since central events have a number of tracks such that the algorithm resolution is negligible with respect to the luminous region size. In order to estimate the luminous region in Pb–Pb collisions, a simple cut on the multiplicity of the event is applied: for those events the beam size and the luminous region coincide. Fig. 4.17 shows the trend of the position of the beam spot as a function of time[2], for the fill 1373 taken in the night between the 26th and the 27th September 2010. This fill lasted 12 hours. Fig. 4.18 shows the beam sizes of the three coordinates. The position of the collisions in x and y is very stable over the full fill, with maximum variation around 10 μm. The x coordinate is close to the nominal centre of ALICE, while the y coordinate is shifted by 1.8 mm. The z position drift is related to the emittance growth that clearly affects also the z size: during the fill, the beam size in that coordinate increases of about 1 cm. The beam sizes in x and y directions are stable around 120 μm.

Fig. 4.19 shows the luminous region for the same pp fill for which position and size were shown. The luminous region in the x coordinate is about 55 μm, in y about 10 μm less. The uncertainties on the luminous region are computed in a conservative approach considering the uncertainties on the variation parameters of the resolution fit function.

Fig. 4.20 shows the luminous region measured in Pb–Pb collisions for a part of fill 1533. This fill was taken the 30th November 2010 and it lasted 8 hours. The value of the luminous region are similar as for the pp case.

For both cases, only x and y were shown since the luminous region for the z coordinate coincides with its size. In the z direction the vertexer resolution is negligible with respect to the interaction region spread, which is of the order of 6 cm.

Fig. 4.21 shows a comparison of the four LHC experiments measurements of the lu-

[2]The time shown in the plot is the UTC time in second at Geneva time

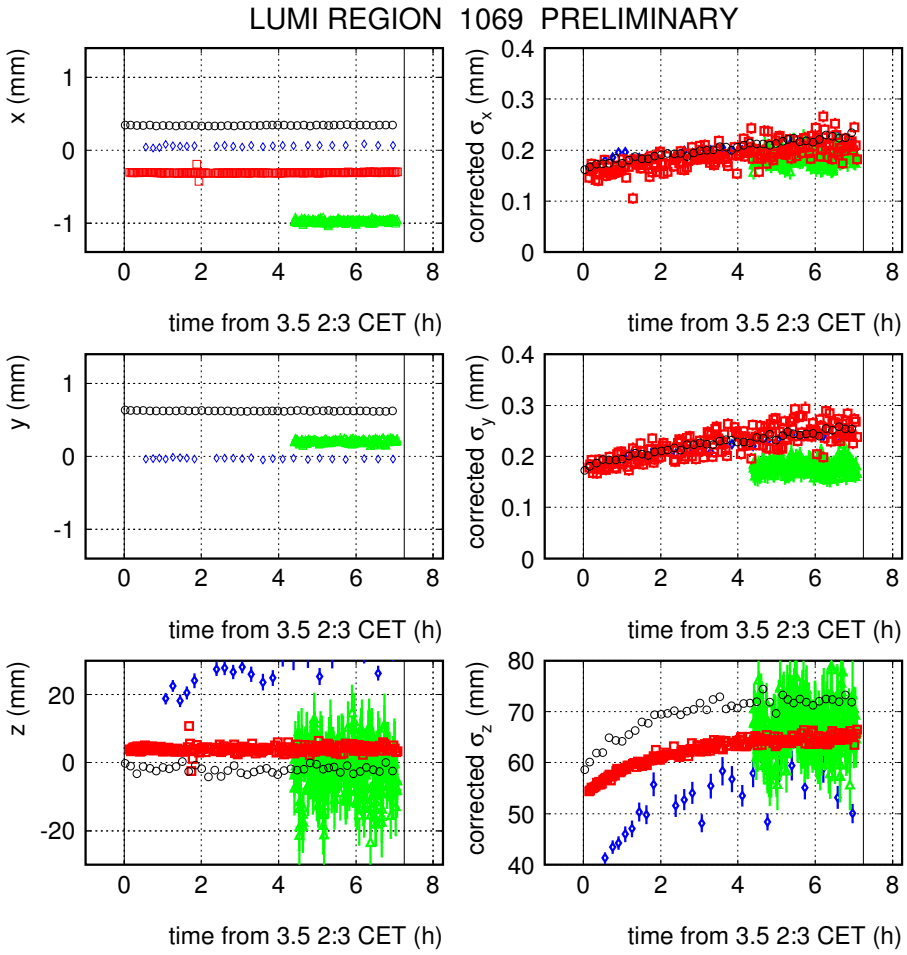

Figure 4.21: Comparison pf the luminous region position and sizes for the four LHC experiments: ALICE (red), ATLAS (black), CMS (green), LHCb (blue).

minous region positions and sizes. The ALICE data points are the red symbols. The positions of the interaction points are slightly different for each experiment, mainly due to the orbits of the beams. The luminous region sizes (especially in x and y) are comparable.

5 $\mathrm{D}^0 \to \mathrm{K}^-\pi^+$ reconstrunction in Pb–Pb collisions

This chapter is mainly dedicated to the description of the D^0 analysis performed in Pb–Pb collisions with the ALICE experiment. The goal of the analysis is the measurement of the D^0 invariant yields, that constitue the numerator of the nuclear modification factor (described in the next chapter).

In the first part of the chapter, the general strategy for D meson analysis will be introduced in its different parts. The characteristics of the typical weak charm decay will be also described, together with the steps followed to perform to the cross section measurement.

The strategy for the D^0 meson reconstruction in Pb–Pb collisions will be discussed in the second section. The $\mathrm{D}^0 \to \mathrm{K}^-\pi^+$ decay kinematic will be described, as well as the Monte Carlo comparison between the selection variables in signal and background candidates that will be used to select the former. A detailed description of the different steps as the raw yield extraction, the efficiencies calculations and the feed down correction method will be also given. The second section will end with a description of the systematic errors study and the results on the invariant yield of the D^0 in Pb–Pb collisions.

The last part of this chapter will be devoted to the results obtained, with the same analysis procedure, in *pp* collisions at $\sqrt{s} = 7$ TeV and at $\sqrt{s} = 2.76$ TeV and to the results on the total charm production cross section.

5.1 D mesons reconstruction strategy in ALICE

A common strategy has been defined to measure D mesons within the ALICE experiment. The analysis strategy is based on an invariant mass analysis of reconstructed pairs or triplets of tracks (also called candidates) that could be the products of a D meson decay. Candidates should be displaced from the primary vertex and come from a reconstructed secondary vertex. The p_{t}-dependent cross section is computed starting from the raw signal yield extracted with an invariant mass analysis. These yields are then corrected using efficiencies computed with a Monte Carlo simulation. An additional correction is then estimated in order to consider only prompt D mesons. The absolute normalization is then performed. The yields can be computed from the formula:

$$\left.\frac{\mathrm{d}N^{\mathrm{D}^0}}{\mathrm{d}p_{\mathrm{t}}}\right|_{|y|<0.5} = \frac{1}{2}\frac{1}{\Delta y\,\Delta p_{\mathrm{t}}}\frac{\left. f_{\mathrm{prompt}}(p_{\mathrm{t}}) \cdot N^{\mathrm{D}^0\ raw}(p_{\mathrm{t}})\right|_{|y|<y_{\mathrm{fid}}}}{(\mathrm{Acc}\times\epsilon)_{\mathrm{prompt}}(p_{\mathrm{t}}) \cdot \mathrm{BR} \cdot N_{\mathrm{evt}}}\,. \tag{5.1}$$

where the different terms in the formula will be explained in the following.

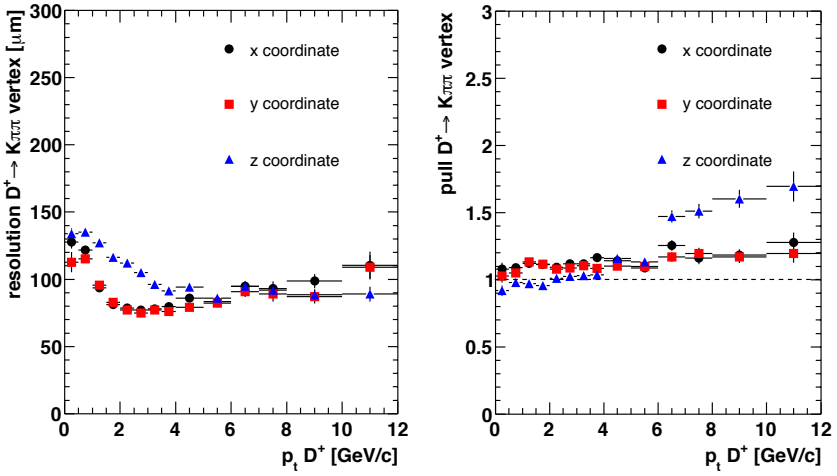

Figure 5.1: $D^+ \to K^-\pi^+\pi^+$ secondary vertex resolution (left) and pulls (right) for the x, y and z coordinates as a function of the p_t of the D^+.

Secondary vertex reconstruction

Tracks are grouped in pairs (for D^0) or triplets (for D^+, D_s^+, Λ_c and so on) following the charge ordering of the decay channel, defining objects called "candidates". For each candidate a secondary vertex is computed as the point of closest approach between the two (or more) reconstructed tracks.

The algorithm for the reconstruction of secondary vertices originated by n-prongs decay ($n > 2$) is the same as the one described in Sec. 4.1.2, to find the primary vertex position using tracks. Tracks are approximated as straight lines close to the primary vertex. This approximation can produce a significant worsening in the measurement of the displaced vertex; to avoid this situation a distance d between the secondary vertex and the straight line is considered to measure the discrepancy between the helix and the tangent line.

Fig. 5.1 shows the secondary position resolution and pulls as a function of the p_t of the D^+ (taken as example). At low p_t the daughter tracks are affected by multiple scattering and resolution worsten. For intermediate p_t the resolution is about 70 μm. It worsten at higher p_t due to the increased momentum of the charmed particle and therefore its decay products get more collinear with the meson flight line direction.

Raw signal extraction $N^{D^0\ raw}(p_t)$

The invariant mass analysis is based on a "cut" and count approach in which candidates are selected on the basis of typical kinematical and geometrical properties that characterize the single tracks and the reconstructed secondary vertices. The high tracking spatial precision provided by the ITS detector (Sec. 3.4.1) allows to reconstruct the primary vertex position with high precision and, then, to tag displaced tracks with distances to the interaction point of few tens of microns. Measuring the separation between the primary and the secondary vertices is the key point to select signal candidates among the huge number of those obtained by combinatorial background associations. The variables used to select the signal are described in the next section, considering those for the $D^0 \to K^-\pi^+$ decay channel that is the case under study for this thesis.

The signal extraction is based also on Particle IDentification (PID) information provided mainly by the TOF (Sec. 3.4.2) and the TPC (Sec. 3.4.1). Detectors PID is mainly used to select candidates with one track identified as a kaon.

The invariant mass distribution, obtained after applying topological cuts and PID, is fitted to extract the raw signal yield ($N^{\mathrm{D\ raw}}(p_{\mathrm{t}})$). The fitting function is made up of a Gaussian term to describe the signal and an exponential or polynomial function to model the background.

Correction for detector acceptance and selection reconstruction and efficiency $(\mathrm{Acc} \times \epsilon)_{\mathrm{prompt}}(p_{\mathrm{t}})$

In order to compute the total number of D mesons produced and decayed, the raw yield is divided by a correction factor $(\mathrm{Acc} \times \epsilon)$ that considers the efficiency of the tracking and candidates selection cuts and detector acceptance. This efficiency factor is estimated using Monte Carlo simulations that describe at the relative per cent level the detector geometry and response.

Feed down correction f_{prompt}

Due to the high energy of the LHC collisions, the fraction of D mesons that come from B mesons decay is large, especially for high p_{t}. From FONLL calculations [50] the cross section for a prompt D^0 of about 8 GeV/c is comparable with a D^0 of about 5 GeV/c coming from a B decay (Fig. 2.1 right). From FONLL calculations, at low p_{t} the fraction of secondary D mesons should be around 5% but the uncertainties on this value are quite large, reaching a lower value around 12%. For higher-pt D mesons ($p_{\mathrm{t}} = 15$ GeV/c for example) the fraction of feed-down is around 15%.

Due to the large lifetimes of B mesons ($c\tau \sim 460 - 490\ \mu m$), the applied selection cuts enhances the contribution of secondary D mesons. It is important then to take into account this component and subtract it.

The fraction of prompt D mesons after the selection cuts is defined f_{prompt} and it enters in the yield calculation as shown in Eq. (5.1). To quantify this correction (f_{prompt}) to the cross section, a method that relies on theoretical calculations (FONLL [50], EvtGen [148]) has been used, since B cross section and decays are well reproduced in these predictions. For the pp analysis, the feed down contribution to the D^0 cross section has also been cross checked with a data driven method. In this case, the different shape of the impact parameter distributions of primaries and secondaries D is used. This approach was developed by CDF collaboration [110].

Cross-section normalization

The raw yield corrected for efficiencies is then divided by the branching ratio of the corresponding decay channels, in order to compute the total number of D mesons, not only decaying in the studied channel. The measurement of the yields (or the cross sections) is done for both particles and antiparticles. A factor 1/2 has also to be considered to take into account particles only.

For pp collisions, to correct from the p_{t}-differential invariant yield to the cross section, the integrated luminosity analyzed is needed. The integrated luminosity can be obtained considering a reference process for which the cross section is known, and normalizing to the number of events in which this process occurs in the analyzed sample.

Table 5.1: Average values of the number of participating nucleons, the number of binary collisions and of the nuclear overlap function for the considered centrality classes, expressed as percentiles of the inelastic cross section.

centrality class	$\langle N_{\rm part} \rangle$	$\langle N_{\rm coll} \rangle$	$\langle T_{\rm AA} \rangle$ (mb^{-1})
0–20%	308 ± 3	1211 ± 131	18.93 ± 0.74
40–80%	46 ± 2	77 ± 8	1.20 ± 0.07
0–10%	357 ± 4	1503 ± 170	23.48 ± 0.97
10–20%	261 ± 4	923 ± 100	14.43 ± 0.57
20–40%	157 ± 3	439 ± 44	6.85 ± 0.28
40–60%	69 ± 2	128 ± 13	2.00 ± 0.11
60–80%	23 ± 1	27 ± 2	0.42 ± 0.03

5.2 D^0 in Pb–Pb collisions

In this section the analysis flow will be presented together with the results for the $D^0 \to K^-\pi^+$ decay channel studied in Pb–Pb collisions with data collected in 2010 by the ALICE experiment. The same procedure has been followed for the *pp* collisions data, for which the cross section results will be described in Sec. 5.3.2 and 5.3.3.

The Pb–Pb data used for the analysis was collected during November and December 2010, as described in Sec. 3.6. The total number of minimum bias events used for the analysis is about 1.9×10^7. The analysis of the D^0 yields measurement in Pb–Pb collisions will be presented for two different centrality classes 0-20% and 40-80%, for which about 3.1×10^6 and 6.3×10^6 events have been used, respectively.

In the next chapter, results on the nuclear modification factor as a function of centrality will also be shown. For that measurement, 5 centrality classes were considered (0-10%, 10-20%, 20-40%, 40-60% and 60-80%), using the same data sample.

pp results are then scaled by nuclear overlap function factors and compared with the Pb–Pb results in the correspondent centrality class. In Table 5.1, a summary of the nuclear overlap function values and the number of participant nucleons for the different centrality classes are shown.

5.2.1 Raw signal extraction

Together with the topological properties of the $D^0 \to K^-\pi^+$ decay channel, in this section the main variables used to enhance the signal-to-background ratio will be introduced. The topology of the decay is displayed in Fig. 5.2. The impact parameter of the track (d_0) is defined as the distance between the back propagated track in the plane transverse to the beam direction and the primary vertex (see also Sec. 3.8). The impact parameter is used to identify tracks displaced from the interaction point. For the $D^0 \to K^-\pi^+$ decay, two opposite sign tracks are displaced from the interaction point by about 100 μm.

The pointing angle $\theta_{\rm point}$ is defined as the angle between the sum of the reconstructed tracks momenta and the flight line of the D^0 candidate, where this flight line is defined as the line joining the interaction point and the hypothetical secondary vertex of the candidate.

The θ^* angle is the angle between the kaon trajectory in the D^0 centre of mass system (c.m.s.) and the D^0 flight line, taken as the boost direction. Let's consider a mother particle with decay length $c\tau$ that decays in two particles. In the ultra-relativistic limit ($E \sim p$), the typical impact parameter of each decay prong is about $\sim c\tau$. Fig. 5.3 shows

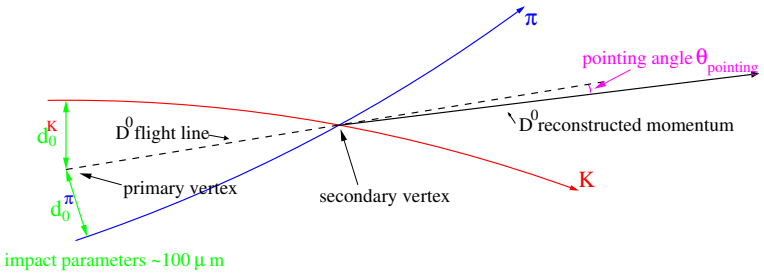

Figure 5.2: Schematic view of $D^0 \to K^-\pi^+$ decay channel. Impact parameter of the tracks and the pointing angle are drown

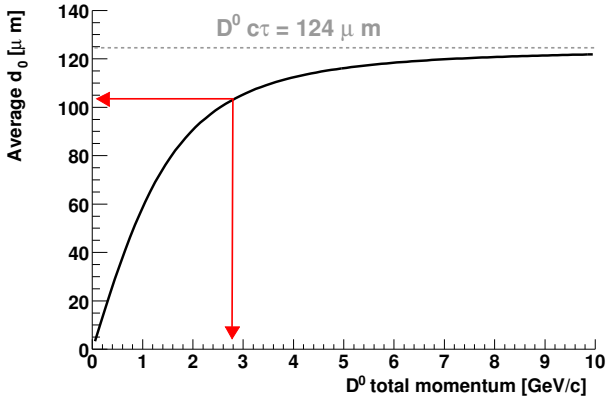

Figure 5.3: Mean impact parameter in the transverse plane for D^0 decay products as a function of momentum. The arrows indicate the average momentum expected in the central rapidity region.

the trend of the average impact parameter of the decay products as a function of the D^0 transverse momentum [144]. This impact parameter is of the order of 100 μm for a D^0 with p_t of about 3 GeV/c.

Selection cut variables

The selection on the cut variables has been optimized by studying the distributions for the signal and background candidates with a Monte Carlo study. This study allows to understand the main variables that can be used in order to reject background candidates and to select as much signal as possible. For Pb–Pb collisions a Monte Carlo HIJING [127] simulation has been used, where in each event 20 PYTHIA [123] $c\bar{c}$ events have been embedded to increase the number of D mesons. The same Monte Carlo simulation has been used to compute the efficiency and acceptance corrections.

The variables used to improve the signal-to-background ratio can be subdivided in two classes: single track variables and candidate variables.

General cuts on the event properties are first applied. The event should have a interaction vertex reconstructed with the VertexerTracks algorithm to assure a good resolution, to separate secondary vertices (Sec. 4.3). Only events with the z coordinate of the vertex in the region $|z| < 10$ cm are used for the analysis.

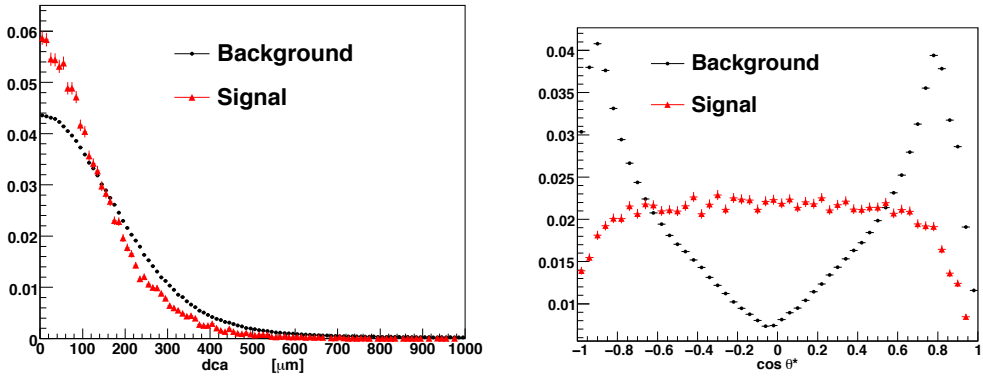

Figure 5.4: Distance of closest approach of signal (red) and background (blue) D^0 candidates obtained with a *pp* PYTHIA Monte Carlo (left). Distribution of the cosine of the θ^* angle for signal and background candidates(right). For signal the distribution is flat due to the isotropic emission with respect to the c.m.s of the D^0.

Tracks are first selected using quality selections on the track reconstruction in the detector. These quality cuts are related to:

- the number of clusters the track has in the TPC ($N_{\rm cl} > 70$),
- the track acceptance ($|\eta| < 0.8$),
- the quality of the fit in the Kalman filter procedure ($\chi^2/dof < 2$).

Tracks should have at least one point in one of the two layers of the SPD, in order to reject secondaries.

The single track cuts applied are on the *impact parameter* with respect to the primary vertex and on the single track *transverse momentum*. As already shown in Sec. 3.10, the impact parameter resolution in Pb–Pb collisions is about 50 μm for tracks with $p_{\rm t} \sim 1$ GeV/c. A minimum cut on the impact parameter of the tracks reduces the number of primary tracks, while a maximum cut can reject those with large displacement, like strange or beauty hadrons decays and particles coming from photon conversions in the detector material. For low $p_{\rm t}$ D^0 the main contribution to the impact parameter comes from the detector resolution, more than the real $c\tau$ of the D^0, due to multiple scattering effects.

The *distance of closest approach (dca)* between two tracks is the length of a segment minimizing the distance between the two tracks trajectories. If two tracks come from the same point the ideal dca should be zero. The measured dca is determined by detector resolution on the track position.

Most of the background is made of primary tracks: their dca distribution is strongly correlated with the impact parameter resolution. The dca cut is effective in rejecting the background pairs if a cut on the minimum impact parameter is applied (Fig. 5.4 left).

In the D^0 reference system, the pion and the kaon are emitted isotropically with three momenta of equal magnitude and opposite direction. The θ^* angle is computed in two different mass hypotesis (D^0 and $\bar{D^0}$) to correlate both charged tracks with the possibility of being a kaon. Due to the isotropic production in the c.m.s, the $\cos\theta^*$ distribution for signal pairs is almost flat. The background distribution peaks close to ± 1. For $|\cos\theta^*| \sim 1$

a drop of the number of candidates is visible, due to the cuts applied in the reconstruction and to detector acceptance effects (Fig. 5.4 right).

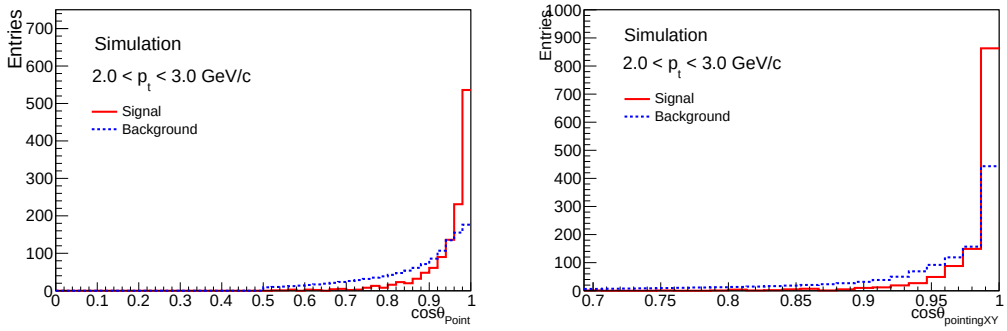

Figure 5.5: Distribution of the cosine of the pointing angle for signal and background candidates measured in Pb–Pb Monte Carlo (left). Distribution of the cosine of the pointing angle measured in the transverse plane with respect to the beam line for signal and background candidates measured in a HIJING charm enriched Monte Carlo (right)

The *pointing angle* (θ_{point}) has been already introduced in the previous section and in Fig. 5.2. For background pairs there is no correlation between the reconstructed momentum and the reconstructed flight line, since the secondary vertex is an artifact of the finite tracking resolution. For a signal candidate the flight line direction is determined by the D^0 three-momentum direction and the cosine of the pointing angle distribution is peaked at 1. The comparison between Monte Carlo distributions of signal and background are shown in Fig. 5.5 (left).

The pointing angle can be defined with respect the full reference frame of the decay or also considering only the transverse plane (defined as xy plane). In this plane as shown in Sect. 4.3 the size of the luminous region is much smaller with respect to the z coordinate. The primary vertex resolution is thus better in the xy plane. Considering the pointing angle defined in the transverse plane, it is then possible to introduce a new cut variable that allows to better separate background candidates with respect to the signal ones. This variable ($\theta_{\text{point XY}}$) was used only in the Pb–Pb analysis, to cope with the larger background. The comparison between signal and background is shown in Fig. 5.5 (right). The distribution for the $\cos\theta_{\text{point XY}}$ is more "peaked" close to 1 with respect to the pointing angle 3D, especially for the signal candidates.

The *product of impact parameters* ($d_{0\ \text{K}} \times d_{0\ \pi}$) is built considering the single track impact parameters and the charge of the tracks: for a signal candidate, the product would be negative. Due to detector resolution, the distribution of the signal shows both positive and negative sides but it is asymmetric with respect to zero. For background candidates, composed of randomly associated primary tracks with opposite charges, the distribution is symmetric (Fig. 5.6 left).

Another important variable used only in the Pb–Pb analysis is the normalized decay length measured in the transverse plane (L_{XY}). The decay length in the transverse plane with respect to the beam line is divided (normalized) by the error on the decay length measurement. As Fig. 5.6 (right) shows, background dominates at small normalized decay lengths. In case of a charm or beauty decay, the particles are displaced and the measurement of decay length is more precise. At low p_{t} ($p_{\text{t}} < 2$ GeV/c) the decay length starts suffering also from detector resolution effects and also for signal candidates it can be less precise. In that case the selection cut needs to be released.

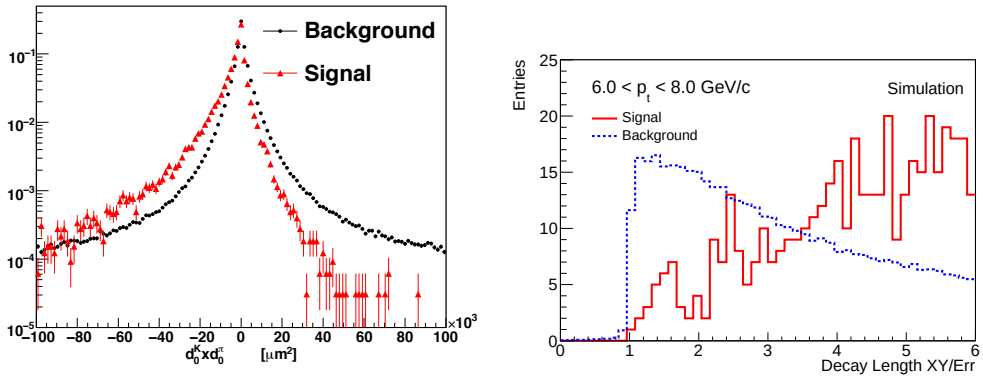

Figure 5.6: Products of the impact parameter of signal and background candidates measured in *pp* Monte Carlo. The asymmetric distribution is typical of signal candidates (left). Normalized decay length distributions for signal and background candidates measured in Pb–Pb Monte Carlo simulation (right).

For D^0 with $p_t < 3$ GeV/c, an additional selection has been applied in order to reject the combinatorial background. Both tracks of the D^0 candidate must have a hit in the inner layer of the SPD detector. This selection reduces the signal by a factor proportional to the dead zones of this layer ($\sim 15\%$) but it reduces the background by a factor 2.

The values used as selection cuts were chosen in order to reject as much background as possibile without losing too much signal. The adopted criterion is to try to maximize the statistical significance, checking that the invariant mass position and width are compatible with the Particle Data Group (PDG) ones [145].

The statistical significance is defined as

$$\mathbf{S} = \frac{S}{\sqrt{S+B}} = \sqrt{S}\frac{1}{\sqrt{1+\frac{1}{r}}}, \tag{5.2}$$

with S and B the signal background candidates after cuts and $r = S/B$ the signal-to-background ratio, that depends on the "power" of the cuts. The significance describes how much the signal emerges above the fluctuations of the background.

For the Pb–Pb analysis the most efficient cuts are the cosine of the pointing angle in the xy plane and the normalized decay length, in addition to the products of the impact parameters. In Tables 5.2 and 5.3 the values of the selection cuts, described previously and used for the analysis in Pb–Pb collisions are reported. Different selection cuts have been used in central events events and peripheral ones, due to the different amount of background in the events of the two centrality classes. For peripheral events the selection cuts are looser, since the background is smaller. With the selection cuts shown in the tables, other cuts are applied for both centrality classes and for all p_t ranges:

- the difference between the mass of the reconstructed candidates and the PDG D^0 mass has to be smaller than 0.4 GeV,
- $|\cos\theta^*| < 0.8$,
- the p_t of the two charged tracks has to be larger than 0.7 GeV/c, [1]

[1] This cut is different for D^0 with $p_t < 2$ GeV/c

Table 5.2: Selection cuts applied for D^0 reconstruction in Pb–Pb collisions in 0-20% centrality class.

p_t GeV/c	dca (cm)	$d_{0\ K} \times d_{0\ \pi}$ (cm^2)	$cos\theta_{\text{point}}$	$\lvert cos\theta_{\text{point XY}}\rvert$	L_{XY}
$2 < p_t < 3$	$250. \times 10^{-4}$	$-45000. \times 10^{-8}$	0.97	0.998	7
$3 < p_t < 4$	$250. \times 10^{-4}$	$-36000. \times 10^{-8}$	0.95	0.998	5
$4 < p_t < 5$	$250. \times 10^{-4}$	$-27000. \times 10^{-8}$	0.95	0.998	5
$5 < p_t < 6$	$250. \times 10^{-4}$	$-21000. \times 10^{-8}$	0.92	0.998	5
$6 < p_t < 8$	$270. \times 10^{-4}$	$-14000. \times 10^{-8}$	0.88	0.998	5
$8 < p_t < 12$	$300. \times 10^{-4}$	$-5000. \times 10^{-8}$	0.85	0.998	5
$12 < p_t < 16$	$350. \times 10^{-4}$	$-1000. \times 10^{-8}$	0.83	0.998	8

Table 5.3: Selection cuts applied for D^0 reconstruction in Pb–Pb collisions in 40-80% centrality class.

p_t GeV/c	dca (cm)	$d_{0\ K} \times d_{0\ \pi}$ (cm^2)	$cos\theta_{\text{point}}$	$\lvert cos\theta_{\text{point XY}}\rvert$	L_{XY}
$2 < p_t < 3$	$250. \times 10^{-4}$	$-40000. \times 10^{-8}$	0.95	0.991	5
$3 < p_t < 4$	$250. \times 10^{-4}$	$-36000. \times 10^{-8}$	0.95	0.993	5
$4 < p_t < 5$	$250. \times 10^{-4}$	$-27000. \times 10^{-8}$	0.95	0.995	5
$5 < p_t < 6$	$250. \times 10^{-4}$	$-21000. \times 10^{-8}$	0.92	0.998	5
$6 < p_t < 8$	$270. \times 10^{-4}$	$-14000. \times 10^{-8}$	0.88	0.998	5
$8 < p_t < 12$	$300. \times 10^{-4}$	$-5000. \times 10^{-8}$	0.85	0.995	5
$12 < p_t < 16$	$350. \times 10^{-4}$	$-1000. \times 10^{-8}$	0.83	0.995	4

- the impact parameter of the two D^0 prongs has to be smaller than 1000×10^{-4} cm to reject very displaced tracks.

Particle IDentification strategy

For the D^0 analysis, the Particle IDentification (PID) is used to identify the kaon in the candidate and remove the high combinatorial background coming from the association of two pions. Kaons (and pions) are identified via the energy loss deposit in the TPC (Sec. 3.4.1) and the velocity measurements in the TOF (Sec. 3.4.2). These two detectors can separate kaons and pions from other particles in different momentum ranges. For both detectors a track can be identified with units of resolution of the difference between the measured and the expected signal ($n\sigma$ cut method). For the D^0, the PID strategy is aimed at identifying the single tracks, reducing the background, without any loss of the signal.

In the TPC a 2σ cut was applied to identify both pions and kaons. If the track energy loss (dE/dx) signal is between 2 and 3σ from the expected value, it is kept as non-identified. In the momentum range $0.6 < p < 0.8$ GeV/c, the selection applied goes down to 1σ, because pion and kaon expectations become closer. In the full momentum if the energy loss differs by more than 3σ from the expected value, the hypotesis is discarded.

If the track arrives at the TOF a 3σ cut on its expected arrival time is applied. Kaons are identified up to $p = 2$ GeV/c; for larger momenta, particles are considered as non-identified, since the signal bands of pions and kaons start to overlap and the contamination effect is not negligible anymore.

For the pion identification, only TPC information was used, while both detectors were used for kaon identification. In case TOF and TPC were in contradiction, tracks were kept as non-identified.

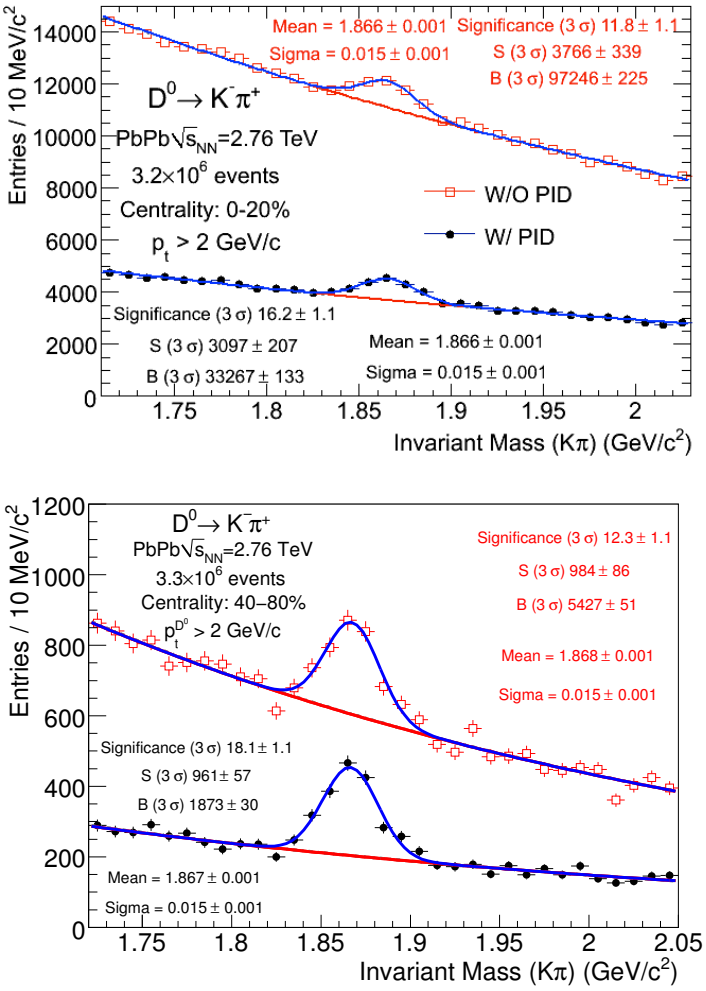

Figure 5.7: Invariant mass distribution for D^0 with $p_t > 2$ GeV/c in case PID selection is not applied (red) and it is applied (blue). Top plot refers to the centrality class 0-20%, Bottom plot to the 40-80%.

Two-prongs candidates were accepted as (D^0, $\bar{D^0}$, or both) or rejected, following the compatibility with the $K^{\pm}\pi^{\mp}$ final state. The comparison of the invariant mass distribution obtained without and with PID shows a reduction by a factor of 3 in the combinatorial background especially for the low-p_t region, while preserving close to 100% of the signal. Fig. 5.7 shows the effect of the PID selection for central (top) and peripheral (bottom) events for D^0 with $p_t > 2$ GeV/c. For the 0-20% events, the figure shows a study done with a set of selection cuts that was not the final, but the PID effect was checked also for the final analysis and it does not depend on the selection cuts applied.

Invariant mass fit

The $K^{\pm}\pi^{\mp}$ invariant mass distribution can be considered as the sum of a Gaussian function representing the D^0 signal plus a background shape that can be approximated with polynomial or exponential functions, depending on the p_t region considered. The fit is performed in two steps using the Minuit package [146].

The side-bands of the invariant mass histogram are fitted with the chosen background function. The region outside the peak is taken between $3\sigma(M) < |M - M_{D^0}| < 5\sigma(M)$ where no signal is present. Three possible background shapes are used in this first step: exponential, linear, second order polynomial. This first step allows to obtain a first estimate on the total amount of background.

Then, the total fit is performed using as a starting point of the fit parameters, the information about background obtained from the first step. The signal is fitted with a Gaussian convoluted with the background function used in the first step. The amount of S and B are extracted from the fit parameters together with their errors.

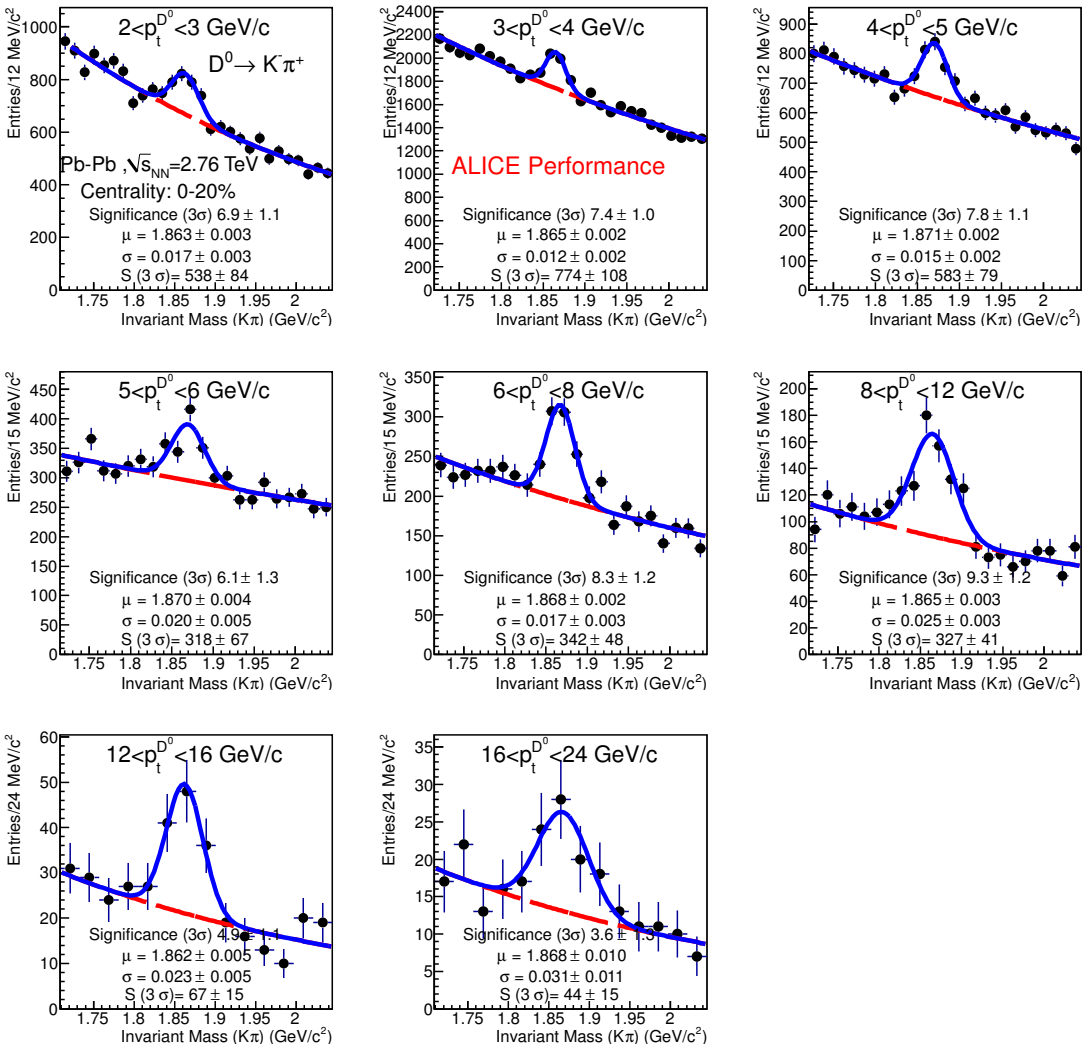

Figure 5.8: D^0 Invariant mass analysis for events in the centrality class 0-20% from p_t = 2 GeV/c up to p_t = 24 GeV/c [151].

Fig. 5.8 shows the invariant mass distributions for the D^0 in 8 p_t bins, from 2 up to 24 GeV/c in the 0-20% centrality class [151]. All peaks are clearly visible and the significance is equal or larger than 5 for all p_t bins, except the last one (16-24 GeV/c). Fig. 5.9 shows the invariant mass analysis for the D^0 in 8 p_t bins from 1 up to 16 GeV/c in the 40-80% centrality class [151]. In both cases, the mean value of the distributions are compatible

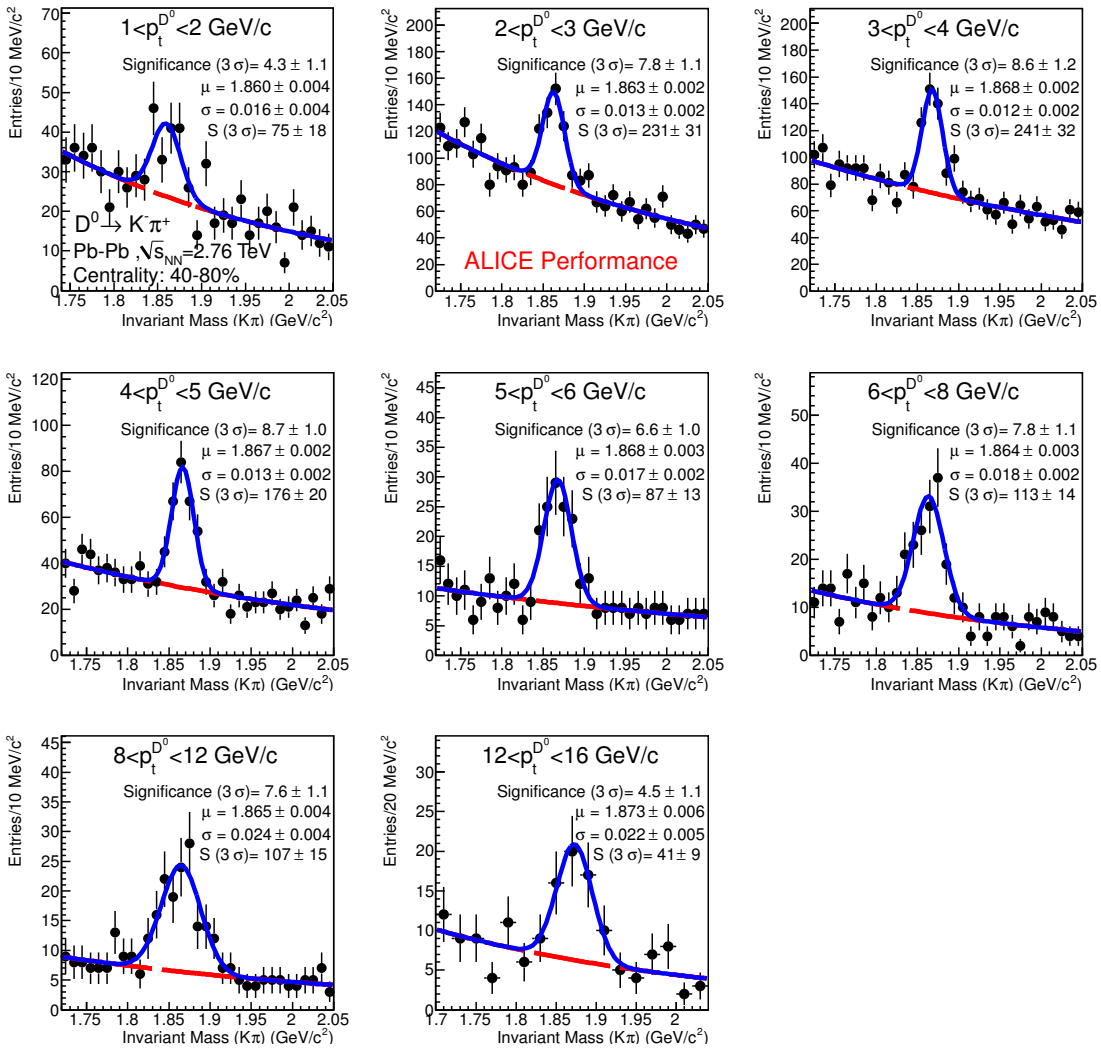

Figure 5.9: D^0 Invariant mass analysis for events in the centrality class 40-80% from $p_t = 1$ GeV/c up to $p_t = 16$ GeV/c [151].

with the PDG values [145]. The widths of the distributions are compared in Fig. 5.10. For central Pb–Pb collisions (left) the agreement is quite good a part for two p_t bins where the background shape can be different in the charm enriched Monte Carlo sample and it can influence the width determination. Peripheral Pb–Pb collisions are compared with the pp measurement at $\sqrt{s} = 7$ TeV. The results of two samples are in good agreement (Fig. 5.10 right).

The numbers of signal, background candidates and significance are reported in two summary tables (Tabs. 5.4, 5.5) one for each centrality class.

5.2.2 Efficiency determination

The raw yield extracted from the invariant mass analysis ($\mathbf{N}^{\mathrm{D^0\ raw}}$) is only a fraction of the total number of D^0 produced in the collisions. D^0 may not be reconstructed for different reasons: detector acceptance, vertex and track reconstruction efficiencies, selection cuts

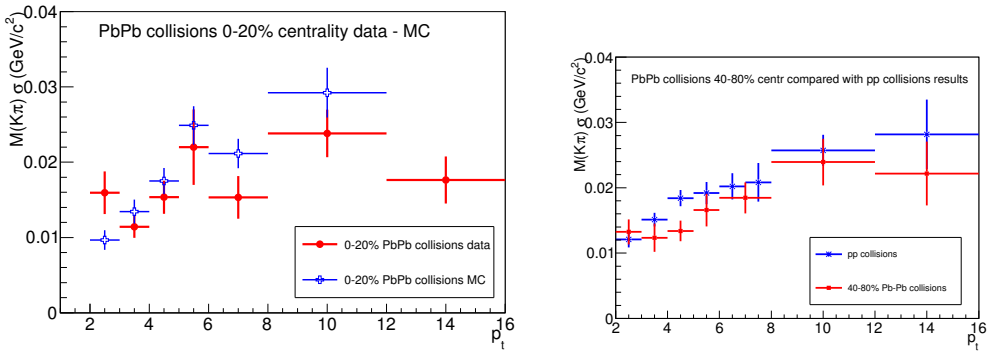

Figure 5.10: Comparison of the width of the invariant mass distribution obtained in central Pb–Pb collisions for data and Monte Carlo (left). Comparison of the width of the invariant mass distribution measured in peripheral Pb–Pb collisions and *pp* collisions at $\sqrt{s} = 7$ TeV. (right).

Table 5.4: Signal, background and significance for D^0 candidates in the 0-20% centrality class.

p_t (GeV/c)	Signal	Background	Significance
2-3	538 ± 84	5581 ± 39	6.9 ± 1.1
3-4	774 ± 46	10241 ± 45	7.4 ± 1.0
4-5	583 ± 79	5002 ± 35	7.8 ± 1.1
5-6	318 ± 67	2359 ± 27	6.1 ± 1.3
6-8	342 ± 48	1361 ± 19	8.3 ± 1.2
8-12	327 ± 41	964 ± 19	9.3 ± 1.2
12-16	67 ± 15	120 ± 7	4.9 ± 1.1

on the candidates. In order to recover the total yield, it is necessary to correct for the reconstruction efficiencies using Monte Carlo simulations.

The D^0 mesons generated and decayed in the $D^0 \to K^-\pi^+$ channel are counted ($N^{D^0}_{gen}$) and "monitored", along the simulation, reconstruction and analysis chain. The first part of the chain is related to the simulation and the D^0's are defined as reconstructable. In the reconstruction part, D^0 candidates are first checked to come from a real generated D^0. The analysis part is the last step where analysis cuts on the candidates are applied as it is done in the data; after this also the PID selection is considered.

The number of reconstructed D^0 mesons after the analysis and PID steps defines the numerator to compute the efficiencies ϵ. For the denominator the number of "reconstructable" D^0 is used, not all D^0 generated but only those, for which all decay products are in the detector acceptance ($|\eta| < 0.8$).

Since the charm production has a lower cross section then other processes, the computation of this efficiencies is, usually, performed on MC sample where charm production is enhanced and D mesons are forced to decay in the channels under study.

To compute the acceptance and efficiency correction the HIJING event generator [136] has been used, where for each event about 20 $c\bar{c}$ PYTHIA [149] events have been injected on top of the Pb–Pb events. The *pp* events have been embedded to the HIJING ones preserving the centrality correspondance with the Pb–Pb collisions.

Fig. 5.11 (left) shows the acceptance × efficiencies correction factors for $D^0 \to K^-\pi^+$

Table 5.5: Signal, background and significance for D^0 candidates in the 40-80% centrality class.

p_t (GeV/c)	Signal	Background	Significance
2-3	231 ± 31	640 ± 12	7.8 ± 1.1
3-4	241 ± 32	545 ± 11	8.6 ± 1.2
4-5	176 ± 20	237 ± 7	8.7 ± 1.0
5-6	87 ± 13	83 ± 5	6.6 ± 1.0
6-8	113 ± 14	98 ± 5	7.8 ± 1.0
8-12	107 ± 15	92 ± 5	7.6 ± 1.1
12-16	41 ± 9	42 ± 4	4.5 ± 1.1

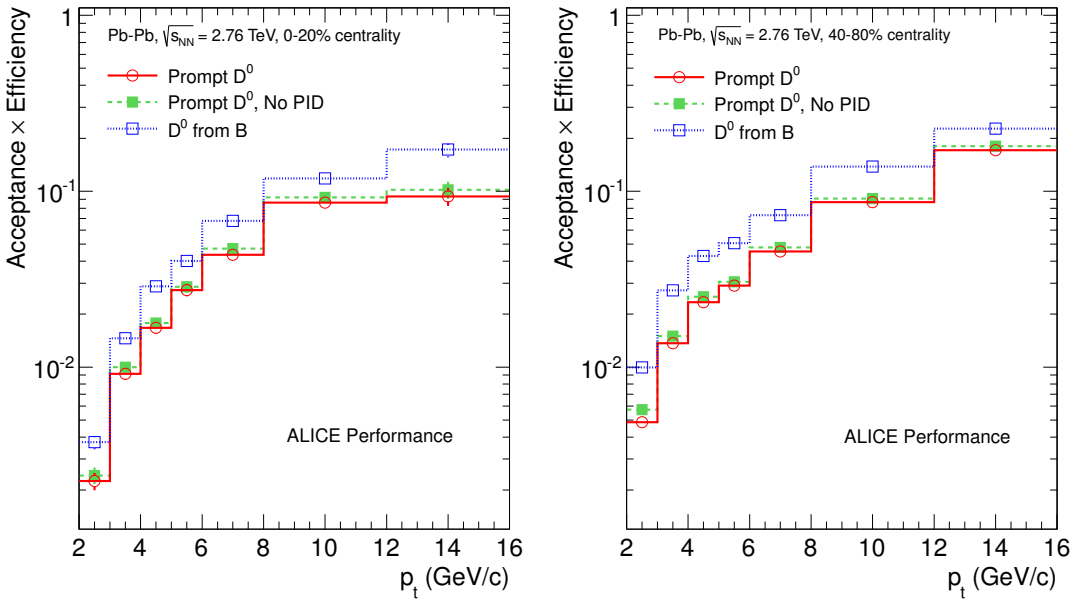

Figure 5.11: Acceptance × efficiency correction factors computed for 0-20% (left) and 40-80% (right) centrality classes [151].

decay, for the 0-20% centrality class [151]. At low p_t, the selection cuts are tighter and the efficiencies are of the order 0.5%, while for increasing p_t the efficiencies increase up to 10% for $p_t > 8$ GeV/c. The efficiency without PID selection is also shown for comparison: the efficiencies with and without PID are almost the same, indicating that this selection is fully efficient for the signal. The efficiencies for D mesons cooming from B hadrons decay are also shown. These efficiencies are larger by a factor 2, since it is easy to select secondary D since they are more displaced from the primary vertex. In Fig 5.11 (right) the same three curves are shown for the centrality class 40-80%. At low p_t the efficiencies are larger with respect to those in the 0-20% central events due to looser selection cuts, while for $p_t > 8$ GeV/c they are comparable with the 0-20% ones.

5.2.3 Feed-down correction

The raw yields, obtained from the invariant mass analysis, contain both prompt and secondary D^0. An additional correction to estimate the fraction of feed-down from B is needed, before applying the corrections. Two different methods have been studied to

compute this correction factor: a Monte Carlo based approach and a data-driven one. For these first analyses on LHC data, theoretical predictions for beauty cross section have been used; the data-driven approach was used as cross check only in the *pp* analysis, since this method requires very large statistics.

FONLL predictions have been used to compute the fraction of beauty that enters in the analysis, together with EvtGen package to better describe the kinematics $B \to D$ [148]. Two approaches have been followed to correct the raw yield and estimate a systematic uncertainty on the feed-down subtraction.

The FONLL calculations of primary and secondary D^0 cross section in *pp* collisions at 7 TeV for $|y| < 0.5$ have been shown in Fig. 2.1 (right).

The first Monte Carlo based approach relies on the FONLL calculation of the secondary D^0 cross section. It consists on subtracting, to the D^0 raw yield, the expected secondary raw yield evaluated as the FONLL cross section corrected by the acceptance, reconstruction and analysis cuts efficiency and normalized to the analyzed integrated luminosity. The mathematical formulation is quoted in Eq. (5.3). The upper and lower uncertainties of the FONLL calculation are considered to evaluate the feed-down subtraction uncertainties.

$$\frac{d^2N^{raw}_{B\to D}}{dydp_{\rm t}} = (L_{\rm int} \times \times BR_b \times \Delta y \times (Acc \times \epsilon)_{B\to D}) \times \frac{d^2\sigma^{\rm FONLL}_{B\to D}}{dydp_{\rm t}} \tag{5.3}$$

The second Monte Carlo based approach relies on the ratio primary over secondary D^0 given by the FONLL calculation. It depends on the primary and secondary $p_{\rm t}$ distributions and on the ratio of their cross sections, but does not rely on the absolute normalization. The feed-down contribution is evaluated through the relative ratio primary/secondary of the D^0 raw yields, considering the FONLL cross section corrected by acceptance, reconstruction and analysis cuts. The measured raw yield is then multiplied by this corrective factor ($f_{prompt}(p_{\rm t})$) to obtain the prompt D^0 cross section. The FONLL uncertainties are propagated to evaluate the uncertainty on the feed down subtraction: the estimate of primary and secondary D^0 are correlated and the calculation of the upper primary contribution corresponds to the upper secondary contribution. The same for lower estimate.

$$f_{prompt}(y, p_{\rm t}) = 1/\left(1 + \frac{(Acc \times \epsilon)_{B\to D}}{(Acc \times \epsilon)_{c\to D}} \times \frac{\frac{d^2\sigma^{\rm FONLL}_{B\to D}}{dydp_{\rm t}}}{\frac{d^2\sigma^{\rm FONLL}_{c\to D}}{dydp_{\rm t}}}\right) \tag{5.4}$$

The two Monte Carlo methods are then combined together in only one uncertainty. Since FONLL beauty calculations seem to better agree with the data measurement at different energies and rapidities, the central value of the calculation is taken from the first method. The feed-down subtraction uncertainties are defined by the envelope of the uncertainties coming from both methods. The uncertainties are asymmetric with values of +4% and -24% at low-$p_{\rm t}$ and at high-$p_{\rm t}$ the error ranges from +5% to -7%, for Pb–Pb central collisions.

For Pb–Pb collisions an additional factor is taken into account, it represents the nuclear modification factor of the D mesons from B decay, that is for the moment unknown. A description of the method and the error related to this assumption will be presented in the next chapter. This contribution has to be taken into account and it results in an additional systematic uncertainty on the measurement.

Only for the *pp* analysis also a data driven method has been used to check the FONLL calculation on the prompt D^0 and it will be described in the next section.

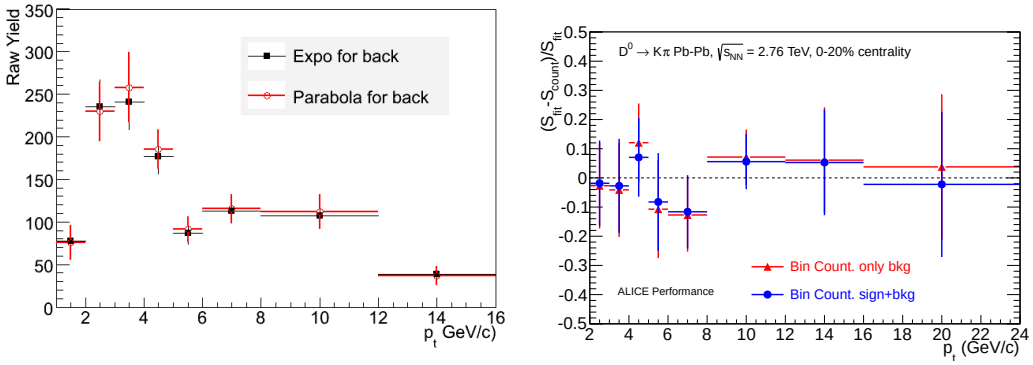

Figure 5.12: Comparison of the raw yield extracted with exponential and polynomial background functions for events in the class 40-80% (left). Ratio of the raw yield extracted with invariant mass fit of the signal and bin counting methods in 0-20% central events (right).

5.2.4 Systematic uncertainties on the invariant yield

Many possible sources of systematic uncertainties of the analysis have been considered for all different steps of the analysis. Different strategies for the yield extraction have been considered as well as different selection cuts or a different Monte Carlo p_t shape. In this section the main sources of systematic uncertainties will be presented and summarized, then, in Tables 5.6 and 5.7

The systematic uncertainties have been considered, taking into account many possible sources:

- *yield extraction* - the invariant mass spectra analysis was done repeating the fit for each p_t bin in a different mass range and with a different function to describe the background: a second order polynomial instead of an exponential. In Fig 5.12 (left) results are shown for the centrality class 40-80%. The raw yield extracted with two different background functions are compatible within 5%.

  A method based on counting the signal candidates in the invariant mass distribution bin-by-bin (after subtracting the background estimate from a fit to the side bands) was also used. Fig. 5.12 (right) shows the deviation of the bin counting method with respect to the case used for the results (signal estimated with the fit) for the 0-20% centrality class. Each p_t bin has two points: the comparison with the bin counting, method is performed first only with the fit of background function (red points) and then with the fit of background plus signal (blue points). The two methods are compatible within statistical errors, the maximum deviation is slightly larger than 10%.

  The total systematic uncertainties on the yield extraction has been assigned by taking the larger results on the bin counting and on the yield extraction with different background functions.

- *tracking efficiency* (including the effect of the track selection) - it was estimated comparing in data and simulation the probability of track finding in the TPC and track prolongation from TPC to ITS and by varying the track quality selections. The results on the tracking efficiencies in Pb–Pb were shown in Sec. 3.10. The track prolongation from TPC to ITS was found to be described in simulation at the level

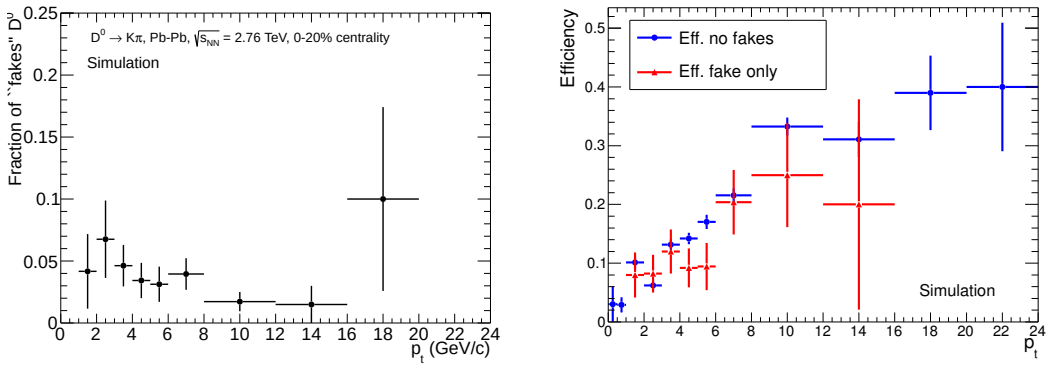

Figure 5.13: Ratio of D^0 reconstructed with a wrong hit associated in the ITS ("fake" D^0) studied with a Monte Carlo HIJING simulation for 0-20% central events (left). Selection efficiency as a function of p_t for D^0 reconstructed with wrong hit association (red) and without (blue).

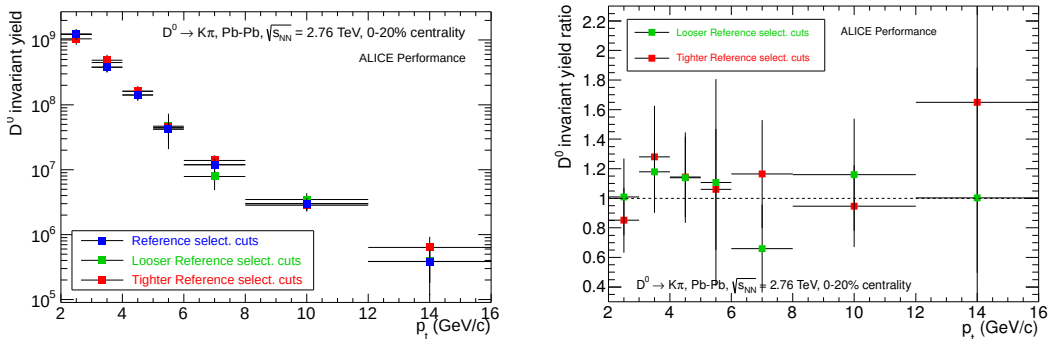

Figure 5.14: D^0 invariant p_t spectra measured with three different sets of selection cuts (right). Ratio of the D^0 invariant yields for looser and tighter cuts over the yields obtained with the selection cuts used as reference. The overall variation is around 10% within one sigma (left).

of 5% in the whole p_t range relevant for this analysis. Its centrality dependence, which is limited to ±3% in this range, was found to be reproduced within 1.5% in the Monte Carlo (Figs. 3.15, 3.16).

Due to the high multiplicity environment in central collisions, it is necessary also to study the probability of wrongly associating an ITS hit to the track, specially in the two pixel layers, where the impact parameter can be modified. The effect of this wrong association to tracks was studied in the simulation. The fraction of the D^0 meson candidates with at least one decay track with wrong hit associations, increases with increasing centrality (due to higher detector occupancy) and it decreases for increasing p_t. In the centrality class 0-20% (Fig. 5.13 left), it ranges from 7% to 1% in the transverse momentum interval $2 < p_t < 20$ GeV/c. It was also verified that the selection efficiencies are compatible, within statistical uncertainties, between D mesons with and without wrong hit associations (Fig. 5.13 right). This is due to the fact that the mis-associated hit is typically very close in space to the correct one.

The systematic uncertainty from track reconstruction amounts to 6% for single

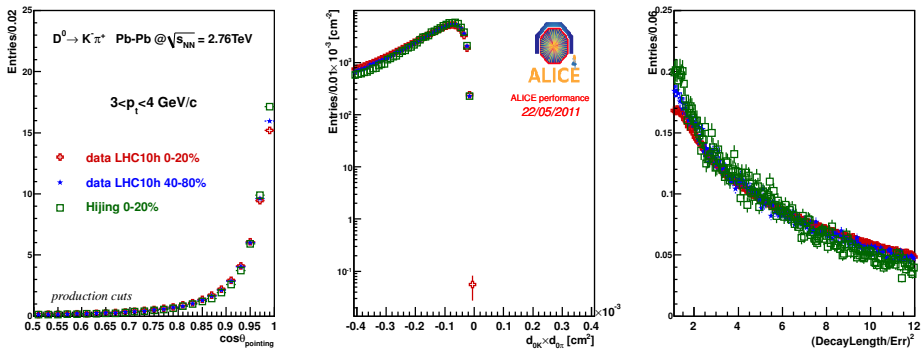

Figure 5.15: Comparison of the distribution measured in the 0-20% central collisions with those simulated in the Monte Carlo. The distribution shows very good agreement for both central and peripheral collisions.

tracks, which results into a 12% for the two body decay of the D^0 meson.

- *correction for selection cuts efficiency* - it was evaluated by repeating the analysis with different sets of selection cuts and defined as half the spread of the corrected yield obtained. Four different sets of cuts have been tried in order to test the cut stability. The cut on the pointing angle XY and on the normalized decay length have been varied considering a looser and a tighter value with respect to the default ones for both variables. The looser cuts have been selected with the constraint of the possibility to fit the lower $p_{\rm t}$ bin, since it is the one with higher background. Four different set of cuts have been considered: both looser, both tighter, one loser and one tighter and viceversa. For all sets of cuts the raw yields have been extracted and the corresponding efficiencies have been computed. In Fig. 5.14 the results of this study were shown, for the looser and tighter sets of selection cut: a 10% uncertainty on the selection cut variation has been evaluated studying the ratios of the yields obtained with looser or tighter selection cuts over those used as a reference.

- *residual detector misalignment effect, not fully described in the simulation* - it was estimated with a scaling on the single track impact parameter. In particular a constant 10% difference is added to the impact parameter resolution obtained in the data, together with a linear $p_{\rm t}$ dependent increase (15% at 10 GeV/c).

  The relative variation of efficiency, both for prompt and secondary D mesons, was found to be 8% at $p_{\rm t} = 2 - 3$ GeV/c and negligible for $p_{\rm t} > 5$ GeV/c. This effect was not included explicitly in the uncertainty estimation, since it is accounted for in the cut variation study.

  Further checks were performed by comparing the distributions in the data and in Monte Carlo of the variables used for candidate selection. In particular Fig. 5.15 shows the comparison for pointing angle, the products of the impact parameters and the normalized decay length for central (0-20%) and peripheral (40-80%) collisions. The comparison shows good agreement between the distributions and no dependence on centrality.

- *PID selection* - it was estimated to be -5% +15% in the most central collisions by comparing the corrected signals extracted with and without this selection (Fig. 5.7).

For the 40-80% centrality class the errors are -5% and +10% for this selection.

- *simulated shape of the* D^0 *meson transverse momentum distribution* - it was studied by varying the shape of the nuclear modification factor (that will be described in the next chapter). A variation in this shape would reflect on a variation on the p_t shape of the yield of the D^0. To perform this study, the variation of the nuclear modification factor has been computed considering the spread between the central values and those at the higher side of the systematic uncertainties. The total effect was found to be around 3% for $p_t < 3$ GeV/c and less than 1% at higher p_t.

  The p_t-differential yields for D^0 and $\bar{D^0}$ mesons, extracted separately, were found to be in agreement within the statistical uncertainties of about 20-25%.

- *secondary D mesons from B decay* - it has been described in the previous section (Sec. 5.2.3).

The total systematic uncertainties on the data are summarized in the Tables 5.6 and 5.7 for the 0-20% and 40-80% centrality classes respectively.

Table 5.6: Systematic uncertainties on the D^0 invariant yield measurements (0-20%).

Source	2-3	3-4	4-5	5-6	6-8	8-12	12-16 (GeV/c)
Yield Extraction	8%	8%	8%	8%	8%	8%	10%
Tracking efficiency	12%	12%	12%	12%	12%	12%	12%
Cut Efficiency	10%	10%	10%	10%	10%	10%	10%
PID efficiency (up)	+15%	+15%	+15%	+15%	+15%	+15%	+15%
PID efficiency (low)	-10%	-10%	-5%	-5%	-5%	-5%	-5%
MC p_t shape	3%	3%	1%	1%	1%	1%	1%
FONLL Feed down (up)	+4%	+4%	+4%	+5%	+6%	+5%	+5%
FONLL Feed down (low)	-24%	-16%	-14%	-12%	-10%	-9%	-7%
Branching Ratio	1.2%						

Table 5.7: Systematic uncertainties on the D^0 invariant yield measurements (40-80%).

Source	2-3	3-4	4-5	5-6	6-8	8-12	12-16 (GeV/c)
Yield Extraction	5%	5%	5%	5%	5%	5%	5%
Tracking efficiency	12%	12%	12%	12%	12%	12%	12%
Cut Efficiency	10%	10%	10%	10%	10%	10%	10%
PID efficiency (upper)	+10%	+10%	+10%	+10%	+10%	+10%	+10%
PID efficiency (lower)	-5%	-5%	-5%	-5%	-5%	-5%	-5%
MC p_t shape	3%	3%	1%	1%	1%	1%	1%
FONLL Feed down (up)	+4%	+5%	+5%	+7%	+6%	+6%	+6%
FONLL Feed down (low)	-16%	-13%	-11%	-9%	-9%	-8%	-7%
Branching Ratio	1.2%						

5.2.5 D^0 invariant yield in Pb–Pb collisions

The transverse momentum distributions dN/dp_t of prompt D^0 mesons are presented in Fig. 5.16 from 2 up to 16 GeV/c [151]. Red symbols represent the invariant spectra measured in Pb–Pb 0-20% central collisions, light red ones represent the spectra measured

for the 40-80% centrality class. Blue points are obtained considering the D^0 invariant yield obtained in *pp* collisions at $\sqrt{s} = 2.76$ TeV (this measurement will be explained in Sect. 6.1.1) scaled by the corresponding nuclear overlap function ($\langle T_{AA} \rangle$). Dark blue points refer to the 0-20%, light blue points to the 40-80% centrality classes. From these results, it is clearly visible that in Pb–Pb collisions D^0 mesons are suppressed with respect to the superimposition of simple *pp* collisions. The suppression is clearly visible for central events, while for peripheral events is smaller.

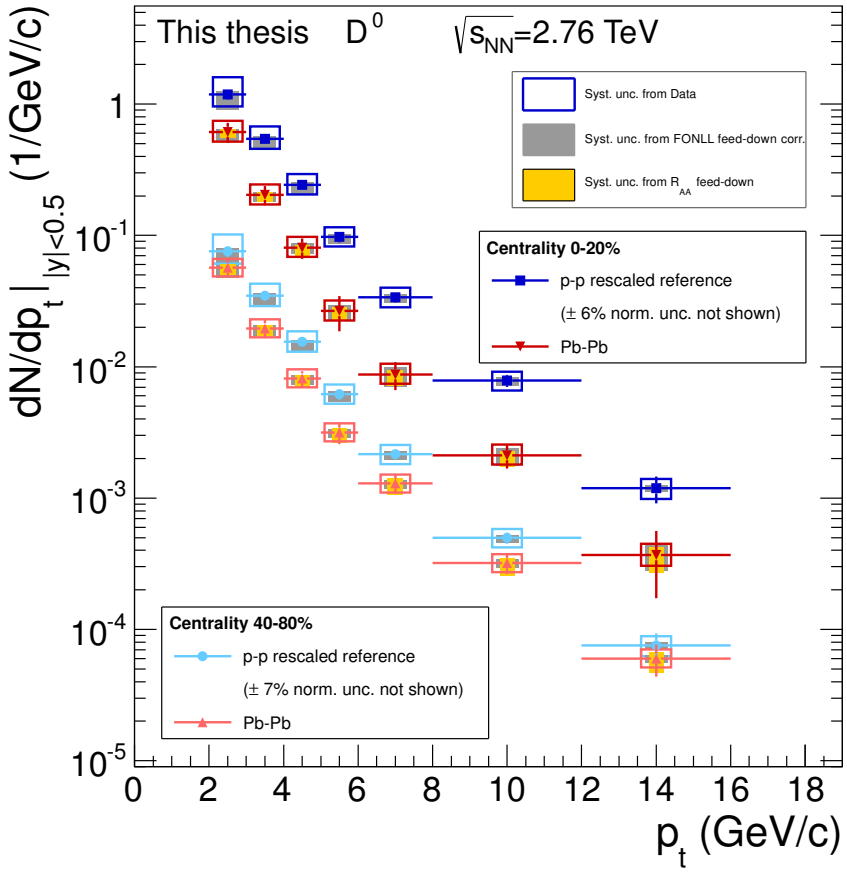

Figure 5.16: D^0 invariant yield measured in Pb–Pb collisions in the 0-20% and 40-80% centrality classes, compared with the *pp* reference at the same energy [151].

The boxes in Fig. 5.16 represent the data systematic uncertainties, the grey boxes are the uncertainties coming from the B feed down subtraction procedure. Yellow boxes are related to the hypothesis on the beauty nuclear modification factor that will be described in Sec. 6.1.2

Details for the scaling in *pp* collisions will be given in the next chapter (Sec. 6.1.1).

5.3 D^0 in *pp* collisions at $\sqrt{s} = 7$ TeV and $\sqrt{s} = 2.76$ TeV

As described in section 3.6, ALICE took data both in Pb–Pb and *pp* collisions during the first year of running of the LHC. The measurement of the charm cross section in *pp* collisions is very important to test pQCD calculations and to have a reference measurement

for the nuclear modification factor. ALICE measured the D meson cross section at $\sqrt{s} = 7$ TeV [155] and at $\sqrt{s} = 2.76$ TeV [157]. For both analyses the procedure is the same as the one described in the previous section for Pb–Pb collisions.

Starting from the invariant yield, a normalization to a known process is needed to compute the absolute cross section. This procedure is described in the first part of this section. The measurement at $\sqrt{s} = 7$ TeV is performed using 3.14×10^8 events collected in 2010 with minimum bias trigger that correspond to an integrated luminosity of about $L_{\rm int} = 5$ nb^{-1}. The measurement at $\sqrt{s} = 2.76$ TeV is done with 6.3×10^7 events ($L_{\rm int} = 1.1$ nb^{-1}) collected in 2011 during a special run, where LHC delivered pp collisions at the same energy as the Pb–Pb ones.

5.3.1 Normalization to the cross section

The integrated luminosity is defined as the number of events in which a given known process occurs ($N_{\rm ref}$) over the cross section of this process $\sigma_{\rm ref}$:

$$L_{\rm int} = \frac{N_{\rm ref}}{\sigma_{\rm ref}} \tag{5.5}$$

For this analysis as for other ALICE analyses, the measurement is computed using the cross section of the minimum bias trigger events. Events belonging to this trigger class have fired at least one FAST-OR chip in the SPD detector or one of the scintillators of the VZERO detector. The measurement of the ALICE minimum bias trigger cross section is divided in two parts: the online measurement of the VZERO-AND cross section (taken as reference process) and the scaling of this cross section to the minimum bias one, with an offline analysis.

The measurement of a known reference process can be performed with a van der Meer (vdM) scan technique [152]. In the vdM scan the luminosity L is varied by changing the distance between the two beams horizontally and vertically with respect to the plane transverse to the beam axis. This variation can be correlated with the trigger rate of the reference process, measured online. Another important part of the vdM scan is the luminosity measurement and in particular the beams intensity determination that is performed using LHC beams instruments based on inductive current pickup devices. Also the monitor of the beam position and size during the scan has to be taken into account because directly related to the variation of the trigger rate.

ALICE measured with the vdM technique the cross section of events that give signals in both sides of the VZERO scintillator detector (VZERO-AND) [153]. Those events are mainly non single diffractive events and they are a subsample of the minimum bias events. Offline, it is then possible to compute the ratio of minimum bias events with also the double signal in the VZERO. This ratio has been measured to be $\sigma_{\rm pp,\ VZERO-AND}/\sigma_{\rm pp,\ MB} \sim 0.87$ at both energies and it was found to be stable within 1% over the analyzed data sample. The cross section of minimum bias events have been measured to be $\sigma_{pp,\ MB} = 62.5 \pm 0.4$ (stat) ± 4.3 (syst) mb at $\sqrt{s} = 7$ TeV [154].

To cross-check this measurement, another process has been used for which its cross section has been measured: the production of at least a charged primary charged particle in the collision. This method has also been called the "candle". Instead of considering minimum bias events, the production of at least a primary particle in the event is taken as reference process. This method can also allow a straight-forward comparison with the other LHC experiments, if the same "candle" is adopted. In this case, it has been consider the production of at least one charged primary particle in the region $|\eta| < 0.9$ and with

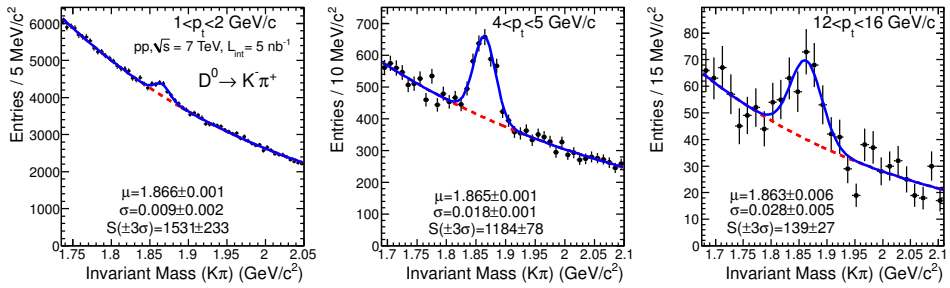

Figure 5.17: D^0 invariant mass spectra reconstructed in pp collisions at $\sqrt{s} = 7$ TeV for three different p_t bins ($1 < p_t < 2$ GeV/c, $4 < p_t < 5$ GeV/c, $12 < p_t < 16$ GeV/c) [155].

$p_t > 0.5$ GeV/c. This cross section has been measured to be $\sigma_{pp,\ candle} = 44.25 \pm 0.26$ (stat) ± 3.09 (syst) mb. Using then the number of events with at least one "candle" in the event, corrected for particle reconstruction efficiencies, it is possible to compute the normalization factor for the candle process. The normalization factor is defined as the number of events divided for the corresponding cross section. For the VZERO-AND and the "candle" processes the normalization factors have been found to be in agreement within the 4% systematic uncertainties.

5.3.2 D^0 cross section at $\sqrt{s} = 7$ TeV

A complete review of these results, for the three mesons D^0, D^+ and D^{*+}, can be found in [155].

Raw yield extraction

The D^0 signal in pp collisions is clearly visible in 9 p_t bins, from 1 up to 16 GeV/c. In Fig. 5.17 the peaks shown for the p_t interval $1 < p_t < 2$ GeV/c, $4 < p_t < 5$ GeV/c, $12 < p_t < 16$ GeV/c. The analysis is performed as in Pb–Pb collisions, extracting the signal with the fit of the invariant mass distribution. The means and the r.m.s of the mass peak are compatible with the PDG values, within errors. The selection cuts used to extract the signal are looser than the Pb–Pb ones, since the background is much lower and cuts can be released accordingly.

Corrections

Proton-proton collisions were simulated using the PYTHIA 6.4.21 event generator with Perugia-0 tuning [149, 150]. Only events containing D mesons were transported through the apparatus and reconstructed. The efficiency has been extracted separately for prompt D mesons and D mesons from B hadrons decays. At low p_t, efficiencies are of the order of 1% or less, at higher p_t the efficiencies increase and flatten about 10-20% for D^0 and D^+ and 30% for D^{*+}. The efficiencies without particle identification selections indicate the fully efficient PID selection. As for Pb–Pb collisions, efficiencies for mesons coming from beauty hadrons decays are larger about by a factor of 2, due to the fact that feed-down D mesons are more displaced from the primary vertex, because of the larger B mesons lifetime. For D^{*+} the topological cuts on secondary vertices have been released for $p_t > 4$ GeV/c for the very low background and the efficiencies are almost the same for the two cases.

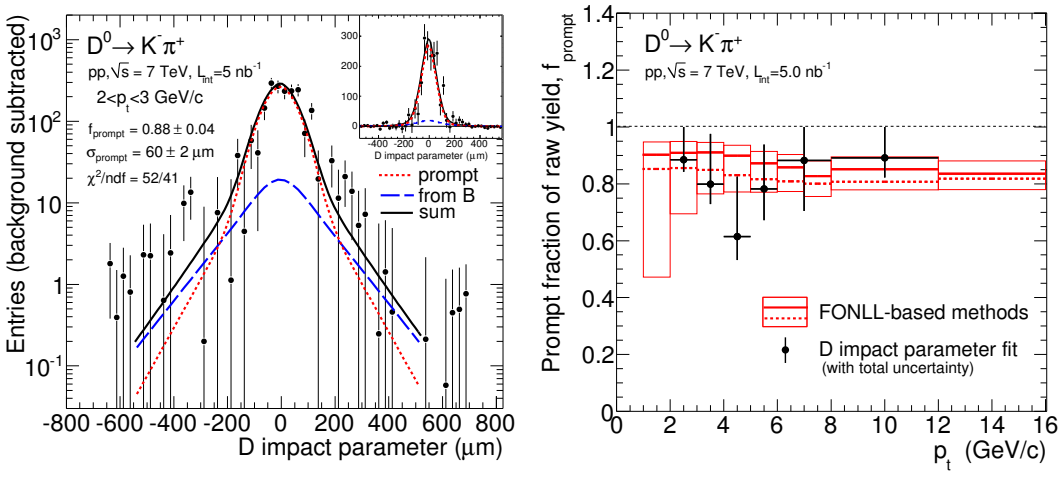

Figure 5.18: Example of D^0 impact parameter combined fit of prompt and non prompt mesons for $2 < p_t < 3$ GeV/c (left). Prompt fraction f_{prompt} of D^0 raw yield as a function of p_t, for the FONLL based methods and for the impact parameter fit method (right) [155].

Feed-down subtraction was performed with pQCD FONLL calculations as described for Pb–Pb collisions. Due do to the higher statistics available, the method was checked with a data-driven method. The prompt fraction of D^0 mesons in the reconstructed yield has been estimated based on the measured impact parameter distribution of D^0 candidates in each p_t interval, as done also by the CDF Collaboration [110]. This method exploits the different shapes of the distribution of the impact parameter of prompt and feed-down (displaced) D mesons. The impact parameter distribution of D^0 mesons was obtained from the one measured for candidates with invariant mass in the range $|m - M_{D^0}| < 2\sigma$, after subtracting the background contribution, estimated in the side-bands. The prompt fraction was estimated by fitting the resulting impact parameter distribution with a two-component function. The first component is a detector resolution term, modelled by a Gaussian and an exponential term, describing the impact parameter of prompt D mesons. The second component accounts for the reconstructed impact parameter distribution of D from B decay, which is modelled by a convolution of the same detector resolution term with a double-exponential function describing the true impact parameter of secondary D mesons. The fit parameters are the width of the Gaussian and the fraction of prompt D mesons, that is the relative weight of prompt and secondary D mesons components. An example of such a fit is shown in Fig. 5.18 (left) for the D^0 mesons in the transverse momentum interval $2 < p_t < 3$ GeV/c. The prompt fraction of D^0 mesons, measured with this data driven method for $2 < p_t < 12$ GeV/c is shown in Fig 5.18 (right). In the same figure also the fraction of prompt D mesons computed with FONLL calculation is shown and the agreement between the two is evident. Because of the large background for $p_t < 2$ GeV/c and the poor statistics available for $p_t > 12$ GeV/c, this method was used in the pp analysis as a check of the FONLL-based prompt fraction estimation.

Cross section results

Fig. 5.19 shows the p_t-differential inclusive cross section for prompt D^0 [155]. The error bars represent the statistical uncertainties, while systematic uncertainties are shown as boxes around the data points. The systematic uncertainties have been evaluated, as for

Pb–Pb, taking into account various contributions.

The measured D^0 cross section is also compared to two theoretical predictions, FONLL [50] and GM-VFNS [53]. Both calculations use CTEQ6.6 parton distribution functions [156] and vary the factorization scales μ_F and μ_R (introduced in Sec. 2.1.1) independently in the ranges $0.5 < \mu_F/m_t < 2$, $0.5 < \mu_R/m_t < 2$, with the constraint $0.5 < \mu_F/\mu_R < 2$, where $m_t = \sqrt{p_t^2 + m_c^2}$. The central value of the GM-VFNS predictions lies systematically above the data, while FONLL predictions lies below the data, as already observed also in previous lower energy experiments [110]. The first point for the cross section is measured in the range $1 < p_t < 2$ GeV/c, this measurement probes the gluon distribution in the x range of a few 10^{-4}.

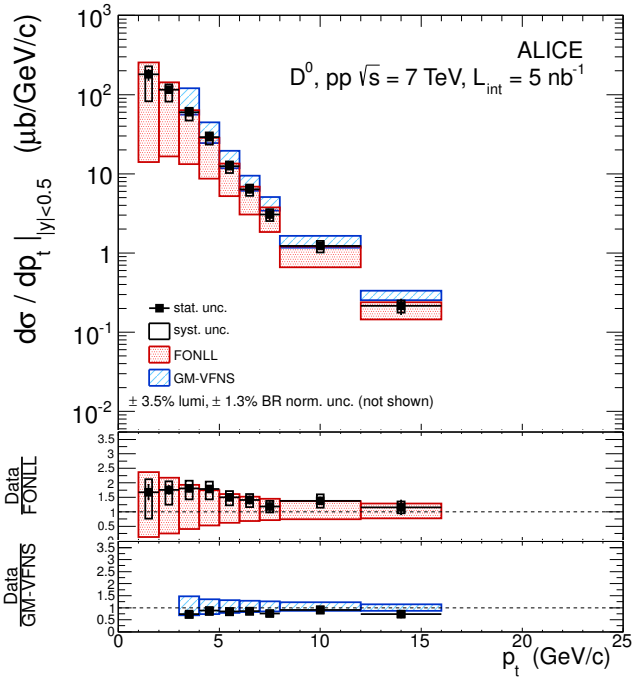

Figure 5.19: D^0 cross section measured in pp collisions at $\sqrt{s} = 7$ TeV in the range $1 < p_t < 16$ GeV/c. The measurement is compared with FONLL [50] and GM-VFNS [53] calculations [155].

5.3.3 D^0 cross section at $\sqrt{s} = 2.76$ TeV

The pp data at $\sqrt{s} = 2.76$ TeV have been delivered and collected in only 3 days of the LHC running and they allowed to measure the D^0, D^+ and D^{*+} cross sections, from $2 < p_t < 8$ GeV/c [157].

Raw yield extraction

The analysis of this data sample has been performed as all the other described so far. The low statistics is the main feature of this data set and it has to be considered when discussing this analysis. The raw yield extraction has been done with looser selection cuts than those at $\sqrt{s} = 7$ TeV since the total number of D^0 signals is very low. A new dedicated study on the selection cuts has been performed in order to better calibrate the

signal and the background of this data sample, taking into account also the stability of these selections to avoid signal fluctuations.

Cross section results

Corrections have been computed as it was done at $\sqrt{s} = 7$ TeV with a, accordingly tuned, Monte Carlo study for the selection efficiencies and using pQCD FONLL calculations for the feed-down contributions. Results of the D^0 cross section are shown in Fig. 5.20 (left) [157]. Also in this case, the error bars represent the statistical uncertainties and the boxes surrounding the point represent the systematic uncertainties.

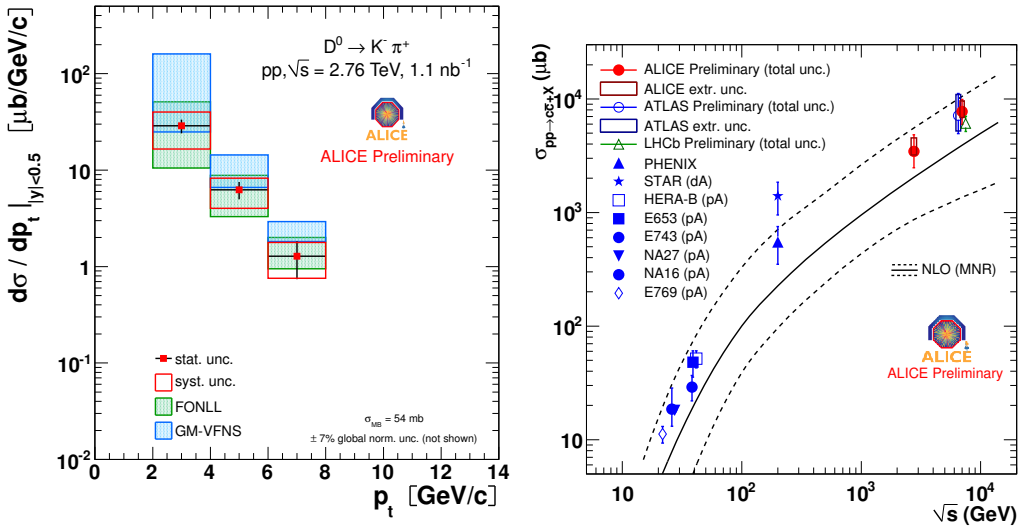

Figure 5.20: D^0 cross section measured in pp collisions at $\sqrt{s} = 2.76$ TeV in the range $2 < p_t < 8$ GeV/c. The measurement is compared to FONLL [50] and GM-VFNS [53] calculations (left). Total charm production cross section measured by ALICE (red points) at $\sqrt{s} = 2.76$ TeV and $\sqrt{s} = 7$ TeV. Results are compared with other LHC experiments [158, 159] and NLO calculations [49]. Both show good agrement with ALICE points (right) [157].

Results are compared with FONLL [50] and GM-VFNS [53] calculations. Also at this energy, the FONLL seems to underestimate a bit the measured values and GM-VFNS results overestimate the data, although both calculations are compatible with the measurement within systematic uncertainties.

Once measured the three mesons p_t-integrated visible cross section, it is possibile to measure the total charm production cross section using an extrapolation procedure. Using FONLL pQCD calculation [50], it is possible to extrapolate down to $p_t = 0$ these cross section results and in the full rapidity range. Combining then these results, according to the different branching fractions, the total charm production cross section at $\sqrt{s} = 7$ TeV was computed. The same was done for $\sqrt{s} = 2.76$ TeV. The results, shown in Fig. 5.20 (right) for both energies, are in agreement with NLO calculations [49], proving the good agreement of this theory with data over three orders of magnitude. ALICE data points (red) are also in agreement with what has been measured by the ATLAS [158] and LHCb [159] experiments.

6 D^0 nuclear modification factor

This chapter presents the results on the nuclear modification factor for the D^0 meson, measured with the ALICE experiment at the LHC. As already pointed out, this is the first direct measurement of charm energy loss in ultra-relativistic heavy-ion collisions. Previous measurements were done with electrons coming from charm and beauty decays but without separating the two contributions.

The first part of the chapter is dedicated to the ingredients needed to define the nuclear modification factor $R_{\rm AA}$. The *pp* reference at the same energy as Pb–Pb collisions is computed by scaling, using FONLL calculations, the ALICE measurement at $\sqrt{s} = 7$ TeV. The other main ingredient for the nuclear modification factor is an hypotesis on beauty $R_{\rm AA}$ when secondary D^0's are subtracted.

The second part of the chapter is focused on the nuclear modification factor results as a function of $p_{\rm t}$ and as a function of the collision centrality.

The last part of the chapter is dedicated to the comparison with results obtained with other two charmed mesons D^+ and D^{*+} with the ALICE experiment. A comparison also with charged particle nuclear modification factor will be shown and with theoretical models.

6.1 D^0 Nuclear Modification Factor in Pb–Pb collisions: ingredients

6.1.1 *pp* scaled reference

The nuclear modification factor measurement is based on the comparison of the yield measured in *pp* and Pb–Pb collisions at the same energy. In the LHC 2011 run with *pp* collisions at $\sqrt{s} = 2.76$ TeV, ALICE collected about 6.3×10^7 events in 3 days, that allowed to measure the D^0 cross section only up to 8 GeV/c due to the low statistics.

It was thus necessary to have another procedure to obtain the *pp* reference at $\sqrt{s} = 2.76$ TeV, especially for the heavy-flavour sector, where the required statistic is higher with respect to other measurements.

The *pp* reference can be obtained using the 7 TeV measurement [155] and scale it down to lower energies using pQCD calculations. It was already shown [160] using MNR [49] NLO calculations, at the energies $\sqrt{s} = 5.5$ TeV and 14 TeV, that the ratio of the cross sections at the two energies is not much dependent on the choice of the calculation parameters (factorization scales and quark mass). Following this approach, the ALICE charm cross section measured at 7 TeV has been scaled to 2.76 TeV using FONLL calculations. In order to validate the procedure, the cross section has also been scaled to $\sqrt{s} = 1.96$ TeV and compared to the results from the CDF experiment [110].

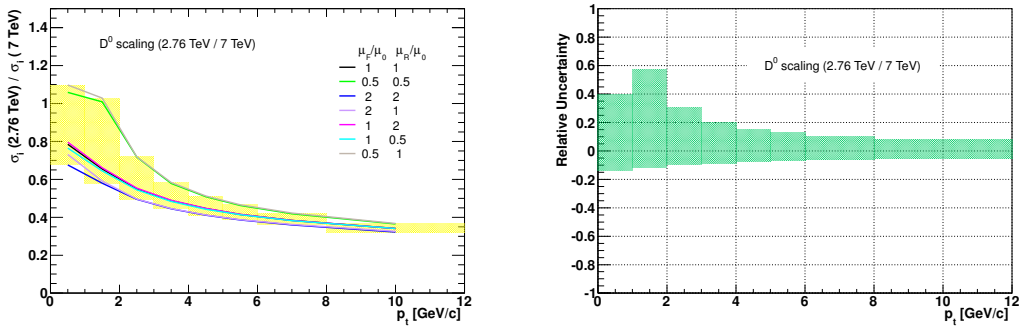

Figure 6.1: D^0 FONLL scaling to 2.76 TeV from 7 TeV binning considering different hypotheses as the parameter of the theoretical calculations (right). Relative uncertainties of the scaling factor considering the different hypotheses shown in the right panel (left).

Procedure

The procedure followed to scale ALICE 7 TeV results is based on the FONLL pQCD calculations, other pQCD calculations have been considered as cross check. The FONLL driven scaling is evaluated considering the different sets of scales: factorization scale μ_{F}, renormalization scale μ_{R} and c quark mass values m_{c}. The parameters $\mu_{\mathrm{F}} = \mu_{\mathrm{R}}$ and $m_{\mathrm{c}} =$ 1.5 GeV were used as central value of the calculation. A standard parameters variation is, then, considered to evaluate the theoretical uncertainty on the charm production cross section: $0.5 < \mu_F/m_t < 2$, $0.5 < \mu_R/m_t < 2$, with the constraint $0.5 < \mu_F/\mu_R < 2$, where $m_t = \sqrt{p_{\mathrm{t}}^2 + m_{\mathrm{c}}^2}$. The quark mass was varied within $1.3 < m_{\mathrm{c}} < 1.7$ GeV.

The procedure to compute the FONLL scaling factor from 7 TeV to an energy of α TeV starts from the rebin of the FONLL predictions for $\sigma(\alpha)$ and $\sigma(7$ TeV) for the different sets of scales and quark masses, according to the ALICE 7 TeV p_{t} binning of the measurement [1]. The second step of the procedure is the estimate of the ratio of the two cross sections estimate by FONLL: $\sigma(\alpha)/\sigma(7$ TeV). The central value is defined by the central predictions at both energies, the uncertainties are defined by the envelope of the ratio of the predictions for different sets of parameters, always keeping the same parameters at the two energies. Once the theoretical scaling factor is computed, it is multiplied by the ALICE 7 TeV measurement and the uncertainties are propagated correspondingly from the scaling FONLL factor and from the measurement.

Results

In Fig. 6.1 (left) results for the D^0 scaling factor are shown. The factors obtained with different sets of scales are drawn with solid lines, while the resulting uncertainties is drawn with a yellow band. The scaling factors depend mainly on the value of the factorization scale, with almost no dependence on the renormalization scale. Indeed, for the same heavy quark p_{t}, different Bjorken x ranges are probed at these two different energies. Also the parton distribution functions at different Q^2 values are probed by changing the factorization scale. The value of the mass of the charm quark is not changing the scaling factor. The scaling factor varies a function of p_{t}, especially below 5 GeV/c, where it reaches about 50% variation, while for higher p_{t} the variation is less pronounced. In

[1] The procedure is used for all open heavy flavour observable measured by ALICE. This part will be focused on the D mesons scaling and results will be shown for the D^0.

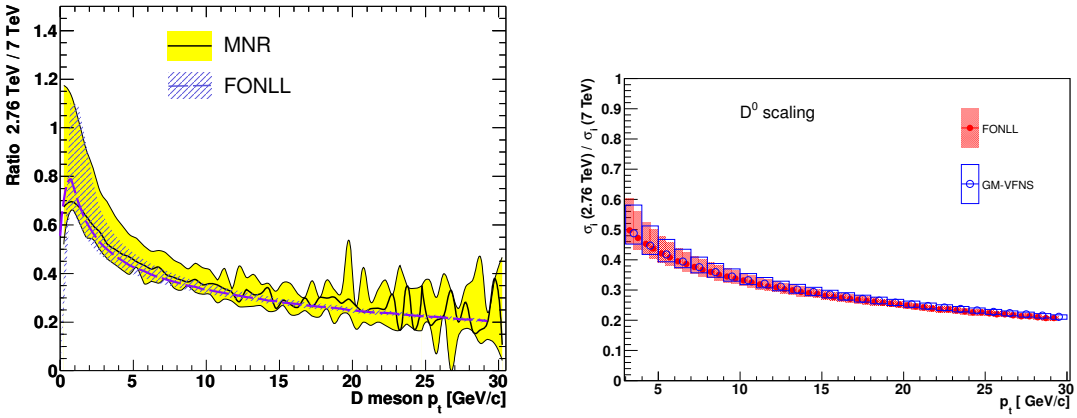

Figure 6.2: D^0 MNR scaling to 2.76 TeV from 7 TeV (yellow band) compared to FONLL scaling (purple band). Results of the two methods are totally in agreement and the FONLL uncertainties are smaller than the MNR ones (left). D^0 FONLL scaling factor compared with the one obtained using GM-VFNS approach (right).

Fig. 6.1 (right) the relative uncertainty is shown. The effect of the factorization scales is reflected also in the error, which is larger for low p_t, where the spread between the different hypotheses is larger.

The FONLL scaling has been compared to that obtained with MNR [49] and GM-VFNS [53], using the same procedure. The comparison between MNR and FONLL calculations for D^0 mesons (Fig. 6.2 left) shows that the scaling factors agree with each other but that the MNR uncertainties are larger. The comparison of D^0 scaling factors computed with FONLL and GM-VFNS calculations is shown in Fig. 6.2 (right) and the agreement is clearly visibile.

The FONLL scaling factor will be taken as a reference since its uncertainty is smaller than the MNR one.

Comparisons with data

Two comparisons with data have been performed in order to "validate" the scaling procedure. The first comparison is with CDF results at $\sqrt{s} = 1.96$ TeV [161]. The second comparison is with the measured D mesons cross section at 2.76 TeV [157]. The limited statistics available at this energy does not allow to use these results as a reference for $R_{\rm AA}$. It was thus decided to use the pQCD calculation based scaling factors and cross check it where possible with the measured results.

Fig. 6.3 (left) shows the D^0 cross section scaled to 1.96 TeV [161] (purple points with blue boxes) compared with CDF results [110]. The two cross sections are in agreement within uncertainties. Fig. 6.3 (right) shows the p_t-differential cross section at $\sqrt{s} = 2.76$ TeV obtained by scaling the ALICE results at $\sqrt{s} = 7$ TeV. In the figure the systematic uncertainties coming from the FONLL scaling and "inherited" from the ALICE measurement are shown separately and combined together in the purple empty boxes.

Within the p_t range 2-8 GeV/c it is also possible to compare the scaling with the ALICE results obtained from the pp data at $\sqrt{s} = 2.76$ TeV [157]. Fig. 6.4 (left) shows the D^0 cross section (already presented in section 5.3.3). In Fig. 6.4 (right), the ratio of the

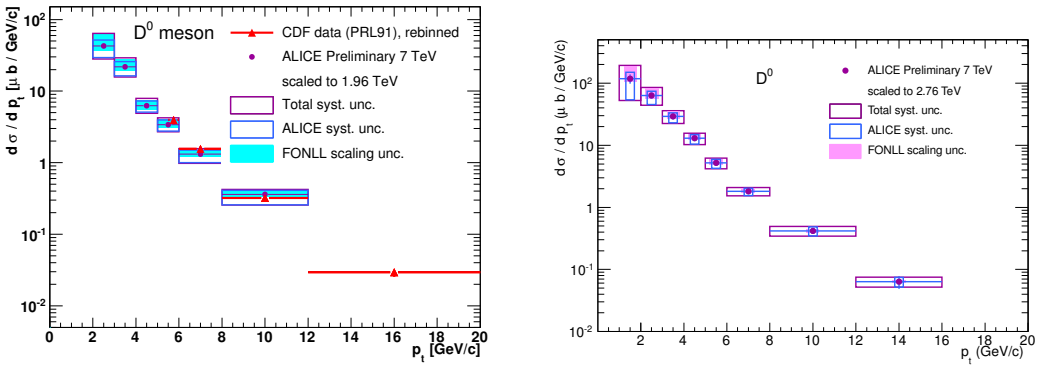

Figure 6.3: Comparison of the D^0 ALICE 7 TeV measurements scaled to 1.96 TeV with the CDF measurement (right). D^0 cross section at 2.76 TeV obtained from the scaling of the 7 TeV method using pQCD calculations (left).

cross section obtained with the measurement over the one obtained with the pQCD scaling method is shown. The ratio is in agreement with unity within statistical and systematic uncertainties.

These two important results showed clearly the validity of the scaling procedure and to obtain a reference for the nuclear modification factor of the D^0 meson.

6.1.2 b quark energy loss hypothesis

As described in Sec. 5.2.3, the contribution of D mesons coming from beauty decays has been computed and subtracted from the raw yield with FONLL calculations. With respect to pp, in Pb–Pb collisions there is the additional complication that also beauty quarks hadron can interact with the medium and loose energy. The resulting beauty $R_{\rm AA}$ is unknown, for the moment. Recently, the CMS experiment has measured the nuclear modification factor for displaced J/Ψ mesons coming from B decays [166]. This measurement will be described together with other recent open heavy flavour results in Sec. 6.3.3.

For the analysis of the prompt D mesons $R_{\rm AA}$, an hypotesis on the nuclear modification factor of the beauty ($R_{\rm AA}^{\rm feed-down}$) is adopted [151]. The central value of both $dN/dp_{\rm t}$ and $R_{\rm AA}$ is calculated considering equal the nuclear modification factor for secondary and prompt D mesons ($R_{\rm AA}^{\rm feed-down} = R_{\rm AA}^{\rm prompt}$). This hypotesis is then varied in the range $0.3 < R_{\rm AA}^{\rm feed-down}/R_{\rm AA}^{\rm prompt} < 3$ in order to consider extreme and opposite scenarios. This variation enters as a systematic uncertainty on the results. The contribution of this energy loss hypotesis is at most 30% as shown in Fig. 6.5. There, the relative prompt D^0 yield variation as a function of $R_{\rm AA}^{\rm feed-down}/R_{\rm AA}^{\rm prompt}$ is shown for four different $p_{\rm t}$ intervals.

Considering the resulting values of $R_{\rm AA}^{\rm prompt}$ that will be shown in the next section, the variation of the hypotesis on $R_{\rm AA}^{\rm feed-down}/R_{\rm AA}^{\rm prompt}$ corresponds to values of the nuclear modification factor of secondary D mesons in a range of about $0.17 - 1.5$ at low $p_{\rm t}$ and $0.08 - 0.75$ at high $p_{\rm t}$.

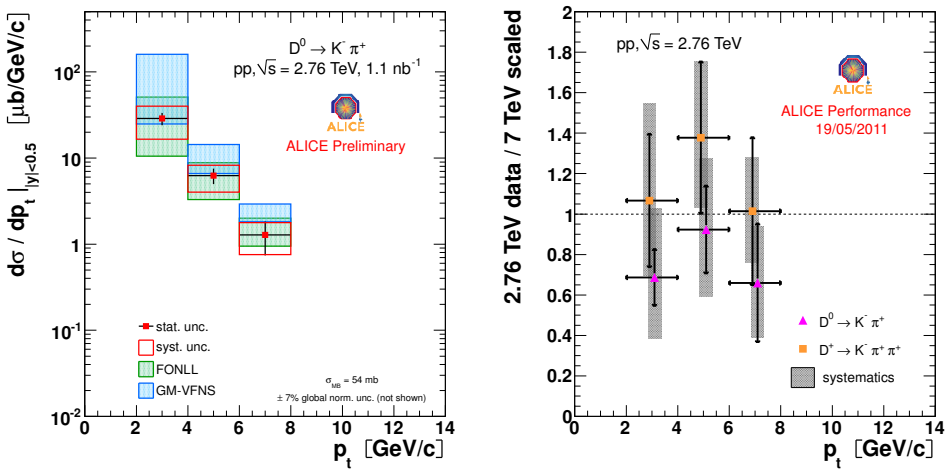

Figure 6.4: ALICE measured D^0 cross section at $\sqrt{s} = 2.76$ TeV (right). Ratio of the cross section measured at 2.76 TeV over the cross section obtained with the scaling procedure starting with the 7 TeV ALICE measurement (left).

6.2 D^0 Nuclear Modification Factor in Pb–Pb collisions: results

As already introduced in Sec. 2.1.4, the nuclear modification factor is defined as the ratio of the yield measured in A–A collisions in a given centrality class, divided by the reference cross section in *pp* collisions, scaled by the average nuclear overlap function, for that A–A centrality class (Eq. 6.1):

$$R_{\mathrm{AA}}(p_{\mathrm{t}}) = \frac{dN_{\mathrm{AA}}/dp_{\mathrm{t}}}{\langle T_{\mathrm{AA}} \rangle \times d\sigma_{pp}/dp_{\mathrm{t}}} = \frac{dN_{\mathrm{AA}}/dp_{\mathrm{t}}}{\langle N_{\mathrm{coll}} \rangle \times dN_{pp}/dp_{\mathrm{t}}} \tag{6.1}$$

Table 6.1 shows the average values for the number of participating nucleons in the collision, the number of binary collisions and the values of the nuclear overlap function, for the centrality classes used for the results. The number of participant in the collisions can be estimated using the Glauber model calculation [15]. In this model, the nuclear density for ^{208}Pb is modeled with a Woods-Saxon distribution for a spherical nucleus with a radius of 6.62 fm and a skin depth of 0.546 fm, based on data from low energy electron-nucleus scattering experiments [147]. A hard-sphere exclusion distance of 0.4 fm between nucleons is used. Nuclear collisions are modeled by randomly displacing the two colliding nuclei in the transverse plane [20].

Before showing the results obtained for the D^0 nuclear modification factor, the systematic uncertainties will be described.

6.2.1 Systematic uncertainties on R_{AA}

The sources of systematic uncertainties on the R_{AA} measurement are: the reference cross section for *pp* collisions, the Pb–Pb invariant yield and the average nuclear overlap function for the different centrality classes.

For the *pp* reference there are two contributions that need to be considered. The scaling factor uncertainties were shown in the first section of this chapter. They arise from the variation of the calculation parameters. The other contribution comes from the systematic uncertainties on the ALICE 7 TeV measurement [155].

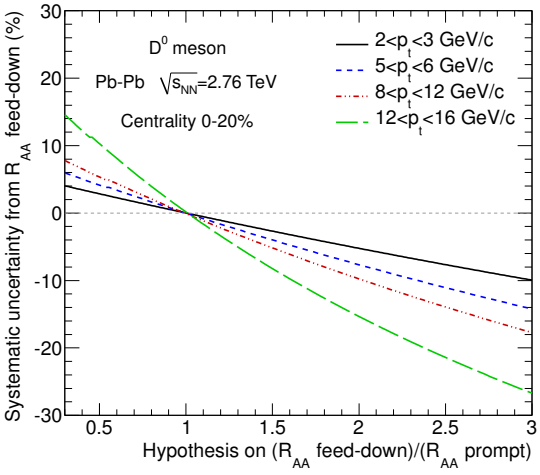

Figure 6.5: Relative variation on the prompt charm yield as a function of the hypothesis on the beauty energy loss, expressed in term of the ratio $R_{\rm AA}^{\rm feed-down}/R_{\rm AA}^{\rm prompt}$ [151].

Table 6.1: Average values of the number of participating nucleons, the number of binary collisions and of the nuclear overlap function for the considered centrality classes, expressed as percentiles of the inelastic cross section.

centrality class	$\langle N_{\rm part}\rangle$	$\langle N_{\rm coll}\rangle$	$\langle T_{\rm AA}\rangle$ (mb^{-1})
0–20%	308 ± 3	1211 ± 131	18.93 ± 0.74
40–80%	46 ± 2	77 ± 8	1.20 ± 0.07
0–10%	357 ± 4	1503 ± 170	23.48 ± 0.97
10–20%	261 ± 4	923 ± 100	14.43 ± 0.57
20–40%	157 ± 3	439 ± 44	6.85 ± 0.28
40–60%	69 ± 2	128 ± 13	2.00 ± 0.11
60–80%	23 ± 1	27 ± 2	0.42 ± 0.03

The systematic uncertainties on the invariant yield extraction have been discussed in Sec. 5.2.4. The nuclear overlap function systematic errors are shown in Table 6.1.

For $R_{\rm AA}$, the *pp* and Pb–Pb uncertainties were added in quadrature, except for the feed-down contribution deriving from FONLL uncertainties, that partly cancels in the ratio. This contribution was evaluated by comparing the $R_{\rm AA}$ values obtained with the two methods for feed-down subtraction described in Sec. 5.2.3 and with different heavy quark masses, factorization and renormalization scales used in FONLL calculations. The same method and the same set of FONLL parameters were used for *pp* and Pb–Pb data, so as to take into account the correlations of these sources in the numerator and denominator of the nuclear modification factor.

Table 6.2 shows a summary of all the systematic uncertainties that enter in the $R_{\rm AA}$ calculations for all $p_{\rm t}$ bins, for both centrality classes 0-20% and 40-80% [151]. The normalization uncertainty has two contributions: the normalization uncertainty on the cross section in *pp* collisions at 7 TeV (3.5%) and the error on the nuclear overlap function (Table 6.1).

Table 6.2: Systematic uncertainties on the D^0 R_{AA}

(0-20%CC) Source	2-3	3-4	4-5	5-6	6-8	8-12	12-16 (GeV/c)
Data syst. *pp* and Pb–Pb	$^{+42}_{-27}$%	$^{+33}_{-24}$%	$^{+30}_{-23}$%	$^{+29}_{-23}$%	$^{+28}_{-23}$%	$^{+27}_{-23}$%	$^{+31}_{-27}$%
Data syst. *pp*	17%	14%	14%	14%	15%	15%	17%
Data syst. Pb–Pb	$^{+24}_{-19}$%	$^{+22}_{-17}$%	$^{+22}_{-17}$%	$^{+22}_{-17}$%	$^{+21}_{-16}$%	$^{+21}_{-16}$%	$^{+25}_{-21}$%
$\sqrt{s}$-scaling *pp* ref.	$^{+30}_{-1}$%	$^{+20}_{-9}$%	$^{+15}_{-8}$%	$^{+12}_{-7}$%	$^{+10}_{-6}$%	$^{+8}_{-5}$%	$^{+6}_{-5}$%
Feed-down & En. Loss	$^{+21}_{-17}$%	$^{+15}_{-19}$%	$^{+15}_{-22}$%	$^{+14}_{-26}$%	$^{+15}_{-34}$%	$^{+14}_{-32}$%	$^{+27}_{-51}$%
FONLL Feed-down	$^{+12}_{-1}$%	$^{+6}_{-3}$%	$^{+4}_{-6}$%	$^{+5}_{-8}$%	$^{+8}_{-13}$%	$^{+7}_{-11}$%	$^{+14}_{-19}$%
Beauty En. loss	$^{+7}_{-19}$%	$^{+8}_{-21}$%	$^{+10}_{-24}$%	$^{+9}_{-23}$%	$^{+10}_{-26}$%	$^{+11}_{-26}$%	$^{+14}_{-19}$%
Norm.	5%						
(40-80%CC) Source	2-3	3-4	4-5	5-6	6-8	8-12	12-16 (GeV/c)
Data syst. *pp* and Pb–Pb	$^{+39}_{-26}$%	$^{+31}_{-23}$%	$^{+28}_{-23}$%	$^{+27}_{-23}$%	$^{+26}_{-23}$%	$^{+25}_{-23}$%	$^{+26}_{-24}$%
Data syst. *pp*	17%	14%	14%	14%	15%	15%	17%
Data syst. Pb–Pb	$^{+18}_{-15}$%	$^{+18}_{-15}$%	$^{+18}_{-15}$%	$^{+18}_{-16}$%	$^{+18}_{-15}$%	$^{+18}_{-15}$%	$^{+18}_{-16}$%
$\sqrt{s}$-scaling *pp* ref.	$^{+30}_{-1}$%	$^{+20}_{-9}$%	$^{+15}_{-8}$%	$^{+12}_{-7}$%	$^{+10}_{-6}$%	$^{+8}_{-5}$%	$^{+6}_{-5}$%
Feed-down & En. Loss	$^{+20}_{-20}$%	$^{+14}_{-23}$%	$^{+15}_{-23}$%	$^{+14}_{-24}$%	$^{+13}_{-25}$%	$^{+14}_{-28}$%	$^{+12}_{-28}$%
FONLL Feed-down	$^{+10}_{-1}$%	$^{+4}_{-2}$%	$^{+4}_{-2}$%	$^{+3}_{-3}$%	$^{+2}_{-1}$%	$^{+1}_{-2}$%	$^{+1}_{-1}$%
Beauty En. loss	$^{+8}_{-21}$%	$^{+10}_{-24}$%	$^{+10}_{-25}$%	$^{+11}_{-26}$%	$^{+11}_{-26}$%	$^{+12}_{-28}$%	$^{+12}_{-27}$%
Norm.	8%						

6.2.2 R_{AA} as a function of transverse momentum

The left panel of Fig. 6.6 shows the nuclear modification factor of D^0 mesons as a function of p_t, measured in the 0-20% central events. The vertical bars represent the statistical uncertainties, typically about 20-25%. The total p_t-dependent systematic uncertainties, drawn with the empty boxes, include all the contributions described in the previous section except for the normalization uncertainties that is shown with a filled gray box at $R_{AA} = 1$.

The D^0 R_{AA}, in the 0-20% central events, shows a clear suppression that reaches a factor 3-4 for $p_t > 5$ GeV/c, where the R_{AA} value is about 0.25-0.3. For lower p_t, the suppression seems to be reduced to a factor of 2 ($R_{AA} = 0.5$) but with about 50% global systematic uncertainties.

The right panel of Fig. 6.6 shows the nuclear modification factor for the D^0 in events belonging to the 40-80% centrality class. The suppression is reduced for these more peripheral events with $R_{AA} \sim 0.7$ for $p_t > 5$ GeV/c.

For completeness, Fig. 6.7 shows again the D^0 R_{AA} but with separate systematic uncertainties contributions. The empty boxes shows the data systematic errors, the violet full boxes represent the contribution of the secondary D^0 subtraction and the pink ones the effect of the beauty energy loss variation hypothesis.

6.2.3 R_{AA} as a function of centrality

The nuclear modification factor has also been studied as a function of 5 centrality (0-10%, 10-20%, 20-40%, 40-60% and 60-80%). Results are presented as a function of the average number of participating nucleon in the collisions $\langle N_{part} \rangle$, for the considered centrality classes [151]. Fig. 6.8 (top) shows the results in the p_t range $2-5$ GeV/c and the right panel of the same figure for the p_t range $6-12$ GeV/c. In both figures, the contribution to the systematic uncertainties which is fully correlated between centrality classes (normalization, feed-down corrections and beauty energy loss) is shown with filled boxes. The uncorrelated

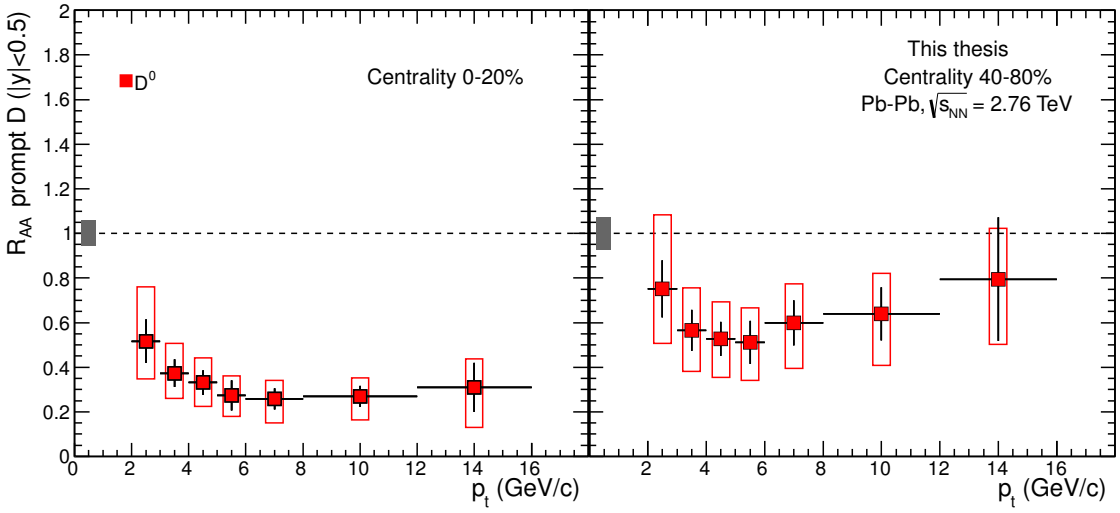

Figure 6.6: $R_{\rm AA}$ for D^0 meson in the 0-20% (left) and 40-80% (right) centrality classes. Statistical (bars), systematic (empty boxes), and normalization (full box) uncertainties are shown [151].

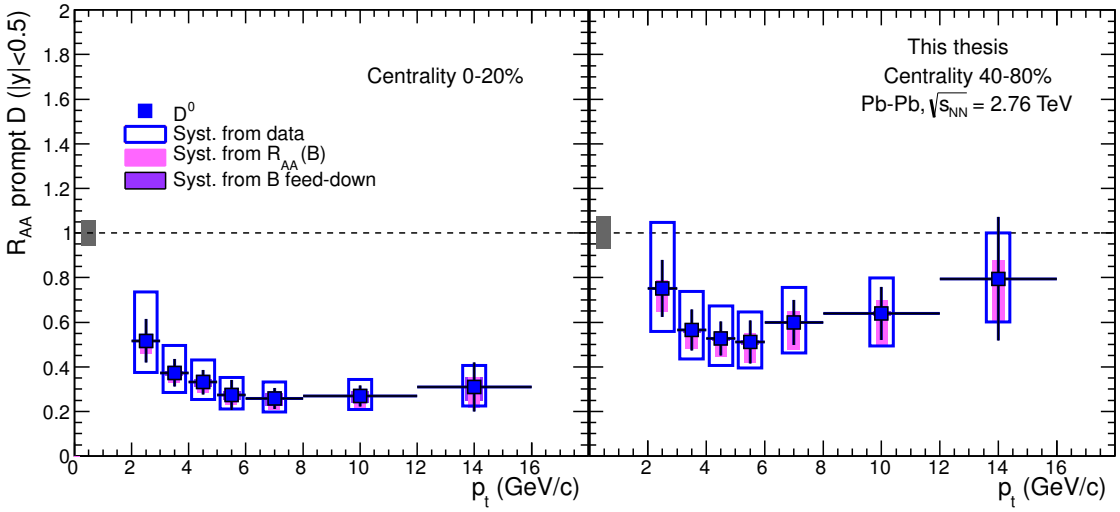

Figure 6.7: $R_{\rm AA}$ for D^0 meson in the 0-20% (left) and 40-80% (right) centrality classes. Data systematic (empty boxes), beauty feed-down systematic (violet boxes) and secondary D mesons energy loss systematic (pink boxes) uncertainties are shown separately [151].

systematic uncertainties, coming from data, are shown with empty boxes[2]. For the $p_{\rm t}$ range $6-12$ GeV/c (bottom), the suppression decreases when going from central to peripheral collisions, showing a clear dependence on the number of the participants in the collisions. For the $p_{\rm t}$ range $2-5$ GeV/c the dependence of the suppression on centrality seems less pronounced.

[2]The uncertainty on the scaled reference is taken into account in the data systematic uncertainty

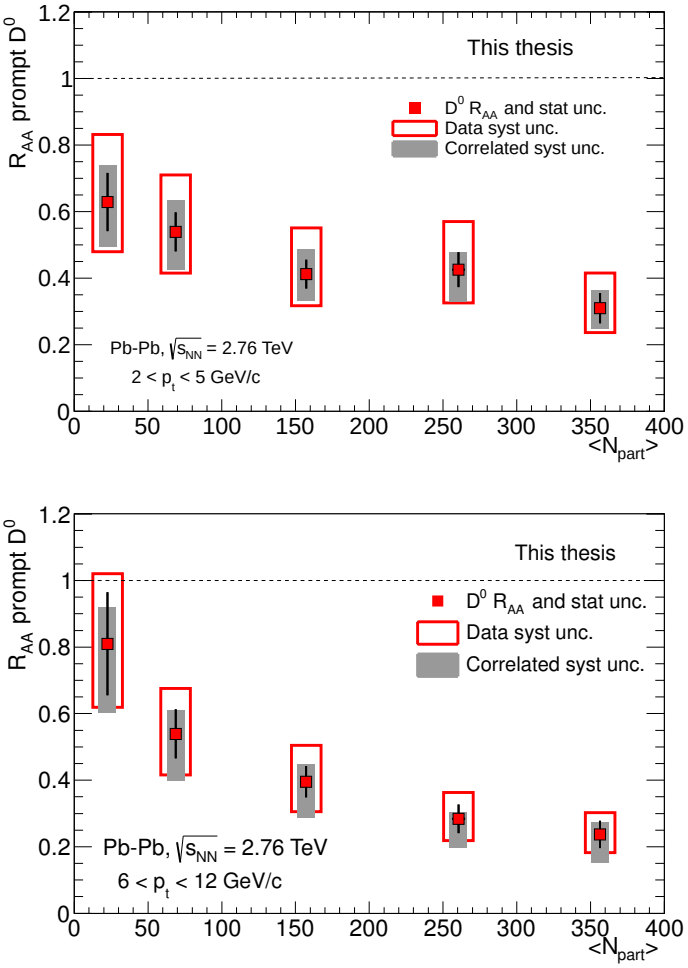

Figure 6.8: D^0 nuclear modification factor as a function of the number of participant in the collisions for $2 < p_t < 5$ GeV/c (top) and $6 < p_t < 12$ GeV/c (bottom) [151].

6.2.4 Comparison with D^+ and D^{*+}

ALICE measured also the nuclear modification factor for the D^+ and D^{*+} mesons, with the same analysis strategy as the one described in details for the D^0 [151]. The results are shown in Fig. 6.9, where a fair agreement for the three measurements for both centrality classes is visible. The p_t bins are slightly different with respect to the D^0 ones, due to the lower statistical significance for D^+ and D^{*+}.

For the comparisons that will be shown in the following sections, an average nuclear modification factor of the three mesons has been computed. The contribution of D^0, D^+ and D^{*+} are weighted by their statistical uncertainties to compute the average. The resulting R_{AA} is very close to the D^0 one, since it is the meson with smaller uncertainties. The systematic uncertainties are propagated quadratically with the same weights, except for the contributions from tracking efficiencies and from the B feed-down subtraction, which are treated as fully correlated between the three mesons.

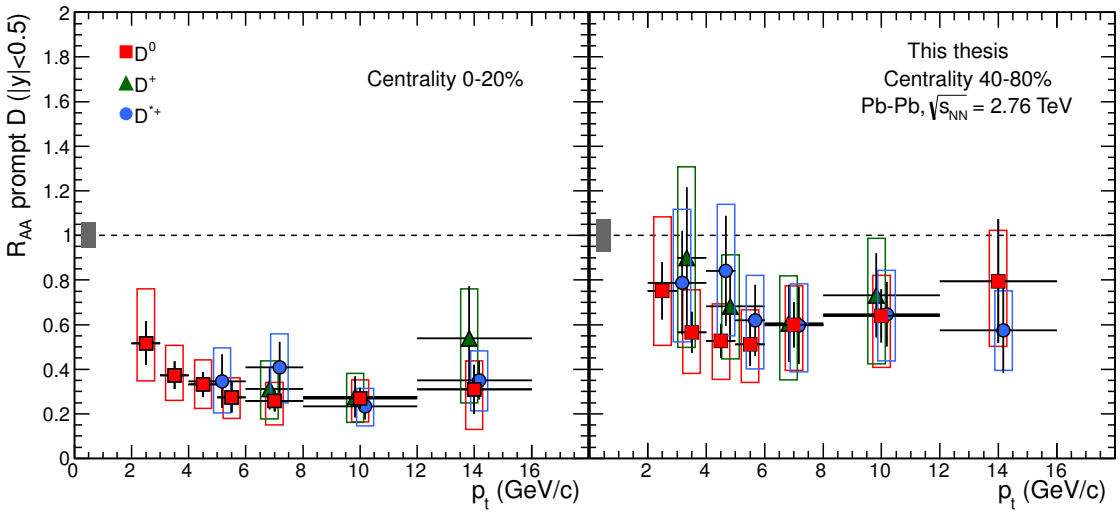

Figure 6.9: R_{AA} for D^0, D^+, and D^{*+} in the 0-20% (left) and 40-80% (right) centrality classes. Statistical (bars), systematic (empty boxes), and normalization (full box) uncertainties are shown [151].

6.3 D mesons nuclear modification factor: comparisons

6.3.1 Nuclear shadowing

Parton energy loss is the predominant final state effect. However, also initial state effect are expected to influence R_{AA}, as discussed in Sec. 2.1.4. The initial hard scattering probability is reduced at low x and Q^2 due to the nuclear modification of the PDFs. In the kinematic range relevant for charm production at the LHC energies, the main effect is the nuclear shadowing, which reduces the partons distribution functions, especially for gluons, for parton fractional momenta x below 10^{-2}.

The expected effect of shadowing on the D mesons R_{AA} was estimated using MNR next-to-leading order pQCD calculation [49] with CTEQ6M parton distribution functions [162] and EPS09 next-to-leading order parametrization [163] of their nuclear modification. The uncertainties band determined by the EPS09 uncertainties is shown in Fig. 6.10 (left) together with the averaged D mesons R_{AA} [151]. The shadowing-induced effect on R_{AA} is limited to $\pm 15\%$ for $p_t > 6$ GeV/c, suggesting that the strong suppression observed in the data is likely to be a final state effect.

6.3.2 Charged hadrons

As already introduced in Sec. 2.2.2, to understand the colour charge and parton mass dependences of parton energy loss, it would be required to compare the R_{AA} of D and π mesons. Since final results on the pion R_{AA} at the LHC are not yet available, D meson results are compared to the charged hadron nuclear modification factor computed in the same centrality class [151]. Preliminary results [164] have shown that charged pion R_{AA} coincides with that of charged hadrons above $p_t \sim 5$ GeV/c and it is lower by about 30% at 3 GeV/c, due to the proton contribution at low-p_t in the charged hadrons R_{AA}. The comparison is reported in Fig. 6.10 (right) and it shows that the average D mesons nuclear modification factor is close to that of charged hadrons. Considering, that

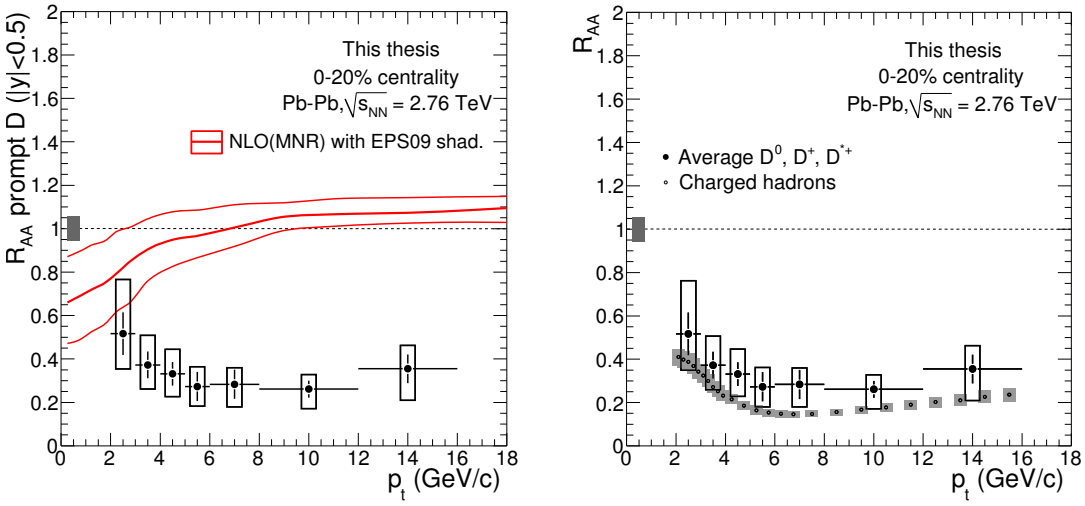

Figure 6.10: Averaged $R_{\rm AA}$ of D mesons in the 0–20% centrality class compared to: left, the expectation from NLO pQCD [49] with nuclear shadowing [163]; right, the $R_{\rm AA}$ of charged hadrons in the same centrality class [151].

systematic uncertainties of D mesons $R_{\rm AA}$ are partially correlated with $p_{\rm t}$, there is an indication that the suppression for D mesons may be larger than for charged hadrons.

6.3.3 Comparison with other open heavy flavor measurements

ALICE measured also the electron spectra in Pb–Pb collisions with the 2010 data [165]. The measurement is based on the track reconstruction with ITS and TPC (Sec. 3.4.1) and the particle identification based on the TOF velocity measurement and TPC energy loss. As it was done in the PHENIX and STAR experiments, the cocktail method has been used also in ALICE to model the background, made of electrons not coming from heavy flavour hadron decays. The preliminary ALICE measurement of the π^+ in Pb–Pb collisions was used as starting point to define the different contributions of the cocktail using the $m_{\rm t}$ scaling approach.

The inclusive electron spectra were measured up to 6 GeV/c and the background, estimated from the cocktail method, has been subtracted. The resulting spectrum has been compared with the one obtained pp collisions at 7 TeV, scaled at 2.76 TeV, to obtain the nuclear modification factor. The suppression goes from a factor 1.5 to about 4 from 1.5 to 6 GeV/c, as it is shown in Fig. 6.11 (black points). As mentioned in Sec. 2.4.1 the heavy flavour decay electrons spectrum is the sum of charm and beauty contributions, the relative contributions dependes on the considered $p_{\rm t}$. The large systematic uncertainties on the electron measurement mainly arise from the electron PID and from the cocktail subtraction, especially that at low $p_{\rm t}$.

With 2010 data, the CMS experiment measured also the nuclear modification factor of displaced J/Ψ mesons that come from beauty decays [39]. This measurement shows the first nuclear modification factor for beauty hadrons. Due to the limited statistics the non-prompt J/Ψ $R_{\rm AA}$ is shown in the centrality bin 0-20% and in one $p_{\rm t}$ bin, $6.5 < p_{\rm t} < 30$ GeV/c (green symbol in Fig. 6.11). The result indicates an agreement with the ALICE electrons measurement, within the large experimental uncertainties. No conclusions can

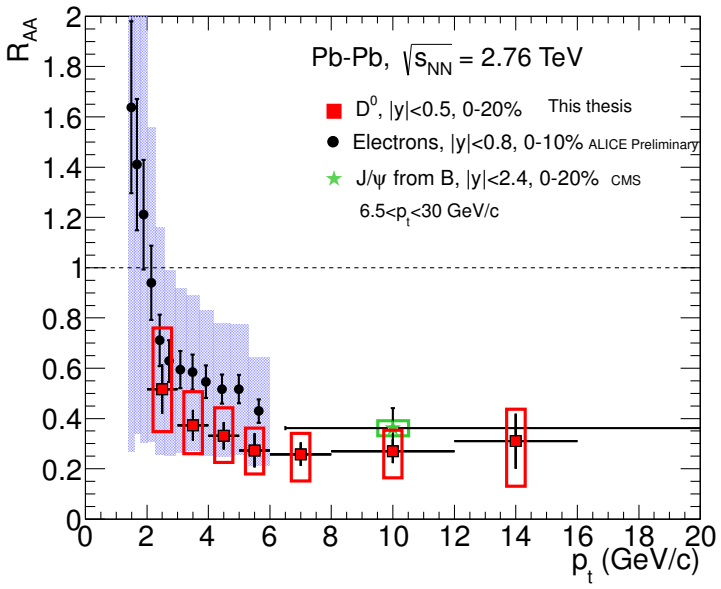

Figure 6.11: D^0 $R_{\rm AA}$ compared with heavy flavour electrons $R_{\rm AA}$ measured by ALICE [165] and displaced J/Ψ measured by CMS [39].

be drown so far on the comparison of the D mesons and displaced J/Ψ suppressions.

6.3.4 Comparison with theoretical models

The average nuclear modification factor of D mesons is compared with models that implement energy loss, as discussed in Sec. 2.2.3.

In Fig. 6.12 (left) the average D mesons $R_{\rm AA}$ is compared with eight models. The right-hand panel of the same figure shows the comparison of the charged hadron $R_{\rm AA}$ with those models that can also predict energy loss for light hadrons. In the following, a brief description of the models will be given together with a comment on the comparison with data.

I This model proposed by Sharma, Vitev and Zhang is based on the DGLV approach (Sec. 2.2.3), considering only the radiative energy loss mechanism [167]. Within the same energy loss formalism the model predicts the suppression for both light and heavy meson final states.

The results shown in Fig. 6.12 (left) for this model overestimate the ALICE results. Within the same approach it is possible to consider also in medium D meson dissociation [168] and the agreement with data is much better in this case.

Also the charged hadron $R_{\rm AA}$ is in agreement with the one measured by ALICE starting from about $p_{\rm t} > 4$ GeV/c.

II This model is based on the WHDG approach presented in Sec. 2.2.3 [169]. The method is based on DGLV calculations considering both collisional and radiative energy loss with realistic geometrical fluctuations of the medium.

The predictions for the charged hadrons $R_{\rm AA}$ are obtained by constraining the model parameters with RHIC 0-5% π^0 $R_{\rm AA}$ and assuming that the QGP density scales

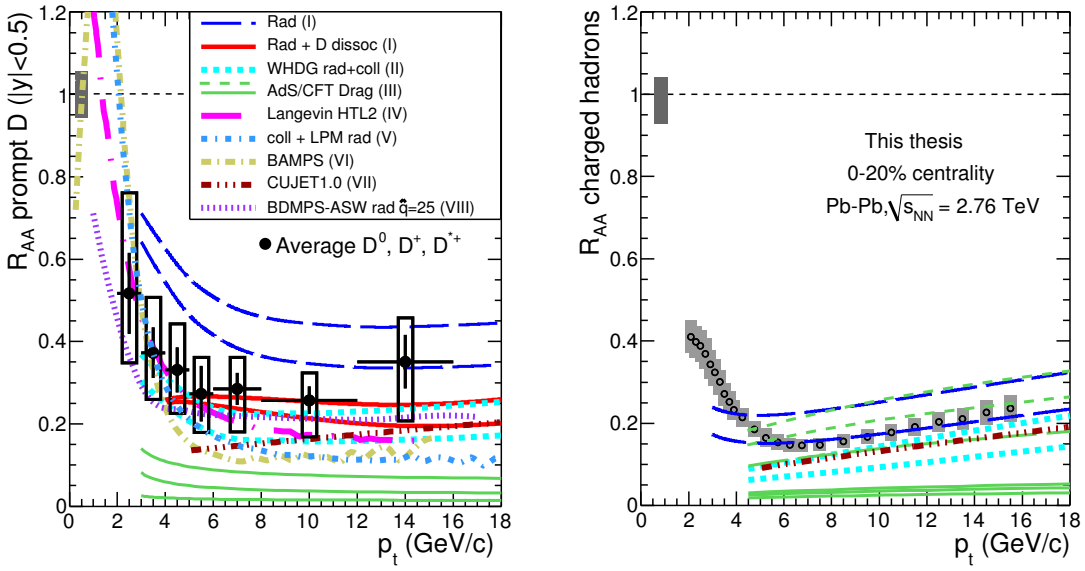

Figure 6.12: Average R_{AA} of D mesons (left) and R_{AA} of charged hadrons (right) in the 0-20% centrality class compared to several model calculations.

from RHIC to LHC with the observed charged multiplicity. The charged hadron suppression measured at the LHC was found to be smaller than expected, when considering the increased energy density from RHIC to LHC. Due to this parameter of the calculation, that need further tuning, the model seems to underestimate the R_{AA} of charged hadrons.

The model seems to be quite in agreement with ALICE data, for what concerns the heavy quark energy loss.

III This calculation is based on the AdS/CFT approach shown in Sec. 2.2.3 [170].

In the AdS/CFT drag model used to compute the heavy and light quark energy loss, the Feynman diagrammatic approach in 4D was replaced by a string derivation in 5 dimensions [172]. As for the previous method it is assumed that the medium density scales from RHIC to LHC, with observed charged multiplicity.

The three AdS/CFT drag curves, shown in the plot, cover the possible parameter space associated with the duality between QCD parameters and Super Yang-Mills theory in 4 dimensions [171].

Both for D meson and charged hadrons nuclear modification factors the suppression is overestimated with this AdS/CFT calculation.

IV This model is based on the framework of Langevin dynamics in the background of an expanding deconfined medium described by ideal and viscous hydrodynamics [173]. As shown in Sec. 2.2.3, this model cannot provide a prediction for light mesons nuclear modification factor, since the starting point of the model is the heavy quark dynamics within the medium.

The transport coefficients for the heavy quark are then obtained by matching the hard-thermal-loop results for soft collisions with the pQCD calculation for hard

scattering. From these transport coefficients, the heavy-quark spectra are obtained and compared with the *pp* one to build the R_{AA} The agreement with ALICE results is good.

V The pQCD model presented in [174] is based on a collisional energy loss mechanism for heavy quarks. With respect to other models, this takes into account the running of the strong coupling and an infrared regulator in the t-channel which is adjusted to compare the energy loss as calculated in a thermal loop approach. This last point is "inherited" from QED plasma [175]. The energy loss in the plasma, computed with pQCD matrix elements, agrees with the one calculated in a hard thermal loop approach.

No prediction is computed for light hadrons R_{AA}. For the D mesons R_{AA}, the calculation is lower than the ALICE measurement.

VI The partonic transport model can be also be computed with a Boltzmann approach to multi-parton scattering (BAMPS) [177]. The difference with respect to what shown in Sec. 2.2.3 is the numerical solution of the Boltzmann equation to understand the charm dynamics. In the BAMPS approach, the full space-time evolution of the QGP is obtained by solving the Boltzmann equation for on-shell partons and pQCD interactions. Together with interactions involving light and heavy quark also the radiative process $gQ \rightarrow gQg$ is considered.

As for the other transport models, no predictions for charged particles R_{AA} are available but the comparison with ALICE D mesons R_{AA} (and flow [176, 177]) is good.

VII The CUJET1.0 model is an extension of DGLV and WHDG models based on the opacity series approach [178]. The CUJET1.0 is a Monte Carlo technique used for jet tomography and it includes several dynamical features that requires larger computational power. Some of the main improvements are related to: dynamical jet interaction potentials, higher order opacity corrections, elastic in addition to radiative fluctuating energy loss distributions.

The CUJET1.0 model seems to be quite in reasonable agreement with both ALICE measurements, but slightly underestimates both.

VIII The BDMPS-ASW model is based on radiative parton energy loss, as introduced in Sec. 2.2.3 [67]. This method can test the colour charge (quark-gluons) and the mass dependence (light-heavy quarks) of parton energy loss. The medium induced parton energy loss depends on the in-medium path length and on the density of the medium by the time-dependent BDMPS transport coefficient $\hat{q}$, which characterizes the average squared momentum transferred from the medium to the hard parton per unit path length.

The BDMPS model is compared with ALICE D mesons results, in case of a transport coefficient $\hat{q} = 25$ GeV^2/fm. The comparison between data and calculation is good. There is no up-to-date calculation for charged hadrons nuclear modification factor for this model.

To summarize, among the models that compute both observables, radiative energy loss with in-medium D meson dissociation (I) and radiative + collisional energy loss in WHDG (II) and CUJET1.0 (VII) approaches describe reasonably well at the same time

charm and light-flavour suppression. The first model considers a medium density tuned to describe the jet suppression at LHC, shown in Sec. 2.3.3. For the radiative + collisional models the medium energy density is scaled accordingly to charged multiplicity density, from the value considered to describe the pion suppression at RHIC. At the LHC the charged hadron suppression is not much stronger than RHIC, despite the large energy increase. This could explain why these models underestimate slightly the charged hardon $R_{\rm AA}$ at LHC.

Conclusions

This thesis was focused on the measurement of the charmed hadron nuclear modification factor, measured in Pb–Pb collisions at $\sqrt{s_{\rm NN}} = 2.76$ TeV. For the first time, the measurement has been performed with the esclusive reconstruction of D mesons, via their hadronic channel decay. At variance with what was achieved in previous measurements, these new results give access to the direct study of the energy loss of the charm quark.

The nuclear modification factor is used to study in-medium energy loss effects. This quantity is computed as the ratio of the particle yields measured in A–A collisions, for a given centrality class, over the yields measured in *pp* collisions, scaled by the corresponding number of binary collisions. An in-medium effect is visible if the ratio goes below 1, since the A–A collisions cannot be consider as a simple superimposition of *pp* collisions, after having consider properly the initial state effects. Charm quark behaviour is important to study the mass and colour charge dependence of parton energy loss.

In this thesis, the measurement of the nuclear modification factor of the $\rm D^0$ meson was presented. The measurement was performed as a function of the transverse momentum of the $\rm D^0$ and as a function of the centrality of the collision. $R_{\rm AA}$ versus transverse momentum was measured in the range $2 < p_{\rm t} < 16$ GeV/c. For the 0-20% centrality class, it indicates a clear suppression that reaches a factor 3-4 for $p_{\rm t} > 5$ GeV/c, where the $R_{\rm AA}$ is about 0.25-0.3. For lower $p_{\rm t}$, the suppression seems to be reduced to a factor of 2. The overall systematic uncertainties on the measurement range between 30% and 50%, depending on different contributions, that vary as a function of $p_{\rm t}$. In the 40-80% centrality class, the suppression is reduced, with $R_{\rm AA} \sim 0.7$ for $p_{\rm t} > 5$ GeV/c. $R_{\rm AA}$ was also studied as a function of the centrality of the collisions for two $p_{\rm t}$ ranges: $2 < p_{\rm t} < 5$ GeV/c, $6 < p_{\rm t} < 12$ GeV/c. The results were presented as a function of the average number of participating nucleons in the collision, for the corresponding centrality classes (0-10%, 10-20%, 20-40%, 40-60%, 60-80%). For the higher $p_{\rm t}$ range considered, the suppression decreases when going from central to peripheral collisions, showing a clear dependence on the number of the participants. For $2 < p_{\rm t} < 5$ GeV/c, the centrality dependence of the suppression is less pronounced. ALICE measured the nuclear modification factor of three D mesons: $\rm D^0$, $\rm D^+$ and $\rm D^{*+}$, with the same analysis strategy. The three measurements are in good agreement.

The $R_{\rm AA}$ observable can be affected by initial state effects in Pb–Pb collisions. The initial hard scattering probability is reduced at low x and Q^2 due to the nuclear modification of the PDFs (nuclear shadowing). The expected effect of shadowing on the D mesons $R_{\rm AA}$ was estimated using MNR next-to-leading order pQCD calculation with EPS09NLO shadowing parameter. This effect on $R_{\rm AA}$ is expected to be $\pm 15\%$ for $p_{\rm t} > 6$ GeV/c, suggesting that the strong suppression observed is likely to be a final state effect. A p–Pb run would allow to study the effect of nuclear shadowing directly on the data. Already in 2011, a study for a possible p–Pb run was started. Machine experts are considering the hypotesis of performing this run in November 2012.

D meson results were also compared with the charged hadron nuclear modification factor, computed in the same centrality class, in order to study the mass and colour charge dependence of the energy loss. The two measurements are very close and, considering that systematic uncertainties of D mesons R_{AA} are partially correlated with p_t, there is an indication that suppression of D mesons may be larger than for charged hadrons.

The ALICE results were also compared with theoretical models that implement predictions for charm energy loss. The different models consider several energy loss mechanisms and different dynamics of the heavy quarks within the medium. Among the eight models considered, five can predicts both D mesons and charged hadrons nuclear modification factors, while three are based on the transport model that starts from the dynamics of heavy quarks in the medium, without considering light quarks interaction with it. Among the models that compute both observables, radiative energy loss with in-medium D mesons dissociation and two approaches radiative plus collisional energy loss describe reasonably well both charm and light-flavour suppressions.

In November 2011, an high luminosity Pb–Pb run was performed. This run would allow to study the D mesons R_{AA} with reduced statistical and systematic uncertainties and for higher and lower D mesons p_t ($p_t < 2$ GeV/c and $p_t > 16$ GeV/c). The measurement at very low p_t can be important to test the dead cone effect in the region where it should be more relevant. The higher-p_t measurement would give information on heavy quark energy loss, in the p_t region where the charged hadrons R_{AA} rises more rapidly than predicted by several of the energy loss models. Another very important measurement is the v_2 for heavy quarks, to study their thermalization in the strongly interaction medium.

Bibliography

[1] J. Chadwick, Nature 192, **312** (1932)

[2] M. Gell-Mann, Phys. Lett. 8 **3**: 214–215 (1964).
G. Zweig, CERN Report No.8182/TH.401. (1964)

[3] R. Feynman, Princeton University Press. (1985).

[4] O. W. Greenberg and C. A. Nelson, Phys. Rept. **32**, 69 (1977).

[5] S. Bethke, Prog. Part. Nucl. Phys. **58** (2007) 351 [hep-ex/0606035].

[6] D. J. Gross and F. Wilczek, Phys. Rev. Lett. **30**, 1343 (1973).

[7] H. D. Politzer, Phys. Rept. **14**, 129 (1974).

[8] F. Karsch, *et al.* Phys. Rev. B **478**, (2000) 447.

[9] K.G. Wilson, Phys. Rev. D **10**, (1974) 2445.

[10] O. Kaczmarek, F. Zantow, Phys. Rev. D **71** 114510 (2005) [hep-lat/0503017].

[11] R. D. Pisarski and F. Wilczek, Phys. Rev. D **29** (1984) 338.

[12] F. Karsch, E. Laermann, Phys. Rev. D **50**, 6954, 6962 (1994)

[13] P. Braun-Munziger and J. Stachel, NATURE **448** (2007) 302, 309.

[14] J.D. Bjorken, Phys. Rev. D **27**, Number 1 (1983).

[15] M. L. Miller, K. Reygers, S. J. Sanders and P. Steinberg, Ann. Rev. Nucl. Part. Sci. **57**, 205 (2007) [arXiv:nucl-ex/0701025].

[16] J. Pearson, $http://www.jpoffline.com/physics_docs/y3s6/nuclearphysics_ln.pdf$

[17] S. Margetis *et al.* [NA49 Collaboration], Phys. Rev. Lett. **75**, (1995) 3814.

[18] B. Abelev *et al.* [STAR Collaboration], Phys. Rev. C **79**, 034909 (2009) [arXiv:0808.2041 [nucl-ex]].

[19] B. Abelev *et al.* [The ALICE Collaboration], Phys. Rev. Lett. **105**, 252301 (2010) [arXiv:1011.3916 [nucl-ex]].

[20] K. Aamodt *et al.* [ALICE Collaboration], Phys. Rev. Lett. **106** (2011) 032301 [arXiv:1012.1657 [nucl-ex]].

[21] A. Toia for the ALICE Collaboration, Quark Matter 2011 proceedings [arXiv:1107.1973 [nucl-ex]].

[22] B. Abelev *et al.* [STAR collaboration] Phys. Rev. C **79** (2009) 034909

[23] M. Floris for the ALICE Collaboration, Quark Matter 2011 proceedings [arXiv:1108.3257 [nucl-ex]].

[24] J. Adams *et al.* [STAR collaboration] Phys. Rev. C **72** (2005) 014904 [arXiv:nucl-ex/0409033]

[25] R. J. Fries, B. Muller, C. Nonaka and S. A. Bass, Phys. Rev. C **68**, 044902 (2003) [nucl-th/0306027].

[26] K. Aamodt *et al.* [The ALICE Collaboration], Phys. Rev. Lett. **105**, 252302 (2010) [arXiv:1011.3914 [nucl-ex]].

[27] R. Snellings for the ALICE Collaboration, Quark Matter 2011 proceedings [arXiv:1106.6284 [nucl-ex]].

[28] J. Adams *et al.* [STAR Collaboration], Nucl. Phys. A **757**, 102 (2005) [arXiv:nucl-ex/0501009].

[29] A. Kalweit for the [ALICE Collaboration], Strangeness in Quark Matter 2011 proceedings

[30] J. Rafelski, J. Letessier and G. Torrieri, Phys. Rev. C **64**, 054907 (2001) [Erratum-ibid. C **65**, 069902 (2002)] [nucl-th/0104042].

[31] K. Fanebust *et al.* [NA57 Collaboration], J. Phys. G: Nucl. Part. Phys. 28 1607 (2002)

[32] M. Nicassio for the [ALICE Collaboration], Strangeness in Quark Matter 2011 proceedings

[33] R. Hagedorn, CERN Rept. 71 (1971);
E. Shuryak, Phys. Lett. B **42**, 357 (1972);
J. Rafelski, and M. Danos, Phys. Lett. B **97**, 279 (1980);
R. Hagedorn *et al.*,ZPhys. C **27**, 541 (1985).

[34] A. Tounsi and K. Redlich, hep-ph/0111159.

[35] T. Matsui and H. Satz, Phys. Lett. B **178** (1986)

[36] R. L. Thews and M. L. Mangano, Phys. Rev. C **73**, 014904 (2006) [nucl-th/0505055].

[37] M. C. Abreu *et al.* [NA50 Collaboration], Phys. Lett. B **477**, 28 (2000).

[38] A. Adare *et al.* [PHENIX Collaboration], [arXiv:hep-ph/0306077]

[39] S. Chatrchyan *et al.* [CMS Collaboration], arXiv:1201.5069 [nucl-ex].

[40] Z. Tang [STAR Collaboration], J. Phys. G G **38**, 124107 (2011) [arXiv:1107.0532 [hep-ex]].

[41] P. Pillot [ALICE Collaboration], J. Phys. G G **38**, 124111 (2011) [arXiv:1108.3795 [hep-ex]].

[42] P. Braun-Munzinger and J. Stachel, arXiv:0901.2500 [nucl-th].

[43] A. Andronic, P. Braun-Munzinger, K. Redlich and J. Stachel, J. Phys. G G **38**, 124081 (2011) [arXiv:1106.6321 [nucl-th]].

[44] X. Zhao and R. Rapp, Nucl. Phys. A **859**, 114 (2011) [arXiv:1102.2194 [hep-ph]].

[45] Y. -p. Liu, Z. Qu, N. Xu and P. -f. Zhuang, Phys. Lett. B **678**, 72 (2009) [arXiv:0901.2757 [nucl-th]].

[46] R. Reed for the STAR Collaboration, Quark Matter 2011 proceedings [arXiv:1109.3891 [nucl-ex]].

[47] V.N. Gribov, L.N. Lipatov, Sov. J Nucl. Phys. **15** (1972) 438 and 675; G. Altarelli, G. Parisi, Nucl. Phys. B **126** (1977) 298; Yu.L. Dokshitzer, Sov. Phys. JETP **46** (1977) 641

[48] G. Altarelli, M. Diemoz, G. Martinelli and P. Nason, Nucl. Phys. B **308** (1988) 724.

[49] M. Mangano, P. Nason and G. Ridolfi, Nucl. Phys. B **373** (1992) 295.

[50] M. Cacciari *et al.*, Phys. Rev. Lett. **95** (2005) 122001

[51] V.G. Kartvelishvili, A.K. Likhoded, and V.A. Petrov, Phys. Lett. B **78**, 615 (1978).

[52] M. Cacciari, S. Frixione, M. L. Mangano, P. Nason and G. Ridolfi, JHEP **0407**, 033 (2004) [hep-ph/0312132].

[53] B.A. Kniehl *et al.*, Phys. Rev. Lett. **96** (2006) 012001

[54] K.J. Eskola *et al.*, arXiv:hep-ph/0110348.

[55] D. d'Enterria, [arXiv:0902.2011v2 [nucl-ex]]

[56] P. Arnold, G.D. Moore and L.G.Yaffe, JHEP **0011**, 057, (2001)

[57] S. Peigné and A. Peshier, [arXiv:0810.5702 [hep-ph]]

[58] P. Arnold, G.D. Moore and L.G.Yaffe, JHEP **0011**, 057, (2001)

[59] M. Djordjevic, M. Gyulassy, Nucl. Phys. A **733** 265 (2004)

[60] Y.L. Dokshitzer, V.A. Khoze and S.I. Troian, J. Phys. G **17**, 1602 (1991); Y.L. Dokshitzer and D.E. Kharzeev, Phys. Lett. B **519**, 199 (2001).

[61] R. Baier, Y. Dokshitzer, A. Mueller, S. Peignè and D. Shiff, Nucl. Phys. B **483**, 291 (1997).

[62] U.A. Weidmann, Nucl. Phys. B **582** 409, (2000).

[63] C.A. Salgando and U.A. Weidmann, Phys. Rev. Lett. **89**, 092303 (2002).

[64] B.G. Zakharov, JEPT Lett. **63**, 952 (1996).

[65] B.G. Zakharov, JEPT Lett. **65**, 615 (1997).

[66] C.A. Salgado and U.A. Wiedemann, Phys. Rev. Lett. **89**, 092303 (2002)

[67] N. Armesto, A. Dainese, C. A. Salgado and U. A. Wiedemann, Phys. Rev. D **71**, 054027 (2005) [hep-ph/0501225].

[68] M. Gyulassy, P. Levai and I. Vitev, Nucl. Phys. B **571** 197 (2000).

[69] M. Djordjevic and M. Gyulassy, Phys. Lett. B **560**, 37 (2003) [nucl-th/0302069].

[70] M. Djordjevic and M. Gyulassy, Nucl. Phys. A **733**, 265 (2004) [nucl-th/0310076].

[71] S. Wicks, W. Horowitz, M. Djordjevic and M. Gyulassy, Nucl. Phys. A **784**, 426 (2007) [nucl-th/0512076].

[72] X.F. Guo and X.N. Wang, Phys. Rev. Lett **85**, 3591, (2000).

[73] X.N. Wang and X.F. Guo, Nucl. Phys. A **696**, 788 (2001).

[74] J. L. Nagle, Eur. Phys. J. C **49** (2007) 275 [nucl-th/0608070].

[75] J.M. Maldacena, Adv. Theor. Math. Phys. **2**, 231, (1998), [Int. J. Theor. Phys. **38** 1113 (1999)] E. Witten, Adv. Theor. Math. Phys. **2**, 505, (1998).

[76] H. Liu, K Rajagopal and U.A. Wiedemann, JHEP **0703**, 066 (2007).

[77] C. P. Herzog, A. Karch, P. Kovtun, C. Kozcaz and L. G. Yaffe, JHEP **0607**, 013 (2006) [hep-th/0605158].

[78] B. Svetitsky, Phys. Rev. D **37** (1988) 2484.

[79] A. Beraudo, J.P. Blaizot, C. Ratti, arXiv:0812.1130v1 [hep-ph]

[80] A. Beraudo, A. De Pace, W.M. Alberico, A. Molinari. arXiv:0902.0741v2 [hep-ph]

[81] M. Monteno, W.M. Alberico, A. Beraudo, A. De Pace, A. Molinari, M. Nardi, F. Prino. Quark Matter 2011 proceedings arXiv:1107.0256v1

[82] V. Greco, H. van Hees and R. Rapp, arXiv:1110.4138 [hep-ph].

[83] P. Petreczky and K. Petrov, Phys. Rev. D **70**, 054503 (2004) [hep-lat/0405009].

[84] V. Greco, C. M. Ko and P. Levai, Phys. Rev. C **68**, 034904 (2003) [nucl-th/0305024].

[85] H. van Hees, V. Greco and R. Rapp, Phys. Rev. C **73**, 034913 (2006) [nucl-th/0508055].

[86] M. Gyulassay, M. Plumer, Phys. Lett. **B243**, 432, (1990); X.N. Wang, M. Gyulassy, Phys. Rev. Lett. **68**, 1480 (1992).

[87] A. Adare *et al.* [PHENIX Collaboration], Phys. Rev. Lett. **101**, 232301 (2008).

[88] B. Muller, Phys. Rev. C **67**, 061901 (2003).

[89] I. Vitev and M. Gyulassy, Phys. Rev. Lett. **89**, 252301 (2002). I. Vitev, J. Phys. G. **30**, S791 (2004).

[90] A. Dainese, C. Loizides and G. Paic, Eur. Phys. J. C **38**, 461 (2005).

[91] S. Turbide, C. Gale, S. Jeon and G.D. Moore Phys. Rev. C **72**, 014906 (2005).

[92] S.A. Bass *et al.* [arxiv:0808.0908 [nucl-th]]

[93] S. Adler *et al.* [PHENIX Collaboration], Phys. Rev. C **76**, 034904 (2007).

[94] A. Adare *et al.* [PHENIX Collaboration], [arXiv:0903.4886 [nucl-ex]]

[95] V.S. Pantuev, JTEP Lett. **85**, 104 (2007).

[96] J. Otwinowski for the ALICE Collaboration, Quark Matter 2011 proceedings arXiv:1110.2985v1

[97] C. Adler *et al.* [STAR Collaboration], Phys. Rev. Lett. **90** 082302 (2003).

[98] S.S. Adler *et al.* [PHENIX Collaboration], Phys. Rev. Lett. **97** 052301 (2006).

[99] J. Adams *et al.* [STAR Collaboration], Phys. Rev. Lett. **95** 152301 (2005).

[100] J. Adams *et al.* [STAR Collaboration], Phys. Rev. Lett. **97** 162301 (2006).

[101] J. Adams *et al.* [STAR Collaboration], Phys. Rev. Lett. **97** (2006) 162301 [arXiv:nucl-ex/0604018].

[102] K. Aamodt *et al.* [ALICE Collaboration], Phys. Rev. Lett. **107** (2011) 032301

[103] K. Aamodt *et al.* [ALICE Collaboration], [arXiv:1110.0121v1 [nucl-ex]]

[104] M. van Leeuween [STAR Collaboration], [arxiv:0808.4096 [nucl-ex]]

[105] M. Ploskon [STAR Collaboration], Nucl. Phys. A **830**, 255c (2009).

[106] S. Chatrchyan *et al.* [CMS Collaboration], Phys. Rev. C **84** (2011) 024906 [arXiv:1102.1957 [nucl-ex]].

[107] S.S. Adler *et al.* [PHENIX Collaboration], Phys. Rev. Lett. **94** 232301 (2005).

[108] CMS Physics Analysis Summary, CMS-PAS-HIN-10-005.

[109] S. Chatrchyan et al. (CMS Collaboration), Phys. Rev. Lett **106** (2011) 212301 [arXiv:1102.5435 [nucl-ex]]

[110] D. Acosta *et al.* [CDF Collaboration], Phys. Rev. Lett. **91** (2003) 241804 [hep-ex/0307080].

[111] A. Abulencia *et al.* [CDF Collaboration], Phys. Rev. D **75** (2007) 012010 [hep-ex/0612015].

[112] A. Adare *et al.* [PHENIX Collaboration], Phys. Rev. Lett. **97** (2006) 252002 [hep-ex/0609010].

[113] Y. Zhang, J. Phys. G G **38** (2011) 124142 [arXiv:1106.6078 [nucl-ex]].

[114] B. I. Abelev *et al.* [STAR Collaboration], arXiv:0805.0364 [nucl-ex].

[115] A. Adare *et al.* [PHENIX Collaboration], Phys. Rev. C **84** (2011) 044905 [arXiv:1005.1627 [nucl-ex]].

[116] L. Evans, (ed.), P. Bryant, (ed.), JINST **3** (2008) S08001.

[117] http://lpcc.web.cern.ch/LPCC/

[118] K. Aamodt *et al.* [ALICE Collaboration], JINST **3** (2008) S08002.

[119] F. Carminati, (Ed.) *et al.* [ALICE Collaboration], J. Phys. G **G30** (2004) 1517-1763.

[120] G. Alessandro, (Ed.) *et al.* [ALICE Collaboration], J. Phys. G **G32** (2006) 1295-2040.

[121] ALICE Off-line framework, AliRoot, http://aliceinfo.cern.ch/Offline

[122] R. Brun, F. Rademakers, Nucl. Instrum. Meth. **A389** (1997) 81-86. ROOT, http://root.cern.ch.

[123] T. Sjostrand, Comput. Phys. Commun. 82 (1994) 74; T. Sjostrand, S. Mrenna and P. Skands, JHEP 2006 05 (2006)

[124] R. Brun et al., CERN Program Library Long Write-up, W5013, GEANT Detector Description and Simulation Tool (1994).

[125] S. Agostinelli et al, Geant4 A Simulation Toolkit CERN-IT-20020003 (2003), KEK Preprint 2002-85, SLACPUB- 9350; Nucl. Inst. Meth. **A** 506 250 http://http://geant4.web.cern.ch/geant4/

[126] Fassò A *et al.*, Proc. Computing in High Energy and Nuclear Physics (La Jolla, CA), (2003) http://www.slac.stanford.edu/econf/C0303241/proc/papers/MOMT004.PDF

[127] X.-N. Wang and M. Gyulassy, Phys. Rev. D **44** 3501 (1991).

[128] P. Saiz *et al.*, Nucl. Inst. Meth. **A 502** (2003) 437-440 .

[129] http://alien.cern.ch.

[130] P. Bilior, Nucl. Instrum. Methods 225 (1984) 352; M. Regler and R. Fruhwirth, Reconstruction of Charged Tracks, Proc. of the Advanced Study Institute on Techniques and Concepts in High Energy Physics, Plenum Publ. Corp., (1989); R. Fruhwirth, Application of the Filter Methods to the Reconstruction of Tracks and Vertices in Events of Experimental High Energy Physics, HEPHY-PUB 516/88, Vienna (1988);

[131] B. Batyunya, Yu. Belikov, K. Safarik, ALICE Internal Note, ALICE-INT-97-24 (1997)

[132] KAamodt *et al.* [ALICE Collaboration], JINST **5** (2010) P03003. [arXiv:1001.0502 [physics.ins-det]].

[133] A. Rossi for the ALICE collaboration, [arXiv:1101.3491v1 [physics.ins-det]].

[134] V. Blobel and C. Kleinwort, contribution to the Conference on Advanced Statistical Techniques in Particle Physics, Durham, March, 18-22, 2002.

[135] A. Rossi, PhD thesis Università degli studi di Trieste (2009).

[136] X.N. Wang and M. Gyulassy, Phys. Rev. D **44** 3501 (1991)
M. Gyulassy and X.N. Wang, Comput. Phys. Commun. **83** 307-31 (1994)
http://www-nsdth.lbl.gov/xnwang/hijing/

[137] E. Bruna, A. Dainese, M. Masera and F. Prino, ALICE Internal Note 2009-018 (2009)

[138] V. Karimäki, CMS Note 1997/051 (1997).

[139] P.Z. Skands, Multi-Parton Interaction Workshop, Perugia, Italy, 28-31 Oct. 2008, arXiv:0905.3418[hep-ph] (2009), Perugia-0 (320) tune

[140] R. Engel, J. Ranft, S. Roesler, Phys. Rev. **D 52**, 1459 (1995)

[141] KAamodt *et al.* [ALICE Collaboration], Eur. Phys. J. C **65**, 111 (2010) [arXiv:0911.5430 [hep-ex]].

[142] K. Aamodt *et al.* [ALICE Collaboration], Eur. Phys. J. C **68**, 345 (2010) [arXiv:1004.3514 [hep-ex]].

[143] BAbelev *et al.* [The ALICE Collaboration], Phys. Rev. Lett. **105**, 252301 (2010) [arXiv:1011.3916 [nucl-ex]].

[144] A. Dainese, *Charm production and in-medium QCD energy loss in mucleus-nucleus colliisons with ALICE. A performance study,* PHD thesis (2003).

[145] K. Nakamura *et al.* (Particle Data Group), J. Phys. **G 37**, 075021 (2010) and 2011 partial update for the 2012 edition.

[146] F. James,
MINUIT Function Minimization and Error Analysis, CERN program Library Long Writeup D506.
http://www.asdoc.web.cern.ch/wwwasdoc/minuit/minmain.html

[147] H. De Vries, C.W. De Jager, and C. De Vries, Atom. Data Nucl. Data Tabl. **36**, 495 (1987). Since the Woods-Saxon parameters for 208Pb are not available, we use the values for 207Pb. Note that the Bessel-Fourier coefficients for the two nuclei are similar.

[148] D.J. Lange, Nucl. Instrum. Methods **A462** (2001) 152.

[149] T. Sjostrand, S. Mrenna, P. Skands, JHEP **05** (2006) 026

[150] P. Skands, [arXiv:0905.3418] (2009).

[151] ALICE Collaboration, paper in preparation. "Suppression of high transverse momentum D mesons in central Pb–Pb collisions at $\sqrt{s_{\rm NN}} = 2.76$ TeV."

[152] S. van der Meer, ISR-PO/68-31, KEK68-64

[153] K. Oyama for the ALICE collaboration, Quark Matter 2011 Proceedings [arXiv:1107.0692v1]

[154] M. Gagliardi, arXiv:1109.5369 [hep-ex].

[155] [ALICE Collaboration], arXiv:1111.1553 [hep-ex].

[156] P.M. Nadolsky *et al.*, Phys. Rev. **D78** (2008) 013004.

[157] A. Dainese, J. Phys. G G **38**, 124032 (2011) [arXiv:1106.4042 [nucl-ex]].

[158] ATLAS collaboration, internal note: ATLAS-CONF-2011-017 (2011).

[159] LHCb collaboration, internal note: LHCb-CONF-2010-013 (2010).

[160] B. Alessandro *et al.* [ALICE Collaboration], J. Phys. **G32** (2006) 1295.

[161] R. Averbeck, N. Bastid, Z. C. del Valle, P. Crochet, A. Dainese and X. Zhang, arXiv:1107.3243 [hep-ph].

[162] J. Pumplin *et al.*, JHEP **0207** (2002) 012.

[163] K. J. Eskola, H. Paukkunen and C. A. Salgado, arXiv:0903.1956 [hep-ph].

[164] H. Appelshauser for the ALICE Collaboration, J. Phys. **G38** (2011) 124014.

[165] S. Masciocchi [ALICE Collaboration], J. Phys. G G **38**, 124069 (2011) [arXiv:1109.6436 [nucl-ex]].

[166] CMS collaboration, CMS-PAS-HIN-10-006 (2011).

[167] Z. -B. Kang and I. Vitev, Phys. Rev. D **84**, 014034 (2011) [arXiv:1106.1493 [hep-ph]].

[168] R. Sharma, I. Vitev and B. -W. Zhang, Phys. Rev. **C80** (2009) 054902.

[169] W. A. Horowitz and Y. .V. Kovchegov, J. Phys. G G **38**, 124064 (2011) [arXiv:1106.5456 [hep-ph]].

[170] W. A. Horowitz, arXiv:1108.5876 [hep-ph].

[171] W. A. Horowitz, arXiv:1011.4315 [hep-ph].

[172] C.P. Herzog, A. Karch, P. Kovtun, C. Kozcaz, and L.G. Yaffe, JHEP **07**, 013 (2006), hep-th/0605158.

[173] W. M. Alberico, A. Beraudo, A. De Pace, A. Molinari, M. Monteno, M. Nardi and F. Prino, Eur. Phys. J. C **71**, 1666 (2011) [arXiv:1101.6008 [hep-ph]].

[174] P. B. Gossiaux, R. Bierkandt and J. Aichelin, Phys. Rev. C **79**, 044906 (2009) [arXiv:0901.0946 [hep-ph]].

[175] E. Braaten and M.H. Thoma, Phys. Rev. **D 44**, 1298 (1991)

[176] C. Bianchin [for the ALICE Collaboration], arXiv:1111.6886 [hep-ex].

[177] J. Uphoff, O. Fochler, Z. Xu and C. Greiner, arXiv:1112.1559 [hep-ph].

[178] A. Buzzatti and M. Gyulassy, arXiv:1106.3061 [hep-ph].

Acknowledgements

I would really like to thank all the people that in these three years allowed me to learn so much and to make me enjoy doing research. First of all, I would like to thank Andrea Dainese: he followed me in every moment of my PhD, he was always available for discussion in case of any doubts, questions or problems I had in these three years. I'm also very grateful to Giuseppe Viesti for his prompt helpfulness in every moment. I would like also to thank all the ALICE Padova group that allowed me to spent two years of my PhD at CERN, during the most exciting moment since 15 years: the staring of the LHC. I would like to thank Federico and Rosario for their experience and the fruitful discussions I had with them in these three years, Chiara has been a "co-PhD" with the sharing of all the problems and the experiences we had, but she become also a good friend; it was a pleasure to work with Andrea on the analysis, on this thesis and I'm really grateful to him for his time spent in chatting and discussing about physics, music and so on. I would like also to thank all the other members of the ALICE Padova group: Claudio, Andrea, Sandra, Marcello, Daniela, Francesca, Maurizio, Xianbao and Carlo.

The two years CERN experience was really amazing. I had the possibility to work and to know many people coming from all over the world. I shared informations, experiences and nights with them learning and talking about physics but not only. As rappresentative of these two years there, I would like to thank Annalisa, Chiara and Zaida. Each of them helped me in a part of my work that entered in this thesis and they are really smart and amazing colleagues and also good friends.

Last, I would like to thank my family for being always with me even if some kilometers away.